Imperial College London

Improving the Stability of Organometallic Halide Perovskite Photoactive Layers and Solar Cells via Film Passivation with Iodide Salts

Xiangnan Bu

Faculty of Nature Science
Department of Chemistry

- July 2019 –

A thesis submitted in fulfilment of the requirements for the degree of Doctor of Philosophy

The copyright of this thesis rests with the author. Unless otherwise indicated, its contents are licensed under a Creative Commons Attribution-NonCommercial 4.0 International Licence (CC BY-NC).
Under this licence, you may copy and redistribute the material in any medium or format. You may also create and distribute modified versions of the work. This is on the condition that: you credit the author and do not use it, or any derivative works, for a commercial purpose.
When reusing or sharing this work, ensure you make the licence terms clear to others by naming the licence and linking to the licence text. Where a work has been adapted, you should indicate that the work has been changed and describe those changes.
Please seek permission from the copyright holder for uses of this work that are not included in this licence or permitted under UK Copyright Law.

DECLARATION OF ORIGINALITY

Except where specific reference is made, all images, figures and experimental results contained in this thesis is the result of my own work. It has not been submitted either in whole or in part to satisfy any degree requirement at this or any other university. The thesis does not exceed 100,000 words in length.

Xiangnan Bu

London

July 2019

ABSTRACT

Methylammonium lead halide perovskite materials are receiving great attention as promising candidates for industrial applications, but their long-term stability when used in solar devices remains problematic. In particular, the perovskite layers based on $CH_3NH_3PbI_3$ (methylammonium lead iodide, MAPI) experience severe degradation caused by oxygen and light. An understanding of this process, and how to enhance stablility, is distinctly important in the evolution of devices utilising perovskite.

The systematic study of MAPI-based solar cells is investigated in first results chapter. Factors such as compact layer thickness, mesoporous layer thickness, $TiCl_4$ surface treatment and Spiro-OMeTAD oxidation are studied. Furthermore, the issues of how photo- and oxygen-induced degradation, and thus the superoxide formation, will affect the efficiency and stability of the perovskite devices are addressed.

The second results chapter builds on the knowledge that iodide vacancies in MAPI crystals are the most-preferred sites for superoxide formation. First, a film passivation technique was devised using methylammonium iodide (MAI) coating. The treatment could effectively reduce the suface defects and improve device stability by inhibiting superoxide generation. Second, the relation between superoxide formation and device stability as a function of bromide composition for Br-I mixed halide solar cells is examined.

Use of an alternative passivating agent, namely phenylethylammonium iodide (PEAI) shows that it is highly effective on enhancing film and device stability under light and oxygen without reducing performance. The results confirm that this iodide salt could help to reduce problematic vacancies and therefore lower superoxide yields and improve device stability.

Extending the investigation further, in final results chapter, a novel Iodide Salt Assisted Anti-solvent Treatment (ISAAT) for preparing MAPI layer is developed. The ISAAT strategy could effectively enhance the morphology and crystallinity of the perovskite films. With ISAAT treatment, devices are more stable and efficient than without treatment. More importantly, this ISAAT method shows more reproducibility than direct PEAI treatment, thereby elucidating an effective methodology of future design and optimisation of perovskite solar cells with better efficiency, long-term durability and reproducibility.

ACKNOWLEDGEMENTS

Over the course of my PhD study I wish to express my scincere gratitude to many people for their unfailing help, intellect and friendship, without whom this work would not have been possible.

First, I would like to thank my first supervisor, Prof. Saif Haque, for taking me on as an MRes student, and then accepting me once again when I applied to undertake a PhD. Thanks go to Saif for providing a superior workplace, although working in the basement of the Chemistry Department may sometimes feel rather unglamorous. Saif has a truly exceptional academic brain, and has always supported me throughout my PhD career with dedication and kindness.

I have also benefitted a great deal from the support given by our internal and external collaborators for providing materials, and experimental and theoretical assistance: for physics – Prof. Jenny Nelson, Dr. Xingyuan Shi; for materials – Dr. Martyn McLachlan, Tian Du, Brady Lin; for Chemistry – Prof. James Durrant, Dr. Xiaoe Li, Dr. Pabitra Shakya, Kim Jinhyun; from the University of Bath, UK – Prof. Saiful Islam, Dr. Alex Aziz. Closer to home, several current and past members of our research group deserve a special mention for the help and guidance they have given me: first is Dr Thomas Rath for his extreme kindness and patience and uncountable helpful ideas, thanks to Robert for his help on TCSPC, Luis for X-Ray diffraction and many useful discussions, Dong and Thana for SEM measurements, Dr. Irene for her organic chemistry knowledge, Dr. Jose and Dr. Simon for their guidance on fabricating devices, Nicholas for his PL guidance on superoxide tests, and Dr. Andy and Micheal Brown for setting me going in the lab.

From home, my deep gratitude goes to my father Mr Fanbin Bu and my mother Mrs Ruihua Zhang for their thoughtful financial support during my PhD study, and the Department of Chemistry at Imperial College, London, which has been my home-from-home for many years.

Finally, thanks a million to my wife Mrs Mowei Gao, not only for supporting me in whatever I do, but also for providing such a welcoming, happy, stress-relieving retreat whenever I needed it.

TABLE OF CONTENTS

Declaration of Originality **3**
Abstract **5**
Acknowledgements **6**
Table of Contents **7**
List of Publications **10**
List of Figures **11**
List of Tables **19**
Frequently Used Acronyms and Abbreviations **20**
Chapter 1 Introduction **21**
1.1. Unsustainable Reliance on Fossil Fuels **21**
1.2. Renewable Technologies **22**
1.3. References **24**
Chapter 2 Background Knowledge **25**
2.1. Introduction to Photovoltaic Technologies **25**
2.1.1. Semiconductors and P-N Junction 25
2.1.2. Inorganic Solar Cells 28
2.1.3. Organic Solar Cells (OPVs) 29
2.1.4. Dye Sensitized Solar Cells (DSSCs) 31
2.2. Overview of the Progress on Perovskite Solar Cells (PSCs) **33**
2.3. Photovoltaic Parameters in Perovskite Solar Cells (PSCs) **36**
2.3.1. Power Conversion Efficiency (PCE) 36
2.3.2. Short Circuit Current Density (J_{sc}) 39
2.3.3. Open Circuit Voltage (V_{oc}) 40
2.3.4. Fill Factor (FF) 41
2.4. Recent Progress on the Stability of Perovskite Solar Cells **42**
2.4.1. Phase Stability 43
2.4.2. Thermal Stability 44
2.4.3. Moisture 46
2.4.4. UV Irradiation 47
2.4.5. Oxygen 48

2.5. Motivations and Layout of Thesis **51**
2.6. References **54**
Chapter 3 Experimental Methods **63**
3.1. Materials **63**
3.2. Solar Cell Fabrication **64**
3.2.1. Substrate Preparation and Fabrication of Metal Oxide Films 64
3.2.2. Titanium Tetrachloride ($TiCl_4$) Surface Treatment 64
3.2.3. Synthesis and Preparation of Perovskite Active Layer 65
3.2.4. Preparation of Perovskite Films with Iodine Salt Coating 65
3.2.5. Preparation of Hole Transporting Layer and Scraping 66
3.2.6. Thermal Evaporation 66
3.2.7. Measurement of Material Stability under Oxygen and Light 67
3.3. Physical and Optical Characterization Techniques **68**
3.3.1. Current-Voltage Characterizations (J-V) 68
3.3.2. External Quantum Efficiency Measurement (EQE) 69
3.3.3. Scanning Electron Microscopy (SEM) 69
3.3.4. Steady State UV-Visible Absorption Spectroscopy (UV-VIS) 69
3.3.5. Steady State Photoluminescence Spectroscopy (PL) 69
3.3.6. Transient Absorption Spectroscopy (TAS) 70
3.3.7. Time Resolved Photoluminescence Spectroscopy (TCSPC) 72
3.3.8. X-Ray Diffraction (XRD) 72
3.3.9. Superoxide Probe Testing (SPT) 73
3.4. References **74**
Chapter 4 The Influence of the Crystal Size on the Light and Oxygen Induced Degradation of Perovskite Solar Cells **75**
4.1. Abstract **75**
4.2. Introduction **76**
4.3. Experimental **78**
4.4. Results and Discussion **80**
4.4.1. Parameters Affecting the Efficiency and Stability of the Perovskite Solar Cell 80
4.4.2. Correlations of Crystal Size, Superoxide Formation and Device Parameters 91
4.5. Conclusion **96**
4.6. References **97**

Chapter 5 Methylammonium Iodide Salt Treatment on Methylammonium Lead Triiodide and Bromide Mixed Halide Perovskite Solar Cells for Enhanced Stability 99

5.1. Abstract 99

5.2. Introduction 100

5.3. Experimental 101

5.3.1. Iodide Salt Treatment Device Fabrication 101

5.3.2. $MAPbI_3$ and $MAPbBr_3$ Solutions and Film Fabrication 102

5.3.3. $MAPb(I_{1-x}Br_x)_3$ Film Fabrication 102

5.4. Results and Discussion 103

5.4.1. Methylammonium Iodide (MAI) Salt Treatment in MAPI Perovskite Solar Cells 103

5.4.2. MAI Treatment in Bromine (Br)-Substituted Perovskite Solar Cells (PSCs) 115

5.5. Conclusion 129

5.6. References 130

Chapter 6 Phenylethylammonium Iodide as a Surface Passivation Agent for Enhanced Efficiency and Stability of $CH_3NH_3PbI_3$ Perovskite Films and Solar Cells 132

6.1. Abstract 132

6.2. Introduction 133

6.3. Experimental 136

6.4. Results and Discussion 139

6.5. Conclusion 156

6.6. References 157

Chapter 7 A Facile Iodide Salt Additive Assisted Treatment for Enhanced Efficiency, Stability and Reproducibility of $CH_3NH_3PbI_3$ Perovskite Films and Solar Cells 160

7.1. Abstract 160

7.2. Introduction 161

7.3. Experimental 163

7.3.1. $CH_3NH_3PbI_3$ Film with Iodide Salt Assisted Anti-solvent Treatment (ISAAT) 163

7.4. Results and Discussion 164

7.5. Conclusion 185

7.6. References 186

Chapter 8 Conclusions and Future Outlook 188

LIST OF PUBLICATIONS

- **Fast oxygen diffusion and iodide defects mediate oxygen-induced degradation of perovskite solar cells**. Nicholas Aristidou, Christopher Eames, Irene Sanchez-Molina, **Xiangnan Bu**, Jan Kosco, M. Saiful Islam, and Saif A. Haque*. *Nature Communications* 2017 (8).

- **Surface passivation of perovskite films via iodide salt coatings for enhanced stability of organic lead halide perovskite solar cells**. **Xiangnan Bu,** Robert J.E. Westbrook, Luis Lanzetta, Dong Ding, Thana Chotchuangchutchaval, Nicholas Aristidou and Saif A. Haque*. *Solar RRL 2018 (1800282).*

- **Understanding the enhanced stability of bromide substitution in lead iodide perovskites.** Alex Aziz, Nicholas Aristidou, **Xiangnan Bu**, Lilian Watson, M. Saiful Islam and Saif A. Haque* *Energy & Environmental Science* (unpublished manuscript)

- **Improved charge collection via sulphur doping on bismuth iodide thin films for photovoltaic application.** Bowon Yoo, Dong Ding, Jose M. Marin-Beloqui, Luis Lanzetta, **Xiangnan Bu,** Thomas Rath and Saif. A. Haque* *ACS Applied Energy Materials* (unpublished manuscript)

LIST OF FIGURES

Figure 2-1: Energy level diagram representing the formation of semiconductors. (a) Combination of two Atomic Orbitals (AOs) resulting in two Molecular Orbitals (MOs), with one energy higher (known as the 'anti-bonding MO'), and one energy lower (known as the 'bonding MO') than the sum of individual AOs. (b) Combination of more atoms leads to the formation of more bonding and anti-bonding MOs. (c) In a crystal there are many orbitals, so energies appear continuous and are named as 'bands'. The bonding MO is named as the valence band (VB), and anti-bonding MO is the conduction band (CB). The crystal shows metallic behaviour if two bands overlaps. If there is a 'gap' between bands then the crystal is either a semiconductor or an insulator. 26

Figure 2-2: Schematic of a typical p-n junction solar cells doped with n-type and p-type impurities. 27

Figure 2-3: Schematic mechanisms of an organic semiconductor heterojunction solar cells (organic photovoltaics, OPVs). The compound with the smaller ionization potential (IP) is known as the 'electron donor' (e.g.P3HT) while that with the larger electron affinity (EA) is referred to as the 'electron acceptor' (e.g. PCBM). Upon photo-excitation, the exciton is dissociated into freely moved charges at the acceptor/donor interface which undergo further transport to the anode (e.g. ITO) and cathode (eg. Al). HOMO: highest occupied molecular orbital, LUMO: lowest unoccupied molecular orbital. 29

Figure 2-4: Schematic construction and working principle of a dye-sensitized solar cell (DSSC) with liquid-electrolyte based on mesoporous TiO_2 photoanode and I^- / I_3^- redox couple. FTO = fluorine-doped tin oxide; WE= working electrode. CB = conduction band**;** $E_{F:}$ electron quasi-Fermi level**.**..... 31

Figure 2-5: Standard crystal structure of the cubic metal halide perovskites with a chemical formula of ABX_3. Position A is occupied by organic or inorganic cation A (green), whereas position B (grey) and X (purple) are occupied by metal cations and halides, respectively.[13] 33

Figure 2-6: Schematic current-voltage (J-V) curve for a photovoltaic device measured in the dark (black dashed line) and under illumination (red line). The short-circuit current density (J_{sc}) and open-circuit voltage (V_{oc}) are illustrated, along with the value at which the solar cell generates the most power (P_m). The fill factor (FF) is a description of the 'squareness' of the curve and is calculated from the ratio of the red and blue squares. 36

Figure 2-7: (a) Equivalent circuit for a device consisting of a current source (delivering I_{sc}), a diode, and two resistances which represent the non-ideal case in a single device – a shunt resistance (R_{sh}) in parallel, and a series resistance (R_s) in series. (b) J-V curve of an illuminated solar cell under a variation of R_s and R_{sh}. 38

Figure 2-8: Proposed degradation mechanism for perovskite solar cells under the influence of UV illumination. (a) The surface of TiO_2 contains many oxygen vacancies (Ti^{3+}) that act as electron-donating sites. The electrons of these sites interact with molegular oxygen from atmosphere to form a charge transfer complex (O_2^- -Ti^{4+}) (shown as δ^- - δ^+). (b) Upon UV illumination, the photogenerated holes react with oxygen radicals absorbed at surface oxygen vacancy, forming a hole in the valence band (VB), which further recombines with the electrons in the oxygen vacancy, leading to O_2 to desorb. (c) Upon photo excitation of the perovskite, electrons can inject either (1) into the conduction band or (2) directly in the deep surface traps. (d) The deeply trapped electrons are recombined with holes on HTM, leading to a decrease in J_{sc} and the degradation of the perovskite solar cells. (Image modified from reference [125]). 47

Figure 2-9: The envisaged principle for the formation of superoxide species and MAPI degradation. (a) The energy level diagrams of mesoporous (mp) TiO_2 or Al_2O_3/MAPI interfaces illustrating smoothly electron transfer. Transfer of photo-excited electrons from MAPI photoactive layer to oxygen leads to superoxide formation. In case of mp-Al_2O_3, electrons stay on the MAPI photoactive layer and is then transferred to ambient oxygen. In case of mp-TiO_2, the electrons can be extracted rapidly by mp-TiO_2 layer and can effectively compete with electron transfer to oxygen leading to lower superoxide formation

and thus greater lifetime for perovskite layer. (b) The overall reaction of MAPI degradation. The cascade reaction is induced by a deprotonation reaction from organic cation by superoxide created under illumination and oxygen.[173] 48

Figure 2-10: Normalized power conversion efficiency (PCE) as a function of illumination time for $CH_3NH_3PbI_3$ (MAPI) solar cells under light and oxygen for three different solar cell architectures. Device 1: FTO/compact-TiO_2/mp-TiO_2/MAPI/**S**piro-OMeTAD/Au (red); Device 2: FTO/compact-TiO_2/MAPI/**S**piro-OMeTAD/Au (black); Device 3: FTO/compact-TiO_2/mp-Al_2O_3/MAPI/spiro-OMeTAD/Au (green).[119] 49

Figure 3-1: Schemes of the fabrication procedure for perovskite solar cells with MAPI as active layer... 66

Figure 3-2: Experimental setup used for film degradation under dry air and light. (a) Schematic representation of experimental set-up. (b) Photograph of setup showing sample rack. Note: up to four samples could be measured simultaneously under identical conditions using this apparatus. 67

Figure 3-3: Experimental set up of the solar simulator system used for conducting fresh and stability measurement of our perovskite solar cells. (a) Keithley 2400 sourcemeter for measuring generated photocurrent. (b) LCS-100^{TM} solar simulator system and (c) computer for showing the J-V curves and key photovoltaic parameters..... 68

Figure 3-4: Schematic diagram demonstrating the transient absorption spectroscopy (TAS) equipment used in this project. (Either dry N_2 or dry air was used as the sample gas) 70

Figure 3-5: Typical types of data generated by FR and TR modes of TAS. (a) FR spectrum. (b) TR decay trace. 71

Figure 4-1: Schematic illustration of the reaction between $CH_3NH_3PbI_3$ (MAPI) and O_2. (a) Oxygen diffusion is incorporated into the crystal lattice, (b) photoexcitation occurs at MAPI layer and create electrons and holes (c) superoxide formation from O_2, and (d) degradation of MAPI to I_2, CH_3NH_2, PbI_2 and H_2O.[18] 77

Figure 4-2: (a) Current-voltage curves of $CH_3NH_3PbI_3$ (MAPI) perovskite solar cells using the spray pyrolysis method for different thicknesses of compact TiO_2 layer (thickness is based on the number of spraying cycles). The solid line refers to the forward bias scan (from SC to FB) and the dash line refers to the reverse biasscan (where 'R' represents 'reverse') (from FB to SC) (b) The current-voltage curves of the best devices (compact layer thickness = 50 nm) using spin coating and spray pyrolysis for making compact TiO_2 layer. The structure of device is FTO/c- TiO_2 /mp-TiO_2 /Perovskite/Spiro-OMeTAD/Au (where '/' represents interface)..... 81

Figure 4-3: Performance of key device parameters (a) Jsc; (b) Voc; (c) FF and (d) PCE as a function of compact layer thickness using the spray pyrolysis method. 81

Figure 4-4: Current-voltage curves of $CH_3NH_3PbI_3$ (MAPI) perovskite solar cells with thicknesses of 350 nm, 400nm, 700nm and 800nm respectively at forward (SC-FB, solid lines) and reverse (FB-SC, dashed lines) scan. The experiment are carried out under continuous AM 1.5G one sun illumination (100 mW/cm^2) with a scan rate of 25 mV/s.. 84

Figure 4-5: (a) Light- and (b) Dark current-voltage curves of $CH_3NH_3PbI_3$ (MAPI) perovskite solar cells with different concentrations of $TiCl_4$ post treatment on top of mesoporous TiO_2 layer, all curves were performed under reverse scan conditions (FB-SC). The measurements are carried out under AM 1.5G one sun illumination (100 mW/cm^2) with a scan speed of 25 mV/s. 86

Figure 4-6: Performance of key device parameters (a) Jsc; (b) Voc; (c) FF and (d) PCE as a function of the concentrations of $TiCl_4$ post treatment. 86

Figure 4-7: (a) Power conversion efficiency (PCE) of the $CH_3NH_3PbI_3$ (MAPI) perovskite solar cells with Spiro-OMeTAD aging at different periods of time. Aging time is also an important factor on device performance. According to the test result, 48 hours of aging time resulted in best device efficiency. (b) Current-Voltage curves of MAPI perovskite solar cells with Spiro-OMeTAD aging for 48 hours (red line) and without aging (black line) under forward (SC-FB, solid line) and reverse scan (FB-SC, dashed line).88

Figure 4-8: (a) Current-voltage curve of the optimized $CH_3NH_3PbI_3$ (MAPI) perovskite solar cell measured under light (black line) and dark (red line) conditions. (b) External quantum efficiency (EQE) spectra of the same device. 89

Figure 4-9: The histograms of (a) J_{sc} from I-V curves, (b) V_{oc} and (c) Fill factor and (d) PCE for an amount of 27 $CH_3NH_3PbI_3$ perovskite solar cells. 90

Figure 4-10: (a), (b) and (c): Surface SEM images of small (100 nm), medium (150 nm) and large (250 nm) crystal size of $CH_3NH_3PbI_3$ (MAPI) films deposited on cleaned glass substrates; (d), (e) and (f): Current-voltage characteristics of MAPI perovskite solar cells based on small (100 nm), medium (150 nm) and large (250 nm) crystal size. All devices using FTO/c-TiO_2/mp-TiO_2/$CH_3NH_3PbI_3$ /Spiro-OMeTAD/Au architecture, and were degraded under continuous one sun illumination and dry air-flow. 92

Figure 4-11: (a) The superoxide yield plot comparing the formation of superoxide for $CH_3NH_3PbI_3$ (MAPI) treated with small (100 nm), medium (150 nm) and large (250 nm) crystal size; (b) Normalised power conversion efficiency (PCE) loss for photovoltaic devices employing MAPI with small (100 nm), medium (150 nm) and large (250 nm) crystal size using FTO/c-TiO_2/mp-TiO_2/perovskite/Spiro-OMeTAD/Au architecture. 93

Figure 4-12: (a), (b) and (c): Surface SEM images of $CH_3NH_3PbI_3$ (MAPI), $Cs_{0.15}FA_{0.85}PI_3$ (CsFAPI) and $CH_3NH_3PbI_{3-x}Cl_x$ (MAPIC) films deposited on cleaned glass substrates; (d), (e) and (f): Current-voltage characteristics of MAPI perovskite solar cells based on MAPI, CsFAPI and MAPIC active layer. All devices used FTO/c-TiO_2/mp-TiO_2/perovskites /Spiro-OMeTAD/Au architecture, and were degraded under continuous one sun illumination and dry air-flow. 94

Figure 4-13: (a) Superoxide yield plot comparing the generation of superoxide for $CH_3NH_3PbI_3$ (MAPI), $Cs_{0.15}FA_{0.85}PI_3$ (CsFAPI) and $CH_3NH_3PbI_{3-x}Cl_x$ (MAPIC) films; (b) Normalised power conversion efficiency (PCE) loss for photovoltaic devices employing $CH_3NH_3PbI_3$ (MAPI), $Cs_{0.15}FA_{0.85}PI_3$ (CsFAPI) and $CH_3NH_3PbI_{3-x}Cl_x$ (MAPIC) using FTO/c-TiO_2/mp-TiO_2/perovskites/Spiro-OMeTAD/Au architecture. 95

Figure 5-1: Schematic representation of possible O_2 binding and reduction sites in $CH_3NH_3PbI_3$ (MAPI) in the crystal lattice and corresponding superoxide formation energy: **(a)** Face site neighbouring four iodide ions, **(b)** neutral iodide vacancy (with a photoelectron on the defect site) and negatively charged lead **(c)**, and methylammonium **(d)** vacancies (with no photoelectron on them since this was found to be unphysical).[18] 105

Figure 5-2: Atomic structure of $CH_3NH_3PbI_3$ (MAPI) showing **(a)** superoxide ion, O_2^-, occupying an iodide vacancy, VI × (for clarity, a pseudo-cubic sub-region of the structure is shown and not the full tetragonal supercell used in the calculations). **(b)** Comparison of relative size of iodide and superoxide anions (using ionic radius of I^- and for superoxide ion interpolation between covalent radius in O_2 and ionic radius of O^{2-}). **[18]** 106

Figure 5-3: Schematic of oxygen diffusion pathways and associated degradation regions of MAPI particles. **(a)** O_2 diffusion in inter-particle regions and initial reaction with particle surfaces over a timescale of hours leading to reduction in device efficiency, open circuit voltage and photocurrent, and **(b)**,

O_2 diffusion into particle bulk regions over a time scale of days leading to a phase change from the photo-absorbing perovskite phase into the non-absorbing lead iodide phase. 107

Figure 5-4: Schemes of the MAI iodide salt passivation procedure for perovskite solar cells with $CH_3NH_3PbI_3$ (MAPI) as active layer. 108

Figure 5-5: (a) Current-voltage curves of initial performances of $CH_3NH_3PbI_3$ (MAPbI) devices without iodide salt coating (black) and with MAI coating in various concentrations of 1 mM (dark red), 2.0 mM (dark cyan), 6 mM (orange) and 10 mM (violet). Devices were measured using xenon lamp AM1.5 simulated solar spectrum with a scan rate of 0.125 V/s. The initial device is held at open circuit conditions for 60 seconds to stabilise and then scanned from 0 V to 1.2 V, both illuminated current (solid line) and dark current (dashed line) are recorded. (All results are backward scan FB-SC). **(b)** The External Quantum Efficiency (EQE) spectra of devices without and with various concentrations of MAI coating. All devices are fabricated in FTO/compact-TiO_2/mesoporous-TiO_2/perovskite (iodide salt)/Spiro-OMeTAD/Au architecture. (Open circuit voltage: V_{oc}; short circuit current density: J_{sc}; Fill Factor: FF; power conversion efficiency: PCE.) 109

Figure 5-6: Influence of the MAI salt concentration on current-voltage hysteresis of the MAPI devices. The devices are measured in reverse scan (FB-SC) and forward scan (SC-FB) under simulated AM1.5 100 mW cm^{-2} sunlight with **(a)** MAPI (black), **(b)** 1 mM (dark red), **(c)** 2.0 mM (dark cyan), **(d)** 6 mM (orange) and **(e)** 10 mM (violet) of MAI salt coated on MAPI perovskite solar cells. The scan rate is 0.125 V/s for all devices. 110

Figure 5-7: Current-voltage curves obtained during degradation for $CH_3NH_3PbI_3$ (MAPI) devices without and with methylammonium iodide (MAI) treatment in varies concentrations of: 1mM, 2mM, 6mM and 10mM. All devices are fabricated in FTO/compact-TiO_2/mesoporous-TiO_2/perovskite (iodide salt)/Spiro-OMeTAD/Au architecture and were under continuous illumination for a period of five hours. 112

Figure 5-8: (a) Short term stability test (normalised efficiency loss) for the same devices with and without methylammonium iodide (MAI) salt coating in various concentration of 1 mM (dark red), 2.0 mM (dark cyan), 6 mM (orange), 20 mM (violet) and for a period of 5 hours. **(b)** Superoxide yield plot comparing the generation of superoxide for MAPI treated with different concentrations and without methylammonium iodide (MAI) salt coating. The normalised fluorescence intensity increase of the HE probe at 610 nm (excitation at 520 nm). $I_F(t)$ is the fluorescence maximum at time t, whilst $I_F(t_0)$ is the background fluorescence intensity. $I_F(t)/ I_F(t_0)$ ratio corresponds to yield of superoxide generation for perovskite films. 113

Figure 5-9: Long-term stability test (normalised efficiency loss) for devices employing $CH_3NH_3PbI_3$ (MAPI) without (black) and with (violet) MAI salt coating in 10 mM salt coating for a period of 500 hours. The temperature was kept constant at 25°C. 114

Figure 5-10: (a) Superoxide yield generation for the films under oxygen and light conditions for $MAPb(I_{1-x}Br_x)_3$ where x = 0, 0.1, 0.2, 0.5, 0.75 and 1. Superoxide yields increase as the Iodide content increases. (b) Normalised absorbance decays as a function of aging under oxygen and light conditions for $MAPb(I_{1-x}Br_x)_3$ where x = 0, 0.1, 0.2, 0.5, 0.75 and 1. Films become more stable as the bromine content increases. 117

Figure 5-11: Calculated reaction energies for the degradation reactions with respect to the different bromide compositions in $CH_3NH_3Pb(I_{1-x}Br_x)_3$ system. (See Equations 5 and 6 in the text). (unpublished manuscript) 118

Figure 5-12: H-bonding between H_N and X in a) $CH_3NH_3PbI_3$ and b) $CH_3NH_3PbBr_3$. (The violet ball represent iodide ions and the red ball represents smaller bromide ions). (unpublished manuscript) 119

Figure 5-13: Current-voltage curves for $MAPb(I_{1-x}Br_x)_3$ devices with composition between x = 0 to x = 1. 120

Figure 5-14: Normalised efficiency loss for devices with bromide composition of between $x = 0$ to $x = 1.0$ in $MAPb(I_{1-x}Br_x)_3$ under continuous solar simulator illumination. 122

Figure 5-15: Transient absorption spectra traces for $x = 0.2$ in $MAPb(I_{1-x}Br_x)_3$ film composition, with and without a 0.01M salt treatment after 0 and 60 minutes of exposure to oxygen and light illumination. 123

Figure 5-16: **(a)** Current-voltage curves of $MAPb(I_{1-x}Br_x)_3$ (x=0.1) perovskite devices with different concentrations of MAI coating; **(b)** EQE spectra of same devices without MAI and with 10 mM of MAI coating at $x = 0.1$; **(c)** Current-voltage curves of $MAPb(I_{1-x}Br_x)_3$ (x=0.2) perovskite devices with different concentrations of MAI coating; **(d)** EQE spectra of the same devices without MAI and with 10 mM of MAI coating at $x = 0.2$. (Open circuit voltage: V_{oc}; short circuit current density: J_{sc}; Fill Factor: FF; External Quantum Efficiency: EQE.) 125

Figure 5-17: (a) short-term stability (normalised efficiency loss) for Br-I mixed halide perovskite devices with different concentrations of MAI salt coating at $x = 0.1$. **(b)** Short term stability (normalised efficiency loss) for Br-I mixed halide perovskite devices with different concentrations of MAI salt coating at $x = 0.2$. 127

Figure 5-18: Long-term stability test (normalised efficiency loss) for devices employing only MAPI (black); Br-I mixed halide perovskite devices without (orange) and with 10 mM of methylammonium iodide (MAI) (navy) salt coating at $x = 0.1$; and Br-I mixed halide perovskite devices without (dark red) and with 10 mM MAI salt coating (orange) at x = 0.2. All devices are tested under illumination for 500 hours. 128

Figure 6-1: Schemes of PEAI iodide salt passivation method for perovskite solar cells with $CH_3NH_3PbI_3$ (MAPI) as an active layer..... 139

Figure 6-2: Illustration of two possible modes of direct iodine salt coating of PEAI salt solution on top of $CH_3NH_3PbI_3$ (MAPI) layers. **(a)** Cross section of the multi-crystalline MAPI layer with MA^+ and I^- vacancies (surface defects shown as white semicircles). The excess ions such as PEA^+ and I^- present in the PEAI coating layers could potentially fill the surface lattice vacancies (shown as brown circles) to passivate the film shown as **(b)**. Alternatively, the excess ions could displace surface PEA^+ and/or I^- through ion exchange to generate a composite perovskite with a MAPI core being coated inside a stabilized perovskite outer layer incorporating the alternating $PhEtNH_3^+$ cation shown as **(c)**. 140

Figure 6-3: XRD spectra of the (a) non-passivated perovskite film and phenylethylammonium iodide (PEAI) salt passivated perovskite films with various iodide salt concentrations of (b) 2.5 mM, (c) 5.0 mM, (d) 10 mM and (e) 20 mM. 141

Figure 6-4: Top-view SEM images of the non-passivated $CH_3NH_3PbI_3$ (MAPI) perovskite film (a) and phenylethylammonium iodide (PEAI) iodide salt passivated perovskite films with different iodide salt concentrations of (b) 5 mM, (c) 10 mM and (d) 20 mM. 142

Figure 6-5: UV-VIS absorbance data collected from methylammonium lead iodide (MAPI) films coated with various concentrations of phenylethylammonium iodide (PEAI) of 2.5 mM (red), 5.0 mM (blue), 10 mM (magenta) and 20 mM (green). Inset: Zoom in of the UV-VIS absorbance data in the range of 700 – 800 nm. 143

Figure 6-6: (a) UV-Vis absorption spectra of samples of a pristine $CH_3NH_3PbI_3$ (MAPI) film; (b) MAPI coated with 10 mM of phenylethylammonium iodide (PEAI); (c) Normalised absorbance decay at 750 nm for the stability of pristine MAPI and MAPI treated with different concentrations of phenylethylammonium iodide (PEAI). Films were aged under dry air flow and illumination (25 mW/cm^2) for a period of 3 days; (d) Normalised absorbance decay at 750 nm under illumination (25 mW/cm^2) and dry air flow for pristine MAPI and MAPI coated with phenylethylammonium iodide (PEAI) and methylammonium iodide (MAI), films were measured under the same condition as (a)-(c) for 5 days. 144

Figure 6-7: (a) Superoxide yield plot comparing the generation of superoxide for MAPI treated with different concentrations and without phenylethylammonium iodide (PEAI) salt passivation. The normalised fluorescence intensity increase of the HE probe at 610 nm (excitation at 520 nm). $I_F(t)$ is the fluorescence maximum at time t, whilst $I_F(t_0)$ is the background fluorescence intensity. $I_F(t)/ I_F(t_0)$ ratio corresponds to yield of superoxide generation for perovskite films; (b) Superoxide yield plot comparing the generation of superoxide for pristine MAPI and MAPI coated with phenylethylammonium iodide (PEAI), methylammonium iodide (MAI). 145

Figure 6-8: Time-correlated single-photon counting (TCSPC) measurement for non-passivated perovskite film (black) and phenylethylammonium iodide (PEAI) salt passivated with different concentrations of 2.5 mM (red), 5.0 mM (blue), 10 mM (magenta) and 20 mM (green). 146

Figure 6-9: The current-voltage measurement of initial performances of devices without and with various concentrations of PEAI coating. All devices are fabricated in FTO/compact-TiO_2/mesoporous-TiO_2/perovskite (salt)/spiro-OMeTAD/Au architecture and are recorded under reverse scan (FB-SC).. 147

Figure 6-10: Influence of the PEAI salt concentration on current-voltage hysteresis of the MAPI devices. The devices are measured in reverse scan (FB-SC) and forward scan (SC-FB) under simulated AM1.5 100 mW cm^{-2} sunlight with (a) MAPI (black), (b) 2.5 mM (red), (c) 5 mM (blue), (d) 10 mM (magenta) and (e) 20 mM (green) PEAI salt coated on MAPI perovskite solar cells. The scan rate is 0.125 V/s for all devices. 149

Figure 6-11: (a) Short term stability test (normalized efficiency loss) for devices with and without phenylethylammonium iodide (PEAI) coating in various concentration of 2.5 mM (red), 5.0 mM (blue), 10 mM (magenta), 20 mM (green) and with methylammonium iodide (MAI) coating (dark yellow) for a period of 5 hours; (b) Long term stability test (normalized efficiency loss) for devices employing MAPI (black) without and with phenylethylammonium iodide (PEAI) coating in 10 mM (magenta) and with 10 mM methylammonium iodide (MAI) coating (dark yellow) for a period of 500 hours. The temperature is constantly at 25°C. 151

Figure 6-12: (a) Current-voltage measurement of initial performances of devices without iodide salt coating (black), with 10 mM of PEAI (magenta) and 10 mM of MAI (dark yellow) salt coating. Devices were measured using xenon lamp AM1.5 simulated solar spectrum at a scan rate of 0.125 V/s. The initial device is held at open circuit conditions for 60 seconds to stabilise and then scanned from 0 V to 1.2 V, both illuminated current (solid line) and dark current (dash line) are recorded. (b) The EQE spectra of devices without and with various concentrations of PEAI coating. All devices are fabricated in FTO/compact-TiO_2/mesoporous-TiO_2/perovskite (salt)/spiro-OMeTAD/Au architecture. 153

Figure 6-13: Transient absorption spectroscopy kinetic decays of MAPI films without iodide salt coating (black), with 10 mM PEAI (magenta) and 10 mM MAI (dark yellow) salt coating. All samples were excited with a pump wavelength of 567 nm and an average pulse power of 25 μJ cm^{-2}. The probe wavelength of 1600 nm was used to probe the resulting holes in spiro-OMeTAD..... 154

Figure 6-14: Histogram of the power conversion efficiency (PCE) obtained for 54 devices with PEAI salt coating (magenta) and 54 devices pristine MAPI (black). (All devices are measure in reverse scan and are fabricated at different time) 155

Figure 7-1: Schematic representation of three different methods of fabricating perovskite solar cells with $CH_3NH_3PbI_3$ as an active layer. (a) Standard Method; (b) Direct iodide salt coating; (c) Iodide salt assisted anti-solvent treatment (ISAAT). 163

Figure 7-2: UV-VIS absorbance collected from $CH_3NH_3PbI_3$ (MAPI) perovskite films without (black) and with various concentration of phenylethylammonium iodide (PEAI), iodide salt assisted anti-solvent treatment (IAAST) at a concentration of 5 mM (green), 10 mM (brown), 15 mM (blue) and 20 mM (red) (DE represents diethyl ether). 165

Figure 7-3: UV-Vis absorption spectra of (a) pristine $CH_3NH_3PbI_3$ (MAPI) film (black); (b)-(e) $CH_3NH_3PbI_3$ (MAPI) films incorporating various concentrations of phenylethylammonium iodide (PEAI) iodide salt assisted anti-solvent treatment (ISAAT) under dry air and light illumination for a period of 14 days; (f) Normalized absorbance decay at 750 nm for pristine MAPI and MAPI with different concentrations of PEAI using ISAAT treatment. Films were aged under dry air flow and illumination (25 mW/cm^2) for a period of 14 days**.** 166

Figure 7-4: (a) Steady-state photoluminescence (PL) spectra of MAPI perovskite films with and without various concentrations of PEAI iodide salt assisted anti-solvent treatment (ISAAT) (all samples use diethyl ether as anti-solvent). Inset: PL intensity changes for different concentrations of PEAI assisted anti-solvent treatment. (b) Time-correlated single-photon counting (TCSPC) spectra of MAPI perovskite films with and without various concentrations of PEAI iodide salt assisted anti-solvent treatment (ISAAT). 168

Figure 7-5: (a) XRD patterns of $CH_3NH_3PbI_3$ (MAPI) perovskite layers prepared with $PhEtNH_3I$ (PEAI) iodide salt assisted anti-solvent treatment (ISAAT) at various concentrations: 0 mM (black), 5 mM (green), 15 mM (blue) and 20 mM (red); and (b) the FWHM value (black) and average crystallite sizes (orange) of perovskite thin films as a function of various PEAI concentrations in anti-solvent..... 171

Figure 7-6: Top-view SEM images of the (a) non-passivated $CH_3NH_3PbI_3$ perovskite film and films employing phenylethylammonium iodide ($PhEtNH_3I$) iodide salt assisted anti-solvent treatment (ISAAT) with different iodide salt concentrations of (b) 5 mM, (c) 10 mM and (d) 15 mM and (e) 20 mM. Inset: Corresponding SEM images of each films with higher magnification..... 173

Figure 7-7: Superoxide yield plot comparing the generation of superoxide for $CH_3NH_3PbI_3$ treated with and without phenylethylammonium iodide ($PhEtNH_3I$) iodide salt assist anti-solvent treatment (ISAAT) (the iodide salt is first dissolved in IPA and then mixed with diethyl ether as an anti-solvent). The normalised fluorescence intensity increase of the HE probe at 610 nm (excitation at 520 nm). $I_F(t)$ is the fluorescence maximum at time t, whilst $I_F(t_0)$ is the background fluorescence intensity. $I_F(t)/ I_F(t_0)$ ratio corresponds to yield of superoxide generation for perovskite films..... 174

Figure 7-8: Raw transient absorption spectroscopy data, showing the obtained kinetic decay traces for $CH_3NH_3PbI_3$ films (a) without $PhEtNH_3I$ iodide salt and (b)-(e) with various concentrations of $PhEtNH_3I$ iodide salt assisted anti-solvent treatment (ISAAT). (f) Normalized decay of charge separation losses for the above films over a period of 60 minutes. All films were probed at 1600 nm (tracking concentration of Spiro-OMeTAD hole-polarons) following excitation at 458 nm. 176

Figure 7-9: Transient absorption spectroscopy kinetic decays of $CH_3NH_3PbI_3$ films without iodide salt coating (black) and with 15 mM PEAI (blue) iodide salt assisted anti-solvent treatment (ISAAT). The samples were excited with a pump wavelength of 567 nm and an average pulse power of 25 μJ cm^{-2}. The probe wavelength of 1600 nm was used to probe the resulting holes in Spiro-OMeTAD..... 177

Figure 7-10: (a) Current-voltage measurement of initial performances of devices without and with various concentrations of $PhEtNH_3I$ iodide salt assisted anti-solvent treatment (ISAAT). All devices are fabricated in FTO/compact-TiO_2/mesoporous-TiO_2/$CH_3NH_3PbI_3$(ISAAT)/spiro-OMeTAD/Au architecture and are recorded under reverse scan (FB-SC). (b) EQE spectra of the corresponding devices. 179

Figure 7-11: Influence of the $PhEtNH_3I$ concentration on current-voltage hysteresis of the $CH_3NH_3PbI_3$ devices. The devices are measured in reverse scan (FB-SC) and forward scan (SC-FB) under simulated AM1.5 100 mW cm^{-2} sunlight with (a) MAPI (black), (b) 5 mM (green), (c) 10 mM (brown), (d) 15 mM (blue) and (e) 20 mM (red) $PhEtNH_3I$ (PEAI) salt contained in anti-solvent on $CH_3NH_3PbI_3$ perovskite solar cells. The scan rate is 0.125 V/s for all devices. 181

Figure 7-12: (a) Short term stability test (normalised efficiency loss) for devices with and without phenylethylammonium iodide (PEAI) iodide salt assisted anti-solvent treatment (ISAAT) in various concentrations of 5 mM (green), 10 mM (brown), 15 mM (blue) and 20 mM (red) for a period of 5 hours;

(b) Long term stability test for devices employing $CH_3NH_3PbI_3$ (black) without iodide salt coating, with 15 mM phenylethylammonium iodide (PEAI) iodide salt assisted anti-solvent treatment (ISAAT) (blue) and with 10 mM of phenylethylammonium iodide (PEAI) employing conventional salt coating (magenta) for a period of 500 hours. The temperature is constantly at 25°C. 183

Figure 7-13: Histogram of the J-V measurement in reverse scan (FB-SC) obtained for 54 devices with conventional PEAI treatment (orange) and 54 devices with novel ISAAT treatment, including comparison of all photovoltaic parameters (a) V_{oc}, (b) J_{sc}, (c) FF and (d) PCE..... 184

LIST OF TABLES

Table 4-1: Device parameters of $CH_3NH_3PbI_3$ (MAPI) perovskite solar cells with different thicknesses of compact TiO_2 layers (CL) using the spray pyrolysis (thickness based on number of spraying cycles) and spin coating methods. 82

Table 4-2: Device parameters of $CH_3NH_3PbI_3$ (MAPI) perovskite solar cells with different thicknesses of the mesoporous TiO_2 layers, including 350 nm, 400 nm, 700 nm and 800 nm respectively at forward (SC-FB) and reverse scan (FB-SC). 84

Table 4-3: Device parameters of $CH_3NH_3PbI_3$ perovskite solar cells with different concentrations of $TiCl_4$ post treatment of 0 mM, 20 mM, 40 mM, 60 mM, 80 mM and 100 mM. 87

Table 4-4: Device parameters of $CH_3NH_3PbI_3$ (MAPI) perovskite solar cells with Spiro-OMeTAD as hole-transporting layer with and without aging, device were measured under forward scan and backward scan. (w/o = without). 88

Table 5-1: Device parameters of initial performance for devices based on varied concentration of MAI salt coated on $CH_3NH_3PbI_3$ (MAPI) perovskite films. (FB-SC: reverse scan; SC-FB: forward scan; open circuit voltage: V_{oc}; short circuit current density: J_{sc}; Fill Factor: FF; Power Conversion Efficiency: PCE). 109

Table 5-2: Normalised weight increase for the selected film compositions, as a function of exposure to dry air flux against time. 116

Table 5-3: Photovoltaic parameters of same devices in the composition of x = 0, 0.1, 0.2, 0.5, 0.75, 1.0 in $MAPb(I_{1-x}Br_x)_3$. (Open circuit voltage: V_{oc}; short circuit current density: J_{sc}; Fill Factor: FF; Power Conversion Efficiency: PCE) 120

Table 5-4: Photovoltaic parameters for devices based on $MAPb(I_{1-x}Br_x)_3$ perovskite films in the composition of x = 0.1 and 0.2 without and with different MAI salt concentrations. (Open circuit voltage: V_{oc}; short circuit current density: J_{sc}; Fill Factor: FF; Power Conversion Efficiency: PCE.) 125

Table 6-1: Device performance parameters of initial performance for devices based on the various concentration of $PhEtNH_3I$ (PEAI) coated on MAPI perovskite films. (FB-SC = reverse scan and SC-FB = forward scan; V_{oc} = open circuit voltage, J_{sc}, = short circuit density, FF = Fill Factor, PCE = Power Conversion Efficiency.) 148

Table 7-1: Device performance parameters of the initial performance for devices based on the various concentrations of PEAI Iodide Salt Assisted Anti-solvent Treatment (ISAAT) coated on $CH_3NH_3PbI_3$ (MAPI) perovskite films. (FB-SC = reverse scan; SC-FB forward scan; V_{oc} = open circuit voltage; J_{sc}, = short circuit density; FF = Fill Factor; PCE = Power Conversion Efficiency.) 180

FREQUENTLY USED ACRONYMS AND ABBREVIATIONS

AM1.5	Air mass 1.5
AO	Atomic orbital
CT state	Charge-transfer state
DSC	Differential scanning calorimetry
EA	Electron affinity
EQE	External quantum efficiency
FF	Fill factor
HOMO	Highest occupied molecular orbital
I_{MPP}	Current at maximum power point
IPA	Propan-2-ol
IPCE	Incident photon conversion efficiency
ITO	Indium tin oxide
J_{SC}	Short circuit current density
L_{ex}	Exciton diffusion length
LUMO	Lowest unoccupied molecular orbital
M_n	Number-average molecular weight
MO	Molecular orbital
MW	Mega-Watt
M_w	Weight-average molecular weight
NP	Nanoparticle
ΔOD	Change in optical density
PDI	Polydispersity index
PCBM	[6,6]-phenyl-C61-butyric acid methyl ester
PL	Photoluminescence
PV	Photovoltaic
SEM	Scanning electron microscopy
Spiro-OmeTAD	2,2',7,7'-tetrakis-(N,N-di-4-methoxyphenylamine)9,9'-spirobifluorene
TAS	Transient absorption spectroscopy
TP	Tetrapod
TW	Tera-Watt
UF	Ultrafast
V	Volt
V_{MPP}	Voltage at maximum power point
V_{OC}	Open circuit voltage
XRD	X-ray diffraction

CHAPTER 1

Introduction

1.1. Unsustainable Reliance on Fossil Fuels

One of the key challenges that modern society faces is sourcing energy. To date, most of the world's energy comes from a combination of non-sustainable resources known as 'fossil fuels'.[1] The three most widely used fossil fuels for energy production are coal, natural gas and petroleum. Historically, energy from fossil fuel resources was fundamental in the onset of the industrial revolution, which is followed by a significant progress on technological, social and economical development.[2] Although fossil fuels have played apositive role in development across the globe, they have severely negative impacts as they cause air pollution and emission of carbon dioxide (CO_2) as well as other 'greenhouse gases', which lead to climate change.[3] The 'crisis' is rapidly increasing in scale and it is predicted that coal reserves will be exhausted within 150 years if current production rates are maintained. Recent reports estimate that the demand for oil could outstrip their production by 2020.[4, 5] In considering the situations in some large and rapidly developing countries such as China, India, and Brazil with huge demand for cost-effective, carbon-based fuels,[6] the general consensus is that there needs to be an alternative source of energy which is equally as cheap as conventional fossil fuels, whilst producing less harmful emissions.

Ever since the beginning of the industrial revolution in the mid-18th century, greenhouse gases have caused an obvious increase in the earth surface temperature. This phenomenon has implications in rising sea levels, fluctuating climate patterns, and has resulted in extremely disruptive weather events. Carbon dioxide, one of the most abundant greenhouse gases that

generated from fossil fuel combustion and its continued emission has become a major environmental issue throughout the earth.

However, as fossil fuels have become increasingly more scarce and difficult to find and extract, modern energy generation has shifted towards renewable energy sources before the exhaustion of the conventional fossil energy sources. Some public and governmental policies have started to address the benefit of creating energy in a renewable, low-carbon, and reliable way. In fact, fossil energy does not satisfy any renewable or sustainable energy targets as it releases significant amounts of dentrimental carbon dioxide and other greenhouse gases upon combustion. Indeed, fossil fuels are a non-renewable, depleting resource, and their narrow supply chain poses serious problems of energy security. Nevertheless, since they are the only economically viable energy source that can possibly meet the demands of today's development, many countries have decided to introduce emission offset schemes or emission reduction plans for their businesses.

There is no doubt that future reduction of emissions would be a wise choice. To win the war against climate change, the world's reliance on fossil fuels must be eased. If we wish to maintain our standard of living an alternative sources of energy must be found to make up the energy deficiency.

1.2. Renewable Technologies

Overall global energy demand is estimated to double from its current levels of just over 16 tera-Watts (TW) by 2050, and triple by 2100.[6] By contrast, current report shows that the power originated from the existing renewable resources is around 4% of the world's total energy consumption. In particular, around 75% of this is generated through the application of large-scale hydroelectric power plants. The comparison between this small overall quantity and the combined value for conventional resources of oil, gas, and coal generated power, which accounts for over 80% of the world's energy generation, and the massive infrastructure challenge facing us in converting from a 'carbon-economy' to one dominated by 'clean' technologies, cannot be taken lightly.

Broadly speaking, there are four methods for collecting solar energy and converting it into other useful energies.[6] The first uses biofuels which involves the plants conversion the solar energy into biomass through photosynthesis, or the use of bio-engineered algae to convert the energy directly into fuel.[1] Although this technique is widely used in many applications such as motor fuel, this technique requires large areas of valuable agricultural land. The second method utilises solar energy capture through conversion of the solar energy into heat. This technique has been widely used in many countries for generating hot water. The third technique is 'concentrating' solar energy into heat to drive a turbine. Typically, it includes reflectors that concentrate the sunlight onto a pipe with oil inside which heats up and subsequently travels to an exchanger and heats water that drives an electricity generator. It is clear that the technology for both solar heating and concentrating solar energy are widely understood without any scientific challenges. A fourth method utilises photovoltaic (PV) modules. They have many forms but all share the same quality – mass production is possible, and mobile and micro-scale applications can also generate power in many conceivable situations. [1] Consequently, if combined with an effective storage capacity, then solar power, and in particular PV, is potentially a very promising candidate for a multitude of applications. However, for PV to be considered as a competitive substitute to conventional fossil-fuel resources, the cost per unit energy generated must be included, and are currently very expensive due to the fabrication technique and the extremely sensitive condition they required to operate efficiently. There has been pressure over the past few years to develop cheaper PV technologies. This has inspired us to work on this field and strive to seek the most suitable material or technique for solar cells.

1.3. References

[1] P.J. Crutzen, A.R. Mosier, K.A. Smith, W. Winiwarter, *Springer* **2016**, 227.

[2] P. Hawken, A.B. Lovins, L.H. Lovins, *Natural Capitalism: The Next Industrial Revolution*. **2013:** Routledge.

[3] S.M. Benson, F.M. Orr, *MRS bulletin* **2008**, *33,* 303.

[4] R. Henson, *The Rough Guide to Climate Change: the Symptoms, the Science and the Solutions* **2006**.

[5] Intergovernmental Panel on Climate Change, (I.P.O.C.) *Environmental Policy Collection* **2007**, *27*, 408.

[6] A.B. Stambouli, E. Traversa, *Renewable and Sustainable Energy Reviews* **2002**, *6,* 433-435.

CHAPTER 2

Background Knowledge

This chapter introduces background knowledge and theory which underpins the work presented in this thesis. It starts by introducing semiconductors as the foundation of the photovoltaic (PV) devices followed by an overview of the current state-of-the-art research being performed to develop different generations of devices. Specifically, a review of the recent progress on perovskite solar cells (PSCs) is summarised. From this, the working principles of PV devices are introduced before several key parameters, such as power conversion efficiency (PCE), open circuit voltage (V_{oc}), short circuit current density (J_{sc}) and fill factor (FF), are presented. Attention is then paid to reviewing the recent development on the stability of the perovskite solar cell (PSCs), with particular focus on pioneering approaches being applied to overcome their limitations. It is from these that the research objective and targets of this thesis are derived.

2.1. Introduction to Photovoltaic Technologies

2.1.1. Semiconductors and P-N Junction

Solar cells use semiconductors to convert solar energy into electricity and involve three processes. First, sunlight must be absorbed to excite electrons into a higher energy state to generate electron-hole pairs. Second, free charge carriers must be spatially separated to avoid recombination or decay to their ground states. Third, electron and hole need to be transported towards the corresponding electrode with an external circuit to function. Solar cells also require charge flow directionally through the circuit. Although many materials satisfy these requirements, semiconductors are the only material being used in industry. Therefore it is

important to understand how semiconductors are formed and their key properties that give rise to solar cell applications.

The formation of the semiconductor can be described with molecular orbital (MO) theory.[1] The distribution of electrons within a single atom obeys Pauli's exclusion principle, also present are the quantised energy levels with eigenvalues that satisfy the Schrödinger equation. The eigenfunctions devised from different energy levels define the probability to find an electron at a given location. The energy and its spatial distribution with respect to each energy level is called the 'atomic orbital' (AO). Upon joining two atoms together, they form a new molecular orbitals (MO) and have a new corresponding Schrödinger equation. The term 'bonding' defines the MO that has lower energy than the sum of the individual AO, whereas for MO with higher energy is defined as 'anti-bonding'. Thus, the combination of more atoms results in an increasing number of electrons filling in more MOs. For a crystal with an infinite lattice there are so many MOs with energy levels so close to each other that they appear continuous and are called a'band'. The whole procedure is shown in Figure 2.1.

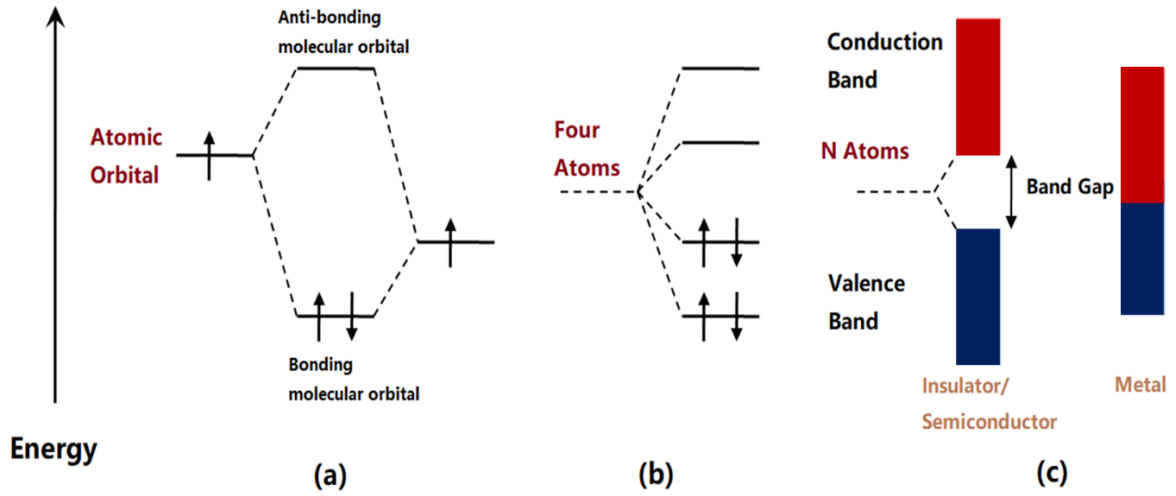


Figure 2-1: Energy level diagram representing the formation of semiconductors. (a) Combination of two Atomic Orbitals (AOs) resulting in two Molecular Orbitals (MOs), with one energy higher (known as the 'anti-bonding MO'), and one energy lower (known as the 'bonding MO') than the sum of individual AOs. (b) Combination of more atoms leads to the formation of more bonding and anti-bonding MOs. (c) In a crystal there are many orbitals, so energies appear continuous and are named as 'bands'. The bonding MO is named as the valence band (VB), and anti-bonding MO is the conduction band (CB). The crystal shows metallic behaviour if two bands overlaps. If there is a 'gap' between bands then the crystal is either a semiconductor or an insulator.

Therefore, a material can be defined as a semiconductor when gap is present between the highest occupied molecular orbital (HOMO) and the lowest unoccupied molecular orbital

(LUMO). For semiconducting crystals, the empty MO band is the 'conduction band' (CB), and the filled MO band is the 'valence band' (VB). The energy between these two bands is named as the 'band gap', with energy (E_g) ranging from ~ 0.5 eV and ~ 4 eV and a conductivity of ~10^3–10^{-8} Scm^{-1}.[2] Within the crystal, the negative charges (electrons) in the CB are free to drift under the electric field within a continuum of empty states. Similarly, the positive charges (holes) in the VB also drift reversely to the direction electrons. Importantly, addition of dopants could effectively tune the intrinsic characteristics of a semiconductor. The dopants could create free charge carriers in one of the bands and so increase the conductance. Semiconductors with sufficient dopants can be made to conduct like metallic materials. The semiconductor can be defined as 'n-type' when electrical conduction is mainly due to the movement of negative electrons. On the other hand, if it is mainly due to the movement of positive holes it is named as a 'p-type' semiconductor. The p-n junction is formed by the combination of n- and p-type semiconductors.[3] In this case, the holes from p-region could diffuse into the n-region with the negative charges leaving in the p-region. The negative charges subsequently recombine with electrons, leading to negatively charged ions in the p-region. Likewise, electrons present at the n-region could also diffuse into the p-region, and the positive charge, in this case, is left in the n-region and create positively charged ions by recombing the holes. Under this circumstances, a 'depletion region' is created when silicon crystal becomes depleted from major charge carriers in the vicinity of the junction. The width of the this region largely influences the current flowing between the junction.[3] It is suggested that a p-n junction can be treated as a diode, allowing electrical current to flow directionally and thus generating an inherent asymmetry inside the semiconductor. The schematic representation of this p-n junction is illustrated in Figure 2.2.

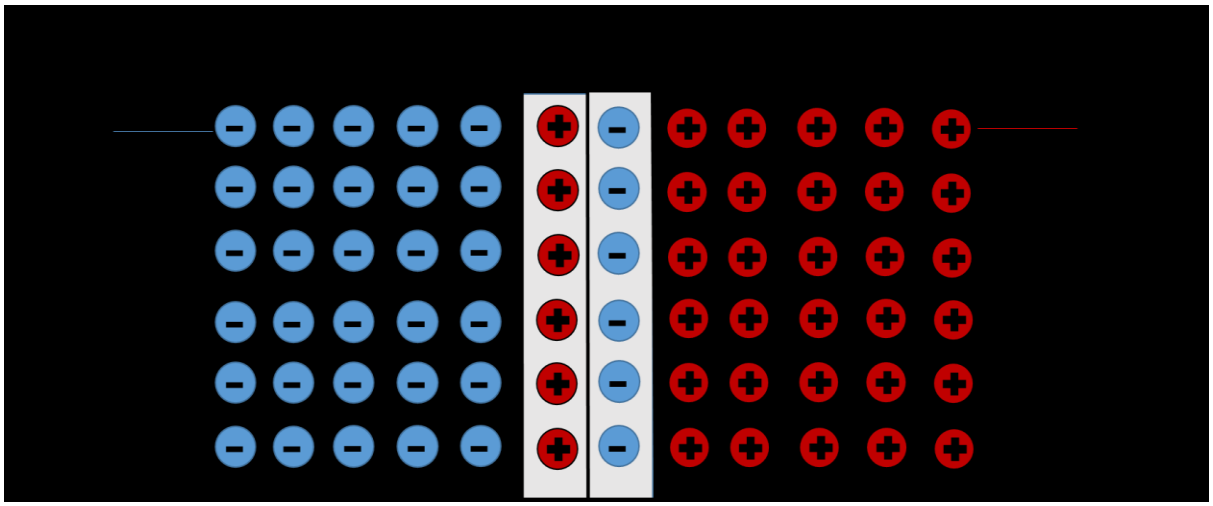


Figure 2-2: Schematic of a typical p-n junction solar cells doped with n-type and p-type impurities.

2.1.2. Inorganic Solar Cells

The research on photovoltaics dates back to 1839, and was carried out by a French chemist called Edmond Becquerel, who first discovered the photovoltaic effect and explained how electricity can be produced from sunlight.[4, 5] However, early devices showed very poor performance. The first solid-state cell was invented by Charles Fritts in 1883,[6] in which selenium coated with a gold layer was first applied as a semiconductor and achieved merely around 1% of power conversion efficiency (PCE). Knowledge of how photovoltaic devices functioned remained limited until the concept of the photoelectric effect was formally introduced by Albert Einstein in 1905.[7] This remarkable discovery eventually led to him winning the Nobel Prize in Physics in 1921. Later on, a group of scientists from Bell laboratories, Gerald Pearson, Calvin Fuller and Daryl Chapin, successfully developed the first silicon photovoltaic device that can be practically used in 1954, which is normally referred to as the 'first generation solar cell'.[8] The invention was a significant breakthrough as silicon was first introduced into a solar cell and obtained around 6% in PCE. Nevertheless, the charge separation in silicon solar cells is based on the p-n junction, and since silicon has a narrow band gap and low absorption coefficient, it usually requires a thick absorption layer grown in a high-purity condition.[9] This significantly increases the fabrication cost and so silicon devices appeared only on satellites or on wing-shaped solar panels for spacecraft. This bottleneck resulted in the development of second generation solar cells employing copper indium gallium selenide (CIGS), cadmium telluride (CdTe) and gallium arsenide (GaAs) as photoactive layer. Over decades the fabrication cost has been reduced sufficiently with progressive developments in manufacturing technology. To date, crystalline silicon devices present ~26.7% in PCEs for single-junction, and ~10.2% for amorphous silicon cells with more reasonable costs.[10] Other semiconductor materials were also investigated and applied to high efficiency devices, such as ~22.1% for CdTe, ~22.9% for CIGS and ~28.8% for GaAs solar cells.[10] However, like silicon PVs, all these inorganic devices require semiconductor materials with high purity during fabrication, and therefore are very expensive. This lead to the development of an emerging PV technology classified as third generation solar cells (also known as 'excitonic solar cells'). This mainly includes three families, the organic solar cells (OPVs),[11] the dye sensitized solar cells (DSSCs)[12] and, more recently, the development of the perovskite solar cells (PSCs).[13]

2.1.3. Organic Solar Cells (OPVs)

Solar cells with organic materials as semiconductor have achieved extensive attention ever since 1986, with a PCE of 1% using phthalocyanine as electron donor (D) and perylene tetracarboxylic derivative as electron acceptor (A).[14] Unlike inorganic solar cells, organic photovoltaics (OPV) not only provide excellent properties but also lower fabrication costs, thus they have potential for mass production.[15-17] Over the past decade, there has been a significant boost in efficiency of OPVs, with PCEs increased from ~5% to 14%. [17, 18] The operating mechanism of OPVs is very similar as inorganic solar cells. In a typical OPV, two typical organic materials, poly(3-hexylthiophene-2,5-diyl) (P3HT), which is normally used as p-type semiconductor and works as an electron donor; the (6,6)-phenyl C61 butyric acid methyl ester (PCBM), known as n-type semiconductor and works as an electron acceptor. They are mixed together to form a bulk-heterojunction structure, as shown in Figure 2.3.

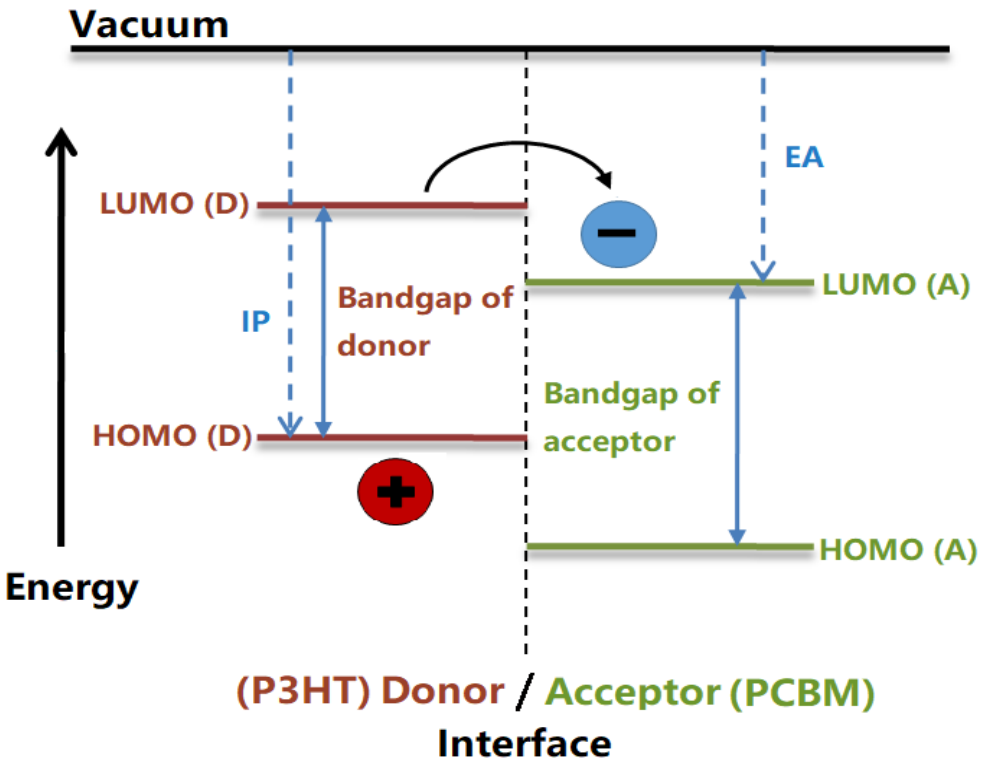


Figure 2-3: Schematic mechanisms of an organic semiconductor heterojunction solar cells (organic photovoltaics, OPVs). The compound with the smaller ionization potential (IP) is known as the 'electron donor' (e.g.P3HT) while that with the larger electron affinity (EA) is referred to as the 'electron acceptor' (e.g. PCBM). Upon photo-excitation, the exciton is dissociated into freely moved charges at the acceptor/donor interface which undergo further transport to the anode (e.g. ITO) and cathode (eg. Al). HOMO: highest occupied molecular orbital, LUMO: lowest unoccupied molecular orbital.

The exciton (coulomb-bound electron-hole pair) is created and possesses a certain lifetime under photo-excitation and dissocated at the P3HT/PCBM (electron donor/acceptor) interface. Since the thermal and electrical energy is insufficient to separate an exciton, the chemical potential difference between electron donor and acceptor is required to overcome the exciton binding energy (E_b) for charge dissociation at the junction interface.[19] However, unlike inorganic solar cells, in which electrons are delocalized and free charge carriers can be created directly in the p-n junction, the excitons in organic solar cells are strongly bounded with high E_b (between 0.1 and 1.4 eV).[20] In this case, the thermodynamic driving force for interfacial charge dissociation as well as the exciton diffusion will limit the efficiency of the organic solar cells.[21] Therefore, a relatively thick absorbing layer is necessary to receive sufficient light harvesting, which ultimately increases the exciton diffusion length betwen the donor/acceptor interface. Interestingly, the invention of bulk-heterojunction OPV cells addressed this problem by mixing both donor and acceptor materials into one bulk-heterojunction structure. The design effectively reduces the exciton diffusion length to afford sufficient light harvesting, thereby improves charge separation and solar cell efficiency.[22] To date, the certified record in device performance for OPVs is held by Nankai University in China, with a PCE of 17.3% in tandem devices, making organic solar cells closer to industrial production.[23]

However, despite the many advantages of organic solar cells over conventional silicon and thin film solar cells, the performance of device is still far behind that of other photovoltaic systems based on inorganic materials.[24, 25] This is mainly due to the nature of low dielectric constants of organic materials, which means that the excitons generated after photoexcitation cannot be thermally dissociated. Instead, the exciton has to be transported to an interface with a material that has a higher energy offset than the exciton's binding energy (E_b), which enables electrons or holes to transfer to the other side, thus separating excitons. Since excitons can only diffuse around ~10 nm before recombination, this limits the thickness and structure of absorbing layer and ultimately produces less efficient organic solar cells.[26, 27] In addition, organic solar cells also suffer from photochemical degradation as compared with inorganic solar cells, which typically last about 25 years.[22] Factors such as morphology, diffusion of electrode and buffer layers, and the presence of oxygen, water, heating and mechanical stress all cause degradation of this type of solar cell.[28] The improvement in device efficiency and long-term stability certainly provide organic solar cells with a great opportunity for commercialization in the future.

2.1.4. Dye Sensitized Solar Cells (DSSCs)

The dye sensitized solar cell (DSSC) is an alternative emerging technology of excitonic solar cells. The concept was firstly introduced by a Chemist called Moser in 1887, demonstrating that photocurrent can be enhanced via a dye-sensitizing halogenated silver plate.[29, 30] The discovery did not draw much attention until the fundamental mechanism was first proposed in 1976, elucidating how dye molecule excitation led to light harvesting and charge separation.[31] The most significant breakthrough occurred in 1991, when O'Regan and Grätzel co-invented dye-sensitized solar cells (DSSCs) with a PCE of ~7%.[32] The major difference between DSSCs and other conventional devices is that light harvesting material, i.e. the dye, is separated from charge carrier transport, enabling this type of device to be fabricated under lower purity conditions and lower cost.[32, 33] The operating principle of DSSCs is shown in Figure 2.4.

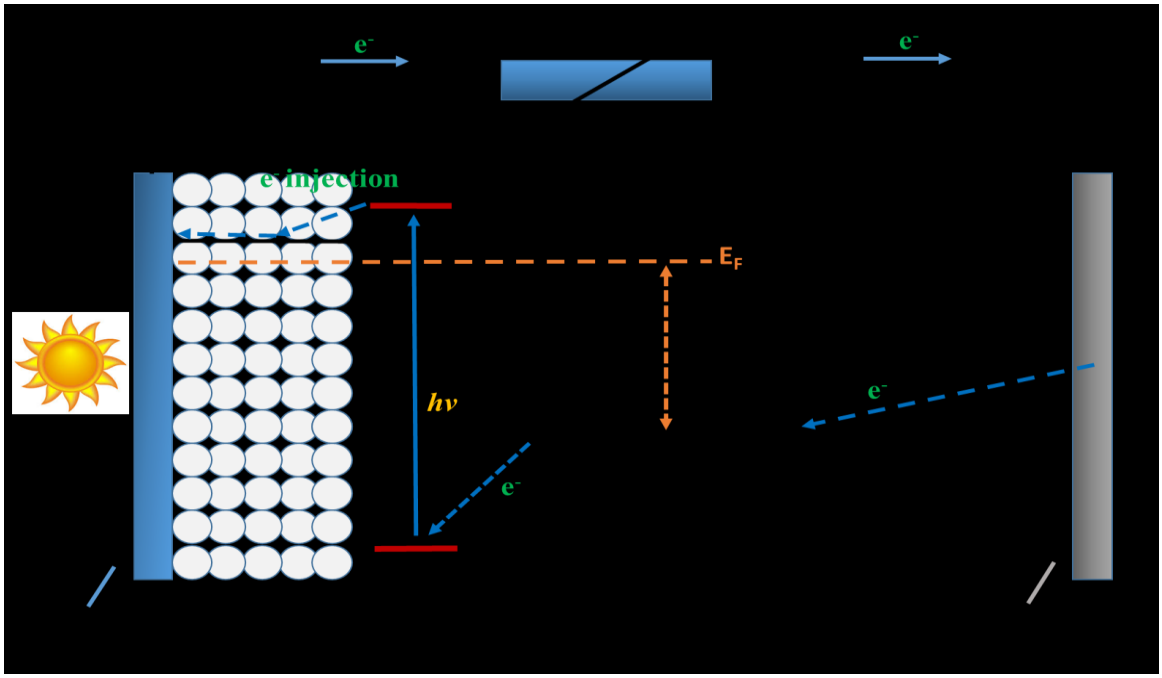


Figure 2-4: Schematic construction and working principle of a dye-sensitized solar cell (DSSC) with liquid-electrolyte based on mesoporous TiO_2 photoanode and I^- / I_3^- redox couple. FTO = fluorine-doped tin oxide; WE= working electrode. CB = conduction band**;** $E_{F:}$ electron quasi-Fermi level**.**

In this diagram, the working electrodes (WE) are prepared when a thin layer of oxide semiconducting material such as TiO_2 is deposited on top of a transparent conducting glass plate such as fluorine-doped tin dioxide (FTO), since these semiconducting layers only absorb very little amounts of light within the UV region. The working electrodes are then immersed under a mixture of molecular sensitizers (dye) and a solvent such that the dye

could covalently bond to the TiO_2 surface. The highly porous structure of TiO_2 and high surface area of electrode enables many dye molecules get attached on the TiO_2 surface, thus increasing light absorption. A separate plate is then produced with an electrolyte and the two plates are joined together to prevent the electrolyte from leaking. Once working, the light absorption in the photosensitizer causes the excitation of the dye molecule, and the electrons are promoted from the ground state (S^o/S^+) to the excited state (S^*) of the dye. Then the excited dye injects electrons into the conduction band (CB) of the mesoporous TiO_2. Afterwards, the dye molecule is oxidized and then regenerated by an electron, which is contributed from a liquid electrolyte with I^- / I_3^- as redox couple that dissolved in an organic solvent (e.g. acetonitrile). On the other hand, the holes are transported from I^- / I_3^- redox couple to the FTO counter-electrode (CE) so that the circuit is completed. The maximum voltage of DSSCs depends on the energy difference between the electrolyte redox potential and the electron quasi-Fermi level (E_F) in the mesoporous TiO_2. During the past few years, tremendous efforts have been invested to improve the device performance of DSSC solar cells,[29, 30, 34, 35] with particular attention paid to designing dye molecules with higher extinction coefficients and wider absorption range;[36-40] investigating alternative redox couples to reduce free carrier recombination;[41-45] seeking more stable and cost effective photoanode materials;[46-50] as well as finding alternatives to replace FTO counter-electrode to satisfy up-scaling production.[51, 52] To date, the best certified device efficiency for DSSCs is 14.1% achieved by Grätzel and EPFL scientists.[53]

In spite of promising device efficiencies achieved for DSSCs devices based on a liquid electrolyte, there are some challenges for this type of solar cell before industrial production becomes possible. For example, an excess amount of triiodide is normally dissolved in the electrolyte to minimize the interfacial recombination. Triiodide is highly corrosive and may cause erosion of the encapsulating layer of solar cells. More importantly, the electrolyte used in DSSCs usually includes polar organic solvents such as acetonitrile, which is highly volatile and is prone to evaporate causing electrolyte leakage inside the device. This could degrade solar cells and so be harmful to their long term stability. In view of this, many attempts have been made to address the problems, and amongst this, developing solid- or quasi-solid-state dye-sensitized solar cell (sDSSCs), in which the original liquid electrolyte is replaced by a more stable solid-state semiconductor as a hole transport material (HTM), has become one of the main directions for future design of DSSCs. [34, 35, 54-72] This led to the further invention of the most popular perovskite materials and solar cells.

2.2. Overview of the Progress on Perovskite Solar Cells (PSCs)

The breakthrough invention of organometallic halide perovskite solar cells (PSCs) has recently revolutionized the third generation solar cells. Within a few years, the device performance has been boomed up to more than 20%.[53, 73-75] This captivating prospect in the rapid development of PSCs is mostly attributed to many remarkable properties of the perovskite materials, such as solution processability,[76, 77] broad solar absorption spectrum,[78] high charge carrier mobility,[79] low non-radiative recombination losses and long charge diffusion length.[13, 80-83] 'Perovskite' was named after a Russian mineralogist called Lev A. Perovski, and for perovskite solar cells (PSCs) it normally includes organic–inorganic lead or tin halide based materials as the photoactive layer.[84] The perovskite material can be represented by the formula ABX_3, where X is an anion whereas A and B represent cations with different particle size (A is larger than B). The general crystal structure of perovskite materials can be shown in Figure 2.5.

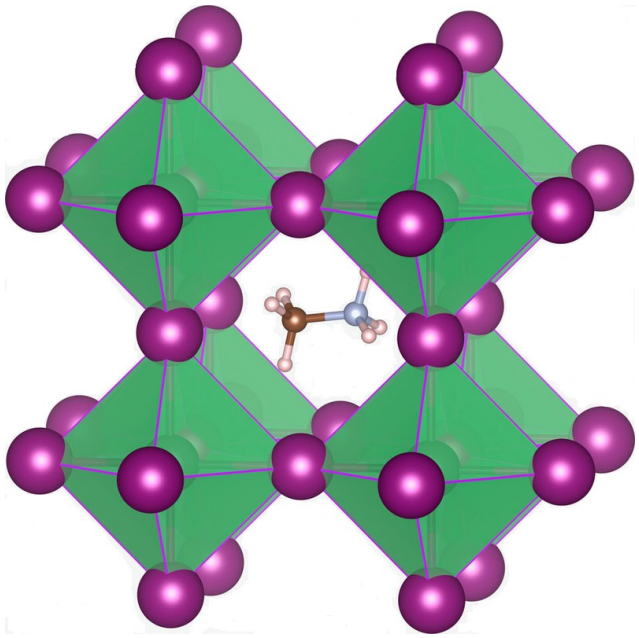


Figure 2-5: Standard crystal structure of the cubic metal halide perovskites with a chemical formula of ABX_3. Position A is occupied by organic or inorganic cation A (green), whereas position B (grey) and X (purple) are occupied by metal cations and halides, respectively.[13]

In this structure, the large cations A are normally represented as inorganic caesium ions or organic cations such as methylammonium ($CH_3NH_3^+$) (R_A=0.18 nm),[85] or formamidinium ($NH_2CH{=}NH_2^+$) (R_A from 0.19 nm to 0.22 nm).[86] The X anion is a halogen ion and is typically iodine (I) (R_X = 0.22 nm), although sometimes bromine (Br) (R_X = 0.196 nm) and

chlorine (Cl) (R_X = 0.181 nm) are also used as mixed halide perovskites.[13] For efficient devices, cation B is mostly lead (Pb) (R_B = 0.119 nm), and tin (Sn) (R_B= 0.110 nm) is also used as a substitute for toxic Pb, but with lower stability.[87] Therefore, the overall compound will be methylammonium lead triiodide ($CH_3NH_3PbI_3$, MAPI), or sometimes mixed with Cl or Br halides to form $CH_3NH_3PbI_{3-x}Cl_x$ and $CH_3NH_3PbI_{3-x}Br_x$ and so on.[88, 89]

The curiosity in organic-inorganic halide perovskite materials dates back to over a century ago.[75] This material did not receive much attention until the recent investigation by Mitzi et al. on transistors and light-emitting diodes (LEDs).[90, 91] The first report of perovskite applied in photovoltaic devices happened in 2006, when Miyasaka and co-workers used $CH_3NH_3PbBr_3$ as sensitizer and mesoporous TiO_2 as electrodes with a PCE of 2.19%.[92] Later on, by substituting Br with I, the PCE was further improved to 3.8%.[93] In 2011, Park et al. used a similar structure by employing TiO_2 surface treatment prior to deposition of perovskite and realized a PCE of 6.5%.[94] However, the fact that liquid electrolytes were used in these devices resulted in serious degradation so that the lifetimes for these cells were as poor as a few minutes. This encouraged researchers to develop perovskite solar cells with solid state electrolytes. The idea became reality in 2012, when Grätzel, Park and their co-workers introduced a small molecule of Spiro-OMeTAD (2,2'7,7'-tetrakis(N,N-di-p-methoxyphenylamine)-9,9'-spirobifluorene) that was previously used in organic LEDs,[95] to the perovskite solar cells and increased efficiency to 9.7%.[96] Another remarkable achievement happened in the same year, in which Snaith et al. also reported using Spiro-OMeTAD as HTM and further extended this application into a wider research field.[97] Several interesting investigations on perovskite solar cells happened at this moment, including application of Cl in mixed halide $CH_3NH_3PbI_{3-x}Cl_x$, which resulted in longer device lifetime, longer diffusion length and more charge carrier transport.[98] Replacing mesoporous TiO_2 with non-conductive mesoporous Al_2O_3, resulted in a PCE of 10.9%.[97] More importantly, the study showed that perovskite material not only absorbs light and initiates photo-induced electrons, but also facilitated transportation of free charge carriers into the corresponding electrodes. This gave rise to the further invention of planar solar cells without mesoporous scaffolds.[83]

Another increase in device efficiency occurred in 2013, Seok, Grätzel and co-workers applied a solid perovskite capping layer next to mesoporous TiO_2 layer, with Spiro-OMeTAD as HTM and obtained a PCE of 12%.[99] In the same year, with a similar device structure, Seok

et al. further enhanced the device efficiency to 12.3%.[100] Specifically, their result highlighted the feasibility of using Br as a replacement of pure I in a mixed halide $CH_3NH_3PbI_{3-x}Br_x$ structure and suggested that Br composition (< 10%) can be tuned to achieve best device performance. On the other hand, a higher Br content (> 20%) could help to improve device stability.[100] The impact of Br composition on the stability and efficiency of the mixed halide perovskite solar cells as well as their mechanisms of degradation will be further studied and discussed in **Chapter 5**. In 2014, Grätzel et al. developed an alternative sequential step deposition technique to produce the perovskite active layer, which significantly improves the surface morphology and confirmed an efficiency of 14.1%.[101] Meanwhile, even more-outstanding device efficiency was reported by Snaith's group with a distinctive planar solar cell architecture that completely eliminated scaffold materials.[102] More importantly, they first proposed a dual source thermal evaporation method of fabricating $CH_3NH_3PbI_{3-x}Cl_x$ as the photoactive layer, leading to even better surface morphology and a more-efficient solar cell with a PCE of 15.4%.[102] Furthermore, Grätzel et al. modified their sequential deposition technique and enabled the growth of $CH_3NH_3PbI_3$ (MAPI) in a cuboid shape, with size being carefully controlled, and achieved a maximum PCE of 17%.[103] Later on, Seok's group obtained a confirmed PCE of 16.2% via employing a Br-I mixed halide perovskite layer (Br = 10% to 15%) with PTAA as HTM and further improved the PCE to 17.9%.[76] In the same year, Yang Yang's group achieved a remarkable device efficiency of 19.3% (fabricated in air) through careful manipulation of the band alignment on ETM/HTM with planar architecture.[104] From 2015 onwards, the development in perovskite solar cells continued apace. Seok et al. from Korea Research Institute of Chemical Technology (KRICT) developed a high quality formamidinium lead iodide ($FAPbI_3$) active layer though intermolecular exchange of dimethylsulfoxide (DMSO) and achieved a maximum PCE of 20.1%.[25] In 2017, with a similar technique, they further introduced excess iodide ions into the organic cation solution and developed a dense and uniform perovskite layer with a certified PCE of 22.1%.[105] To date, the highest certified device efficiency was obtained very recently by You Jingbi's research group from China with a PCE of 23.7%.[106]

2.3. Photovoltaic Parameters in Perovskite Solar Cells (PSCs)

2.3.1. Power Conversion Efficiency (PCE)

In theory, perovskite solar cells (PSCs) possess similar properties to other types of devices. They can be treated as a diode with rectifying characteristics and a photosensitive current source. Photovoltaic (PV) devices can be characterised by carrying out a current-voltage (J-V) measurement, in which many of the fundamental device properties can be observed simultaneously. For instance, parameters such as the short-circuit current density (J_{sc}), the open-circuit voltage (V_{oc}), and the fill factor (FF) that describe the 'squareness' of the J-V curve and thereby the quality of a single device can be measured. The typical J-V curve is schematically shown in Figure 2.6 with device properties measured under dark (dashed line), and illumination (solid red line) conditions.

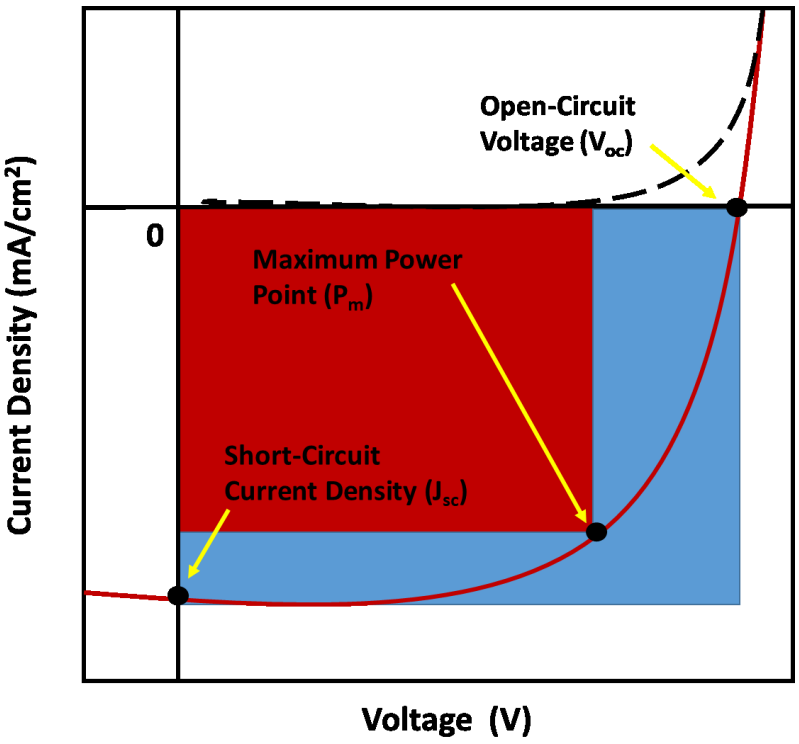


Figure 2-6: Schematic current-voltage (J-V) curve for a photovoltaic device measured in the dark (black dashed line) and under illumination (red line). The short-circuit current density (J_{sc}) and open-circuit voltage (V_{oc}) are illustrated, along with the value at which the solar cell generates the most power (P_m). The fill factor (FF) is a description of the 'squareness' of the curve and is calculated from the ratio of the red and blue squares.

It shows clearly that under without light illumination there is no current flowing through the device as there is no formation of photo-generated charges. However, introducing a voltage across the electrodes initiates a driving force for charge dissociation and transport, resulting in different current densities. According to Figure 2.6, the device is shorted when voltage is zero, and no current flows under dark condition. In contrast, upon illumination the charges are created and transported towards the electrodes so that the short-circuit current is produced. By contrast, the illuminated device under open circuit condition enables flowing of current to produce a potential difference (V_{oc}) with direction opposite from the inherent driving force; therefore neither driving voltage nor current is produced. Figure 2.6 also shows the maximum power point P_m, which describes the highest power output of the given device (shaded red). Overall, the J-V curves provide a direct pathway to quantify the maximum power conversion efficiency (η) for a single device and the equation is shown as follows (Equation (1)).

$$\eta = \frac{P_{out}}{P_{in}} = \frac{V_{mpp}J_{mpp}}{P_{in}} = \frac{V_{oc}J_{sc}FF}{P_{in}} \qquad (1)$$

The P_{in} and P_{out} represent the power that goes in and that is extracted from a given device, respectively. The V_{mpp} and J_{mpp} are the values of voltage and current density at the 'maximum power point'. In reality, it is usually more straightforward to give the efficiency in terms of V_{oc}, J_{sc}, and FF, the 'fill-factor', which defines the ratio of the maximum power output (blue shaded area in Figure 2.6) to the maximum power output a given device could potentially achieve (red shaded area).

It is worth noting that certain standards exist for comparing device performance between the scientific research and industrial community. For accurate and reliable solar cell measurement, the standard is to test devices under AM1.5 condition with a solar simulator. AM stands for air mass and is used to measure the length of atmosphere that sunlight travels through relative to the shortest path from the zenith to the ground.[107] Therefore, AM1.5 spectrum means a path distance of 1.5 times longer than the shortest route corresponding to an angle of 48.2° with an irradiance of 1000 W/m^2 and a temperature of 25 °C.[108]

Nevertheless, solar cells with ideal diode properties cannot be createdbecause power dissipation always exists through parasitic series (R_s) and shunt resistances (R_{sh}). In this case,

the equivalent circuit that allows a representation of a solar cell in non-ideal situations is shown in Figure 2.7 (a). The R_s arises from the resistance of the device materials and contacts and should ideally be zero, whilst the R_{sh} should be infinite in a perfect solar cell. Figure 2.7 (b) further demonstrates how the variation of R_s and R_{sh} would influence the J-V curve and thus the solar cell characteristics. Both R_s and R_{sh} lead to a reduction in the fill factor and make the solar cell less efficient. Specifically, an increase in R_s will lower the slope of the curve near V_{oc} and it means the current is not increasing with voltage at the ideal rate, whereas a decrease in R_{sh} leads to a slope in the J-V curve near J_{sc} due to leakage losses.

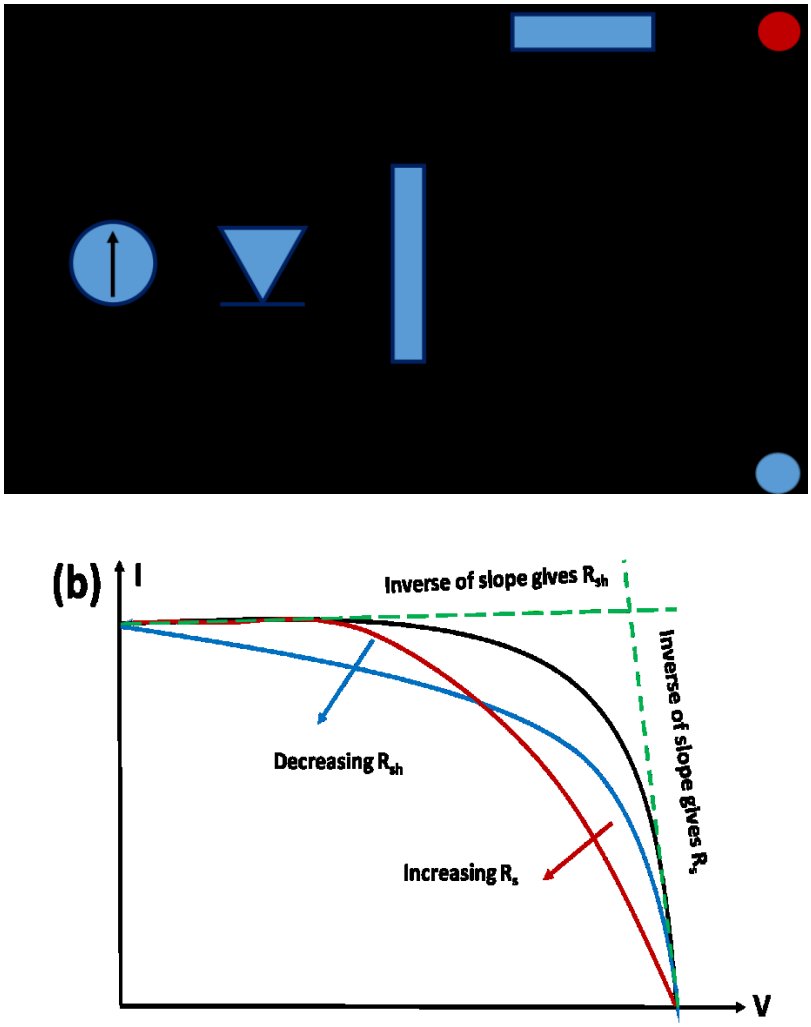


Figure 2-7: (a) Equivalent circuit for a device consisting of a current source (delivering I_{sc}), a diode, and two resistances which represent the non-ideal case in a single device – a shunt resistance (R_{sh}) in parallel, and a series resistance (R_s) in series. (b) J-V curve of an illuminated solar cell under a variation of R_s and R_{sh}.

2.3.2. Short Circuit Current Density (J_{sc})

The short-circuit current density J_{sc} defines the current flowing through unit area of a given device at which the voltage is zero (i.e. the device is shorted). Theoretically, J_{sc} can be obtained by integrating the combined effect of incident photon flux density (N_{ph}) and the quantum efficiency (QE) of devices over photon energy, as shown in Equation (2).

$$\boldsymbol{J_{sc} = q \int_{\lambda_{min}}^{\lambda_{max}} N_{ph}(E) \times QE(E) dE} \qquad (2)$$

In Equation (2), q is the elementary electronic charge with a constant value of ~1.602×10^{-19} C, and E represents the photon energy. QE is the probability that a photon can be converted to an electron, and can be defined as the multiplication of the above three terms in Equation (3): the probability of light absorption, the charge dissociation, and the probability of non-recombined charges prior to being transported to the electrode. It can be seen from Equations (2) and (3) that to maximise J_{sc}, the QE should be maximized in the range of 300 -800 nm, in which the wavelengths for N_{ph} stay the highest.[109]

$$\mathbf{QE} = (\mathbf{1} - \mathbf{q^{-kx}}) \times \mathbf{P(CS)} \times \mathbf{P(1 - CR)} \qquad (3)$$

In Equation (3), k is the extinction coefficient that determines the probability of light absorption, and x represents the thickness of the absorbing layer. In general, a thicker absorbing layer will end up with more light harvesting and a higher extinction coefficient.[110] The charge separation (CS) is dominated primarily by the characteristic of the donor-acceptor (D-A) interface and the charge diffusion length within the absorber.[111, 112] Under ideal conditions, excitons should be formed only within the length of diffusion from the D-A interface. Likewise, the charge recombination (CR) also depends on surface morphology and the concentration of the trap states.[113, 114] Therefore, the J_{sc} of the solar cell can be restricted by inefficient light absorption, inevasible charge separation and charge recombination at the D-A interface.

2.3.3. Open Circuit Voltage (V_{oc})

The open-circuit voltage V_{oc} represents the maximum voltage for a given solar cell to allow charge separation, and is present when current is at 0. The value of V_{oc} depends on the energetics of the actively layer. For simplicity, the V_{oc} can be mathematically expressed according to Equation (4).[9, 115]

$$\boldsymbol{V_{oc} = \frac{kT}{q} \ln\left(\frac{J_L}{J_0} + 1\right)} \qquad (4)$$

In Equation (4), k is the Boltzmann constant, T is the temperature, q is the elementary electronic charge as previously mentioned, J_L is the light-induced current density and J_0 is the diode saturation current density.[115] In general, the variation of J_L is small, whereas the saturation current density J_0 may vary by orders of magnitude, since J_0 is determined by the charge recombination within the solar cell. The V_{oc} can be understood as a measure of charge recombination within the device. It is suggested that V_{oc} can also be determined by the carrier concentration, but since it is not relevant to the present research it will not be introduced in detail.[116] In a solar cell, V_{oc} is also associated with the band gap energy of the absorber (E_g), so the relation of V_{oc} and E_g can be further expressed according to the Equation (5):

$$\boldsymbol{V_{oc} = \frac{E_g}{q} - \frac{kT}{q}\frac{J_L}{J_0}} \qquad (5)$$

In an ideal solar cell, V_{oc} is derived from the separation of the electron and hole quasi-Fermi levels, so V_{oc} is expected to be equal to the bandgap voltage.[117] T is the temperature and q is the elementary electronic charge. In a practical solar cell, however, the present of inherent resistance as well as loss of energy at the interface and charge transport layers always resulted in V_{oc} being below the bandgap voltage. The optimization of the V_{oc} requires minimising losses while still ensuring efficient charge dissociation and transportation. Therefore, for light harvesting to be efficient, the band gap energy (E_g) of absorber must be low enough to receive substantial solar radiation. However, this will reduce the maximum theoretical V_{oc} of the devices. Ultimately, a balance between V_{oc} and J_{sc} is needed to obtain the most efficient device.

2.3.4. Fill Factor (FF)

The fill factor (FF) is essentially a parameter that helps to evaluate the quality of the solar cell, and is much more sensitive as compared with J_{sc} or V_{oc}. As mentioned in the previous section, FF can be expressed as a measurement of the 'squareness' of the J-V curve, a device with a higher voltage normally results in a larger value of FF. The maximum theoretical FF for a given solar cell is calculated by differentiating the power as a function to voltage and finding where it equals 0. For an ideal solar cell, the maximum possible FF can be estimated with respect to the open-circuit voltage, as shown in Equation (6) [118]:

$$\boldsymbol{FF = \frac{v_{oc} - \ln(v_{oc} + 0.72)}{v_{oc} + 1}} \qquad (6)$$

Where 0.72 is a calculated constant and v_{oc} is defined as 'normalized V_{oc}' and is defined by Equation (7):

$$\boldsymbol{v_{oc} = \frac{q}{nkT} V_{oc}} \qquad (7)$$

In Equation (7), q is the elementary electronic charge, T is the temperature, n is the ideality factor that determines junction quality and types of recombination within a solar cell.[118] For a simple type recombination, n equals 1; in cases where recombination is more complicated, the ideality factor might be 2.[118] The high value of n not only reduces FF but also has an adverse effect on V_{oc}. It is suggested that Equation (6) is used only as a good approximation of FF for $v_{oc} > 10$. In practical solar cells, however, the maximum possible FF cannot be achieved due to the parasitic resistance. Therefore, the FF is more commonly worked out by measuring the J-V curve as the ratio of the maximum power output (P_m) from a given device to the product of J_{sc} and V_{oc}, and thus can be mathematically expressed as in Equation (8):

$$\boldsymbol{FF = \frac{P_m}{V_{oc} \times I_{sc}} = \frac{V_m \times I_m}{V_{oc} \times I_{sc}} = \frac{V_m \times J_m}{V_{oc} \times J_{sc}}} \qquad (8)$$

It can be suggested that conditions such as poor interface quality or weak interface charge mobility and lifetime all have an adverse effect on the value of FF. Increasing FF will result in more power output as P_m is nearer to the maximum theoretical power.

2.4. Recent Progress on the Stability of Perovskite Solar Cells

In spite of the rapid development that has been achieved on the efficiency of perovskite solar cells (PSCs) making them potentially very competitive as compared with conventional silicon solar cells, there are still issues to overcome. Device stability is the most challenging aspect. Devices with perovskite layers have exhibited various degrees of degradation under ambient conditions, which is caused by a group of factors that mainly include humidity, oxygen, temperature, UV illumination, mechanical stress and so on.[119] As a result, the material undergoes decomposition reactions within the active layer, which will directly affect its crystal structure, charge transport behaviour and may also offset the stability of other interface layers.[120] The origin of the degradation inside perovskite solar cells can be quite complicated and is not yet fully understood. This is because the degradation reaction is initiated not from a single factor but from the combined effects of several different factors that follow distinctive mechanisms. For instance, without water and oxygen, intrinsic degradation happens in the perovskite layer due to the light illumination or thermal stress.[121] In contrast, in the presence of water and oxygen, the perovskite layer undergoes a hydrolysis reaction owing to the hygroscopic properties of the organic component of perovskite such as methylammonium cations.[122] In general, a commercialised solar cell should remain good in operation continuously under outdoor conditions for about 25 years.[123] The standard condition for testing long-term device stability without encapsulation should be no less than 500 hours under 1 sun illumination.[96] It is worth noting there have been some interesting approaches recently with promising achievements on improving perovskite solar cell stability. Examples include introducing different kinds of doping,[121, 124, 125] employing inorganic electron extraction layers,[126] introducing carbon nanotubes or dopant-free hole transport layers (HTLs),[127-129] developing novel electrodes,[130] or more easily, passivating the perovskite active layer with different materials.[131-134] In the next section, the degradation mechanisms caused by different factors are identified, and a brief review of some state-of-the-art investigations on achieving more stable perovskite solar cells (PSCs) is presented.

2.4.1. Phase Stability

In general, the optoelectronic properties of perovskite materials (such as bandgap, charge carrier mobility etc.) are highly dependent on crystal structure.[135] Therefore, any phase transformation could result in lattice distortion on the perovskite structure. This is detrimental to the electronic properties of the photoactive material and will reduce the device performance. Theoretically, the stability of the 3D perovskite phases can be extensively predicted using a dimensionless constant called the Goldschmidt tolerance factor, t, which is based on its standard chemical structure ABX_3 and the ionic radius r_i of each individual ion (A, B, X) using Equation (9) as follows.[136]

$$t = \frac{r_A + r_X}{\sqrt{2}(r_B + r_X)} \qquad (9)$$

In Equation (9), r_A, r_B and r_X defines the radius of cation A, B and monovalent halide anion X, respectively. Ideally, the BX_6 octahedra is present inside the cubic crystal structure and in this case the value of t is 1. In reality, some imperfections always exist and for a 3D cubic perovskite crystal to be stable the t should be between 0.8 to 1.[137] There is a decrease in the value t (< 0.8) when the ratio of r_A and r_B is too small, which results in a reduction of crystal symmetry and leads to a more-distorted perovskite structure. In contrast, when the ratio of r_A to r_B becomes too large, the tolerance factor t will become greater than 1 and also cause distortion of the perovskite structure. Therefore, for a given B cation, a larger A cation or a smaller X anion will automatically lead to higher t. For instance, the large I^- anion present in $CH_3NH_3PbI_3$ (MAPI) perovskite leads to the formation of a non-stable tetragonal phase (a=b≠c). In replacing I^- with smaller Br^- or Cl^- anions, the distorted tetragonal phase will transform to a cubic phase that is more stable.[138, 139] On the other hand, organic cations A can adopt many different orientations in the perovskite lattice, which means that the tolerance factor t can be very difficult to calculate as absolute radii of organic ions are not fixed.[140] Nevertheless, we can still use the tolerance factor model to qualitatively compare the stability of different perovskite structures based on the relative size of the A cation.

2.4.2. Thermal Stability

For perovskite solar cells to be commercialised, the devices need to be operated under outdoor conditions with temperature normally up to 85 °C or even higher under extreme circumstances.[141, 142] Therefore, exploring the thermal stability of the perovskite materials becomes critical to the development of suitable solar cells. The crystal structure and hence the stability of the absorbing layer relies heavily on the processing temperature as thermal annealing is normally required next to the deposition of the perovskite layer.[143] The absorbing layers such as $CH_3NH_3PbI_3$ (MAPI) undergo an irreversible phase transformation from tetragonal to cubic phase when T is around 55 °C,[144] which greatly affects the device performance. Although some studies showed that even after heating over 100 °C the MAPI perovskite layer still exists as a tetragonal phase. [97, 145, 146] However, further increases of the temperature to a high level (> 150 °C) could result in structural changes, leading to a reduction of solar cell efficiency.[143] This has been confirmed by Yazdi et al. showing that decomposition of MAPI at high temperature results in the generation of HI, CH_3NH_2 and PbI_2, which degraded the perovskite material.[147] Furthermore, Grätzel et al. extended this investigation by conducting thermogravimetric analysis (TGA) and confirmed successive loss of HI and CH_3NH_2 from MAPI upon high temperature.[148] Later on, Philippe et al. studied the exclusive impact of elevated temperature on film degradation for both $CH_3NH_3PbI_3$ (MAPI) and mixed halide $CH_3NH_3PbI_{3-x}Cl_x$ (MAPIC) using X-ray photoelectron spectroscopy (XPS) and identified that perovskites are unstable at higher temperatures (100 °C).[149] Conings et al. further found that MAPI could decompose even under inert atmosphere at 85 °C.[150] Recently, an alternative organic cation formamidinium (FA) with larger radius has been used instead of methylammonium (MA). The tolerance factor in the case of using FA is close to 1 and so it is potentially more suitable for solar cells.[151] Further investigations showed that the thermal stability could be improved by using FA as the organic cation. At 150 °C, the $FAPbI_3$ (FAPI) undergoes phase transformation to tetragonal structure and the film shows no bleaching for 60 minutes whereas MAPI could only endure this temperature for 30 minutes.[66, 78] However, the limitation of FAPI as an absorbing material is that it degrades rapidly when exposed to humidity.[78] In fact, people further observed that two phases exist in FAPI, one is the yellow hexagonal phase and the other is the black trigonal phase. The transformation between these two phases is reversible and is temperature dependent.[152] The obstacles of using FAPI open a pathway for replacing methylammonium (MA) with inorganic cations and one of the most extensively used examples is caesium (Cs).

Unfortunately, at room temperature, $CsPbI_3$ is unable to form perovskite so that an alternative metal cation is required.[153] Interestingly, replacing Pb with tin (Sn) in the case of $CsSnI_3$ showed that it undergoes an irreversible phase transformation from orthorhombic to cubic at around 152 °C whereas $CsSnBr_3$ remains in the cubic structure even at 450 °C.[154] Both of them exhibited superior thermal stability relative to organic cation based perovskites. Nevertheless, the Sn is very unstable in its Sn^{2+} form and is prone to be oxidized to Sn^{4+} under humidity or oxygen and this ended up with self-doping inside perovskites and degraded the $ASnX_3$ films.[152] It can be argued that although pure inorganic perovskites possess advantages over the hybrid perovskites as the aforementioned have no organic cations sensitive to oxygen or moisture; a non-toxic metal cation other than Pb is necessary for obtaining stable perovskite solar cells.

In addition, the decomposition of the hole-transporting materials (HTM) such as Spiro-OMeTAD can also affect the stability of PSCs. Malinauskas et al. observed that fully symmetrical Spiro-OMeTAD is susceptible to crystallize under elevated temperatures. The large crystalline domains initiate degradation of the interface between the HTM layer and absorber and can be decreased by enhancing local asymmetry, such as adding dopants into the Spiro-OMeTAD.[64] Li et al. further highlighted that thermal instability caused by HTM can be addressed by using thermally conductive carbon material other than HTMs as a back contact for PSCs.[155] Alternatively, Bush et al. introduced a solution-processed oxide nanoparticle buffer layer for producing semi-transparent PSCs and achieved stable perovskite at 100 °C in ambient atmosphere without additional sealing.[156] Recently, Saliba et al. reported that by using a mixture of methylammonium (MA) and formamidinium (FA) together with the addition of tiny amount of inorganic cesium ions could form a triple-cation perovskite system with higher resistance to processing temperature as well as greater solar cell efficiency and reproducibility.[121] The result provided a novel strategy for enhancing the thermal stability of the perovskite solar cells and paved the way to their commercialization.

2.4.3. Moisture

Solar cells with perovskite as an absorbing layer are also susceptible to degrade under a humid environment.[157] Essentially, the hygroscopic property of the organic components and the soluble nature of Pb salts cause the degradation of the perovskite solar cells under moisture. [158, 159] Over the past decades, extensive investigations have been carried out to improve the moisture stability. Some recent strategies have included adding a waterproofing tunneling layer,[139, 160] using hydrophobic carbon back contacts,[127] direct encapsulation of the device with polymer,[161] inserting low dimensional perovskites,[162, 163] and applying surface passivation via cross-linking to form a moisture-resistant layer.[164, 165] The degradation mechanisms of perovskite solar cells under humidity have been analyzed by Li et al. in their recent review.[166] Theoretically, the $CH_3NH_3PbI_3$ (MAPI) film becomes yellow under the influence of moisture and decomposes into PbI_2, CH_3NH_2, and HI.[167] Moreover, Leguy et al. pointed out that this degradation reaction could proceed under water vapor, resulting in a reversible reaction in which a hydrated intermediate phase ($MAPbI_3 \cdot H_2O$) is formed.[158] To quantitatively evaluate the influence of moisture on the devices, Yang et al. carried out a measurement in which the different relative humidity (RH) conditions were controlled in a chamber so that the degradation reaction of the MAPI layer can be monitored. They finally confirmed that degradation under moisture started with the hydration reaction of MAPI and ended up with $MA_4PbI_6 \cdot 2H_2O$ and PbI_2.[168] Inspired by this, Niu et al. further tested the moisture stability of MAPI and mixed halide and found that MAPI device remains stable below 50% RH, but degrades over 55% RH.[139] Meanwhile, some computational studies highlighted that the high polarity of H_2O from moisture or water vapor is likely to be responsible for the distortion in the crystal structure of the PSCs.[160, 169] Interestingly, several studies and reviews have pointed out that a moderate amount of water contained in the perovskite film preparation is actually beneficial for perovskite solar cells as it helps to improve the nucleation and crystallization of the perovskites and resulted in better film morphology.[170, 171] Therefore, further investigations are required to gain more insight into the role of water or moisture in the process of perovskite film device fabrication as well as exploring more effective strategies on eliminating its impact on the stability of the perovskite solar cells.

2.4.4. UV Irradiation

Leijtens et al. have showed that degradation of PSCs with mesoporous (mp) TiO_2 can be accelerated under UV illumination.[125] They carried out stability tests for PSCs under ambient conditions and observed that solar cell performance under UV radiation undergoes a more rapid degradation, which is originated from a reduce in J_{sc}.[125] They attributed the phenomenon to the enhanced charge recombination from the mp-TiO_2 layer degradation and is demonstrated schematically in Figure 2.8. The surface of TiO_2 contains many oxygen vacancies, which play the role of donating electrons. Without UV illumination, these vacancies are filled by a charge transfer (CT) complex between TiO_2 and molecular O_2. The UV illumination facilitate TiO_2 exciting on the bandgap, leading to the formation of holes in the valence band (VB). The holes then recombine with the electrons in the CT state, causing molecular O_2 to desorb. This leaves unoccupied vacancies stay as trap state, so that photo-induced electrons from molecular dyes could recombine with holes in the HTM.[125]

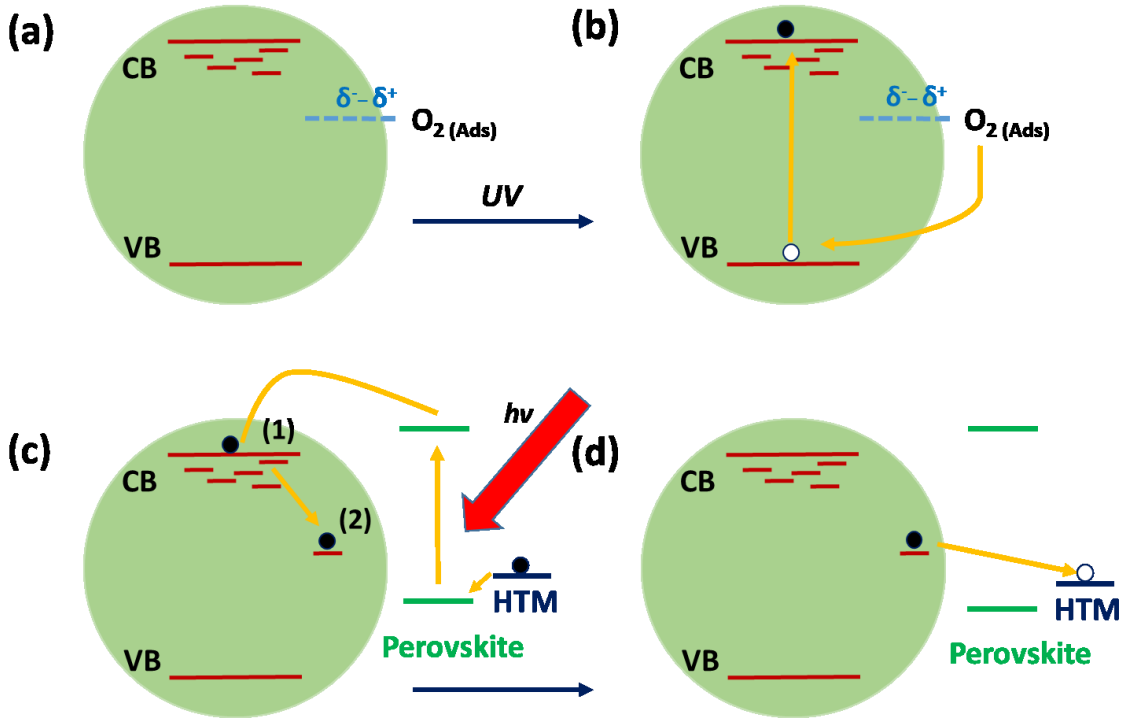


Figure 2-8: Proposed degradation mechanism for perovskite solar cells under the influence of UV illumination. (a) The surface of TiO_2 contains many oxygen vacancies (Ti^{3+}) that act as electron-donating sites. The electrons of these sites interact with molegular oxygen from atmosphere to form a charge transfer complex (O_2^- -Ti^{4+}) (shown as δ^- - δ^+). (b) Upon UV illumination, the photogenerated holes react with oxygen radicals absorbed at surface oxygen vacancy, forming a hole in the valence band (VB), which further recombines with the electrons in the oxygen vacancy, leading to O_2 to desorb. (c) Upon photo excitation of the perovskite, electrons can inject either (1) into the conduction band or (2) directly in the deep surface traps. (d) The deeply trapped electrons are recombined with holes on HTM, leading to a decrease in J_{sc} and the degradation of the perovskite solar cells. (Image modified from reference [125])

2.4.5. Oxygen

Recently, our research group investigated that $CH_3NH_3PbI_3$ (MAPI or $MeNH_3PbI_3$) films is able to degrade at room temperature in moisture-free environments under the influence of light and oxygen.[172] Specifically, it showed that the degradation of perovskite layer under this atmosphere can be much faster with mp-Al_2O_3 than with mp-TiO_2 as electron transporting layer. This suggested that electron extraction from MAPI incorporating mp-TiO_2 could stabilise the film. Further studies confirmed this observation by revealing that the species responsible for MAPI degradation under a combination of light and dry oxygen was the superoxide ($O_2^{\cdot-}$), which is originated from a cascade electron transfer reaction between photo-excited MAPI and the outer molecular oxygen, illustrated in Figure 2.9.[173]

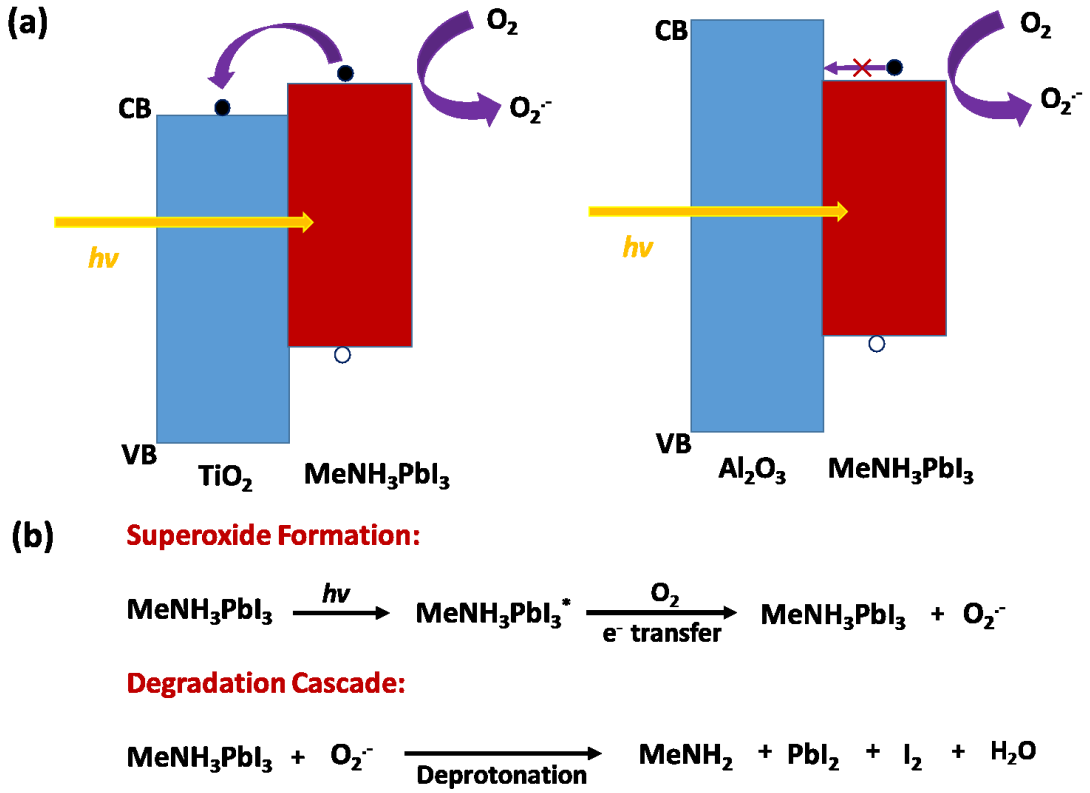


Figure 2-9: The envisaged principle for the formation of superoxide species and MAPI degradation. (a) The energy level diagrams of mesoporous (mp) TiO_2 or Al_2O_3/MAPI interfaces illustrating smoothly electron transfer. Transfer of photo-excited electrons from MAPI photoactive layer to oxygen leads to superoxide formation. In case of mp-Al_2O_3, electrons stay on the MAPI photoactive layer and is then transferred to ambient oxygen. In case of mp-TiO_2, the electrons can be extracted rapidly by mp-TiO_2 layer and can effectively compete with electron transfer to oxygen leading to lower superoxide formation and thus greater lifetime for perovskite layer. (b) The overall reaction of MAPI degradation. The cascade reaction is induced by a deprotonation reaction from organic cation by superoxide created under illumination and oxygen.[173]

Therefore, the mp-TiO_2 layer could facilitate efficient charge extraction by reducing the amount of electrons in MAPI layer available for react with oxygen, thereby reduces yield of superoxide and retard the degradation process. Moreover, it can be suggested that superoxide induced degradation is occurred by means of abstracting an acidic proton from the $CH_3NH_3^+$ cation, which triggers a cascade reaction so that MAPI decompose into CH_3NH_2, PbI_2, I_2 and H_2O. (Figure 2.9b).[173] Recently, it was found that photo-oxidation was the dominant degradation pathway in complete MAPI based perovskite solar cells even at 85% relative humidity (Figure 2.10).[119] The illumination and dry oxygen induced degradation process can be accelerated by an applied external bias due to slower electron extraction.[119] Furthermore, in the condition of V_{oc}, devices degraded rapidly in oxygen even with no illumination as electron is injected into the valence band (VB) of MAPI. This implies that superoxide formation is an electronic effect, which have a significant impact for not only perovskite solar cells, but also diodes and transistors based on $CH_3NH_3PbI_3$.[119]

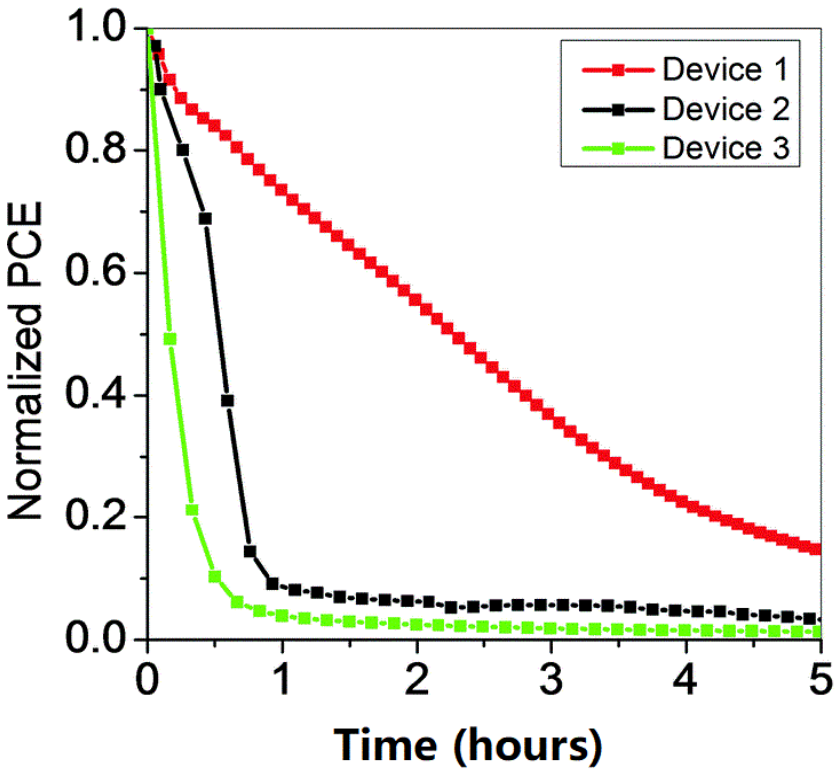


Figure 2-10: Normalized power conversion efficiency (PCE) as a function of illumination time for $CH_3NH_3PbI_3$ (MAPI) solar cells under light and oxygen for three different solar cell architectures. Device 1: FTO/compact-TiO_2/mp-TiO_2/MAPI/Spiro-OMeTAD/Au (red); Device 2: FTO/compact-TiO_2/MAPI/Spiro-OMeTAD/Au (black); Device 3: FTO/compact-TiO_2/mp-Al_2O_3/MAPI/spiro-OMeTAD/Au (green).[119]

Overall, photo-oxidation exhibits a dentrimental effect to all perovskite based solar cells as no polymeric encapsulates is existed to form an effective oxygen inhibitor layer.

Unfortunately, some typical oxygen barriers, for example, metals, glass, or ceramics material are unable to be employed in solution processed PSCs since they are either opaque in texture or incompatible with the substrates. Our research group,[119, 172, 173] and that of Pearson et al.,[174] have independently demonstrated that by incorporating a mp-TiO_2 charge extraction layer into a PSC could effectively enhances its lifetime by alleviating the formation of superoxide species. This was further proved by conducting fluorescent probe studies.[173] However, the fact that substantial amounts of $O_2^{\cdot-}$ were still present at the surface of the perovskite active layer means that device efficiency could greatly deteriorated over a period of only six hours under continuous illumination.[119] Therefore, it is very likely that apart from the application of electron extraction layers alone, further work must be done to sufficiently stabilize PSCs towards oxygen stress. Obviously, the most technologically desirable route to stabilize PSCs is to prevent the degradation cascade reaction by improving perovskite resistance to the superoxide ($O_2^{\cdot-}$).

2.5. Motivations and Layout of Thesis

Having overviewed the progress of solar cell technologies and knowledge of degradation mechanisms of perovskite solar cells under various external factors, it is now possible to give more specific aims and layout of the project as follows:

- First, although stability of perovskite devices under various external conditions has been extensively studied, the understanding of the combination effect of light and oxygen alone on the stability of perovskite solar cells, particularly with mesoporous TiO_2 as electron transporting layer (ETL) remains limited and requires further investigation.

- Second, the basic theory that underpins the light and dry oxygen induced degradation as a result of superoxide generation and its effect on the stability of the perovskite films has been elucidated by our research group. There is a pressing need for extending and testifying this theory in the aspect of solar cells.

- Third, it remains unclear as to how superoxide generation is related to the location of the surface defects (particularly iodide vacancies) on the perovskite layer, and hence the long-term stability of standard and mixed halide perovskite devices needs to be studied.

- Fourth, effectively strategies need to be designed and developed in the fabrication of perovskite active layers and devices to minimize the surface defects to address the oxygen- and light-induced degradation.

Therefore, different results and discussion chapters in this thesis attempt to address some of these fundamental issues to improve our understanding of the perovskite solar cells

Chapter 4 consists of two sections: The first establishes a standard and reproducible procedure for fabricating $CH_3NH_3PbI_3$ (MAPI) perovskite solar cells. Particular attention is paid to the effect of compact layer thickness, mesoporous layer thickness, $TiCl_4$ post treatment and Spiro-OMeTAD oxidation on photovoltaic parameters. Device reproducibility is affected not only by material properties and device architecture, but also by the measuring condition. Specifically, degradation of perovskite solar cells under light and oxygen caused

large variations in device efficiency. Thereby, understanding light- and oxygen-induced degradation and their effect on devices became a major objective of this project. **Section two** builds upon the knowledge obtained from observations that MAPI films generate superoxide (O_2^-) when exposed to light and dry oxygen, which resulted in perovskite degradation. With a main focus on devices, the correlation between perovskite morphology and superoxide formation, and further identified their impact on device stability was investigated. The study also shows that defects on the perovskite layer plays an important role on the solar cell stability, which indicates the direction for further research.

Chapter 5 also includes two sections: **Section one** builds on the basis of our recent finding that iodide vacancies on MAPI surface are the most favourable locations for superoxide generation, which initiates the light- and oxygen-induced degradation. We developed a film passivation technique by direct loading appropriate amounts of methylammonium iodide (MAI) salt solution on top of the perovskite film prior to depositing Spiro-OMeTAD and showed that it could effectively passivate the perovskite film, reduce the number of defects, inhibit superoxide formation and thus improve device stability. **Section two** extended this study to I-Br mixed-halide devices by exploring the correlation between superoxide formation and device stability as a function of bromide composition for $CH_3NH_3Pb(I_{1-x}Br_x)_3$ (MAPBI) solar cells. Moreover, we investigated the effect of defect passivation and found that MAI salt coating could also help in obtaining more-stable mixed halide devices. Nevertheless, stable solar cells were achieved at the expense of losing device efficiency. Addressing this issue led to the introduction of an alternative passivating agent in Chapter 6.

Chapter 6 introduces an alternative iodide salt, namely phenylethylammonium iodide (PEAI) and shows that passivation of the MAPI layer with this material can effectively enhance film and solar cell stability under illumination and oxygen condition with no compromise in device efficiency. Specifically, the observations are consistent with the iodide salt passivation, lowering the iodide vacancies, decreasing the superoxide formation and thus improving solar cell stability. Moreover, the limitations in reproducibility of using this method due to the additional coating step were also identified, which encouraged investigation of a simpler strategy on surface passivation for stable solar cells.

Chapter 7 describes a new approach on device fabrication procedure, namely iodide salt assisted anti-solvent treatment (ISAAT) in the preparation of MAPI layer using PEAI as

agent. The chapter explores the impact of this procedure with a combination of different characterization techniques and shows that the ISAAT treatment could effectively passivate surface defects of the perovskite layer and further enhance their morphology and crystallinity. Devices with this treatment resulted in an efficiency of 17.99%, which is significantly higher than without ISAAT treatment. Furthermore, greater stability and reproducibility were confirmed using the ISAAT method relative to conventional PEAI treatment. The technique brought a more-efficient pathway to the future design and optimisation of perovskite solar cells with greater long term stability and reproducibility.

2.6. References

[1] C.C.J. Roothaan, *Reviews of Modern Physics* **1951**, *23,* 69.

[2] B.V. Suresh, *Solid State Devices and Technology*. 2010: Pearson Education India.

[3] M. Riordan,L. Hoddeson, *Crystal Fire: the Invention of the Transistor and the Birth of the Information Age*. **1998:** WW Norton & Company.

[4] A.-E. Becquerel, *CR Acad. Sci* **1839**, *9,* 1.

[5] M. Grätzel, *Nature* **2001**, *414,* 338.

[6] C.E. Fritts, *American Journal of Science* **1883**, 465.

[7] A. Einstein, *Relativity*. **2013:** Routledge.

[8] D.M. Chapin, C.S. Fuller, G.L. Pearson, *Solar Energy Converting Apparatus*. 1957, Google Patents.

[9] M.A. Green, Solar Cells: Operating Principles, Technology, and System Applications **1982**: Prentice-Hall, Inc,-Englewood Cliffs, NJ, 288.

[10] M.A. Green, Y. Hishikawa, E.D. Dunlop, D.H. Levi, J. Hohl-Ebinger, A.W. Ho-Baillie, *Progress in Photovoltaics* **2018**, *26*.

[11] J. Nelson, *Materials Today* **2011**, *14,* 462.

[12] M.K. Nazeeruddin, E. Baranoff, M. Grätzel, *Solar Energy* **2011**, *85,* 1172.

[13] M. Grätzel, *Nature Materials* **2014**, *13,* 838.

[14] C.W. Tang, *Applied Physics Letters* **1986**, *48,* 183.

[15] M.C. Scharber,N.S. Sariciftci, *Progress in Polymer Science* **2013**, *38,* 1929.

[16] A. Polman, M. Knight, E.C. Garnett, B. Ehrler, W.C. Sinke, *Science* **2016**, *352*.

[17] J. Hou, O. Inganäs, R.H. Friend, F. Gao, *Nature Materials* **2018**, *17,* 119.

[18] Z. Xiao, X. Jia, L. Ding, *Science Bulletin* **2017**, *62,* 1562.

[19] H. Spanggaard,F.C. Krebs, *Solar Energy Materials and Solar Cells* **2004**, *83,* 125.

[20] B.A. Gregg,M.C. Hanna, *Journal of Applied Physics* **2003**, *93,* 3605.

[21] A.A. Bakulin, A. Rao, V.G. Pavelyev, P.H. van Loosdrecht, M.S. Pshenichnikov, D. Niedzialek, J. Cornil, D. Beljonne, R.H. Friend, *Science* **2012**, *335,* 1340.

[22] G. Yu, J. Gao, J.C. Hummelen, F. Wudl, A.J. Heeger, *Science* **1995**, *270,* 1789.

[23] L. Meng, Y. Zhang, X. Wan, C. Li, X. Zhang, Y. Wang, X. Ke, Z. Xiao, L. Ding, R. Xia, *Science* **2018**, *361,* 1094.

[24] K. Yoshikawa, H. Kawasaki, W. Yoshida, T. Irie, K. Konishi, K. Nakano, T. Uto, D. Adachi, M. Kanematsu, H. Uzu, *Nature Energy* **2017**, *2,* 17032.

[25] W.S. Yang, J.H. Noh, N.J. Jeon, Y.C. Kim, S. Ryu, J. Seo, S.I. Seok, *Science* **2015**, *348,* 1234.

[26] Q. Burlingame, C. Coburn, X. Che, A. Panda, Y. Qu, S.R. Forrest, *Nature* **2018**, *554,* 77.

[27] U. Würfel, D. Neher, A. Spies, S. Albrecht, *Nature Communications* **2015**, *6,* 6951.

[28] P. Cheng,X. Zhan, *Chemical Society Reviews* **2016**, *45,* 2544.

[29] M. Grätzel, *Journal of Photochemistry and Photobiology C: Photochemistry Reviews* **2003**, *4,* 145.

[30] A. Hagfeldt, G. Boschloo, L. Sun, L. Kloo, H. Pettersson, *Chemical Reviews* **2010**, *110,* 6595.

[31] H. Gerischer,F. Willig, *Reaction of Excited Dye Molecules at Electrodes*, in *Physical and Chemical Applications of Dyestuffs* **1976**, Springer. 31.

[32] B. O'Regan,M. Grätzel, *Nature* **1991**, *353,* 737.

[33] B. Li, L. Wang, B. Kang, P. Wang, Y. Qiu, *Solar Energy Materials and Solar Cells* **2006**, *90,* 549.

[34] H.J. Snaith,L. Schmidt-Mende, *Advanced Materials* **2007**, *19,* 3187.

[35] J.H. Yum, P. Chen, M. Grätzel, M.K. Nazeeruddin, *ChemSusChem: Chemistry & Sustainability Energy & Materials* **2008**, *1,* 699.

[36] M. Nazeruddin,A. Kay, *Journal of the American Chemical Society* **1993**, *115,* 6382.

[37] M.K. Nazeeruddin, S. Zakeeruddin, R. Humphry-Baker, M. Jirousek, P. Liska, N. Vlachopoulos, V. Shklover, C.-H. Fischer, M. Grätzel, *Inorganic Chemistry* **1999**, *38,* 6298.

[38] P. Wang, S.M. Zakeeruddin, R. Humphry-Baker, J.E. Moser, M. Grätzel, *Advanced Materials* **2003**, *15,* 2101.

[39] T. Horiuchi, H. Miura, K. Sumioka, S. Uchida, *Journal of the American Chemical Society* **2004**, *126,* 12218.

[40] S. Mathew, A. Yella, P. Gao, R. Humphry-Baker, B. Curchod, N. Ashari-Astani, I. Tavernelli, U. Rothlisberger, M.K. Nazeeruddin, M. Grätzel, *Angew Chem Int Ed* **2014**, *49,* 6646.

[41] S.A. Sapp, C.M. Elliott, C. Contado, S. Caramori, C.A. Bignozzi, *Journal of the American Chemical Society* **2002**, *124,* 11215.

[42] S.M. Feldt, E.A. Gibson, E. Gabrielsson, L. Sun, G. Boschloo, A. Hagfeldt, *Journal of the American Chemical Society* **2010**, *132,* 16714.

[43] S.M. Feldt, U.B. Cappel, E.M. Johansson, G. Boschloo, A. Hagfeldt, *The Journal of Physical Chemistry C* **2010**, *114,* 10551.

[44] T. Daeneke, T.-H. Kwon, A.B. Holmes, N.W. Duffy, U. Bach, L. Spiccia, *Nature Chemistry* **2011**, *3,* 211.

[45] T.C. Li, A.M. Spokoyny, C. She, O.K. Farha, C.A. Mirkin, T.J. Marks, J.T. Hupp, *Journal of the American Chemical Society* **2010**, *132,* 4580.

[46] Y. Duan, N. Fu, Q. Liu, Y. Fang, X. Zhou, J. Zhang, Y. Lin, *The Journal of Physical Chemistry C* **2012**, *116,* 8888.

[47] J. Du, J. Qi, D. Wang, Z. Tang, *Energy & Environmental Science* **2012**, *5,* 6914.

[48] Y. Park, J.W. Lee, S.-J. Ha, J.H. Moon, *Nanoscale* **2014**, *6,* 3105.

[49] A.M. Peiró, P. Ravirajan, K. Govender, D.S. Boyle, P. O'Brien, D.D. Bradley, J. Nelson, J.R. Durrant, *Journal of Materials Chemistry* **2006**, *16,* 2088.

[50] X. Mao, R. Zhou, S. Zhang, L. Ding, L. Wan, S. Qin, Z. Chen, J. Xu, S. Miao, *Scientific Reports* **2016**, *6,* 19390.

[51] J.D. Roy-Mayhew, G. Boschloo, A. Hagfeldt, I.A. Aksay, *ACS Applied Materials & Interfaces* **2012**, *4,* 2794.

[52] S. Roy, R. Bajpai, A.K. Jena, P. Kumar, D. Misra, *Energy & Environmental Science* **2012**, *5,* 7001.

[53] *NREL Efficiency Chart* **2017**. The chart is available at https://www.nrel.gov/pv/cell-efficiency.html

[54] E. Stathatos, P. Lianos, A. Surca Vuk, B. Orel, *Advanced Functional Materials* **2004**, *14,* 45.

[55] Q.-B. Meng, K. Takahashi, X.-T. Zhang, I. Sutanto, T. Rao, O. Sato, A. Fujishima, H. Watanabe, T. Nakamori, M. Uragami, *Langmuir* **2003**, *19,* 3572.

[56] Y. Shibata, T. Kato, T. Kado, R. Shiratuchi, W. Takashima, K. Kaneto, S. Hayase, *Chemical Communications* **2003**, 2730.

[57] V. Perera, P. Pitigala, P. Jayaweera, K. Bandaranayake, K. Tennakone, *The Journal of Physical Chemistry B* **2003**, *107,* 13758.

[58] V. Perera,K. Tennakone, *Solar Energy Materials and Solar Cells* **2003**, *79,* 249.

[59] W. Zhang, Y. Wu, H.W. Bahng, Y. Cao, C. Yi, Y. Saygili, J. Luo, Y. Liu, L. Kavan, J.-E. Moser, *Energy & Environmental Science* **2018**.

[60] J. Zhang, M. Freitag, A. Hagfeldt, G. Boschloo, *Solid-state Dye-sensitized Solar Cells*, in *Molecular Devices for Solar Energy Conversion and Storage* **2018**, Springer. 151.

[61] Y. Cao, Y. Saygili, A. Ummadisingu, J. Teuscher, J. Luo, N. Pellet, F. Giordano, S.M. Zakeeruddin, J.-E. Moser, M. Freitag, *Nature Communications* **2017**, *8,* 15390.

[62] B. Xu, E. Sheibani, P. Liu, J. Zhang, H. Tian, N. Vlachopoulos, G. Boschloo, L. Kloo, A. Hagfeldt, L. Sun, *Advanced Materials* **2014**, *26,* 6629.

[63] L. Tao, Z. Huo, Y. Ding, Y. Li, S. Dai, L. Wang, J. Zhu, X. Pan, B. Zhang, J. Yao, *Journal of Materials Chemistry A* **2015**, *3,* 2344.

[64] T. Malinauskas, D. Tomkute-Luksiene, R.d. Sens, M. Daskeviciene, R. Send, H. Wonneberger, V. Jankauskas, I. Bruder, V. Getautis, *ACS Applied Materials & Interfaces* **2015**, *7,* 11107.

[65] B. Xu, H. Tian, L. Lin, D. Qian, H. Chen, J. Zhang, N. Vlachopoulos, G. Boschloo, Y. Luo, F. Zhang, *Advanced Energy Materials* **2015**, *5,* 1401185.

[66] U. Bach, D. Lupo, P. Comte, J. Moser, F. Weissörtel, J. Salbeck, H. Spreitzer, M. Grätzel, *Nature* **1998**, *395,* 583.

[67] B. Lee, J. He, R.P. Chang, M.G. Kanatzidis, *Nature* **2012**, *485,* 486.

[68] P. Wang, S.M. Zakeeruddin, J.E. Moser, M.K. Nazeeruddin, T. Sekiguchi, M. Grätzel, *World Scientific* **2011**, 88.

[69] P. Wang, S.M. Zakeeruddin, P. Comte, I. Exnar, M. Grätzel, *Journal of the American Chemical Society* **2003**, *125,* 1166.

[70] L. Schmidt-Mende, U. Bach, R. Humphry-Baker, T. Horiuchi, H. Miura, S. Ito, S. Uchida, M. Grätzel, *Advanced Materials* **2005**, *17,* 813.

[71] W. Kubo, T. Kitamura, K. Hanabusa, Y. Wada, S. Yanagida, *Chemical Communications* **2002**, 374.

[72] M. Grätzel, *Journal of Photochemistry and Photobiology A: Chemistry* **2004**, *164,* 3.

[73] Q. Jiang, Z. Chu, P. Wang, X. Yang, H. Liu, Y. Wang, Z. Yin, J. Wu, X. Zhang, J. You, *Advanced Materials* **2017**, *29,* 1703852.

[74] T. Singh,T. Miyasaka, *Advanced Energy Materials* **2018**, *8,* 1700677.

[75] M.A. Green, A. Ho-Baillie, H.J. Snaith, *Nature Photonics* **2014**, *8,* 506.

[76] N.J. Jeon, J.H. Noh, Y.C. Kim, W.S. Yang, S. Ryu, S.I. Seok, *Nature Materials* **2014**, *13,* 897.

[77] Q. Chen, H. Zhou, Z. Hong, S. Luo, H.-S. Duan, H.-H. Wang, Y. Liu, G. Li, Y. Yang, *Journal of the American Chemical Society* **2013**, *136,* 622.

[78] G.E. Eperon, S.D. Stranks, C. Menelaou, M.B. Johnston, L.M. Herz, H.J. Snaith, *Energy & Environmental Science* **2014**, *7,* 982.

[79] C. Wehrenfennig, G.E. Eperon, M.B. Johnston, H.J. Snaith, L.M. Herz, *Advanced Materials* **2014**, *26,* 1584.

[80] M.K. Assadi, S. Bakhoda, R. Saidur, H. Hanaei, *Renewable and Sustainable Energy Reviews* **2018**, *81,* 2812.

[81] H.J. Snaith, *The Journal of Physical Chemistry Letters* **2013**, *4,* 3623.

[82] N.-G. Park, *Materials Today* **2015**, *18,* 65.

[83] S.D. Stranks, G.E. Eperon, G. Grancini, C. Menelaou, M.J. Alcocer, T. Leijtens, L.M. Herz, A. Petrozza, H.J. Snaith, *Science* **2013**, *342,* 341.

[84] J.S. Manser, J.A. Christians, P.V. Kamat, *Chemical Reviews* **2016**, *116,* 12956.

[85] N.K. McKinnon, D.C. Reeves, M.H. Akabas, *The Journal of General Physiology* **2011**, *138,* 453.

[86] J.-H. Im, J. Chung, S.-J. Kim, N.-G. Park, *Nanoscale Research Letters* **2012**, *7,* 353.

[87] P. Umari, E. Mosconi, F. De Angelis, *Scientific Reports* **2014**, *4,* 4467.

[88] H. Yu, F. Wang, F. Xie, W. Li, J. Chen, N. Zhao, *Advanced Functional Materials* **2014**, *24,* 7102.

[89] W. Zhu, C. Bao, F. Li, T. Yu, H. Gao, Y. Yi, J. Yang, G. Fu, X. Zhou, Z. Zou, *Nano Energy* **2016**, *19,* 17.

[90] D. Mitzi, S. Wang, C. Feild, C. Chess, A. Guloy, *Science* **1995**, *267,* 1473.

[91] D.B. Mitzi, K. Chondroudis, C.R. Kagan, *IBM Journal of Research and Development* **2001**, *45,* 29.

[92] A. Kojima, K. Teshima, T. Miyasaka, Y. Shirai. *Novel Photoelectrochemical Cell with Mesoscopic Electrodes Sensitized by Lead-halide Compounds (2)*. in *Meeting Abstracts*. **2006**, The Electrochemical Society.

[93] A. Kojima, K. Teshima, Y. Shirai, T. Miyasaka, *Journal of the American Chemical Society* **2009**, *131,* 6050.

[94] J.-H. Im, C.-R. Lee, J.-W. Lee, S.-W. Park, N.-G. Park, *Nanoscale* **2011**, *3,* 4088.

[95] J. Salbeck, N. Yu, J. Bauer, F. Weissörtel, H. Bestgen, *Synthetic Metals* **1997**, *91,* 209.

[96] H.-S. Kim, C.-R. Lee, J.-H. Im, K.-B. Lee, T. Moehl, A. Marchioro, S.-J. Moon, R. Humphry-Baker, J.-H. Yum, J.E. Moser, *Scientific Reports* **2012**, *2,* 591.

[97] M.M. Lee, J. Teuscher, T. Miyasaka, T.N. Murakami, H.J. Snaith, *Science* **2012**, 1228604.

[98] D. Liu,T.L. Kelly, *Nature Photonics* **2014**, *8,* 133.

[99] J.H. Heo, S.H. Im, J.H. Noh, T.N. Mandal, C.-S. Lim, J.A. Chang, Y.H. Lee, H.-j. Kim, A. Sarkar, M.K. Nazeeruddin, *Nature Photonics* **2013**, *7,* 486.

[100] J.H. Noh, S.H. Im, J.H. Heo, T.N. Mandal, S.I. Seok, *Nano Letters* **2013**, *13,* 1764.

[101] J. Burschka, N. Pellet, S.-J. Moon, R. Humphry-Baker, P. Gao, M.K. Nazeeruddin, M. Grätzel, *Nature* **2013**, *499,* 316.

[102] M. Liu, M.B. Johnston, H.J. Snaith, *Nature* **2013**, *501,* 395.

[103] J.-H. Im, I.-H. Jang, N. Pellet, M. Grätzel, N.-G. Park, *Nature Nanotechnology* **2014**, *9,* 927.

[104] H. Zhou, Q. Chen, G. Li, S. Luo, T.-b. Song, H.-S. Duan, Z. Hong, J. You, Y. Liu, Y. Yang, *Science* **2014**, *345,* 542.

[105] W.S. Yang, B.-W. Park, E.H. Jung, N.J. Jeon, Y.C. Kim, D.U. Lee, S.S. Shin, J. Seo, E.K. Kim, J.H. Noh, *Science* **2017**, *356,* 1376.

[106] N.J. Jeon, H. Na, E.H. Jung, T.-Y. Yang, Y.G. Lee, G. Kim, H.-W. Shin, S.I. Seok, J. Lee, J. Seo, *Nature Energy* **2018**, *3,* 682.

[107] W.U. Huynh, J.J. Dittmer, A.P. Alivisatos, *Science* **2002**, *295,* 2425.

[108] E. Lee, *The Magnetic Properties of Materials: International Monographs on Materials Science and Technology*. **1969**, IOP Publishing.

[109] C. Strümpel, M. McCann, G. Beaucarne, V. Arkhipov, A. Slaoui, V. Švrček, C. Del Cañizo, I. Tobias, *Solar Energy Materials and Solar Cells* **2007**, *91,* 238.

[110] J.-P. Berenger, *Journal of Computational Physics* **1994**, *114,* 185.

[111] Y.M. Nam, J. Huh, W.H. Jo, *Solar Energy Materials and Solar Cells* **2010**, *94,* 1118.

[112] T. Stübinger,W. Brütting, *Journal of Applied Physics* **2001**, *90,* 3632.

[113] A. Hagfeldt,M. Graetzel, *Chemical Reviews* **1995**, *95,* 49.

[114] W. Choi, A. Termin, M.R. Hoffmann, *The Journal of Physical Chemistry* **1994**, *98,* 13669.

[115] K.O. Hara,N. Usami, *Journal of Applied Physics* **2013**, *114,* 153101.

[116] R.A. Sinton,A. Cuevas, *Applied Physics Letters* **1996**, *69,* 2510.

[117] W. Ruppel,P. Wurfel, *IEEE Transactions on Electron Devices* **1980**, *27,* 877.

[118] M.A. Green, *Solid State Electronics* **1981**, *24,* 788.

[119] D. Bryant, N. Aristidou, S. Pont, I. Sanchez-Molina, T. Chotchunangatchaval, S. Wheeler, J.R. Durrant, S.A. Haque, *Energy & Environmental Science* **2016**, *9,* 1655.

[120] B. Salhi, Y. Wudil, M. Hossain, A. Al-Ahmed, F. Al-Sulaiman, *Renewable and Sustainable Energy Reviews* **2018**, *90,* 210.

[121] M. Saliba, T. Matsui, J.-Y. Seo, K. Domanski, J.-P. Correa-Baena, M.K. Nazeeruddin, S.M. Zakeeruddin, W. Tress, A. Abate, A. Hagfeldt, *Energy & Environmental Science* **2016**, *9,* 1989.

[122] A. Djurišić, F. Liu, A.M. Ng, Q. Dong, M.K. Wong, A. Ng, C. Surya, *Physica Status Solidi (RRL)–Rapid Research Letters* **2016**, *10,* 281.

[123] Q. Fu, X. Tang, B. Huang, T. Hu, L. Tan, L. Chen, Y. Chen, *Advanced Science* **2018**, *5,* 1700387.

[124] J.H. Kim, P.W. Liang, S.T. Williams, N. Cho, C.C. Chueh, M.S. Glaz, D.S. Ginger, A.K.Y. Jen, *Advanced Materials* **2015**, *27,* 695.

[125] T. Leijtens, G.E. Eperon, S. Pathak, A. Abate, M.M. Lee, H.J. Snaith, *Nature Communications* **2013**, *4,* 2885.

[126] W. Chen, Y. Wu, Y. Yue, J. Liu, W. Zhang, X. Yang, H. Chen, E. Bi, I. Ashraful, M. Grätzel, *Science* **2015**, aad1015.

[127] S.N. Habisreutinger, T. Leijtens, G.E. Eperon, S.D. Stranks, R.J. Nicholas, H.J. Snaith, *Nano Letters* **2014**, *14,* 5561.

[128] F. Zhang, C. Yi, P. Wei, X. Bi, J. Luo, G. Jacopin, S. Wang, X. Li, Y. Xiao, S.M. Zakeeruddin, *Advanced Energy Materials* **2016**, *6,* 1600401.

[129] C. Huang, W. Fu, C.-Z. Li, Z. Zhang, W. Qiu, M. Shi, P. Heremans, A.K.-Y. Jen, H. Chen, *Journal of the American Chemical Society* **2016**, *138,* 2528.

[130] S.S. Shin, E.J. Yeom, W.S. Yang, S. Hur, M.G. Kim, J. Im, J. Seo, J.H. Noh, S.I. Seok, *Science* **2017**, *356,* 167.

[131] H. Tan, A. Jain, O. Voznyy, X. Lan, F.P.G. de Arquer, J.Z. Fan, R. Quintero-Bermudez, M. Yuan, B. Zhang, Y. Zhao, *Science* **2017**, *355,* 722.

[132] X. Li, M.I. Dar, C. Yi, J. Luo, M. Tschumi, S.M. Zakeeruddin, M.K. Nazeeruddin, H. Han, M. Grätzel, *Nature Chemistry* **2015**, *7,* 703.

[133] S. Guarnera, A. Abate, W. Zhang, J.M. Foster, G. Richardson, A. Petrozza, H.J. Snaith, *The Journal of Physical Chemistry Letters* **2015**, *6,* 432.

[134] Y. Shao, Z. Xiao, C. Bi, Y. Yuan, J. Huang, *Nature Communications* **2014**, *5,* 5784.

[135] M. Asghar, J. Zhang, H. Wang, P. Lund, *Renewable and Sustainable Energy Reviews* **2017**, *77,* 131.

[136] V.M. Goldschmidt, *Naturwissenschaften* **1926**, *14,* 477.

[137] A. Amat, E. Mosconi, E. Ronca, C. Quarti, P. Umari, M.K. Nazeeruddin, M. Grätzel, F. De Angelis, *Nano Letters* **2014**, *14,* 3608.

[138] A. Poglitsch,D. Weber, *The Journal of Chemical Physics* **1987**, *87,* 6373.

[139] G. Niu, W. Li, F. Meng, L. Wang, H. Dong, Y. Qiu, *Journal of Materials Chemistry A* **2014**, *2,* 705.

[140] M.T. Weller, O.J. Weber, P.F. Henry, A.M. Di Pumpo, T.C. Hansen, *Chemical Communications* **2015**, *51,* 4180.

[141] A.K. Baranwal, S. Kanaya, T.N. Peiris, G. Mizuta, T. Nishina, H. Kanda, T. Miyasaka, H. Segawa, S. Ito, *ChemSusChem* **2016**, *9,* 2604.

[142] V. Rinnerbauer, A. Lenert, D.M. Bierman, Y.X. Yeng, W.R. Chan, R.D. Geil, J.J. Senkevich, J.D. Joannopoulos, E.N. Wang, M. Soljačić, *Advanced Energy Materials* **2014**, *4,* 1400334.

[143] W. Huang, S. Sadhu, S. Ptasinska, *Chemistry of Materials* **2017**, *29,* 8478.

[144] N. Onoda-Yamamuro, T. Matsuo, H. Suga, *Journal of Physics and Chemistry of Solids* **1990**, *51,* 1383.

[145] J.M. Ball, M.M. Lee, A. Hey, H.J. Snaith, *Energy & Environmental Science* **2013**, *6,* 1739.

[146] C.C. Stoumpos, C.D. Malliakas, M.G. Kanatzidis, *Inorganic Chemistry* **2013**, *52,* 9019.

[147] M.R. Ahmadian-Yazdi, F. Zabihi, M. Habibi, M. Eslamian, *Nanoscale Research Letters* **2016**, *11,* 408.

[148] A. Dualeh, P. Gao, S.I. Seok, M.K. Nazeeruddin, M. Grätzel, *Chemistry of Materials* **2014**, *26,* 6160.

[149] B. Philippe, B.-W. Park, R. Lindblad, J. Oscarsson, S. Ahmadi, E.M. Johansson, H.k. Rensmo, *Chemistry of Materials* **2015**, *27,* 1720.

[150] B. Conings, J. Drijkoningen, N. Gauquelin, A. Babayigit, J. D'Haen, L. D'Olieslaeger, A. Ethirajan, J. Verbeeck, J. Manca, E. Mosconi, *Advanced Energy Materials* **2015**, *5,* 1500477.

[151] G. Kieslich, S. Sun, A.K. Cheetham, *Chemical Science* **2014**, *5,* 4712.

[152] T. Leijtens, G.E. Eperon, N.K. Noel, S.N. Habisreutinger, A. Petrozza, H.J. Snaith, *Advanced Energy Materials* **2015**, *5,* 1500963.

[153] D. Trots,S. Myagkota, *Journal of Physics and Chemistry of Solids* **2008**, *69,* 2520.

[154] D.E. Scaife, P.F. Weller, W.G. Fisher, *Journal of Solid State Chemistry* **1974**, *9,* 308.

[155] X. Li, M. Tschumi, H. Han, S.S. Babkair, R.A. Alzubaydi, A.A. Ansari, S.S. Habib, M.K. Nazeeruddin, S.M. Zakeeruddin, M. Grätzel, *Energy Technology* **2015**, *3,* 551.

[156] K.A. Bush, C.D. Bailie, Y. Chen, A.R. Bowring, W. Wang, W. Ma, T. Leijtens, F. Moghadam, M.D. McGehee, *Advanced Materials* **2016**, *28,* 3937.

[157] H.-L. Yip,A.K.-Y. Jen, *Energy & Environmental Science* **2012**, *5,* 5994.

[158] A.l.M. Leguy, Y. Hu, M. Campoy-Quiles, M.I. Alonso, O.J. Weber, P. Azarhoosh, M. Van Schilfgaarde, M.T. Weller, T. Bein, J. Nelson, *Chemistry of Materials* **2015**, *27,* 3397.

[159] B. Hailegnaw, S. Kirmayer, E. Edri, G. Hodes, D. Cahen, *The Journal of Physical Chemistry Letters* **2015**, *6,* 1543.

[160] X. Dong, X. Fang, M. Lv, B. Lin, S. Zhang, J. Ding, N. Yuan, *Journal of Materials Chemistry A* **2015**, *3,* 5360.

[161] H.C. Weerasinghe, Y. Dkhissi, A.D. Scully, R.A. Caruso, Y.-B. Cheng, *Nano Energy* **2015**, *18,* 118.

[162] L.N. Quan, M. Yuan, R. Comin, O. Voznyy, E.M. Beauregard, S. Hoogland, A. Buin, A.R. Kirmani, K. Zhao, A. Amassian, *Journal of the American Chemical Society* **2016**, *138,* 2649.

[163] I.C. Smith, E.T. Hoke, D. Solis-Ibarra, M.D. McGehee, H.I. Karunadasa, *Angewandte Chemie* **2014**, *126,* 11414.

[164] F. Wang, W. Geng, Y. Zhou, H.H. Fang, C.J. Tong, M.A. Loi, L.M. Liu, N. Zhao, *Advanced Materials* **2016**, *28,* 9986.

[165] X. Li, M.I. Dar, C. Yi, J. Luo, M. Tschumi, S.M. Zakeeruddin, M.K. Nazeeruddin, H. Han, M. Grätzel, *Nature Chemistry* **2015**, *7,* 703.

[166] F. Li,M. Liu, *Journal of Materials Chemistry A* **2017**, *5,* 15447.

[167] G. Niu, X. Guo, L. Wang, *Journal of Materials Chemistry A* **2015**, *3,* 8970.

[168] J. Yang, B.D. Siempelkamp, D. Liu, T.L. Kelly, *ACS Nano* **2015**, *9,* 1955.

[169] E. Mosconi, J.M. Azpiroz, F. De Angelis, *Chemistry of Materials* **2015**, *27,* 4885.

[170] J. Huang, S. Tan, P.D. Lund, H. Zhou, *Energy & Environmental Science* **2017**, *10,* 2284.

[171] C.-G. Wu, C.-H. Chiang, Z.-L. Tseng, M.K. Nazeeruddin, A. Hagfeldt, M. Grätzel, *Energy & Environmental Science* **2015**, *8,* 2725.

[172] F.T. O'Mahony, Y.H. Lee, C. Jellett, S. Dmitrov, D.T. Bryant, J.R. Durrant, B.C. O'Regan, M. Graetzel, M.K. Nazeeruddin, S.A. Haque, *Journal of Materials Chemistry A* **2015**, *3,* 7219.

[173] N. Aristidou, I. Sanchez-Molina, T. Chotchuangchutchaval, M. Brown, L. Martinez, T. Rath, S.A. Haque, *Angewandte Chemie* **2015**, *127,* 8326.

[174] A.J. Pearson, G.E. Eperon, P.E. Hopkinson, S.N. Habisreutinger, J.T.W. Wang, H.J. Snaith, N.C. Greenham, *Advanced Energy Materials* **2016**, *6,* 1600014.

CHAPTER 3

Experimental Methods

This chapter describes an overview of the experimental procedure used to fabricate the hybrid organic-inorganic perovskite solar cells followed by a summary of the characterization techniques used to investigate material and solar cell properties. The chapter provides only a general method for solar cell fabrication. The updated composition and methods for making perovskite devices for specific investigations will be introduced in detail in individual chapters

3.1. Materials

All chemicals (unless otherwise stated) were purchased from Sigma-Aldrich and used as received, except TiO_2 nanoparticles, which were purchased from Dyesol. As is described in **Chapter 5**, the iodine salt methylammonium iodide ($MeNH_3I$) and phenylethylammonium iodide ($PhEtNH_3I$) were synthesized in the laboratory according to previous literature.[1, 2] Methylamine (33 % wt) solution in ethanol (6.2 ml, 0.046 mol) was cooled in an ice bath. Hydroiodic acid (HCl) (37 % wt) mixed in 15 ml ethanol (10 ml, 0.073 mol) was then added dropwise under vigorous stirring. The solution was then stirred (0 °C, 1 hr) and dry under vacuum until the white-yellowish solid was precipitated. Subsequently, ethanol (5 ml) was added to ensure complete precipitation. The solid was then filtered and rinsed with cold ethanol several times. Finally, the recrystallization of the resulting product in diethyl ether solvent rendered the pure compound as a white crystalline solid (6.4 g, 87%). The synthesis of $PhEtNH_3I$ is very similar to $MeNH_3I$ except phenylethylamine (33% wt) solution in ethanol (6.2 ml, 0.046 mol) was employed and was cooled in an as-prepared ice bath. It should be noted that in **Chapters 6** and **7**, both $MeNH_3I$ and $PhEtNH_3I$ crystalline solids used were purchased from Dyesol.

3.2. Solar Cell Fabrication

3.2.1. Substrate Preparation and Fabrication of Metal Oxide Films

The Fluorine doped Tin Oxide (FTO) glass substrates (100 × 25 mm, 2.3 mm thick TEC15, Pilkington) were first etched with zinc metal powder (Sigma) and aqueous hydrochloric acid (HCl; 37% wt), and then cut into pieces with 25 × 25 mm in diameter. All substrates were then rinsed sequentially in acetone, distilled water and isopropyl alcohol (IPA) respectively and were ultrasonically cleaned for 10 minutes during each washing cycle. Subsequently, a compact TiO_2 layer was spin coated onto the cleaned FTO substrates using a solution combining 1000 µl titanium isopropoxide (Aldrich), 150 µl HCl (37%) and 14.5 ml anhydrous ethanol (4000 rpm, 30 s). The films were first sintered (150 °C, 15 min) and then annealed (500 °C, 40 min) in the oven.[3] Next, the mesoporous-TiO_2 film was made using a solution of colloidal anatase TiO_2 nanoparticle paste (Dyesol 18NR-T, 20 nm average particle size) in absolute ethanol (2:7 v/v). The slurry was spun onto the film (4000 rpm, 30 s) with a micropipette tip and was then sintered (500 °C, 45 min).[4-6]

3.2.2. Titanium Tetrachloride ($TiCl_4$) Surface Treatment

Application of $TiCl_4$ solution was adopted in the study as a surface post-treatment. It was previously applied in dye sensitized solar cells (DSSCs) for improving the surface quality of the compact-TiO_2 layer and the photocurrent of the devices,[7] and later found that it is also very helpful on perovskite devices with the combination of mesoporous-TiO_2.[8] The $TiCl_4$ aqueous solution was prepared by adding titanium tetrachloride (Aldrich) into pre-cooled distilled water (~1 °C) at a concentration of ~ 40 mM in an ice bath. The substrates with compact- and mesoporous-TiO_2 layer already fabricated were then immersed into the $TiCl_4$ treatment solution (70 °C, 30 min). Afterwards, samples were rinsed with distilled water and IPA solution, followed by blowing with nitrogen (N_2) to ensure complete dryness. Finally, post-annealing (500 °C, 45 min) processes were carried out and samples were then cooled down to room temperature under ambient conditions.[7, 9]

3.2.3. Synthesis and Preparation of Perovskite Active Layer

The precursor solution of $CH_3NH_3PbI_3$ (MAPI) was prepared inside a nitrogen-filled glovebox. Methylammonium iodide ($MeNH_3I$) and lead iodide (PbI_2) were mixed in a 1:1 mole ratio and dissolved in anhydrous dimethyl sulfoxide (DMSO) and γ-butyrolactone (GBL) solution in 3:7 volume ratio. The resulting solution was then stirred on a hotplate at 60°C overnight (~12 hrs) and was filtered (0.2 μm PTFE syringe filter, Restek) prior to use. The desired perovskite layer was prepared using a consecutive five-step spincoating program inside a glovebox (1000 rpm, 250 rpm/s, 5 s; 4000 rpm, 6500 rpm/s, 25 s; 4000 rpm, 6500 rpm/s, 25 s; 500 rpm, 6500 rpm/s, 5 s and 4000 rpm, 7200 rpm/s, 50 s). While processing, the anti-solvent (normally toluene) drop casting was applied 5 seconds before the end of step three to obtain a uniform and flat intermediate phase. Once this was done, the substrate was heated on a hotplate (100 °C, 15 min). It is worth noting that the spincoating program for making the perovskite active layer varied for different perovskite materials and is introduced in detail in later Chapters.

3.2.4. Preparation of Perovskite Films with Iodine Salt Coating

In instances where iodine salt coating was employed, solutions of $MeNH_3I$ and $PhEtNH_3I$ were prepared and spin coated onto films with the structure FTO/c-TiO_2/mp-TiO_2/MAPI inside a glovebox filled with nitrogen. Next, an appropriate amount of iodine salt passivating solution was deposited over the entire substrate by using a micropipette. The $MeNH_3I$ and $PhEtNH_3I$ salt solutions were prepared by dissolving the respective salt in a mixture of moisture-free 2-propanol and chlorobenzene (375: 625 v/v). All solutions were stirred (60 °C, 24 h), cooled to room temperature and filtered prior to use. When applying the $MeNH_3I$ or $PhEtNH_3I$ treatment, a 80 μL of solution was used to ensure the whole substrate is covered, with a loading time of 20 s. Once this done, a three step consecutive spin coating process was applied to passivate the perovskite layer.[1] The spin coater was opened during the second step to in attempt to facilitate drying of the passivating agent on the perovskite layer. The films were then dried inside a glovebox for a period of 30 minutes under dark condition and without further heat treatment.

3.2.5. Preparation of Hole Transporting Layer and Scraping

The 2,2',7,7'-Tetrakis (N,N-di(4-methoxyphenyl)amino-9,9')-spirobifluorene (Spiro-OMeTAD) was used as the hole transporting layer (HTL) in the project. It was made from a solution of 72.5 mg Spiro-OMeTAD powder (purchased from Merck) in 1 ml anhydrous chlorobenzene (CB). Once this is done, the solution was covered with aluminium foil to avoid oxidation by light and stirred on a hotplate (70 °C, 3 hrs). Subsequently, additions of 17.5 µl lithium bis(trifluoromethane) sulfonimide lithium salt (LiTFSI) (520 mg/mL in acetonitrile*)* and 28.8 µl 4-tert-butylpyridine (TBP) were introduced to Spiro-OMeTAD before using. The solution was then spun on top of the substrates (2000 rpm, 2000 acceleration (acc.), 30 s).[10] After the layer dried completely, it was scratched 7 mm from top and 5 mm from bottom edges, respectively. In case of encapsulation, the sample was further scratched 2 mm from two side edges and the scratched area was cleaned with acetone to remove residual material. Finally, devices were oxidized in a dry box under dark conditions. The whole process to fabricate a MAPI perovskite solar cell is shown in Figure 3.1.

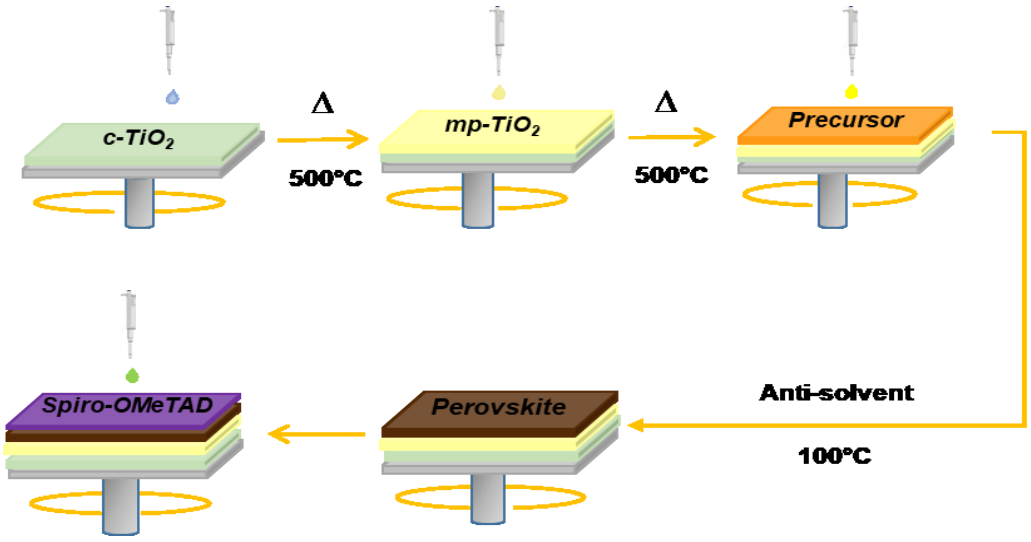


Figure 3-1: Schemes of the fabrication process for perovskite solar cells with MAPI as active layer.

3.2.6. Thermal Evaporation

Finally, a gold electrode of 80-100 nm thickness was thermally evaporated under vacuum (approximately 10^6 T at a rate of 0.2 nm s^{-1}) with an active pixel area of 0.12 cm^2.

3.2.7. Measurement of Material Stability under Oxygen and Light

The perovskite films were deposited on a structure of FTO glass/c-TiO_2/mp-TiO_2 substrates (2000 rpm, 30 s), samples were then placed inside a quartz cuvette. The cuvette was securely encapsulated with a parafilm inside the nitrogen-filled glovebox under dark. Specifically, in order to create a moisture-free and oxygen-rich environment, a flow of dry air (21 % O_2) is passing through the cuvette at 0.5 $Lmin^{-1}$ with a pair of needles. The flow rate was fast enough to inhibit significant backflow of ambient air into the cuvette. To prevent the sample from further influenced by moisture, a stream of dry oxygen was passed through a specific filter including dry calcium chloride and silica gel before entering into the cuvette. This will effectively stop any residual ambient moisture in the compressed air from entering the cuvette. The films were then illuminated continuous with a halogen lamp, with an incident power of around 1.5 $mWcm^{-2}$. A schematic diagram and a photograph of the equipments are shown in Figure 3.2. The film degradation test was carried out by steady-state UV-Vis absorbance measurements. (Perkin-Elmer Lambda 25 UV/VIS Spectrometer).

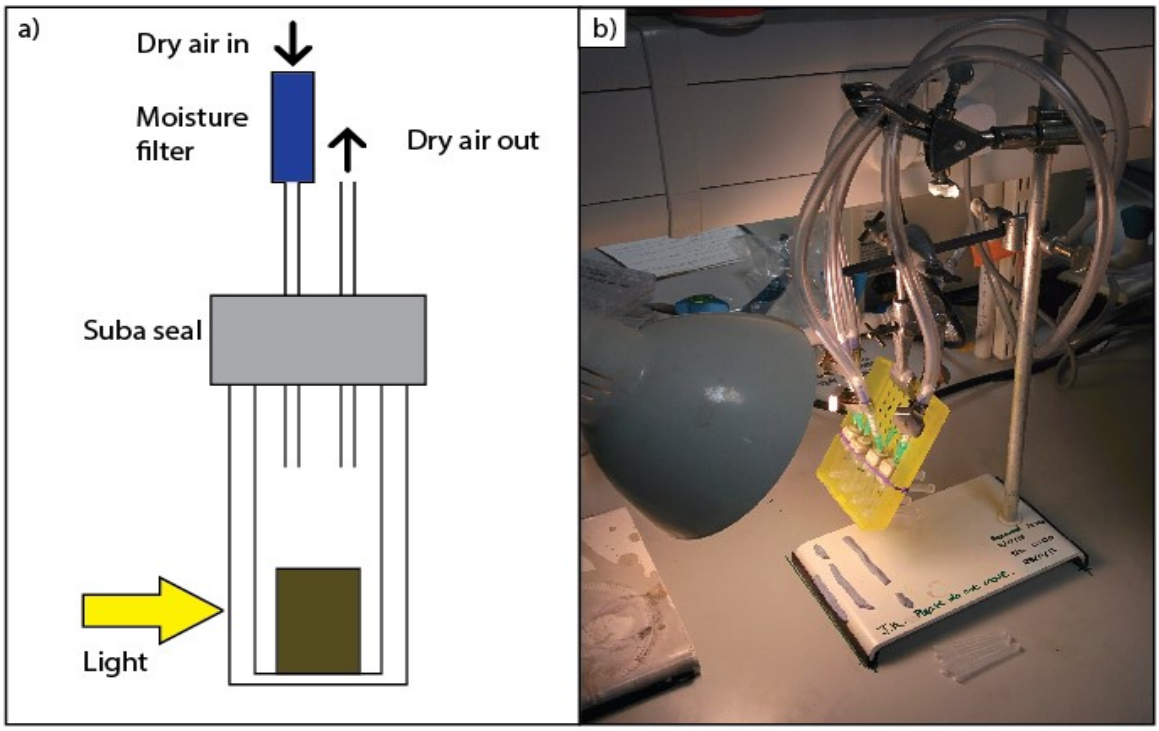


Figure 3-2: The experimental setup for film stability test upon exposure to dry oxygen and light soaking. (a) Schematic representation of how perovskite film is tested in a vial. (b) Photograph showing how multiple samples are measured simultaneously under identical conditions.

3.3. Physical and Optical Characterization Techniques

3.3.1. Current-Voltage Characterizations (J-V)

The J-V characteristics were tested using an AM1.5 solar simulator (Oriel Instruments) and a Keithley 2400 source meter. Prior to measurement, calibration was performed with a silicon photodiode to ensure accuracy of the device parameters. Once measuring, the scans were performed at a standard speed of 0.125 V/s for both forward scan (from J_{sc} to V_{oc}) and backward scan (in the opposite direction). During the stability measurements, a much slower scan rate (0.005 V/s) was applied in an attempt to minimize hysteresis effects encountered during the J-V scan. The devices were placed unmasked under continuous 1 sun illumination during aging and were masked during each scan to ensure the active area (0.12 cm^2) is same for all devices. The photograph of the set up is schematically illustrated in Figure 3.3.

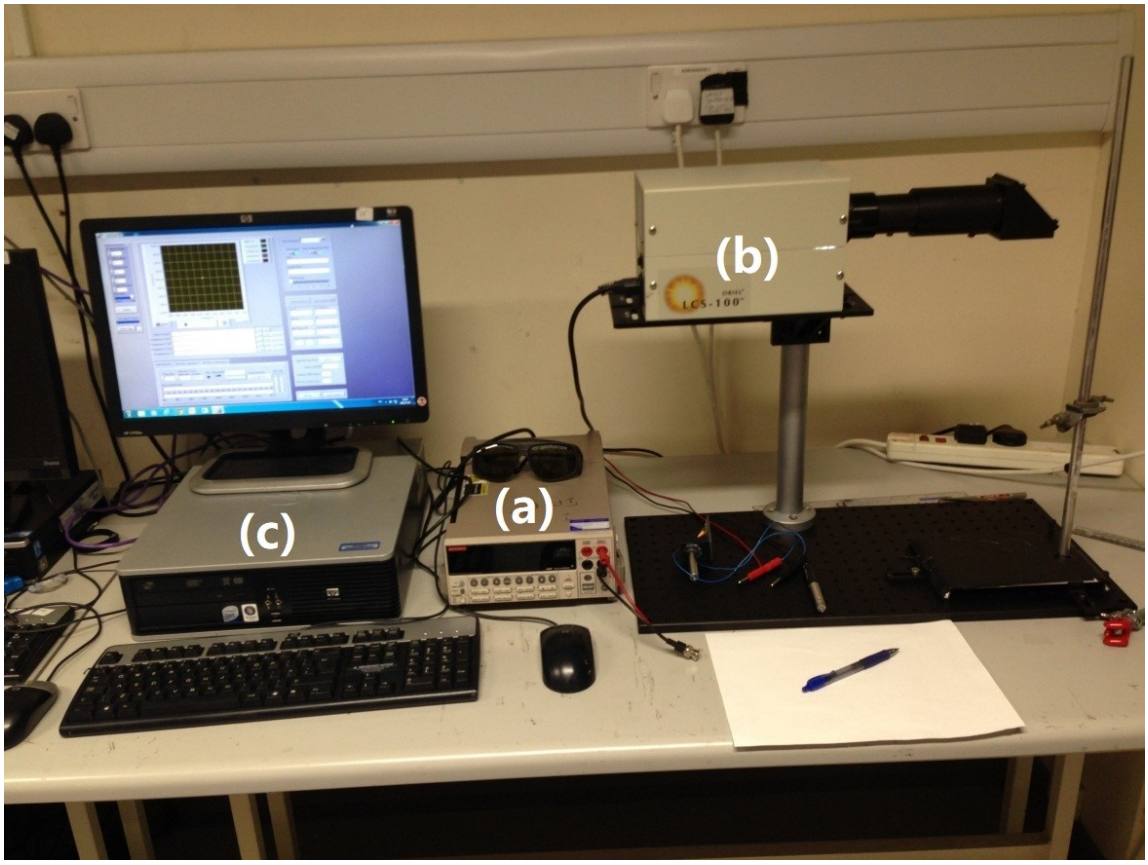


Figure 3-3: Experimental set up of the solar simulator system used for conducting fresh and stability measurement of perovskite solar cells. (a) Keithley 2400 sourcemeter is used for measuring generated photocurrent. (b) LCS-100^{TM} solar simulator system and (c) computer for demonstrating the J-V curves and key photovoltaic parameters.

3.3.2. External Quantum Efficiency Measurement (EQE)

The external quantum efficiency (EQE) is a measure of photon to electron conversion efficiency at a single wavelength at short-circuit (0 V). It is used here to crosscheck the accuracy of the device efficiency obtained from *J-V* characterization. The EQE system consists of a monochromator (Photon Technologies International SID-101) fitted with a 600 lines/mm grating for UV-visible spectroscopy. It was automated with a BC2D20 stepper motor controller (Peter Norberg Consulting Inc.). A chopper wheel was mounted in line with the monochromator to automate the EQE measurement and was connected to the PC via an Arduino in the bias light controller box. The system can estimate J_{sc} according to the obtained EQE spectrum and allow direct comparison with the parameter achieved from the *J-V* measurement.

3.3.3. Scanning Electron Microscopy (SEM)

SEM measurements were carried out on a LEO 1525 Field Emission Scanning Electron Microscope (FEGSEM) operated at 10 kV using an InLens detector.

3.3.4. Steady State UV-Visible Absorption Spectroscopy (UV-VIS)

The steady-state absorption spectra of UV-Vis was performed on a Perkin Elmer Lambda 25 UV-Vis Spectrometer Lambda for absorbance measurement.

3.3.5. Steady State Photoluminescence Spectroscopy (PL)

The photoluminescence emission spectra were measured at room temperature using a Horiba Jobin Yvon Fluorolog-3 spectrofluorimeter.

3.3.6. Transient Absorption Spectroscopy (TAS)

The micro- to millisecond time resolved (TR) TAS characterizations were performed using the equipment shown in Figure 3-4.

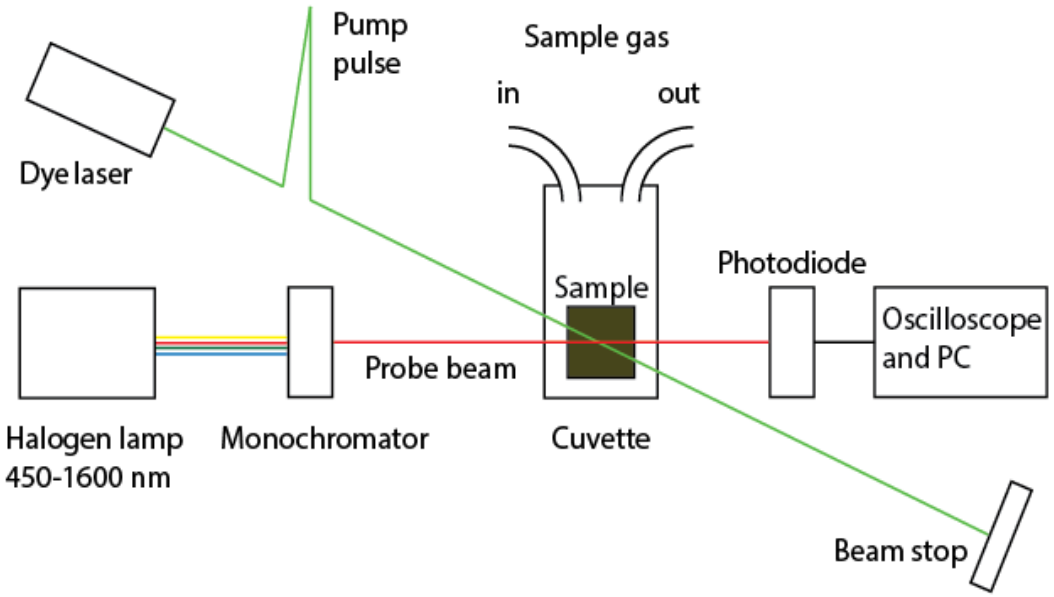


Figure 3-4: Schematic diagram representing the transient absorption spectroscopy (TAS) equipments used in this project. (Either dry N_2 or dry air was used as the sample gas during the measurement)

First, the specimens were pumped by a dye laser (Photon Technology International GL-301, sub-nanosecond pulse width) and followed by an excitation by a pulsed nitrogen laser (Photon Technology International GL-3300). A quartz halogen lamp (Bentham IL1) filtered through a monochromator was then used as the probe beam, and the signal is detected by an $In_xGa_{1-x}As$ photodiode and oscilloscope. It is suggested that all time resolved TAS measurements were applied investigate the relative yield and charge recombination kinetics of the HTM (eg. Spiro-OMeTAD)$^+$ polaron. The measurements were conducted by employing a 567 nm (20 μJ cm^{-2}) pump pulses, and a 1600 nm continuous probe beam. The TAS could effectively work out the lifetime and amount of electron or hole polarons created at an interface between photoactive layer and charge transporting layer. Therefore, it can be defined as a pump-probe experiment, in which a short laser pump pulse with high intensity hits the sample, promoting a fraction of molecules from ground state to an excited state. Later on, a constant probe beam with low intensity was applied to 'observe' the sample at a specific decay time, τ, after the pump hit the sample.

Once measuring, the optical density (OD) of the specimen was recorded before probing as OD, and after probing as OD*. The difference in optical density (ΔOD) between the excited and unexcited sample is calculated according to Equation (1):

$$\Delta OD = OD^* - OD \qquad (1)$$

The ΔOD is closely relevant to the concentration of excited states c, the path length through the specimen l, and the extinction coefficient, ε, which obeys the Beer-Lambert law, as shown in Equation (2):

$$\Delta OD = \varepsilon \cdot c \cdot l \qquad (2)$$

TAS measurements can be either time resolved (TR), or frequency resolved (FR). The TR measurements monitor ΔOD over a range of τ at a constant probe wavelength with a standard decay trace, whereas the FR measurements monitor ΔOD over a range of wavelengths at constant τ. The maximum in the decay trace reveals the initial yield of charge separation at the interface, and the shape of the decay represents charge recombination kinetics; eg. the charge half-life. Figure 3.5 shows the typical types of data generated from FR and TR TAS.

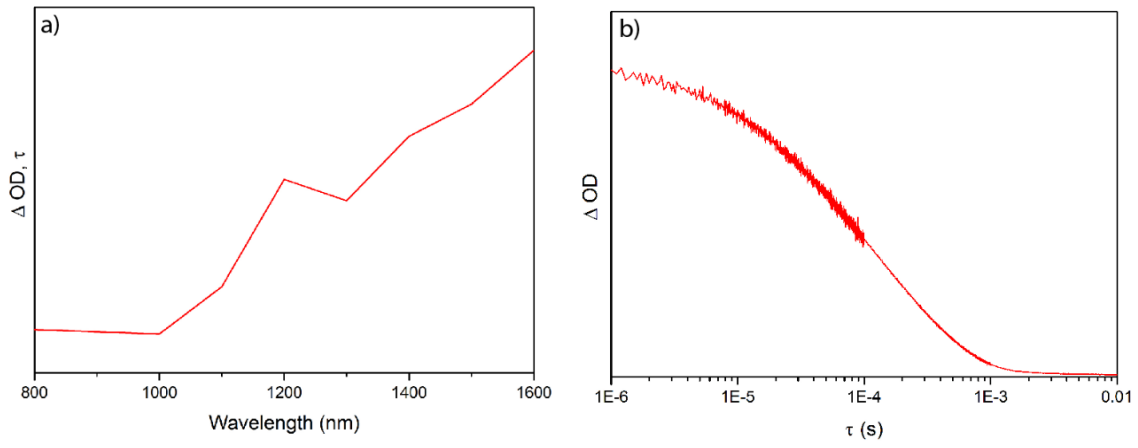


Figure 3-5: Typical traces generated by FR and TR modes of TAS. (a) FR spectrum. (b) TR decay trace.

At the interface between Spiro-OMeTAD and MAPI photoactive layer, the pump pulse could excites one (or both) of the layers and generates excitons, ensuring charge transfer from donor to acceptor of the interface. The excitons can then split into a pair of polarons: $(Spiro\text{-}OMeTAD)^+$ and $(MAPI)^-$. Therefore, the charge dissociation and recombination at the behaviour can be monitored from the trace of either polaron from TR TAS decay.

3.3.7. Time Resolved Photoluminescence Spectroscopy (TCSPC)

The Time-Correlated Single-Photon Counting (TCSPC) experiment were carried out with a Horiba Deltaflex modular fluorescence lifetime system, which employs a PPD 900 detector. Sample excitation was obtained by a 635 nm LED (Horiba N-635L) at an intensity of 18 pJ/pulse and a rate of 1 MHz. The half-life of the prompt pulse was kept 100 ps. The specimens used in microsecond transient absorption spectroscopy tests were taken from a nitrogen-filled glovebox in a sealed quartz cuvette and excited with a dye laser (Photon Technology International Inc. GL-301) with fluence of ~15 μJcm^{-2} and a frequency of 4 Hz. Subsequently, an N_2 laser (Photon Technology International Inc. GL-3300) was applied in order to pump the dye laser. The transient changes in the absorption of the specimen were monitored with a 100W tungsten lamp (Bentham IL1) on an orthogonal optical axis to the excitation beam. The probe wavelength was tuned by a monochromator, and a silicon photodiode (Hamatsu Photonics, S1722-01) was used to detect the probing beam. The signal was then filtered and amplified (Costronics Electronics), and was finally displayed on a digital oscilloscope (Tektronics DPO3012).

3.3.8. X-Ray Diffraction (XRD)

X-ray diffraction (XRD) measurements on thin film samples with glass substrates were measured on a PANalytical X'Pert PRO MRD diffractometer using Ni filtered Cu K_α radiation ($\lambda = 1.5406$ Å) operating at 40 kV and 40 mA. XRD patterns were acquired in the Bragg-Brentano geometry with a standard 2θ step size of 0.01671 degree from 10° to 60° degree at 26 seconds per degree.

3.3.9. Superoxide Probe Testing (SPT)

Firstly, a appropriate amount of 31.7 μM hydroethidine (HE) probe solution was prepared by dissolving 10 mg HE in 10 mL of dry toluene; a period of 10 minutes sonication was then applied to facilitate miscibility of the solvent. Perovskite films were then immersed into a 10 mL of 0.317 μM solution made from the stock solution. The photoluminescence spectra were recorded with an excitation wavelength of 520 nm and 10 mm in slit widths on a Horiba Jobin-Yvon Fluorolog-3 spectrofluorometer. For the experiments with oxygen, dry oxygen was bubbled through the toluene. Spectral mismatch correction for the varying ratio of halide is calculated with the following Equation (3):

$$\frac{I_F(t)}{I_F(t_0)(corrected\ for\ absorption)} = 1 + \frac{I_F(t) - I_F(t_0)}{\beta \times I_F(t_0)} \qquad (3)$$

where $I_F(t)$ is the average fluorescence intensity from 605-615 nm at time t, $I_F(t_0)$ is at t = 0 min and β is the spectral mismatch factor relative to $CH_3NH_3PbI_3$ (MAPI). Since the reaction of photoexcited MAPI with dry molecular oxygen lead to the formation of superoxide species, the ratio of $I_F(t_0)$ to $I_F(t)$ can be represented as the yield of superoxide as a function of testing time.

3.4. References

[1] N. Aristidou, C. Eames, I. Sanchez-Molina, X. Bu, J. Kosco, M.S. Islam, S.A. Haque, *Nature Communications* **2017**, *8,* 15218.

[2] L.N. Quan, M. Yuan, R. Comin, O. Voznyy, E.M. Beauregard, S. Hoogland, A. Buin, A.R. Kirmani, K. Zhao, A. Amassian, *Journal of the American Chemical Society* **2016**, *138,* 2649.

[3] B. Peng, G. Jungmann, C. Jäger, D. Haarer, H.-W. Schmidt, M. Thelakkat, *Coordination Chemistry Reviews* **2004**, *248,* 1479.

[4] A. Kojima, K. Teshima, Y. Shirai, T. Miyasaka, *Journal of the American Chemical Society* **2009**, *131,* 6050.

[5] D.M. Antonelli, J.Y. Ying, *Angewandte Chemie International Edition in English* **1995**, *34,* 2014.

[6] M. Zukalová, A. Zukal, L. Kavan, M.K. Nazeeruddin, P. Liska, M. Grätzel, *Nano Letters* **2005**, *5,* 1789.

[7] B.C. O'Regan, J.R. Durrant, P.M. Sommeling, N.J. Bakker, *The Journal of Physical Chemistry C* **2007**, *111,* 14001.

[8] Y. Zhao, A.M. Nardes, K. Zhu, *Faraday discussions* **2015**, *176,* 301.

[9] S.J. Kim, S.D. Park, Y.H. Jeong, S. Park, *Journal of the American Ceramic Society* **1999**, *82,* 927.

[10] G. Xing, N. Mathews, S. Sun, S.S. Lim, Y.M. Lam, M. Grätzel, S. Mhaisalkar, T.C. Sum, *Science* **2013**, *342,* 344.

CHAPTER 4

The Influence of the Crystal Size on the Light and Oxygen Induced Degradation of Perovskite Solar Cells

4.1. Abstract

*This chapter is structured around two sections. In **Section 1** a standard and reproducible procedure to fabricate $CH_3NH_3PbI_3$ (MAPI) perovskite solar cells is established. We investigate the effect of compact layer thickness, mesoporous layer thickness, $TiCl_4$ surface treatment concentration, and aging time of Spiro-OMeTAD on device efficiency and photovoltaic parameters. Device reproducibility is affected not only by material properties and device architecture, but also by the measuring condition. Specifically, perovskite solar cells degraded rapidly under light and oxygen stress, which resulted in a large deviation on the device efficiency. Understanding light and oxygen induced degradation and their effect on devices is the major objective of this chapter. In **Section 2** MAPI films generating superoxide (O_2^-) when exposed to light and dry oxygen are discussed. This superoxide species could deprotonate methylammonium cation, resulting in material degradation, which affects the stability of perovskite devices. There is a direct correlation between perovskite crystal size, superoxide formation and device stability. Devices with small crystal size in the perovskite layer show a high yield of photo-induced superoxide formation and low device stability. This chapter provides a fundamental understanding of the degradation phenomena which is important for future research and the optimization of more stable perovskite solar cells.*

4.2. Introduction

Organometallic halide perovskite-based materials have received great attention in the photovoltaic industry owing to their excellent optoelectronic properties, such as high absorption coefficient, a bandgap compatible with solar spectrum, excellent carrier lifetimes,[1] good local charge carrier mobility [2] and long charge diffusion lengths.[3] In the past few years, significant breakthroughs have been achieved in perovskite devices with power conversion efficiency (PCE) from 3.8% in 2009 to the recently certified PCE of 23.3%, rivaling the performance of commercial multicrystalline silicon solar cells and indium gallium selenide (CIGS) thin film solar cells. [4-12] More importantly, the excellent device efficiency so far is not confined to a unique type of ideal architecture. Both mesoporous solar cells (derived from solid state dye-sensitized solar cells) and planar heterojunction solar cells have achieved exceptional device performance.[13] In comparison, mesoporous architectures provide a simple and straightforward way to obtain controllable crystallization and high film quality.[5, 14] Therefore, this project concentrated on using a mesoscopic based perovskite solar cell employing the most conventional structure of FTO glass substrates/compact-TiO_2/mp-TiO_2/Perovskite/Spiro-OMeTAD/Au.

In **Section 1** of the present chapter, the most important objective was to establish a standard and reproducible procedure in fabricating $CH_3NH_3PbI_3$ (MAPI) solar cells to support further investigation. This requires a systematic understanding of the processing conditions that relate to the device structure and properties of each layer. The technique for producing the MAPI layer has been widely introduced in previous literature.[6, 15] Attention is paid to optimizing a series of important factors such as thickness of the compact TiO_2 and mesoporous TiO_2 electron transporting layer (ETLs), concentration of $TiCl_4$ treatment, as well as optimizing oxidation status of the Spiro-OMeTAD hole transporting layer (HTL). The reproducibility of this procedure for making MAPI-based solar cells is evaluated. In **Section 2**, issues related to the stability of perovskite solar cells, which is believed to be an important factor of device reproducibility, as studied in the first section, are considered. Specifically, MAPI devices measured in the presence of oxygen and visible light undergo rapid degradation. Our recent study attributed this phenomena to the exposure of MAPI photoactive layers under light and oxygen which leads to the formation of superoxide (O_2^-) species.[16] More interestingly, this reactive O_2^- can deprotonate the methylammonium cation

($CH_3NH_3^+$) of photo-excited $CH_3NH_3PbI_3$*, leading to the formation of PbI_2, water, methylamine and iodine.[17, 18] The process is represented in Figure 4.1.[16-18] Later studies proposed that this light- and oxygen-induced degradation, caused by fast oxygen diffusion, has a direct impact on the stability of both perovskite based films and corresponding devices.[19]

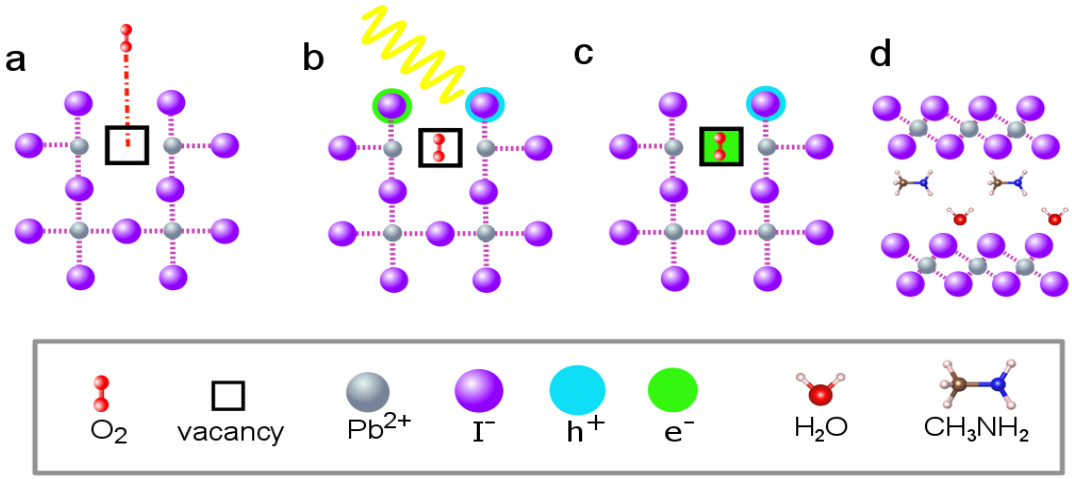


Figure 4-1: Schematic illustration of the reaction between $CH_3NH_3PbI_3$ (MAPI) and O_2. (a) Oxygen diffusion is incorporated into the crystal lattice, (b) photoexcitation occurs at MAPI layer and create electrons and holes (c) superoxide formation from O_2, and (d) degradation of MAPI to I_2, CH_3NH_2, PbI_2 and H_2O.[18]

The next step is to understand the origin of this degradation. Although our previous study on interfacial charge transfer in MAPI films has revealed that electron extraction between layers dominates the severity of this degradation, [17-20] there must be some other factors that contribute to this effect. In general, the perovskite active layer deposited from the solution renders polycrystalline films with various particle sizes and morphologies. To date, much literature has comprehensively studied the impact of the perovskite film morphology on charge carrier transport, device parameters and tolerance to moisture conditions.[1, 13, 21-24] Inspired by these observations, it becomes reasonable to hypothesize that the crystal size presented on the perovskite layer might also affect the degree of oxygen diffusion and facilitate superoxide formation, which in turn leads to the degradation of the perovskite layers and devices. Therefore, the key objective of **Section 2** is to evaluate whether this hypothesis is feasible for perovskite solar cells. Furthermore, attention is paid to investigating the crystal size dependence on superoxide formation and solar cell stability. The study from this chapter reinforces our understanding of the theory of the light- and oxygen-induced degradation of perovskite materials in terms of devices.

4.3. Experimental

4.3.1. Film Fabrication

The samples were deposited onto clean FTO glass substrates of 1 cm by 1 cm in dimension. The substrates were rinsed sequentially in acetone, water and isopropylalcohol (IPA) under sonication for 10 minutes during each washing cycle. Subsequently, a Laurell Technologies WS-650MZ-23NPP Spin Coater was applied to fabricate each functional layers.

(a) $CH_3NH_3PbI_3$: A 1 M solution of $CH_3NH_3PbI_3$ (MAPI) was formed by adding PbI_2 in a 1:1 molar ratio with methylammonium iodide (MAI) in a solvent mixture of 7:3 γ-butyrolactone (GBL) to dimethyl sulfoxide (DMSO). The solution was then spin-coated onto the substrates using a consecutive two-step spin program under nitrogen-filled glovebox. The first spinning cycle was performed at 1000 rpm for 10 s followed by 5000 rpm for 20 s in accordance with previous literature. [25] During the second fabrication step, substrate was drop cast with toluene (~350 mL) and was then annealed at 100°C for 10 minutes under dark.

(b) $CH_3NH_3PbI_3$ (MAPI) Crystal Size Variation: All samples were prepared with controlled crystal size according to the sequential two-step deposition technique described by Grätzel et al.[24] In short, 20 μL of a 1 M solution of PbI_2 powder in DMF solvents was spun onto the FTO substrates at 3000 rpm for 5 s and then at 6000 rpm for another 5 s. The films were then heated at 50˚C for 5 minutes followed by annealing at 100˚C for 5 minutes. Once the films had cooled down to room temperature, application of 200 μl of 0.038 M (large crystals, 250 nm), 0.050 M (medium crystals, 150 nm) and 0.063 M (small crystals, 100 nm) MAI powder in IPA solution were deposited on top of the substrates for 20 s, before spinning at 4000 rpm for 20 s. Films were then annealed at 100 ˚C for 5 minutes.

(c) $Cs_xFA_{1-x}PI_3$ (CsFAPI): The films were prepared with the two-step deposition method in accordance with the previous literature.[26] A precursor solution of PbI_2 in DMF/DMSO (10/1, v/v) with an appropriate amount of caesium iodide (CsI) was spun onto the substrate at 3000 rpm for 35 s, followed by annealing at 50 ˚C for 10 minutes. In the next step, a solution of formamidinium iodide (FAI) dissolved in IPA was drop-cast onto the top of the intermediate

thin film at 4000 rpm for 35 s. The final film was annealed at 200 ˚C for 10 minutes and 150 ˚C for another 60 minutes.

(d) Chlorine treated $CH_3NH_3PbI_3$ (MAPIC): A 1 M solution was created by mixing the $PbCl_2$ and MAI powder in a 1:3 ratio in DMF. The solution was then spin-coated onto substrates at 1000 rpm for 10 s followed by 5000 rpm for 20 s. Annealing was carried out by leaving the films at room temperature for 30 minutes in dark, followed by heating them at 100˚C on hotplate for 90 minutes.

4.3.2. Device Fabrication

FTO coated glass substrates (100 × 25 mm, 2.3 mm thick TEC15, Pilkington) were first etched with Zn powder and aqueous hydrochloric acid (37%), and then cut into 25 × 25 mm pieces followed by cleaning sequentially in acetone, distilled water and isopropylalcohol (IPA) under sonication for 10 minutes during each washing cycle. A compact TiO_2 layer was produced by spin coating a solution including 350µL titanium isopropoxide (Aldrich), 35µL hydrochloric acid (37%) and 5mL anhydrous ethanol at 5000 rpm for 30 s. Subsequently, the as-prepared TiO_2 films were sintered in the oven at 160 °C for 5 minutes and then at 500 °C for 45 minutes. In the next step, a mesoporous-TiO_2 layer was deposited onto the substrate with a solution of 20nm particle transparent titania paste (18NR-T, Dyesol). The solution was spin-coated onto the substrates at 5000 rpm for 30 s. Once spun, the films were dried on a hotplate at 80 °C for 5 mins, and then sintered at 500 °C for 45 mins. The desired perovskite layer was prepared using a consecutive five-step spin program inside the glovebox as previously reported.[19] The Spiro-OMeTAD hole conductor layer was spin coated onto the perovskite films from a solution of 72.3 mg/mL 2,2',7,7'-tetrakis-(N,N-di-p-methoxyphenylamine) 9,9'-spirobifluorene (Spiro-OMeTAD) powder in 1 mL anhydrous chlorobenzene. The Spiro-OMeTAD solution contained additives including 17.5µL lithium bis (trifluoromethane) sulfonimide lithium salt (Li-TFSl) and 28.8µL 4-tert-butylpyridine (tBP) in order to ensure better conductivity is achieved.[19] Finally, a 100 nm-thick gold contact was thermally evaporated on top under vacuum (approximately 10^{-6} Torr at a rate of 0.2 nm/s) with an active pixel area of 0.12 cm^2. All other characterization measurements for the films or devices have already been introduced in the experimental section in **Chapter 3**.

4.4. Results and Discussion

4.4.1. Parameters Affecting the Efficiency and Stability of the Perovskite Solar Cell

Compact Layer (c-TiO_2) Thickness

We first assess the difference in using spray pyrolysis or the spin coating method to fabricate the compact layer. The current-voltage curves and parameters as a function of c-TiO_2 thickness with spray pyrolysis (thickness based on number of spraying cycles) and spin coating method are shown in Figure 4.2, Figure 4.3 and Table 4.1 (all thicknesses were measured with profilometer). It is clear that cells without c-TiO_2 show an almost linear curve (black trace) with low current density (J_{sc}), open-circuit voltage (V_{oc}) and fill factor (FF), resulting in a very low power conversion efficiency (PCE) of 1.12%. As the thickness of c-TiO_2 increases, significant improvement of device parameters are observed as in Figure 4.2 (a). Also observed is the increased rectifying behavior. The highest device efficiency is shown when c-TiO_2 thickness increases to 50 nm (red trace), this corresponding to J_{sc} of 20.86 $mAcm^{-2}$, V_{oc} of 0.77 V and FF of 0.67, resulted in 10.81% device efficiency. Although the FF in the cell with 50 nm c-TiO_2 thickness is slightly lower than that of the 100 nm thick compact layer. This can result from the lower V_{oc} of solar cell with the 100 nm compact layer thickness. Further increase in the thickness of c-TiO_2 (250nm, 500nm) leads to a reduction of device parameters, with the cell efficiency of 7.58 % and 4.22 % respectively. (~30% and ~60% reduce in contrast to PCE of 50 nm compact layer thickness). Also revealed in Figure 4.2 (a) is that increasing the compact layer thickness could reduce recombination, therefore demonstrating better device performance. This is consistent with previous studies.[27] However, further increasing the compact layer thickness decreases the recombination, resulting in reduced cell performance. As a result, devices with 50 nm thickness of c-TiO_2 have the optimal thickness selected for making perovskite solar cells.

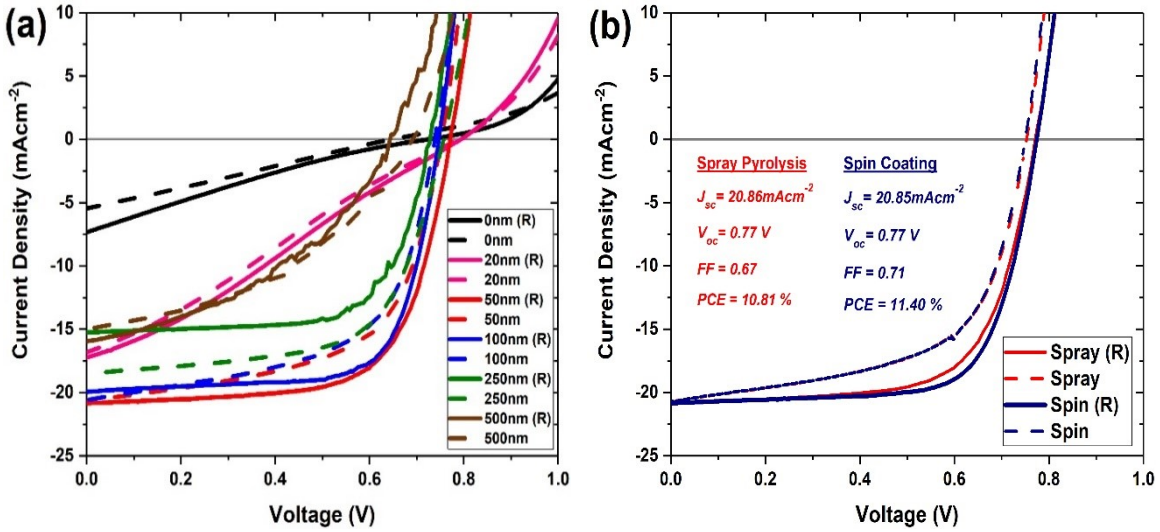


Figure 4-2: (a) Current-voltage curves of $CH_3NH_3PbI_3$ (MAPI) perovskite solar cells using the spray pyrolysis method for different thicknesses of compact TiO_2 layer (thickness is based on the number of spraying cycles). The solid line refers to the forward bias scan (from SC to FB) and the dash line refers to the reverse biasscan (where 'R' represents 'reverse') (from FB to SC) (b) The current-voltage curves of the best devices (compact layer thickness = 50 nm) using spin coating and spray pyrolysis for making compact TiO_2 layer. The structure of device is FTO/c- TiO_2 /mp-TiO_2 /Perovskite/Spiro-OMeTAD/Au (where '/' represents interface).

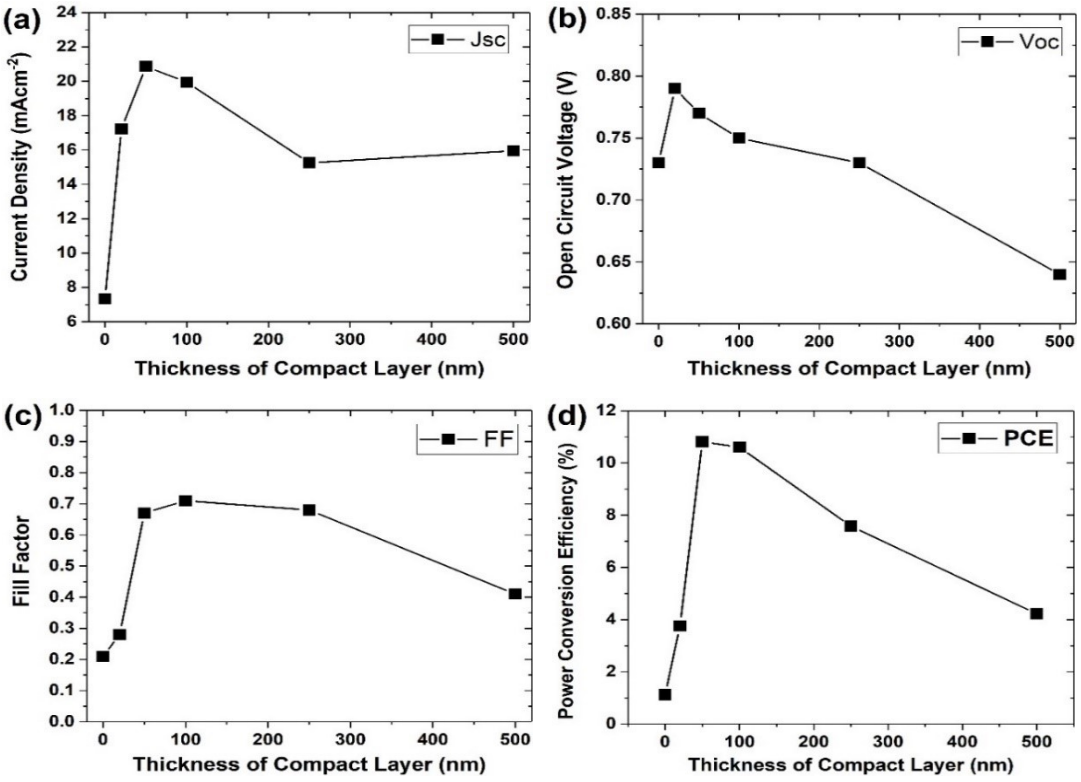


Figure 4-3: Performance of key device parameters (a) Jsc; (b) Voc; (c) FF and (d) PCE as a function of compact layer thickness using the spray pyrolysis method.

Table 4-1: Device parameters of $CH_3NH_3PbI_3$ (MAPI) perovskite solar cells with different thicknesses of compact TiO_2 layers (CL) using the spray pyrolysis (thickness based on number of spraying cycles) and spin coating methods.

Device Type	Thickness of CL (nm)	No. of Spraying Cycles	J_{sc} ($mAcm^{-2}$)	V_{oc} (V)	FF	PCE (%)
Spray Pyrolysis	**0**	**0**	7.34	0.73	0.21	1.12
	20	**2**	17.23	0.79	0.28	3.76
	50	**3**	**20.86**	**0.77**	**0.67**	**10.81**
	100	**4**	19.94	0.75	0.71	10.6
	250	**10**	15.25	0.73	0.68	7.58
	500	**22**	15.95	0.64	0.41	4.22
Spincoat	**50**	**N/A**	**20.85**	**0.77**	**0.71**	**11.4**

We can then compare the device performance of the 50 nm compact layer thickness with different fabrication techniques, spray pyrolysis and spin coating. Figure 4.2 (b) depicts the current-voltage curves with the best device performance for these two techniques. We can see that although both techniques show almost the same V_{oc} and J_{sc}, the FF for device using the spin coating method for the compact layer is higher than that for spray pyrolysis. Besides, the spin coating method requires less sensitive conditions and therefore is easier to reproduce as compared to spray pyrolysis. As a result, throughout the project, the spin coating method was used to fabricate the compact layer.

Mesoporous Layer (mp-TiO_2) Thickness

In the next step, optimizing the mp-TiO_2 layer was achieved through understanding the correlation between layer thickness and device performance. The current-voltage curves and device parameters of $CH_3NH_3PbI_3$ (MAPI) perovskite solar cells with thickness in the range of 350 nm to 800 nm are shown in Figure 4.4 and Table 4.2. It can be seen from the figures that there is a direct relationship between device performance and the thickness of the mesoporous layer. An increase in the mesoporous layer thickness could enhance the device performance. All devices with a mesoporous layer have hysteresis effects, with PCE of the backward scan (FB-SC) higher than the forward scan (SC-FB). The highest device performance appeared with 400 nm in mesoporous layer thickness, with J_{sc} of 16.52 $mAcm^{-2}$, V_{oc} of 0.84 V and FF of 0.67 and PCE of 10.94 %. Further increase in the mesoporous layer thickness (700 nm, 800 nm) resulted in a reduction in PCE. Specifically, at 700 nm the PCE drops to only ~2 % of the highest value obtained at 400 nm. In contrast, at 800 nm in the mesoporous layer thickness the resulted PCE dropped down to ~60 % of the highest efficiency (backward scan). This indicates that the optimum thickness of the mp-TiO_2 layer is achieved in the range of 400–700 nm. Therefore, to save the material used for fabricating devices, 400 nm was used as the mesoporous layer thickness.

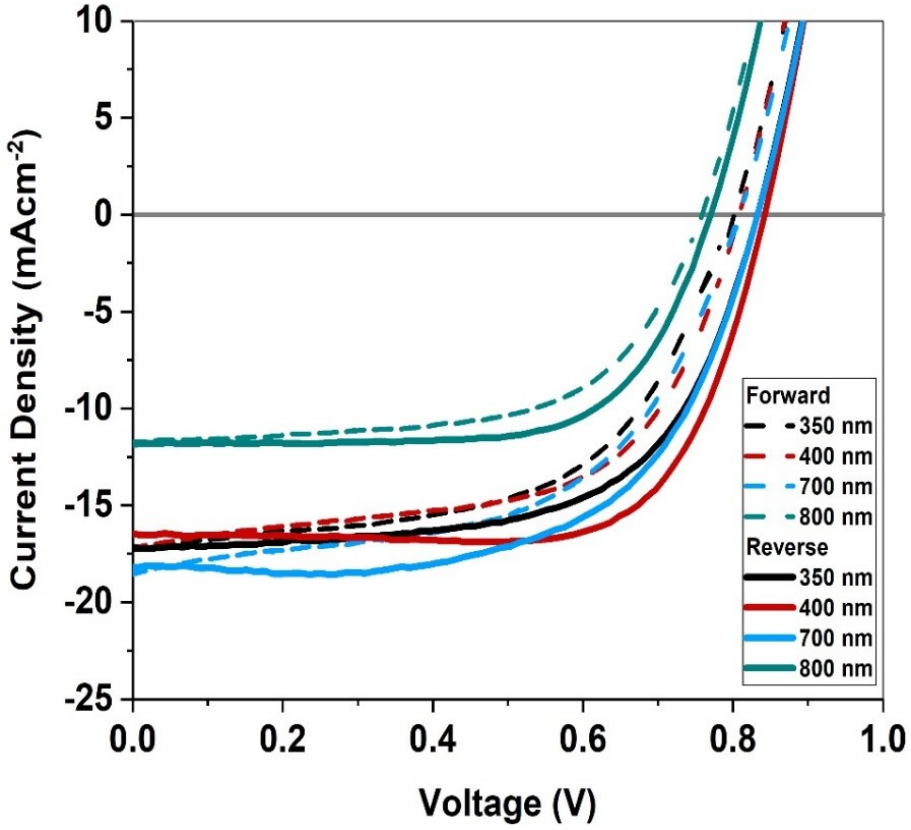


Figure 4-4: Current-voltage curves of $CH_3NH_3PbI_3$ (MAPI) perovskite solar cells with thicknesses of 350 nm, 400nm, 700nm and 800nm respectively at forward (SC-FB, solid lines) and reverse (FB-SC, dashed lines) scan. The experiment are carried out under continuous AM 1.5G one sun illumination (100 mW/cm^2) with a scan rate of 25 mV/s..

Table 4-2: Device parameters of $CH_3NH_3PbI_3$ (MAPI) perovskite solar cells with different thicknesses of the mesoporous TiO_2 layers, including 350 nm, 400 nm, 700 nm and 800 nm respectively at forward (SC-FB) and reverse scan (FB-SC).

Thickness of CL (nm)	Scan Direction	J_{sc} (mAcm^{-2})	V_{sc} (V)	FF	PCE (%)
350	Forward	17.45	0.80	0.61	10.02
	Backward	17.43	0.82	0.63	10.59
400	Forward	17.46	0.80	0.62	10.19
	Backward	**16.52**	**0.84**	**0.67**	**10.94**
700	Forward	18.54	0.78	0.59	10.03
	Backward	18.19	0.83	0.61	10.83
800	Forward	11.72	0.75	0.64	6.62
	Backward	11.81	0.77	0.62	6.64

$TiCl_4$ Surface Treatment

The effects of $TiCl_4$ surface treatment on the device performance of $CH_3NH_3PbI_3$ (MAPI) perovskite solar cells were investigated. Previous studies have demonstrated the effect of $TiCl_4$ as a standard procedure for PSCs.[28, 29] They showed that solar cell performance could be improved by using an appropriate amount of $TiCl_4$, with the devices containing fewer surface defects on the mesoporous layer as well as better electric interconnection between the TiO_2 particles and the mp-TiO_2 layer.[28] Therefore, the treatment of $TiCl_4$ after the mesoporous layer deposition had a significant impact on the MAPI perovskite solar cells' performance, which predominantly depended upon the $TiCl_4$ concentration. However, the exact concentration could be biased with different laboratory conditions. In this study, the main objective was to decide an optimum concentration that leads to best device performance. Devices were fabricated with varied concentrations of $TiCl_4$ treatment 20 mM, 40 mM, 60 mM, 80 mM and 100 mM. The light and dark current-voltage curves as well as the relation between device photovoltaic parameters and $TiCl_4$ concentrations are summarized separately in Figure 4.5, Figure 4.6 and Table 4.3. The best PCE of 11.43% was achieved when 40 mM of $TiCl_4$ was used, which is 18 % greater than that without $TiCl_4$ surface treatment. As shown in Figure 4.6, devices demonstrate a strong correlation between cell parameters and concentrations of the $TiCl_4$ solution. Among these cell parameters, J_{sc} shows larger variations than V_{oc} and FF, resulting in a large difference in PCE, although the 60 mM concentration gives higher J_{sc} than at 40 mM. The FF of device at 60 mM is less than at 40 mM, which leads to lower device performance for 60 mM than at 40 mM. As seen in Figure 4.6, a further increase in the $TiCl_4$ concentration (80 mM, 100 mM) gives a negative effect on the device performance owing to a reduction in J_{sc} and V_{oc}. Overall, the optimum concentration of the $TiCl_4$ surface treatment is 40 mM for MAPI perovskite solar cells.

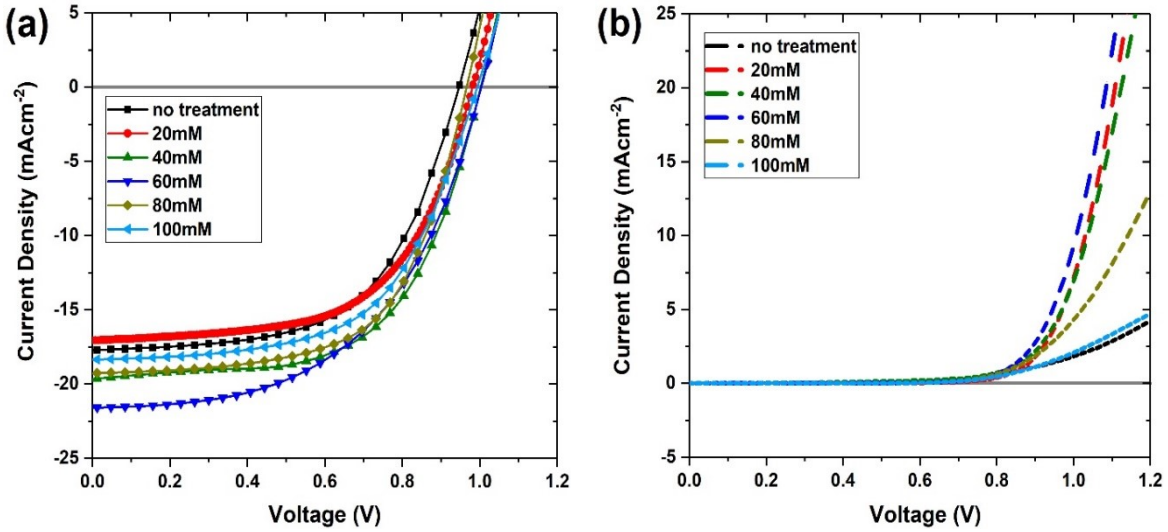


Figure 4-5: (a) Light- and (b) Dark current-voltage curves of $CH_3NH_3PbI_3$ (MAPI) perovskite solar cells with different concentrations of $TiCl_4$ post treatment on top of mesoporous TiO_2 layer, all curves were performed under reverse scan conditions (FB-SC). The measurements are carried out under AM 1.5G one sun illumination (100 mW/cm^2) with a scan speed of 25 mV/s.

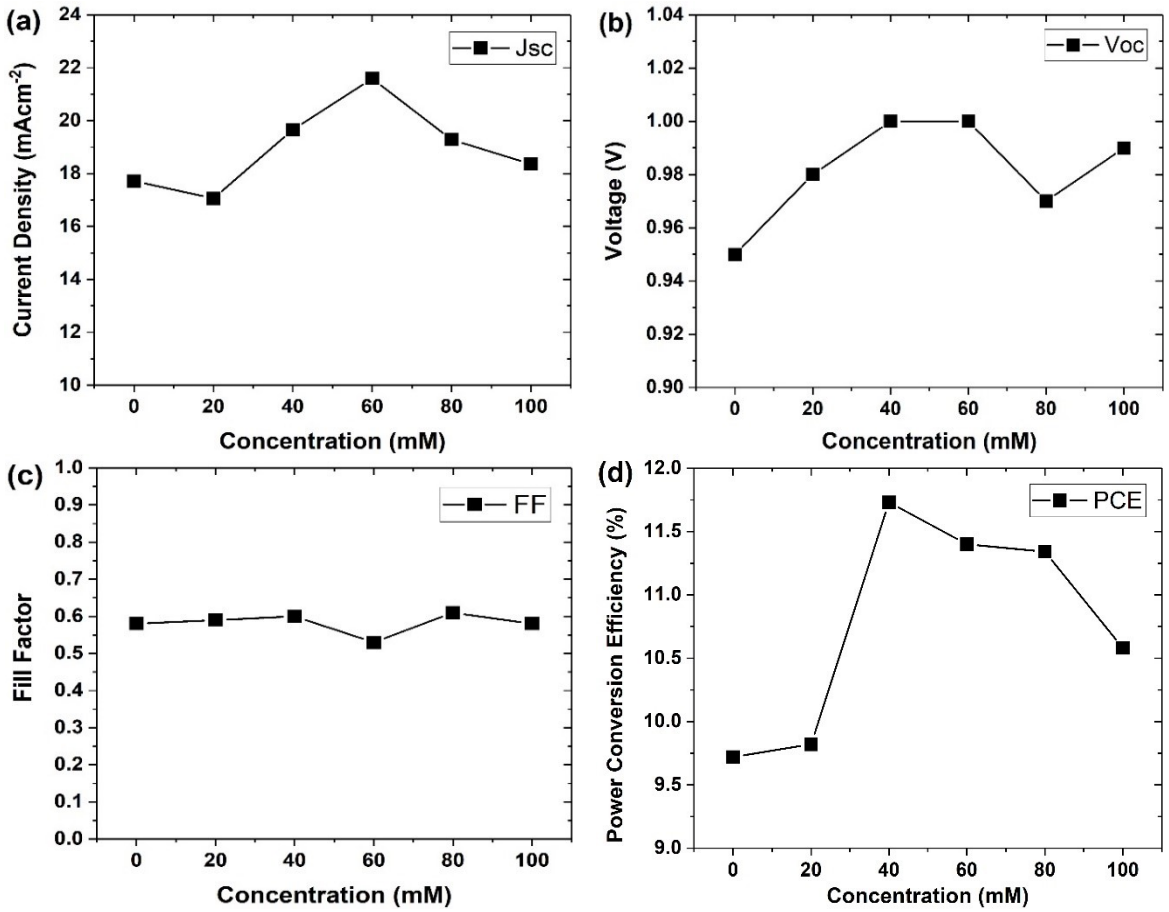


Figure 4-6: Performance of key device parameters (a) Jsc; (b) Voc; (c) FF and (d) PCE as a function of the concentrations of $TiCl_4$ post treatment.

Table 4-3: Device parameters of $CH_3NH_3PbI_3$ perovskite solar cells with different concentrations of $TiCl_4$ post treatment of 0 mM, 20 mM, 40 mM, 60 mM, 80 mM and 100 mM.

Concentration of $TiCl_4$ (mM)	J_{sc} ($mAcm^{-2}$)	V_{oc} (V)	FF	PCE (%)
0	17.72	0.95	0.58	9.72
20	17.06	0.98	0.59	9.82
40	**19.66**	**1**	**0.6**	**11.43**
60	21.59	1	0.53	11.4
80	19.28	0.97	0.61	11.34
100	18.36	0.99	0.58	10.58

Hole-Transporting Layer (Spiro – OMeTAD) Aging

Finally, the effect of aging time on Spiro-OMeTAD on the device performance was studied. The standard procedure of making Spiro-OMeTAD as hole-transporting material (HTM) for $CH_3NH_3PbI_3$ (MAPI) perovskite solar cells has been introduced in previous studies.[19, 30] Although it is widely recognized in the scientific community that fabricating MAPI perovskite solar cells with Spiro-OMeTAD as HTMs requires oxidation prior to measurement, the exact period (or the range) of Spiro-OMeTAD oxidization for best device performance remains unclear and is believed to be dependent on the laboratory conditions. In this case, perovskite devices were fabricated with different periods of oxidation time prior to measurement and monitored their device performance as compared with devices without Spiro-OMeTAD (Spiro) oxidation. The results of the devices with the best period of aging and without aging and device performance as a function of Spiro aging time are illustrated in Figure 4.7 and Table 4.4. Figure 4.7 (a) clearly shows that device efficiency rises with the aging period, with device performance starting from 5.85 % and going up slowly within 10 hours of oxidation. Then the efficiency has a rapid increase between 10-14 hours followed by another moderate increase between 14-18 hours. The phenomena were repeated until aging for 32 hours, after which the efficiency increases continuously. At 48 hours, the device efficiency reached a maximum value, implying that Spiro oxidation reached an optimum level. The device efficiency remains at a peak value for ~4 hours. After 48 hours of Spiro oxidation the device efficiency starts to decrease. It is very likely that the oxygen starts to diffuse into the active layer and causes perovskite degradation, which deteriorates the device efficiency. It can be suggested from the results that the device with the Spiro oxidation is

necessary and has a great impact on device performance and the optimum oxidation period in our case is 48 hours. The comparison between devices without Spiro oxidation and with oxidation (at 48 hours) in Figure 4.7 (b) and Table 4.4 demonstrates more explicitly that with Spiro oxidation, the device efficiency increases up to 10.4% (backward scan) that is ~78% higher than without oxidation. Moreover, it can be seen in Figure 4.8 (b) that Spiro oxidation helps to ease the hysteresis effect, which generally exists in mesoporous-based perovskite solar cells. These observations further clarify Spiro oxidation as an important step in the fabrication of MAPI perovskite solar cells.

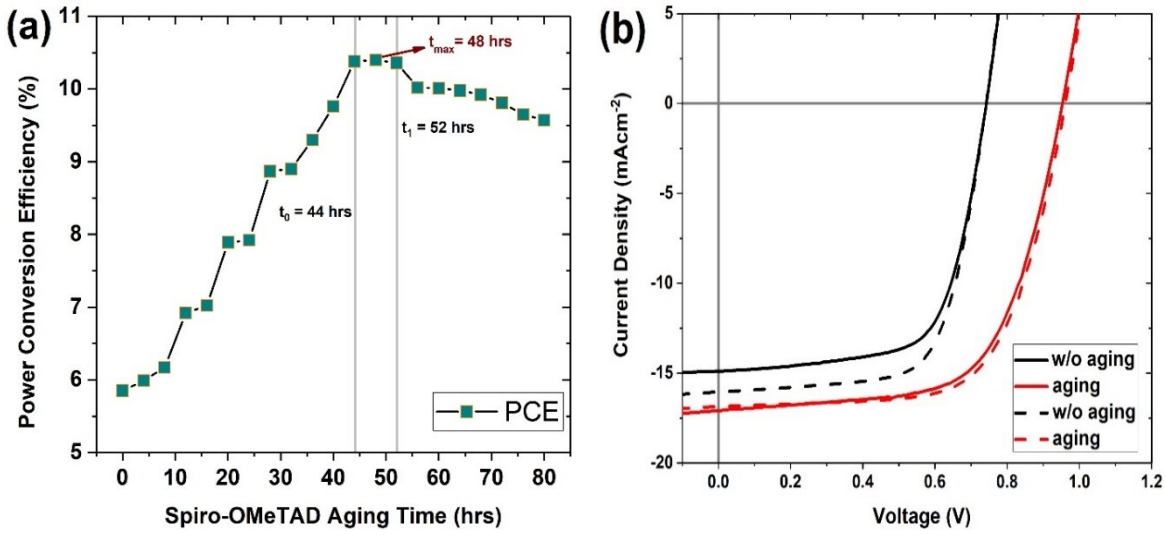


Figure 4-7: (a) Power conversion efficiency (PCE) of the $CH_3NH_3PbI_3$ (MAPI) perovskite solar cells with Spiro-OMeTAD aging at different periods of time. Aging time is also an important factor on device performance. According to the test result, 48 hours of aging time resulted in best device efficiency. (b) Current-Voltage curves of MAPI perovskite solar cells with Spiro-OMeTAD aging for 48 hours (red line) and without aging (black line) under forward (SC-FB, solid line) and reverse scan (FB-SC, dashed line).

Table 4-4: Device parameters of $CH_3NH_3PbI_3$ (MAPI) perovskite solar cells with Spiro-OMeTAD as hole-transporting layer with and without aging, device were measured under forward scan and backward scan. (w/o = without).

Aging 48 hrs	V_{oc} (V)	J_{sc} (mA/cm^2)	FF	PCE (%)
Forward	0.85	17.93	0.69	10.2
Reverse	0.85	17.92	0.71	10.4
w/o Aging	V_{oc} (V)	J_{sc} (mA/cm^2)	FF	PCE (%)
Forward	0.74	14.53	0.65	5.57
Reverse	0.74	15.63	0.67	5.85

Device Efficiency

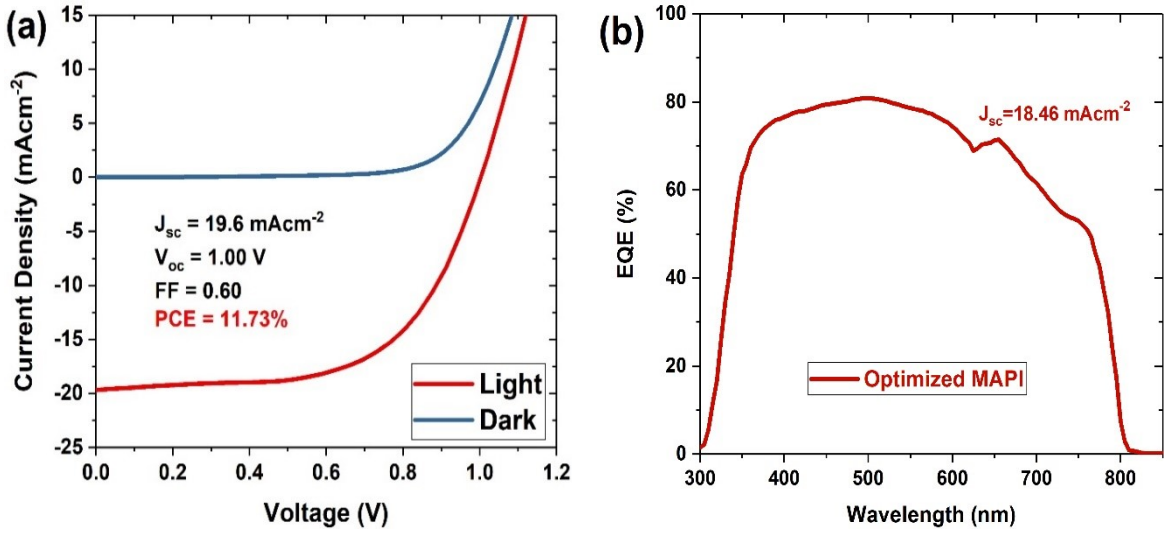


Figure 4-8: (a) Current-voltage curve of the optimized $CH_3NH_3PbI_3$ (MAPI) perovskite solar cell measured under light (black line) and dark (red line) conditions. (b) External quantum efficiency (EQE) spectra of the same device.

Each layer is optimized with the appropriate concentration or thickness to achieve best device performance. The next step is to combine all these optimum conditions and the most effective device curve is shown in Figure 4.8 (a). The best device performance of 11.73% in PCE is achieved, which is higher than any of previous experiments. This further confirms the feasibility of this procedure. Figure 4.8 (b) presents the EQE data obtained from the same device with optimized conditions. The device displayed EQE from 300 to 800 nm and reached over ~75% in the maximum peak. The integrated short current density (J_{sc}) from the EQE measurement is 19.55 $mAcm^{-2}$, which is slightly lower but within 0.2% bias to J_{sc} from the current voltage characteristics. The overall result shows that the J_{sc} is in good agreement with the value obtained from the solar simulator measurement. However, although satisfactory efficiency has been obtained through this fabrication procedure, the device performance is still less than the literature, providing potential for further enhancing device performance through obtaining better morphology of perovskite layers.

Device Reproducibility

The reproducibility of this standard fabrication procedure was tested by making 27 $CH_3NH_3PbI_3$ (MAPI) perovskite solar cells at the same time and all devices were measured under the same conditions. The devices' parameters are shown in Figure 4.9.

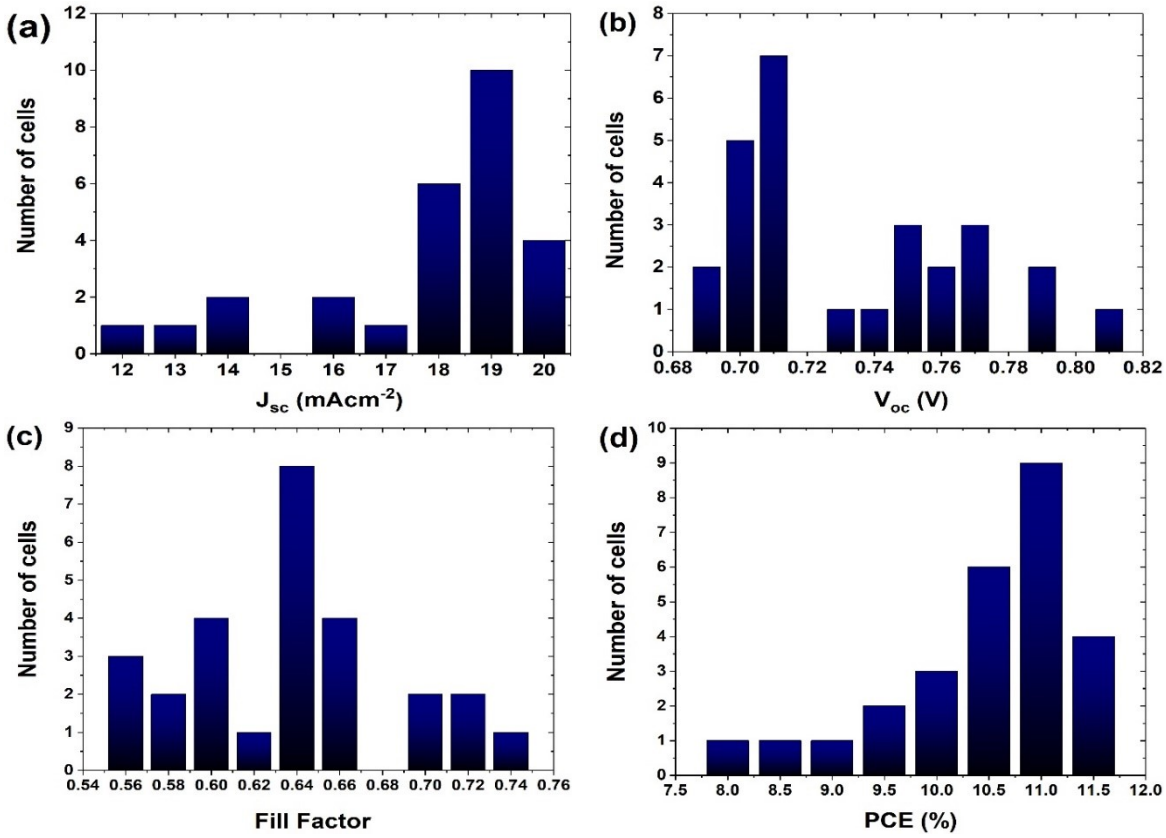


Figure 4-9: The histograms of (a) J_{sc} from I-V curves, (b) V_{oc} and (c) Fill factor and (d) PCE for an amount of 27 $CH_3NH_3PbI_3$ perovskite solar cells.

The results shows that ~81% of the devices achieved > 10% in efficiency. Also, the J_{sc}, V_{oc} and FF varied in a very narrow region, indicating that this method is quite reproducible and can be used as a standard method for future studies. More importantly, apart from the device efficiency, the instability of the perovskite layer and thus the degradation of the perovskite solar cells also plays a dominant role on the reproducibility of the device efficiency. Therefore, understanding and addressing the issue of device degradation becomes the major topic for the rest of this project.

4.4.2. Correlations of Crystal Size, Superoxide Formation and Device Parameters

In Section 4.4.1, a standard fabrication procedure was established for making $CH_3NH_3PbI_3$ (MAPI) perovskite solar cells with a satisfactory device performance (11.73 %) and verified reproducibility, thereby providing a foundation for future studies of this project. It is worth noting that while device reproducibility is affected by device efficiency arising from the different properties of each layer, the instability of the perovskite active layer, in particular, plays a vital role on device results. Exposure of the MAPI active layers to light and oxygen results in superoxide (O_2^-) formation, which could deprotonate the methylammonium cation ($CH_3NH_3^+$) of photo-excited $CH_3NH_3PbI_3^*$ and cause degradation of perovskite.[17] Other studies also show that film microstructure and particle morphologies have a great impact on device performance parameters and stability. In this case, it is reasonable to hypothesise that certain correlation exists between crystal size, superoxide formation and device efficiency and stability.

To test this hypothesis, the stability of films and devices using MAPI as a photoactive layer composed of three different particle sizes, small (100 nm), medium (150 nm) and large (250 nm) were investigated in a systematic manner. The details of the controlled MAPI crystal growth were achieved from the method previously reported by *Grätzel* et al. and are introduced in the experimental section.[24] The representative surface image of these crystals is shown in Figure 4.10 (a–c). Also shown in this figure are current-voltage curves for corresponding devices Figure 4.10 (d–e). All the devices were measured under continuous 1 sun illumination. What needs to be emphasized here is that since MAPI-based devices degraded more rapidly under oxygen diffusion than their corresponding films, as mentioned earlier in the chapter, attention was paid only to the trend of device degradation in the short run. This is so that all these measurements were recorded within five hours, which implies that these MAPI devices do not degrade completely. It is apparent from data in Figure 4.10 that devices with large MAPI crystals (250 nm) are more stable than those with small crystals, this result is consistent with studies on MAPI films. In contrast, the dependence of device efficiency on crystal size is less obvious, which suggested that other factors apart from crystal size (surface defects, vacancies etc.) might also impact on device performance and are investigated in **Chapters 5-7**. It is worth mentioning that the IGA (Intelligent Gravimetric Analyser) results from my peers' work shows that the rate of oxygen uptake for MAPI films

with different crystal sizes are quite similar, all films reaching saturation at around 10 minutes. Therefore, it is reasonable to suppose that the oxygen uptake rate for their devices is also very similar under the same period of time.

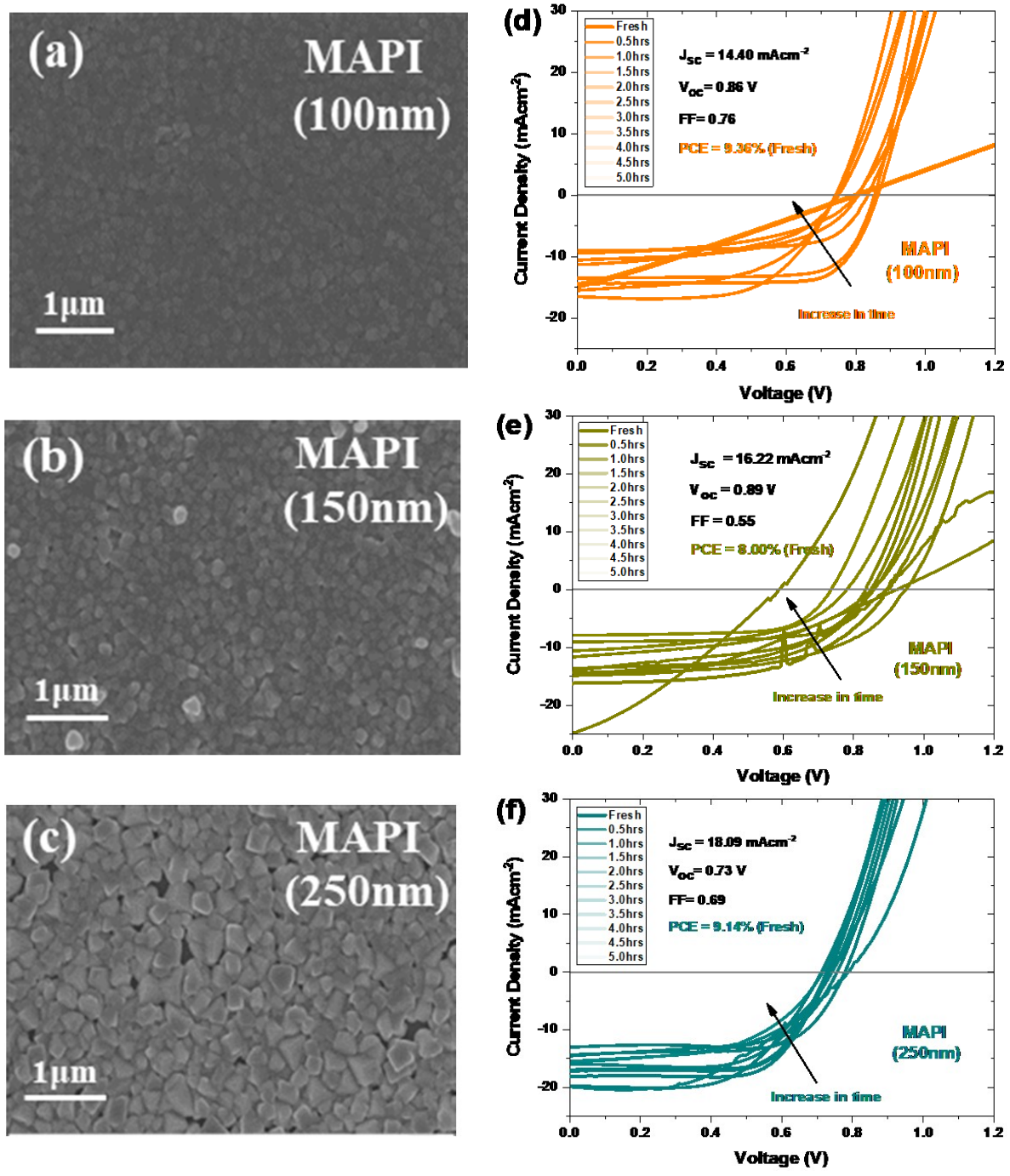


Figure 4-10: (a), (b) and (c): Surface SEM images of small (100 nm), medium (150 nm) and large (250 nm) crystal size of $CH_3NH_3PbI_3$ (MAPI) films deposited on cleaned glass substrates; (d), (e) and (f): Current-voltage characteristics of MAPI perovskite solar cells based on small (100 nm), medium (150 nm) and large (250 nm) crystal size. All devices using FTO/c-TiO_2/mp-TiO_2/$CH_3NH_3PbI_3$ /Spiro-OMeTAD/Au architecture, and were degraded under continuous one sun illumination and dry air-flow.

The possible correlation between MAPI crystal size, device stability and superoxide formation was considered. According to Figure 4.11, a direct relation is observed between MAPI crystal size, superoxide generation yield and device stability under light and oxygen stress. The MAPI with a large crystal size (250 nm) demonstrated a lower superoxide generation yield (Figure 4.11 (a)) and better device stability (Figure 4.11 (b)). Conversely, much higher superoxide generation is observed in smaller crystal size (100 nm) films and the device is more rapidly degraded with efficiency falling to ~34% of its original value within 5 hours. As a result, there is a direct relationship between yield of superoxide generation (and subsequently devices stability) and size of MAPI crystallite. Moreover, given the fact that the films' degradation (on a timescale of days) were much longer than the degradation of corresponding devices (on a timescale of hours),[18] the impact of superoxide formation on MAPI devices is even more significant than MAPI films.

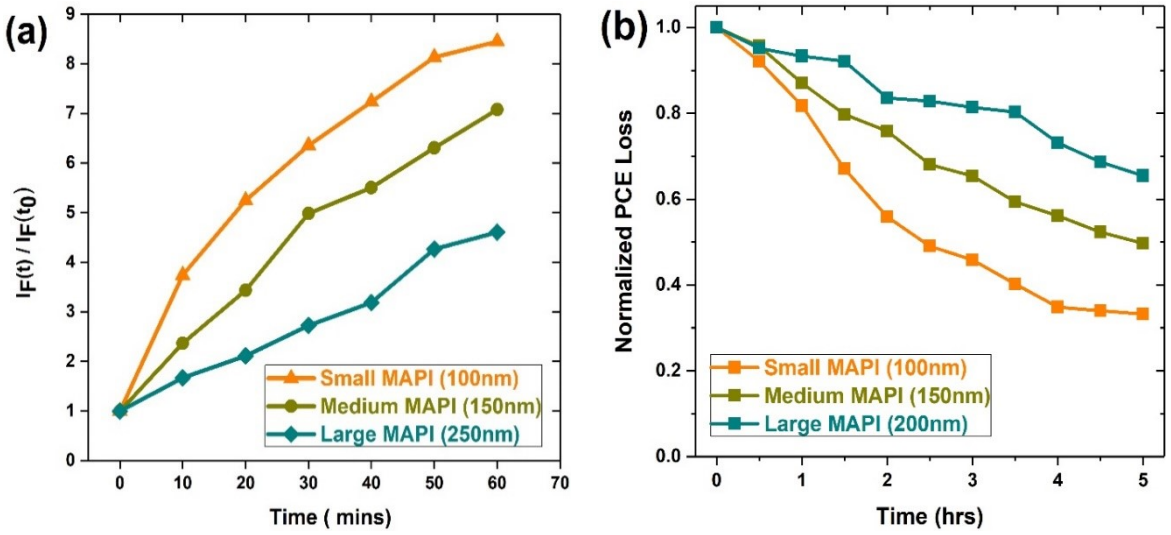


Figure 4-11: (a) The superoxide yield plot comparing the formation of superoxide for $CH_3NH_3PbI_3$ (MAPI) treated with small (100 nm), medium (150 nm) and large (250 nm) crystal size; (b) Normalised power conversion efficiency (PCE) loss for photovoltaic devices employing MAPI with small (100 nm), medium (150 nm) and large (250 nm) crystal size using FTO/c-TiO_2/mp-TiO_2/perovskite/Spiro-OMeTAD/Au architecture.

But what is the correlation between different perovskites? Will they obey the same relationship in crystal size and superoxide yield? To address this problem, the investigation was extended to different lead perovskite materials by selecting $CH_3NH_3PbI_3$ (MAPI), $Cs_xFA_{(1-x)}PI_3$ (CsFAPI) (x = 0.15) and $CH_3NH_3PbI_{3-x}Cl_x$ (MAPIC) for a comparative study. Figure 4.12 (a-c) shows the top view of SEM images of the three perovskites and (d-f) shows corresponding device stability. It can be seen that the crystal size of MAPIC (~450 nm) is larger than CsFAPI (~300 nm) and MAPI (150 nm). Device stability further shows that larger crystal size perovskite leads to more convergence of the current-voltage curves (f) than perovskite with smaller crystal size (d-e). The result further proved the finding that the device stability is directly correlated with the crystal size. Besides, concentration of chloride (Cl) and caesium (Cs) presented in precursor solution of MAPIC and CsFAPI might affect charge carrier recombination and influence device efficiency and stability.[31, 32] However, given very little of Cl and Cs species existed in the precursor it is unlikely to be the main factor for the enhanced stability of the devices.

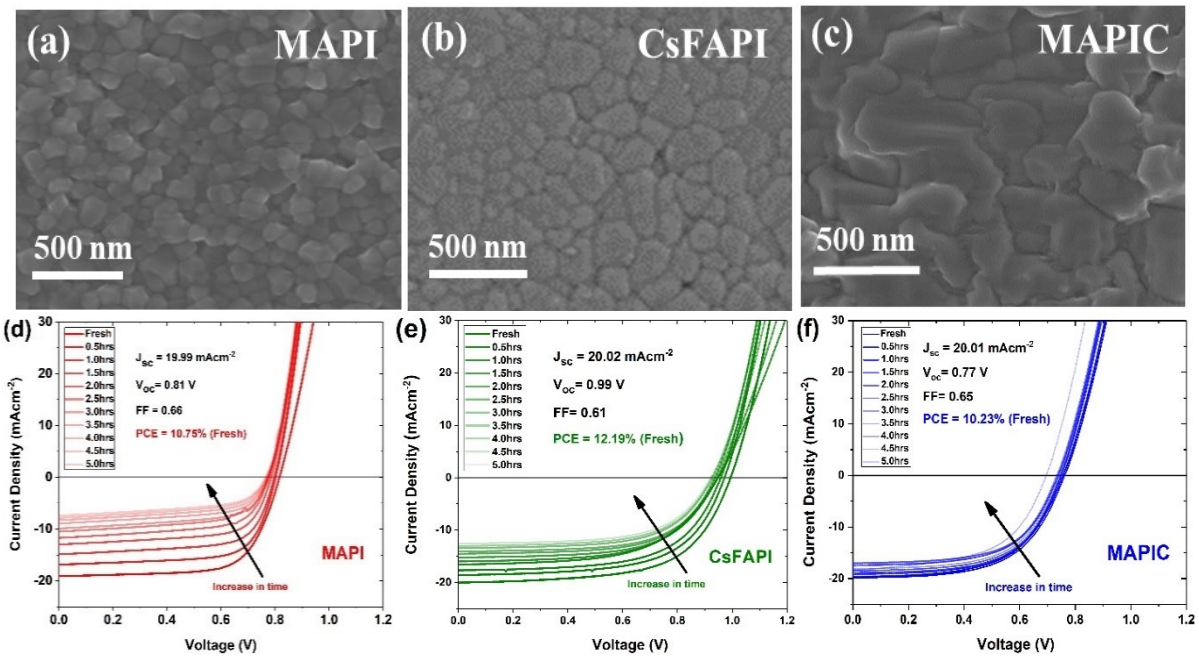


Figure 4-12: (a), (b) and (c): Surface SEM images of $CH_3NH_3PbI_3$ (MAPI), $Cs_{0.15}FA_{0.85}PI_3$ (CsFAPI) and $CH_3NH_3PbI_{3-x}Cl_x$ (MAPIC) films deposited on cleaned glass substrates; (d), (e) and (f): Current-voltage characteristics of MAPI perovskite solar cells based on MAPI, CsFAPI and MAPIC active layer. All devices used FTO/c-TiO_2/mp-TiO_2/perovskites /Spiro-OMeTAD/Au architecture, and were degraded under continuous one sun illumination and dry air-flow.

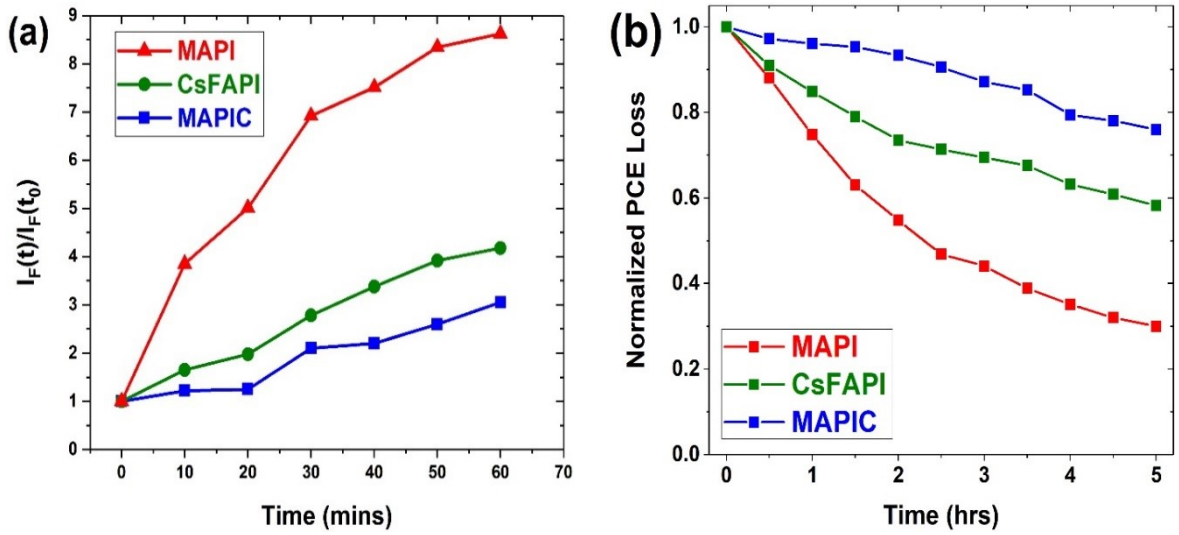


Figure 4-13: (a) Superoxide yield plot comparing the generation of superoxide for $CH_3NH_3PbI_3$ (MAPI), $Cs_{0.15}FA_{0.85}PI_3$ (CsFAPI) and $CH_3NH_3PbI_{3-x}Cl_x$ (MAPIC) films; (b) Normalised power conversion efficiency (PCE) loss for photovoltaic devices employing $CH_3NH_3PbI_3$ (MAPI), $Cs_{0.15}FA_{0.85}PI_3$ (CsFAPI) and $CH_3NH_3PbI_{3-x}Cl_x$ (MAPIC) using FTO/c-TiO_2/mp-TiO_2/perovskites/Spiro-OMeTAD/Au architecture.

Subsequently, we extended our study by investigating the correlation of crystal size, superoxide formation and device stability under the effect of visible light and oxygen stress for three different perovskites, with all devices being un-encapsulated and continuously illuminated under dry air and light. Similar to Figure 4.11, the results in Figure 4.13 reveal that crystal size directly affects superoxide generation yield and device stability. The larger MAPIC crystals generate much less superoxide species than CsFAPI and MAPI and are more stable in devices. Based on these observations and results obtained from MAPI with different crystal sizes, the high sensitivity of the perovskite solar cells to light and oxygen is attributed to the yield of superoxide generation and the size of the crystallite. Even for MAPIC which generate much less superoxide than MAPI, the device is not stable and experienced ~24% efficiency loss over five hours. To address this issue, an effective pathway is necessary to reduce/minimize superoxide formation. This leads onto the next steps in research.

4.5. Conclusion

This chapter first studied how device efficiency of MAPI-based perovskite solar cells is affected by a variety of conditions for different functional layers. To sum up, the optimization of compact TiO_2 layer reveals a high sentivity of device efficiency on the layer thickness. In terms of fabrication technique, spin coating method is more reproducible than spray pyrolysis, although the latter shows more compact film quality. In contrast, the mesoporous TiO_2 layer exhibits more tolerance on film thickness, the fluctuation on device efficiency in the range of 400-700 nm layer thickness is negligible. Interestingly, the $TiCl_4$ treatment, which was shown to be dispensable in some of the literature, appears to be essential in this study as it could effectively improve the interaction between mesoporous layer and photoactive layer. The concentration of $TiCl_4$ is a key factor and is optimized to be 40 mM for MAPI perovskite solar cells with best efficiency. Furthermore, the oxidization of the hole-transporting material Spiro-OmeTAD prior to measuring is necessary to achieve best device performance and minimize hysteresis. Although there is no universally perfect oxidization time, around 48 hours oxidation seems reasonable in this study. A standard procedure to achieve reproducible and satisfactory device performance was established. Subsequently, the chapter focused primarily on the stability of the perovskite solar cells and provided a novel mechanistic insight into light- and dry oxygen-induced degradation of perovskite solar cells. It was observed that superoxide (O_2^-) formation could directly affect the stability of perovskite solar cells and the rate of this degradation is dominated by perovskite crystallite size under light and oxygen: devices with smaller size in perovskite films reveal higher yield of superoxide formation, leading to more rapid device degradation. Inspired by these results, future work will include modification of the device fabrication technique to achieve higher efficiency and more reproducibility, as well as development of a strategy to reduce/minimize superoxide formation within perovskite materials.

4.6. References

[1] D.W. de Quilettes, S.M. Vorpahl, S.D. Stranks, H. Nagaoka, G.E. Eperon, M.E. Ziffer, H.J. Snaith, D.S. Ginger, *Science* **2015**, *348,* 683.

[2] H. Oga, A. Saeki, Y. Ogomi, S. Hayase, S. Seki, *Journal of the American Chemical Society* **2014**, *136,* 13818.

[3] W. Nie, H. Tsai, R. Asadpour, J.-C. Blancon, A.J. Neukirch, G. Gupta, J.J. Crochet, M. Chhowalla, S. Tretiak, M.A. Alam, *Science* **2015**, *347,* 522.

[4] M. Grätzel, *Nature Materials* **2014**, *13,* 838.

[5] M.M. Lee, J. Teuscher, T. Miyasaka, T.N. Murakami, H.J. Snaith, *Science* **2012**, 1228604.

[6] A. Kojima, K. Teshima, Y. Shirai, T. Miyasaka, *Journal of the American Chemical Society* **2009**, *131,* 6050.

[7] W. Chen, Y. Wu, Y. Yue, J. Liu, W. Zhang, X. Yang, H. Chen, E. Bi, I. Ashraful, M. Grätzel, *Science* **2015**, aad1015.

[8] W.S. Yang, J.H. Noh, N.J. Jeon, Y.C. Kim, S. Ryu, J. Seo, S.I. Seok, *Science* **2015**, *348,* 1234.

[9] M. Kaltenbrunner, G. Adam, E.D. Głowacki, M. Drack, R. Schwödiauer, L. Leonat, D.H. Apaydin, H. Groiss, M.C. Scharber, M.S. White, *Nature Materials* **2015**, *14,* 1032.

[10] M. Saliba, T. Matsui, K. Domanski, J.-Y. Seo, A. Ummadisingu, S.M. Zakeeruddin, J.-P. Correa-Baena, W.R. Tress, A. Abate, A. Hagfeldt, *Science* **2016**, *354,* 206.

[11] G.E. Eperon, T. Leijtens, K.A. Bush, R. Prasanna, T. Green, J.T.-W. Wang, D.P. McMeekin, G. Volonakis, R.L. Milot, R. May, *Science* **2016**, *354,* 861.

[12] N.J. Jeon, J.H. Noh, W.S. Yang, Y.C. Kim, S. Ryu, J. Seo, S.I. Seok, *Nature* **2015**, *517,* 476.

[13] T. Salim, S. Sun, Y. Abe, A. Krishna, A.C. Grimsdale, Y.M. Lam, *Journal of Materials Chemistry A* **2015**, *3,* 8943.

[14] H. Kim, C. Lee, J. Im, K. Lee, T. Moehl, A. Marchioro, S. Moon, R. Humphry-Baker, J. Yum, J. Moser, *Journal of Materials Chemistry A* **2012**, *1,* 5628.

[15] J.-H. Im, C.-R. Lee, J.-W. Lee, S.-W. Park, N.-G. Park, *Nanoscale* **2011**, *3,* 4088.

[16] F.T. O'Mahony, Y.H. Lee, C. Jellett, S. Dmitrov, D.T. Bryant, J.R. Durrant, B.C. O'Regan, M. Graetzel, M.K. Nazeeruddin, S.A. Haque, *Journal of Materials Chemistry A* **2015**, *3,* 7219.

[17] N. Aristidou, I. Sanchez-Molina, T. Chotchuangchutchaval, M. Brown, L. Martinez, T. Rath, S.A. Haque, *Angewandte Chemie* **2015**, *127,* 8326.

[18] N. Aristidou, C. Eames, I. Sanchez-Molina, X. Bu, J. Kosco, M.S. Islam, S.A. Haque, *Nature Communications* **2017**, *8,* 15218.

[19] D. Bryant, N. Aristidou, S. Pont, I. Sanchez-Molina, T. Chotchuangchutchaval, S. Wheeler, J.R. Durrant, S.A. Haque, *Energy & Environmental Science* **2016**, *9,* 1850.

[20] A.J. Pearson, G.E. Eperon, P.E. Hopkinson, S.N. Habisreutinger, J.T.W. Wang, H.J. Snaith, N.C. Greenham, *Advanced Energy Materials* **2016**, *6,* 1600014.

[21] M. De Bastiani, V. D'Innocenzo, S.D. Stranks, H.J. Snaith, A. Petrozza, *APL Materials* **2014**, *2,* 081509.

[22] G. Grancini, S. Marras, M. Prato, C. Giannini, C. Quarti, F. De Angelis, M. De Bastiani, G.E. Eperon, H.J. Snaith, L. Manna, *The Journal of Physical Chemistry Letters* **2014**, *5,* 3836.

[23] A. Sharenko,M.F. Toney, *Journal of the American Chemical Society* **2015**, *138,* 463.

[24] J.-H. Im, I.-H. Jang, N. Pellet, M. Grätzel, N.-G. Park, *Nature Nanotechnology* **2014**, *9,* 927.

[25] N.J. Jeon, J.H. Noh, Y.C. Kim, W.S. Yang, S. Ryu, S.I. Seok, *Nature Materials* **2014**, *13,* 897.

[26] J. Huang, P. Xu, J. Liu, X.Z. You, *Small* **2017**, *13,* 1603225.

[27] X. Wang, Y. Fang, L. He, Q. Wang, T. Wu, *Materials Science in Semiconductor Processing* **2014**, *27,* 569.

[28] H.K. Adli, T. Harada, S. Nakanishi, S. Ikeda, *Physical Chemistry Chemical Physics* **2017**, *19,* 26898.

[29] G. Choe, J. Kang, I. Ryu, S.W. Song, H.M. Kim, S. Yim, *Solar Energy* **2017**, *155,* 1148.

[30] R. Sánchez Sánchez,E. Mas Marzá, **2016**.

[31] S. Colella, E. Mosconi, P. Fedeli, A. Listorti, F. Gazza, F. Orlandi, P. Ferro, T. Besagni, A. Rizzo, G. Calestani, *Chemistry of Materials* **2013**, *25,* 4613.

[32] F.K. Aldibaja, L. Badia, E. Mas-Marzá, R.S. Sánchez, E.M. Barea, I. Mora-Sero, *Journal of Materials Chemistry A* **2015**, *3,* 9194.

CHAPTER 5

Methylammonium Iodide Salt Treatment on Methylammonium Lead Triiodide and Bromide Mixed Halide Perovskite Solar Cells for Enhanced Stability

5.1. Abstract

It is shown that iodide vacancies in methylammonium lead triiodide ($CH_3NH_3PbI_3$) crystals are the most-preferred sites for superoxide production, a key element in causing photo- and oxygen-induced degradation. Utilising this characteristic, a film passivation technique was devised by direct loading of the appropriate amount of Methylammonium Iodide (CH_3NH_3I; MAI) on top of the perovskite film prior to depositing Spiro-OMeTAD (a hole transport material for solid-state dye sensitized solar cells and perovskite solar cells). This treatment could effectively passivate the perovskite film, reduce the number of defects and crystal-lattice vacancies, thus inhibiting superoxide formation and improving device stability. The correlation between superoxide formation and device stability as a function of bromide composition for $CH_3NH_3Pb(I_{1-x}Br_x)_3$ solar cells is examined. Increase in bromide content leads to a reduction in superoxide and, as a result, the device stability towards exposure to oxygen and light improves. Further investigation of the role of defect passivation indicated that CH_3NH_3I (MAI) salt could help in obtaining more-stable devices. The observation further confirmed the theory that light- and oxygen-induced solar cell degradation could be attributed to the superoxide formation, which can be effectively alleviated via iodide salt passivation. However, one of the main disadvantages of using MAI treatment is that high-stability devices are achieved only by compromising efficiency, which pointed out the direction for further research.

5.2. Introduction

In **Chapter 4**, it was demonstrated that light and dry oxygen could initiate material degradation of methylammonium lead iodide ($CH_3NH_3PbI_3$, $MAPbI_3$, or MAPI) films through formation of reactive superoxide species. The latter could react with perovskite and break down its initial crystal structure by means of an acid-base reaction between oxygen and methylammonium cations. This process has a dramatic influence on MAPI solar cells. Factors responsible for this degradation were considered by identifying elements that might influence oxygen diffusion into the perovskite active layer and facilitate the oxidative reaction to form superoxide. The correlation between particle size of the perovskite on the yield and superoxide formation and indicated that larger crystal size resulted in less superoxide formation and more device stability. Furthermore, the relationship is not limited to a single perovskite system, such as MAPI, but also other perovskite systems.

In the present chapter, investigation into factors that cause superoxide formation reactions in perovskite crystals on exposure to light and dry oxygen are described. Previous studies have indicated that hybrid perovskite materials are mixed ionic-electronic conductors,[1-5] and significant amounts of defect concentration of I^-, Pb^{2+} and $CH_3NH_3^+$ vacancies present inside $CH_3NH_3PbI_3$ crystals at room temperature could provide a pathway for ion transport or migration, which has a direct impact on the hysteresis of perovskite solar cells.[6] More importantly, recent observations also highlight the importance of these defects on perovskite device degradation.[7] Therefore, it is reasonable to suppose that ionic defects and migration in perovskite might influence oxygen diffusion and thereby affect oxygen- and light-induced degradation. **Chapter 5** provides an in-depth study of the correlation between ionic vacancies and superoxide formation from light and oxygen diffusion. A surface passivation technique is introduced, applying Methylammonium Iodide (MAI) salt on top of the perovskite film. The feasibility of device stability enhancement is discussed. Furthermore, this technique is applied to more complicated bromide-iodide perovskite devices to enhance their stability.

5.3. Experimental

5.3.1. Iodide Salt Treatment Device Fabrication

The fabrication of perovskite solar cells with iodide salt treatment is very similar as the procedure of making standard MAPI solar cells mentioned in **Chapter 4**, but with some parameters change. Fluorine-doped tin oxide (FTO) coated glass substrates (100 × 25 mm, 2.3 mm thick TEC15, Pilkington) were first etched with zinc powder and aqueous hydrochloric acid (HCl, 37%), and then cut into 25 × 25 mm pieces followed by cleaning sequentially in acetone, distilled water and isopropylalcohol (IPA) under sonication for 10 minutes during each washing cycle. A compact titanium oxide (TiO_2) layer was prepared by spin coating a solution comprising 350μL titanium isopropoxide (Aldrich), 35μL HCl (37%) and 5mL anhydrous ethanol at 4000 rpm for 30 s. The TiO_2 films were sintered at 125 °C for 5 mins and then at 500 °C for 45 mins. Next, a mesoporous TiO_2 film was deposited using a solution of 20nm particle transparent titania paste (18NR-T, Dyesol) diluted in 2:7 weight ratio with anhydrous ethanol. The solution was spin-coated onto the substrates at 5000 rpm for 30 s. Once spun, the films were dried on a hotplate at 80 °C for 5mins, and then sintered at 500 °C for 45 mins. The desired perovskite layer was prepared using a consecutive five-step spin program inside a glovebox (1000 rpm for 5s; 1000 rpm for 10s; 4000 rpm for 20s; 500 rpm for 1s; 5000 rpm for 30s) where 500 μL toluene was swiftly dripped onto the surface before the start of the fourth step and then dried at 100 °C for 10 mins. In instances where iodine salt layers were used, 1mM, 2mM, 6mM and 10mM solution of MethylAmmonium Iodide (MAI) with IPA were prepared. The solution was then spin coated onto the perovskite layer using a three-step spin program (4000 rpm for 30s; 500 rpm for 20s, and 4000 rpm for 30s). The Spiro-OMeTAD hole conductor layer was spin coated onto the perovskite films from a solution of 72.3 mg/mL 2,2',7,7'-tetrakis-(N,N-di-4-methoxyphenylamine)9,9'-spirobifluorene (Spiro-OMeTAD) powder in 1 mL anhydrous chlorobenzene. The Spiro-OMeTAD solution contained additives, including 17.5μL lithium bis(trifluoromethane) sulfonimide lithium salt (Li-TFSl) and 28.8μL 4-tert-butylpyridine (tBP). Finally, a 100 nm-thick gold contact was evaporated under vacuum (approximately 10^{-6} Torr at a rate of 0.2 nm/s) with an active area of 0.12cm^2.

5.3.2. $MAPbI_3$ and $MAPbBr_3$ Solutions and Film Fabrication

0.25 g of MAI and 0.78 g PbI_2 was mixed in a 1:1 mole ratio in 1.4 ml of anhydrous gamma-butyrolactone (GBL) and 0.6 ml of dimethyl sulfoxide (DMSO) for 1 hour at 60 °C. It was then removed from the hot plate and left to precipitate overnight. The solution was then filtered with a 0.2 μm membrane in a small plastic tube. This solution was then pipetted in two consecutive spin steps under a nitrogen atmosphere in a glovebox. The first spinning cycle was performed at 2000 rpm for 30 seconds followed by 4000 rpm for 30 seconds. During the second step, the substrate was treated with dry toluene (approximately 500 ml) by drop-casting. The film was heated at 100 °C for 10 minutes. The colour of the films changed from yellow to black immediately after being placed on a hot plate. It is entirely possible that while transporting and measuring, moisture started to corrode methylammonium lead iodide ($MAPI_)$ readily, even though both samples are mostly degraded under the dry air environment. To minimise the amount of moisture getting into the films, the aged films were kept in a closed container with excess of Silica-drying agents underneath before exposure to any characterization techniques. $MAPbBr_3$ solutions and films were created using the same method as described above, except using the bromide derivatives, MABr and $PbBr_2$.

5.3.3. $MAPb(I_{1-x}Br_x)_3$ Film Fabrication

Stock solutions of $MAPbI_3$ and $CH_3NH_3PbBr_3$ were prepared by dissolving stoichiometric ratios of PbX_2 and MAX_3 (where X = I or Br) in a DMSO and GBL solution (7:3) at 1.25 M in concentration and stirred for 60 minutes at 50° and room temperature. To obtain a range of x values in $MAPb(I_{1-x}Br_x)_3$, stock solutions were combined with volumetric ratios. Thin film samples were prepared on glass using the anti-solvent technique adapted from a previously reported method. The glass was washed in soap, acetone, and 2-propanol followed by a 10-minute oxygen plasma treatment. The perovskite precursor solution was coated using a spin-coating procedure using two speeds where toluene was dripped onto the surface during the second step and then dried at 100°C post-deposition. All other characterization techniques are mentioned in the experimental section in **Chapter 3**.

5.4. Results and Discussion

5.4.1. Methylammonium Iodide (MAI) Salt Treatment in MAPI Perovskite Solar Cells

In the introduction (Section 5.2), we have hypothesised that ionic defects and migration inside perovskite might contribute to the superoxide generation upon oxygen diffusion and initiate the oxygen- and light-induced degradation. However, the exact correlation between the superoxide formation and intrinsic vacancies associated with this photo- and light-induced degradation needs to be determined. To address this issue, a team from Bath University, UK, collaborated in the work, employing a combination of experimental and computational techniques to address this question at a microscopic level, based on previous work.[1, 8-10] The dynamics of oxygen diffusion into the perovskite films were observed. The morphology of the film could produce an effect on reaction with oxygen and thus influence the yield of superoxide formation, which degraded the perovskite material.[11] These findings suggest that oxygen enters quickly into perovskite samples and is uniformly distributed throughout the films. More importantly, it was concluded that the high sensitivity of $CH_3NH_3PbI_3$ (MAPI) devices (perovskite solar cells, PSCs) to oxygen could be attributed to the rapid rate of oxygen diffusion.

The relationship between ionic defects and superoxide formation by using simulations *ab initio*, based on Density Functional Theory (DFT) are considered, using calculations which allow the prediction of material behaviour on the basis of quantum mechanical considerations. The reaction with oxygen in the condition of no photo-generated electrons in the perovskite lattice was investigated first. The chemical equation is as follows:

$$\mathbf{4CH_3NH_3PbI_3 + O_2 \rightarrow 4PbI_2 + 2I_2 + 2H_2O + 4CH_3NH_2} \qquad \mathbf{(1)}$$

The enthalpy is + 1.60 eV per O_2 molecule; the positive value implies that without light illumination, this reaction is not energetically favoured. This result proves that the overall degradation has to occur in the presence of both light and oxygen, the O_2 acts as an electron scavenger and absorbs photo-generated electrons according to the reaction $O_2 + e^- = O_2^-$.[8, 10]

Next, the reaction of superoxide species (O_2^-) with the photo-excited perovskite $CH_3NH_3PbI_3^*$ was considered to form I_2, PbI_2, and CH_3NH_2 according to previous literature and Figure 4-1.[8, 11]

$$\mathbf{4CH_3NH_3PbI_3^* + O_2^- \rightarrow 4PbI_2 + 2I_2 + 2H_2O + 4CH_3NH_2} \quad \mathbf{(2)}$$

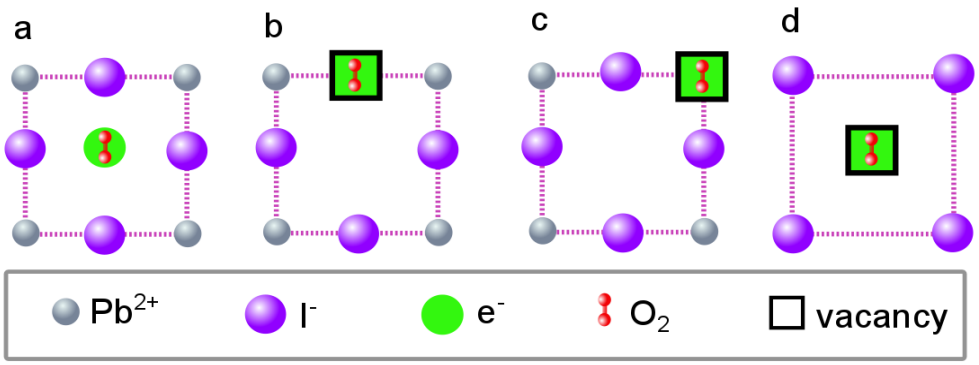
The calculated enthalpy in this case is – 1.40 eV per O_2 molecule and is a negative value, which means that the reaction in Equation (2) is energetically favourable, and both photo-oxidized MAPI and superoxide species (O_2^-) are unstable.

An important question arising, in this case, is that if the oxygen diffusion into the perovskite film causes superoxide formation and degrades the photoactive layer, where is the most favourable site in the crystal lattice for superoxide generation? Recent literature indicates that there is a significant amount of intrinsic Schottky-type defects (combined with anion and cation vacancies) present in $CH_3NH_3PbI_3$ (MAPI) and they can be expressed with Kröger-Vink notation as follows:

$$\boldsymbol{nil \rightarrow V'_{MA} + V''_{Pb} + 3V^{\bullet}_{I} + MAPbI_3} \quad \mathbf{(3)}$$

Where *nil* represents defect-free $CH_3NH_3PbI_3$ (MAPI) lattice, V'_{MA}, V''_{Pb} and $V^{\bullet}_{I}$ represent vacancies with respect to different types of lattice sites, and the superscripts indicate the charge of these defects, e.g. a dot for each positive charge and prime for each negative charge. The whole reaction should be balanced in terms of positive and negative charges.

The formation energy for superoxide generation from oxygen diffusion was calculated on different lattice and vacancy sites in the MAPI crystal structure, and the results are shown in Figure 5-1.[11] It is observed that apart from V''_{Pb}, which shows a positive enthalpy value, other vacancies render negative values. This indicates that superoxide generation from direct electron transfer from perovskite to oxygen is energetically favourable. More importantly, the enthalpy energy from $V^{\bullet}_{I}$ is -1.94 eV, the lowest O_2^- formation energy among all other vacancies. Therefore, it can be suggested that iodide vacancies/defects are the most preferred location for the superoxide formation in the crystal. The result highlighted that iodide vacancies play an important role in facilitating superoxide generation from O_2 diffusion.



Site	a) face	b) $V_I^{\times}$	c) V_{Pb}''	d) V_{MA}'
O_2^- formation energy (eV)	-1.19	-1.94	+0.29	-0.23

Figure 5-1: Schematic representation of possible O_2 binding and reduction sites in $CH_3NH_3PbI_3$ (MAPI) in the crystal lattice and corresponding superoxide formation energy: **(a)** Face site neighbouring four iodide ions, **(b)** neutral iodide vacancy (with a photoelectron on the defect site) and negatively charged lead **(c)**, and methylammonium **(d)** vacancies (with no photoelectron on them since this was found to be unphysical).[18]

Interestingly, it was further observed that the size of an iodide ion is around 4.40 Å, which is very close to the size of 3.42 Å from superoxide species so that the latter are able to restore the full octahedral coordination of Pb^{2+} upon occupying the iodide vacancies, as shown in Figure 5-2.

According to studies described in **Chapters 4** and **5**, so far we have two important observations: (1) There is a direct correlation between crystal size and superoxide formation and hence $CH_3NH_3PbI_3$ device degradation; the larger crystal sizes resulted in less superoxide formation and more device stability, whereas smaller crystal size resulted in more superoxide formation and less device stability. (2) Superoxide formation is always accompanied by material degradation and is most preferred on iodide vacancies, which renders similar ionic size.

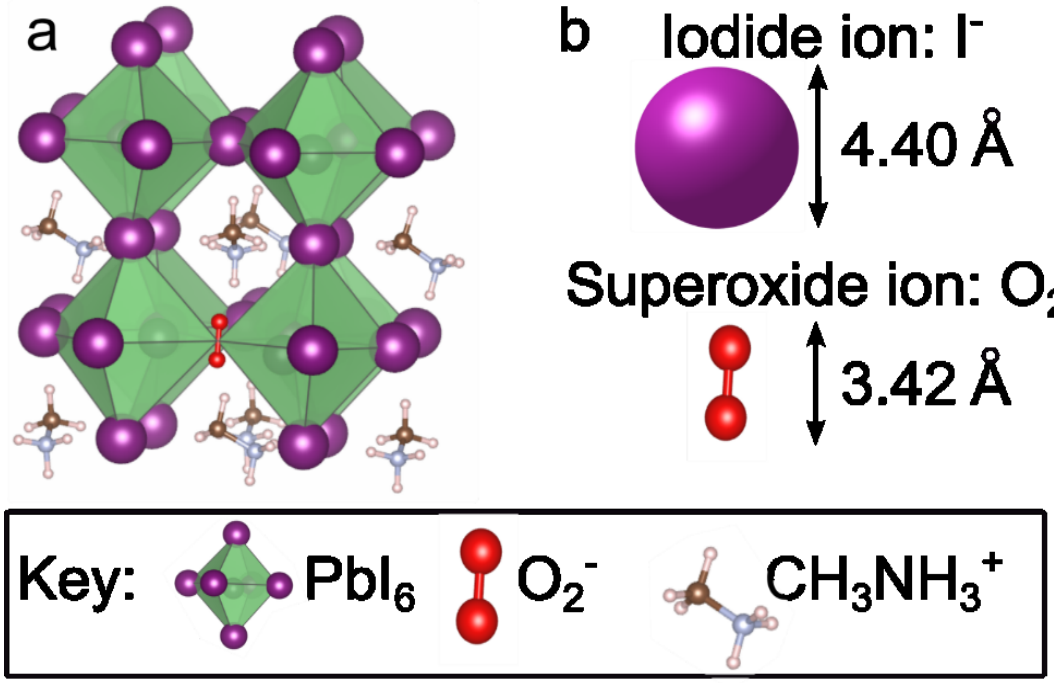


Figure 5-2: Atomic structure of $CH_3NH_3PbI_3$ (MAPI) showing **(a)** superoxide ion, O_2^-, occupying an iodide vacancy, $V_I^\times$ (for clarity, a pseudo-cubic sub-region of the structure is shown and not the full tetragonal supercell used in the calculations). **(b)** Comparison of relative size of iodide and superoxide anions (using ionic radius of I^- and for superoxide ion interpolation between covalent radius in O_2 and ionic radius of O^{2-}). [18]

To rationalize the above findings, a mechanism is proposed here that is depicted in Figure 5-3. The MAPI sample under illumination and oxygen stress provides photo-excited electrons in both bulk and surface sides of the crystal. When oxygen diffuses into the perovskite sample, it could quickly diffuse between crystals and penetrate the inter-particle region within an hour, as shown in Figure 5-3 (a). Subsequently, the superoxide species quickly formes at the surface of the crystals as the O_2 molecule is reduced when occupying iodide vacancies. This process continues within the first few hours, leading to the degradation of the surface of the crystal by preventing the extraction of the photocurrent.[13] This explains the result discussed in **Chapter 4** that MAPI devices degrade rapidly in just a few hours under oxygen and light illumination. In the longer term (several days to weeks), oxygen molecules will further diffuse inside the crystals where they could occupy the bulk of the side iodide vacancies, leading to the complete degradation of the MAPI materials, as illustrated in Figure 5-3 (b). Therefore, it can be suggested that the short term (within a few hours) stability of MAPI is more dependent on surface iodide vacancies and long-term (from a few days to a few weeks) stability is more affected by bulk iodide vacancies. This result also explains the observations made in **Chapter 4** that MAPI based solar cells with smaller crystal size show faster initial

degradation (within 5 hours) than larger-crystal devices. First, the number density of surface vacancies for the small crystals is much higher than for large crystals, the aforementioned provides more superoxide formation sites, and therefore more oxygen molecules are reduced to superoxide, which is associated with more-rapid device degradation under illumination and oxygen. Second, in the longer term (a few days), bulk side vacancies will make their impact on the rate of degradation. The increased degradation rate for smaller crystallites may also originate from the shorter O_2 diffusion length from particle interiors. (The calculation in iodide vacancies and O_2 diffusion length was done by the collaborators and is beyond the scope of this project, so will not be mentioned further in detail here.)

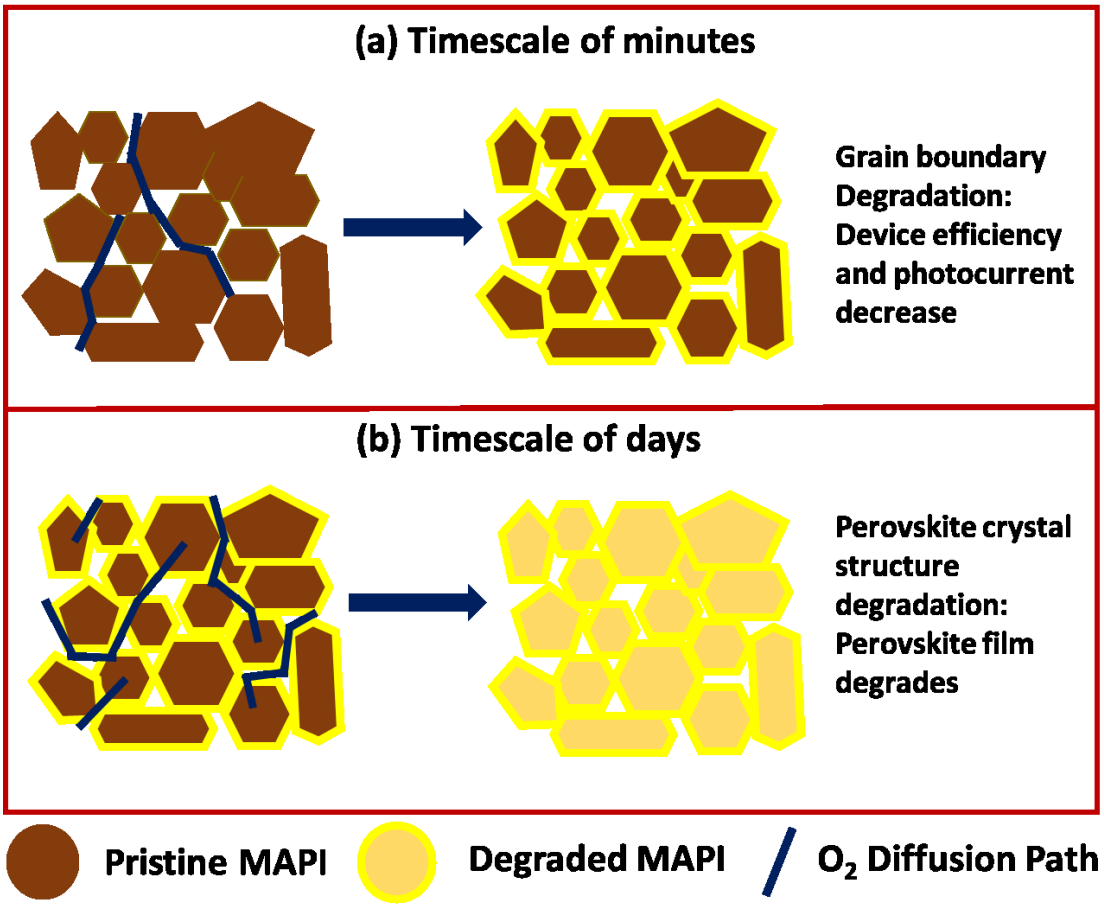


Figure 5-3: Schematic of oxygen diffusion pathways and associated degradation regions of MAPI particles. **(a)** O_2 diffusion in inter-particle regions and initial reaction with particle surfaces over a timescale of hours leading to reduction in device efficiency, open circuit voltage and photocurrent, and **(b)**, O_2 diffusion into particle bulk regions over a time scale of days leading to a phase change from the photo-absorbing perovskite phase into the non-absorbing lead iodide phase.

Therefore, if we want to inhibit superoxide formation and hence decrease the severity of perovskite degradation, we need to minimize the iodide vacancies that exist inside the crystal lattice. To do this, a Methylammonium Iodide (MAI) salt on top of the perovskite films was introduced to evaluate how their stability and device parameters would be influenced. The process is shown in Figure 5-4 as follows.

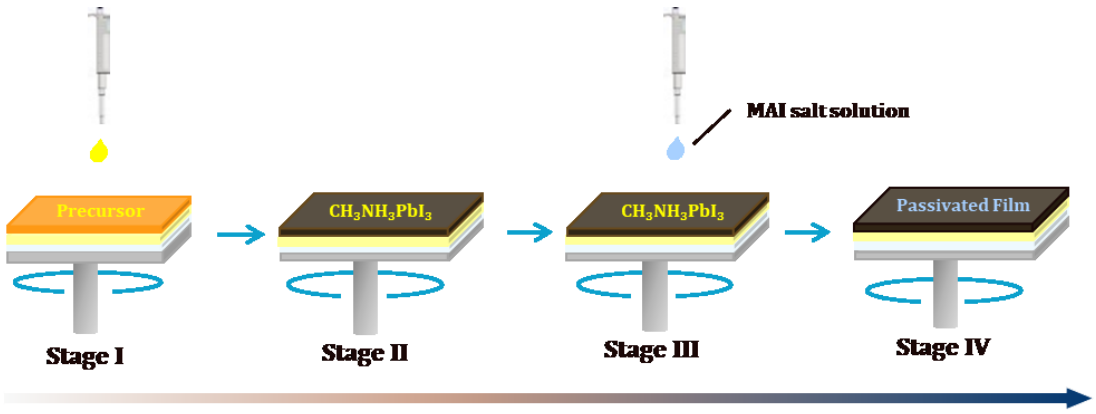


Figure 5-4: Schemes of the MAI iodide salt passivation procedure for perovskite solar cells with $CH_3NH_3PbI_3$ (MAPI) as active layer.

The effect of the iodide salt on solar cell efficiency is examined first: In this case, $CH_3NH_3PbI_3$ (MAPbI) devices without and with different concentrations of MAI coating were fabricated and characterized (details are mentioned in the experimental section, Section 5.3, above). The current-voltage curves and photovoltaic parameters, as well as the External Quantum Efficiency (EQE) spectra for selected devices, are shown in Figure 5-5 and Table 5-1. All devices render typical current-voltage curves in dark and light conditions, indicating that the iodide salt treatment is suitable for solar cell application. Moreover, it was observed that an increase in iodide salt concentration leads to a reduction of open circuit voltage (V_{oc}), short circuit current density (J_{sc}) and Fill Factor (FF). As a result, the Power Conversion Efficiency (PCE) drops from 11.39 % for pristine MAPI to 9.02 % for 10 mM of MAI coating. The EQE spectra from Figure 5-5 (b) further confirmed this finding by showing that the device without iodide treatment displayed higher EQEs from 300 to 850 nm. The EQE of the pristine MAPI device reached 84%, whereas that of the device prepared with 10 mM of MAI post-treatment reached only 76%. It can be suggested that the reduction in EQE is due to a morphology change and a decrease in crystallinity of the perovskite films upon applying MAI treatment. The integrated J_{sc} of MAPI and device with 10 mM MAI coating is 19.11 mA/cm^2 and 17.79 mA/cm^2 respectively, which is within the allowed bias range as compared with values from the current-voltage measurement.

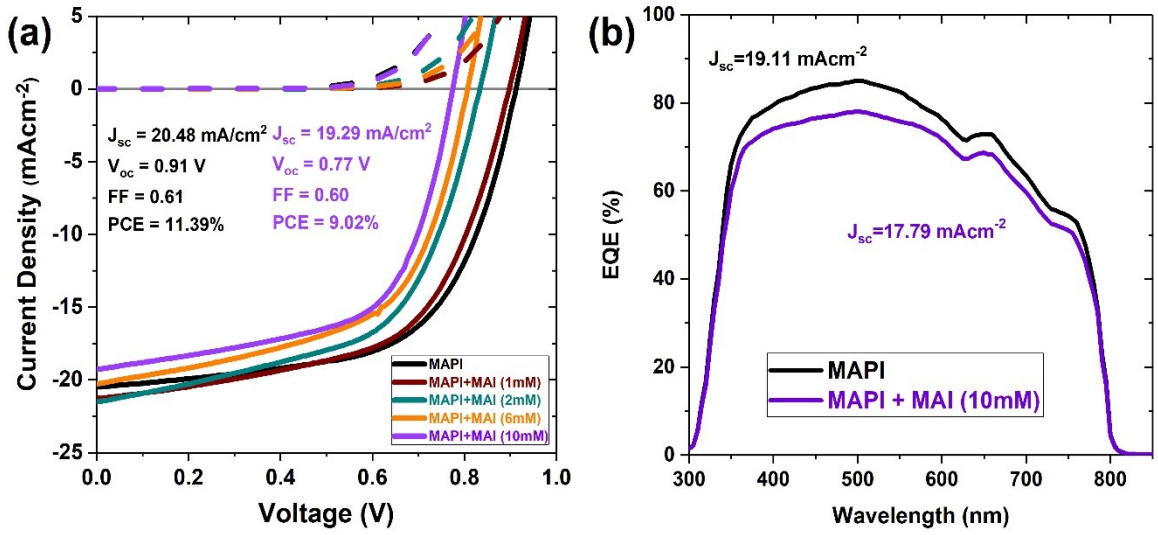


Figure 5-5: (a) Current-voltage curves of initial performances of $CH_3NH_3PbI_3$ (MAPbI) devices without iodide salt coating (black) and with MAI coating in various concentrations of 1 mM (dark red), 2.0 mM (dark cyan), 6 mM (orange) and 10 mM (violet). Devices were measured using xenon lamp AM1.5 simulated solar spectrum with a scan rate of 0.125 V/s. The initial device is held at open circuit conditions for 60 seconds to stabilise and then scanned from 0 V to 1.2 V, both illuminated current (solid line) and dark current (dashed line) are recorded. (All results are backward scan FB-SC). **(b)** The External Quantum Efficiency (EQE) spectra of devices without and with various concentrations of MAI coating. All devices are fabricated in FTO/compact-TiO_2/mesoporous-TiO_2/perovskite (iodide salt)/Spiro-OMeTAD/Au architecture. (Open circuit voltage: V_{oc}; short circuit current density: J_{sc}; Fill Factor: FF; power conversion efficiency: PCE.)

Table 5-1: Device parameters of initial performance for devices based on varied concentration of MAI salt coated on $CH_3NH_3PbI_3$ (MAPI) perovskite films. (FB-SC: reverse scan; SC-FB: forward scan; open circuit voltage: V_{oc}; short circuit current density: J_{sc}; Fill Factor: FF; Power Conversion Efficiency: PCE).

Device Type	Pixel Area (cm^2)	Scan Direction	V_{oc} (V)	J_{sc} ($mAcm^{-2}$)	FF	PCE (%)
MAPI (Ref.)	0.12	FB-SC	0.91	20.48	0.61	11.39
		SC-FB	0.79	21.45	0.54	9.10
+MAI (1mM)	0.12	FB-SC	0.90	21.29	0.58	11.10
		SC-FB	0.84	20.28	0.52	8.88
+MAI (2mM)	0.12	FB-SC	0.83	21.51	0.56	10.10
		SC-FB	0.83	20.81	0.47	8.02
+MAI (6mM)	0.12	FB-SC	0.81	20.28	0.58	9.46
		SC-FB	0.83	15.06	0.58	7.39
+MAI (10mM)	0.12	FB-SC	0.77	19.29	0.60	9.02
		SC-FB	0.79	14.56	0.60	6.96

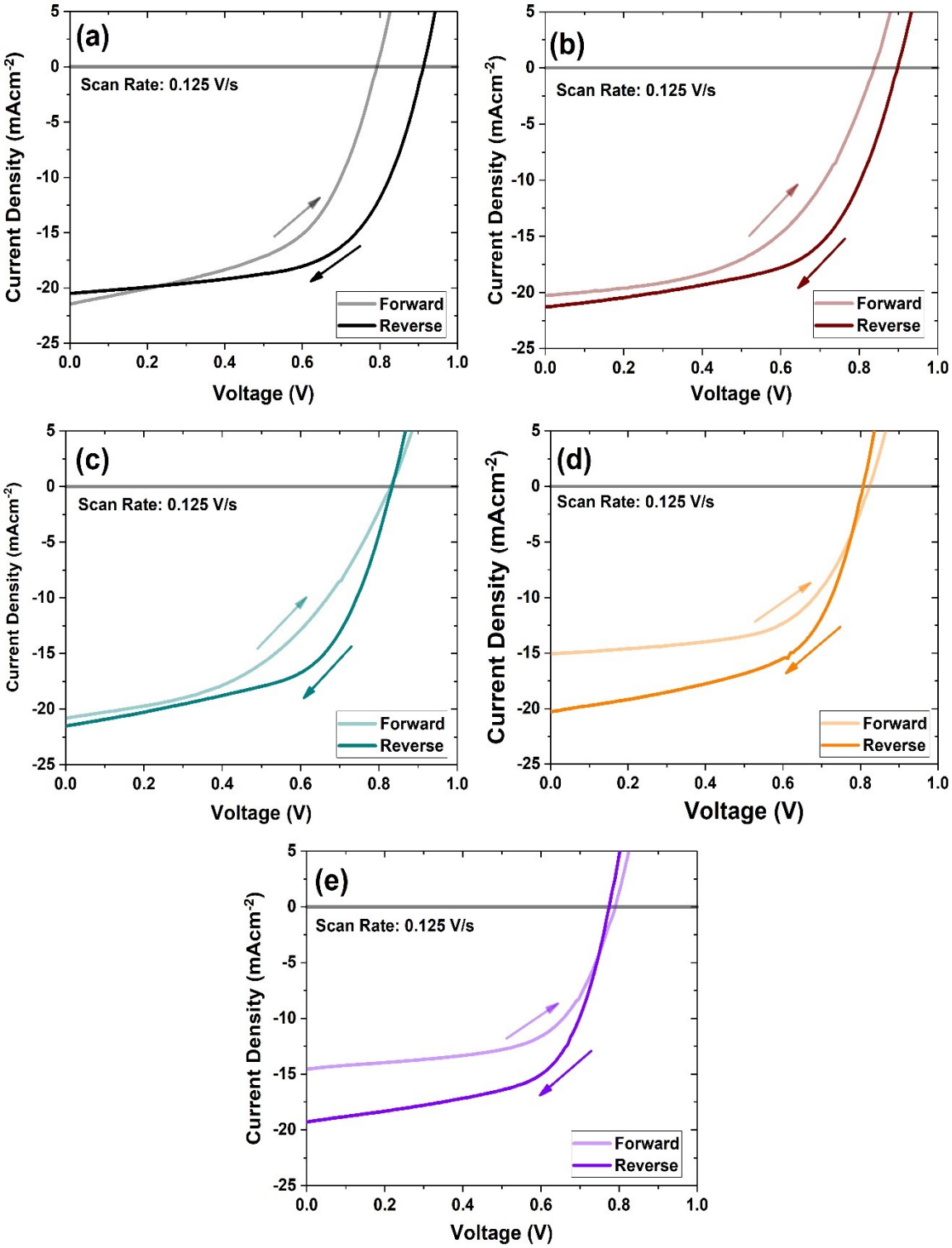


Figure 5-6: Influence of the MAI salt concentration on current-voltage hysteresis of the MAPI devices. The devices are measured in reverse scan (FB-SC) and forward scan (SC-FB) under simulated AM1.5 100 mW cm^{-2} sunlight with **(a)** MAPI (black), **(b)** 1 mM (dark red), **(c)** 2.0 mM (dark cyan), **(d)** 6 mM (orange) and **(e)** 10 mM (violet) of MAI salt coated on MAPI perovskite solar cells. The scan rate is 0.125 V/s for all devices.

The influence of the scanning direction on the performance of the MAPI solar cells fabricated without and with varying concentrations of MAI salt coating was then investigated. The results are shown in Figure 5-6. It is worth noting that all devices suffer from a hysteresis effect, which commonly occurs in MAPI solar cells with mesoporous TiO_2 layers and is believed to be influenced by many factors such as scan rate and ionic migrations.[14-17] The forward scan (SC-FB) and reverse scan (FB-SC) parameters of all devices were recorded according to Table 5-1. To better describe the difference between the efficiency of the forward scan and reverse scan, a quantity called the 'difference factor' according to the following equation was used:

$$\boldsymbol{Difference\ Factor} = \frac{(\eta_{reverse} - \eta_{forward})}{\eta_{reverse}} \qquad \textbf{(4)}$$

In Equation (4), $\eta_{reverse}$ and $\eta_{forward}$ represent the Power Conversion Efficiency (PCE) of the reverse and forward scans, respectively, as shown in Figure 5-6, at a standard scan rate of 0.125 V/s, all devices exhibit a certain degree of hysteresis behavior. In particular, 20.1% of difference factor is achieved for pristine MAPI solar cells, whereas for a 1 mM MAI coating device, this value is 20.7%, slightly higher than without iodide coating. Further increasing the MAI concentration does not lead to reduced hysteresis effect on devices. The difference factors for 2 mM and 6 mM MAI coating are 20.6 % and 21.9 %, respectively, which are even higher than the pristine MAPbI device. When MAI concentration approaches 10 mM, the difference factor rises to 22.8 % and the hysteresis becomes stronger. It is believed that more-severe hysteresis occurring in current-voltage measurements can cause inaccurate estimation of the device efficiency, thereby have adverse effect device reproducibility.[18] It is appreciated that our device efficiency is still lower than published results, which might also contribute to more hysteresis behaviour, owing to less satisfactory morphology. Overall, the limitation of using MAI salt as passivating agent encouraged the search to find alternative materials as well as to develop novel treatment techniques that could address these problems.

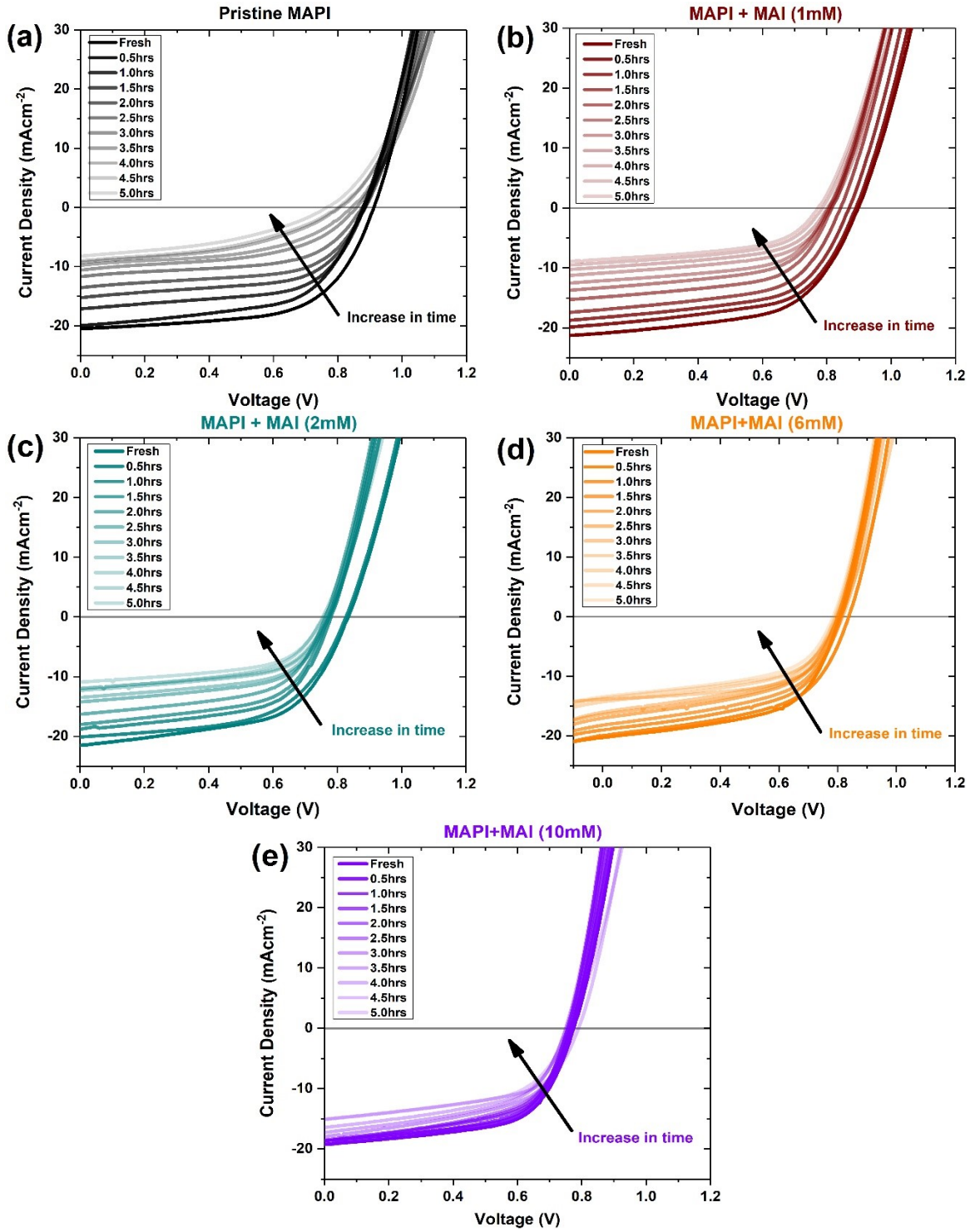


Figure 5-7: Current-voltage curves obtained during degradation for $CH_3NH_3PbI_3$ (MAPI) devices without and with methylammonium iodide (MAI) treatment in varies concentrations of: 1mM, 2mM, 6mM and 10mM. All devices are fabricated in FTO/compact-TiO_2/mesoporous-TiO_2/perovskite (iodide salt)/Spiro-OMeTAD/Au architecture and were under continuous illumination for a period of five hours.

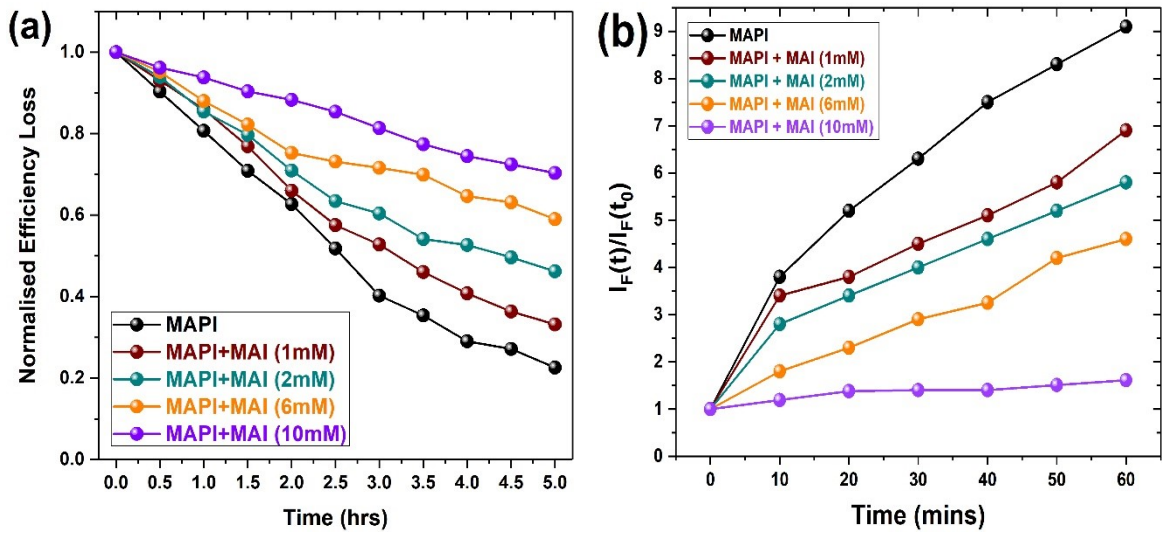


Figure 5-8: **(a)** Short term stability test (normalised efficiency loss) for the same devices with and without methylammonium iodide (MAI) salt coating in various concentration of 1 mM (dark red), 2.0 mM (dark cyan), 6 mM (orange), 20 mM (violet) and for a period of 5 hours. **(b)** Superoxide yield plot comparing the generation of superoxide for MAPI treated with different concentrations and without methylammonium iodide (MAI) salt coating. The normalised fluorescence intensity increase of the HE probe at 610 nm (excitation at 520 nm). $I_F(t)$ is the fluorescence maximum at time t, whilst $I_F(t_0)$ is the background fluorescence intensity. $I_F(t)/ I_F(t_0)$ ratio corresponds to yield of superoxide generation for perovskite films.

Next, the effect of iodide salt passivation on device stability was investigated. To do so, the same batch of devices were used, and their J-V curves measured under continuous illumination for 5 hours. The J-V scan for each individual solar cell is shown in Figure 5-7. It is shown that more MAI concentration leads to more convergence of the J-V curves, which implies more device stability. Moreover, this enhanced stability is directly related to the concentration of MAI salt that is treated on top of the MAPI photoactive layer. Higher concentrations of MAI salt leads to more-stable devices under the oxygen and light condition. To obtain further insight into how device stability under oxygen and light is related to superoxide formation device efficiency was normalized for loss for solar cells with and without iodide coating within the testing period and a comparison made with superoxide probing test, as shown in Figure 5-8. The result reveals explicitly that MAI could effectively passivate crystal defects, reduce superoxide yields and enhance film and device stability.

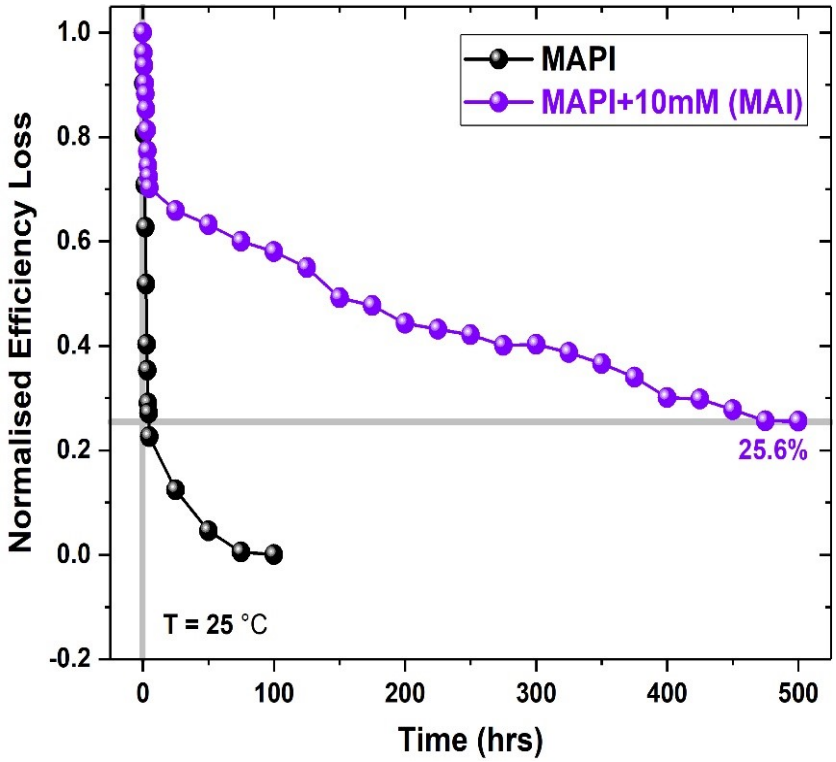


Figure 5-9: Long-term stability test (normalised efficiency loss) for devices employing $CH_3NH_3PbI_3$ (MAPI) without (black) and with (violet) MAI salt coating in 10 mM salt coating for a period of 500 hours. The temperature was kept constant at 25°C.

Finally, the effect of MAI coating on long-term solar cell stability was considered. As noted, MAPI without MAI coating (black) and with 10 mM of MAI coating (violet) are selected and measured under continuous light for 500 hours. Interestingly, a device without salt coating underwent rapid degradation in the first few hours, and then the degradation became less severe until it was fully degraded in 100 hours. In contrast, with MAI coating, the device revealed much longer stability within the testing period, so that after 500 hours there was still 25.6% of the efficiency remaining. This further confirmed that MAI salt is effective in promoting device stability. In addition, this result provides further evidence on our earlier discussion that on a timescale of several days, oxygen starts to diffuse into the bulk side of the crystal lattice, leading to a phase change from photo-absorbing perovskite into non-absorbing lead iodide. The diffusion can be much slower due to the shorter O_2 diffusion length, thereby less superoxide formation and a lower device degradation rate are observed in the longer term. In using MAI salt coating, there will be some iodide salt penetration into the bulk side of the crystal lattice and filling of the iodide vacancies. In this case, even fewer iodide vacancies can be occupied by O_2 molecules, so that the yield of superoxide generation was greatly reduced, leading to even more stable solar cells than non-coated devices.

5.4.2. MAI Treatment in Bromine (Br)-Substituted Perovskite Solar Cells (PSCs)

$CH_3NH_3PbI_3$ (MAPI) under a combination of light and oxygen could form reactive superoxide species (O_2^-), which in turn react with photo-excited MAPI and result in degradation of the perovskite crystal structure. The photo- and oxygen-generated superoxide is facilitated by iodide vacancies/defects present in the perovskite crystal lattice. An effective technique was developed using methylammonium iodide (MAI) and it was found that this treatment could effectively reduce the yield of superoxide, leading to an improvement of the device stability. Recent publications indicate that anion substitution (bromide for iodide) to create a mixed anion perovskite system has shown much longer stability and high device performance. [19-22] Particularly, reports have shown that the mixed halide system $CH_3NH_3Pb(I_{1-x}Br_x)_3$ reveals enhanced stability under ambient conditions and improved tolerance to moisture when bromide composition is increased.[19, 23] Moreover, recent research on degradation induced from oxygen and light illumination in mixed bromide/iodide perovskite suggests that stability is improved as bromide composition is increased. However, the origin of this is not yet clear.

In this section, the research extends into the mixed halide system $CH_3NH_3Pb(I_{1-x}Br_x)_3$ ($MAPb(I_{1-x}Br_x)_3$) with the main objective of understanding the origin of the enhanced stability of these materials. We propose that the mechanisms behind the enhanced stability of $MAPbBr_3$ under light and oxygen may be due to three main factors: (1) Oxygen diffusion into the perovskite layer; (2) thermodynamics of the degradation reaction; and (3) iodide vacancies inside the crystal lattice. This section describes these three factors in detail. In particular, attention is paid to determine the optimum Br content that leads to the best combination of device efficiency and solar cell stability as well as a study of the variation of photovoltaic parameters upon increasing Br composition. The section also continues to explore the role of defect passivation using methylamonium iodide (MAI) salt treatment on obtaining mixed halide (Br-I) perovskite solar cells with greater stability, the optimum iodide salt concentration suitable for mixed halide perovskite solar cells is also examined.

Impact of Oxygen Diffusion on Superoxide Yields

To understand how oxygen diffusion into perovskite films may be affected by bromide replacement, first Isothermal Gravimetric Analysis (IGA) experiments were carried out, in which samples were prepared and sealed under inert conditions, and then the weight increases were probed as a function of time under oxygen inside the chamber.[11] Herein, a series of perovskite films with bromide composition range from x = 0.0 to 1.0 (in $MAPb(I_{1-x}Br_x)_3$) was measured and data is shown in Table 5-2.

Table 5-2: Normalised weight increase for the selected film compositions, as a function of exposure to dry air flux against time.

$MAPb(I_{1-x}Br_x)_3$	Normalised weight t=180s	% Increase
x = 0	1.0165	1.65
x = 0.2	1.0147	1.47
x = 0.5	1.0106	1.06
x = 0.75	1.0083	0.83
x = 1	1.0002	0.02

The table shows that the % increase in oxygen is reduced when adding more bromide, which leads to less oxygen stored in the film. Thisresult could in part account for the decrease in superoxide formation and more perovskite film stability for higher Br content, as shown in Figure 5-10. Figure 5-10 (a) shows that there is a direct correlation between superoxide formation and Br content: increased bromide reduces the photo-induced superoxide generation, which implies greater film stability. More evidence can be obtained from UV-Vis absorption spectroscopy presented in Figure 5-10 (b). It shows that the degradation process occurs as long as iodide is present in the perovskite system. However, as the bromide content increases, the time taken for the perovskite film to degrade becomes longer. The pristine MAPI without bromide (x = 0 in $MAPb(I_{1-x}Br_x)_3$) completely degrades in 100 hours, whilst at x = 0.5, complete degradation takes over 400 hours. In contrast, when no iodide is present in the system, there is almost no degradation within the experimental period. The observation emphasizes that enhanced film stability can be achieved via bromide substitution, and this has important application for solar cell studies.

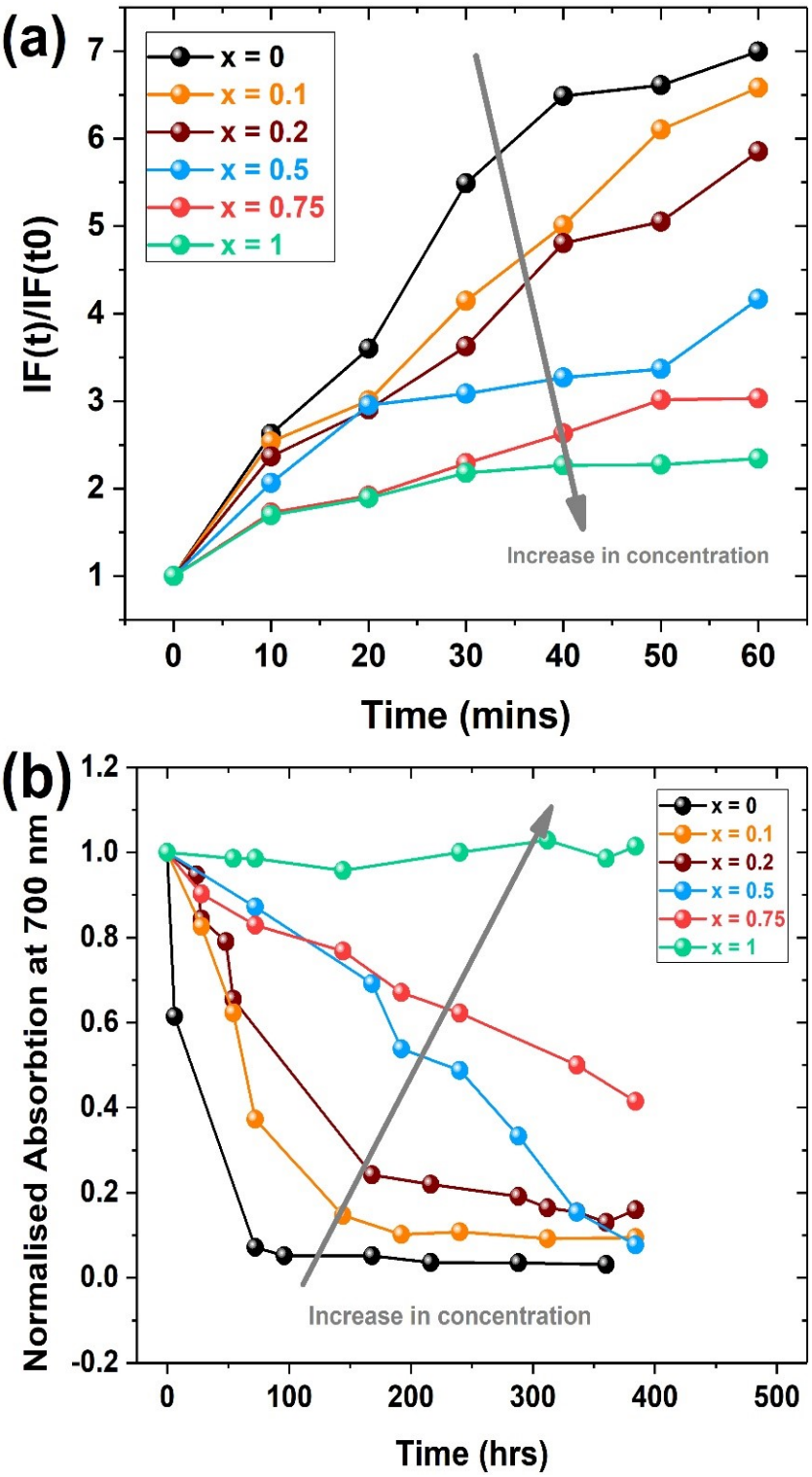


Figure 5-10: (a) Superoxide yield generation for the films under oxygen and light conditions for $MAPb(I_{1-x}Br_x)_3$ where x = 0, 0.1, 0.2, 0.5, 0.75 and 1. Superoxide yields increase as the Iodide content increases. (b) Normalised absorbance decays as a function of aging under oxygen and light conditions for $MAPb(I_{1-x}Br_x)_3$ where x = 0, 0.1, 0.2, 0.5, 0.75 and 1. Films become more stable as the bromine content increases.

Thermodynamic Analysis of the Degradation Process via Bromide Replacement

To understand how mixed halide perovskite degradation is influenced by bromide substitution, collaborators from Bath University carried out *ab-initio* simulations and calculated reaction energy with respect to different bromide content, as shown in Figure 5-11.

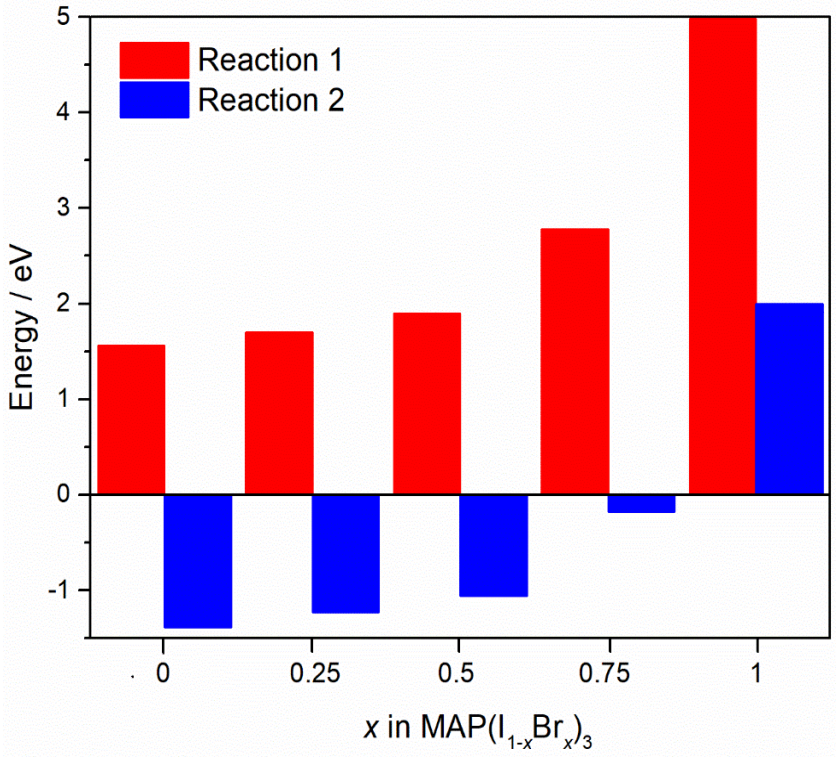


Figure 5-11: Calculated reaction energies for the degradation reactions with respect to the different bromide compositions in $CH_3NH_3Pb(I_{1-x}Br_x)_3$ system. (See Equations 5 and 6 in the text). (unpublished manuscript)

Briefly, when only oxygen is present, the degradation leads to formation of water and lead halide, as shown in Equation (5).

$$\mathbf{4CH_3NH_3PbX_3 + O_2 \rightarrow 4PbX_2 + 2X_2 + 2H_2O + 4CH_3NH_2} \qquad \mathbf{(5)}$$

For $CH_3NH_3PbI_3$ the calculated formation energy through *ab-inito* simulation is + 1.56 eV and is positive, which indicates that degradation reaction without light is not favoured. This is consistent with the observation from previous work.[11] On the other hand, the formation energy for $CH_3NH_3PbBr_3$ (i.e. when x = 1.0 in $MAPb(I_{1-x}Br_x)_3$) is + 4.98 eV, which is even higher than $CH_3NH_3PbI_3$. This means that the energetics for the degradation of this material is even more unfavourable, implying more material stability.

Thus, for the reaction to proceed light is also required. Under light illumination, photo-excited electrons generated within perovskite and oxygen act as electron scavengers to absorb these photo-excited electrons. Next, oxygen will be reduced to superoxide species (O_2^-) and react with the photo-oxidized perovskite according to Equation (6):

$$\mathbf{4CH_3NH_3PbX_3^* + O_2^- \rightarrow 4PbX_2 + 2X_2 + 2H_2O + 4CH_3NH_2} \qquad \mathbf{(6)}$$

In this case, for $CH_3NH_3PbI_3$ the formation energy is -1.56 eV and is negative, the reaction could proceed, and perovskite degradation occurs. In contrast, the value for $CH_3NH_3PbBr_3$ is + 2.00 eV and reaction is still energetically unfavourable. The result is consistent with Figure 5-10 (a) that in $CH_3NH_3PbBr_3$ (x= 1.0 in $MAPb(I_{1-x}Br_x)_3$), almost no superoxide is formed, implying no degradation. Moreover, the energy for mixed-anions shows that even at x = 0.75, the equation (6) is still energetically favourable as the energy is -0.18 eV, which confirmed that more stable perovskite films can be obtained by increasing Br content, as further evidenced in Figure 5-10 (b).

Iodide Vacancies and Crystal Structure Variation upon Br Replacement

The third factor for $CH_3NH_3PbBr_3$ to be more stable than $CH_3NH_3PbI_3$ is a decrease of iodide vacancies upon bromide substitution. This is due to a change in hydrogen-bonding (H-bond) between methylammonium cation and anion. The bromide ion is smaller than iodide and replacing iodide with bromide causes shrinkage of cell volume, leading to shorter H-bond distances between NH_3 group and Br ions, as clearly shown in Figure 5-12. This results in stronger H-bonding and Pb-Br bonding in $CH_3NH_3PbBr_3$ crystal with greater stability.

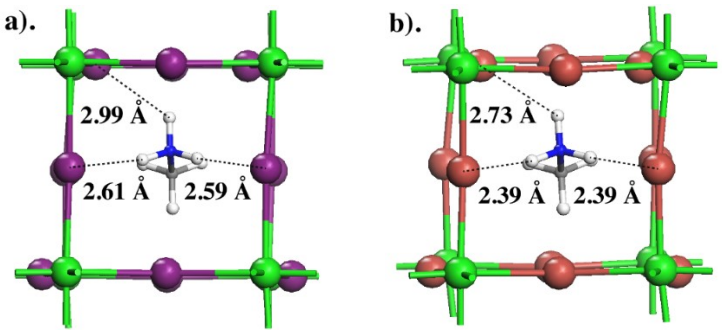


Figure 5-12: H-bonding between H_N and X in a) $CH_3NH_3PbI_3$ and b) $CH_3NH_3PbBr_3$. (The violet ball represent iodide ions and the red ball represents smaller bromide ions). (unpublished manuscript)

Device Performance and Stability as a Function of Bromide Content

Device performance of $MAPb(I_{1-x}Br_x)_3$ as a function of bromide substitution was considered. Devices with x = 0, 0.2, 0.5, 0.75 and 1.0 were fabricated with a structure of FTO/c-TiO_2/mp-TiO_2/$MAPb(I_{1-x}Br_x)_3$/Spiro-OMeTAD/Au. All devices were fabricated with the same procedure mentioned in the previous section. The current-voltage curves and photovoltaic parameters are shown in Figure 5-13 and Table 5-3.

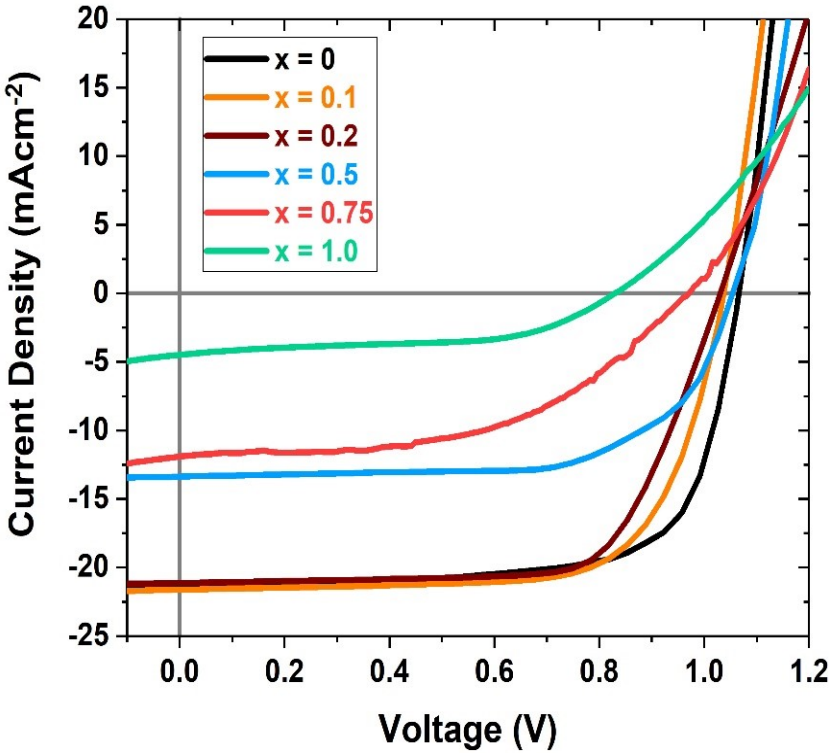


Figure 5-13: Current-voltage curves for $MAPb(I_{1-x}Br_x)_3$ devices with composition between x = 0 to x = 1.

Table 5-3: Photovoltaic parameters of same devices in the composition of x = 0, 0.1, 0.2, 0.5, 0.75, 1.0 in $MAPb(I_{1-x}Br_x)_3$. (Open circuit voltage: V_{oc}; short circuit current density: J_{sc}; Fill Factor: FF; Power Conversion Efficiency: PCE)

Device Type	Pixel Area (cm^2)	V_{oc}(V)	J_{sc} ($mAcm^{-2}$)	FF	PCE (%)
x = 0	0.12	1.07	21.51	0.70	16.14
x = 0.1	0.12	1.04	21.63	0.71	15.85
x = 0.2	0.12	1.03	21.14	0.70	15.26
x = 0.5	0.12	1.05	13.37	0.66	9.32
x = 0.75	0.12	0.91	11.90	0.51	5.94
x = 1.0	0.12	0.83	4.49	0.54	2.02

It can be seen from the above results that as bromide increases, the overall device Power Conversion Efficiency (PCE) decreases. This is consistent with the previous result from UV-Vis absorbance spectra that the increase in bromide content reduces optical properties, in which the band edge experiences a blue-shift and there is less absorption at higher wavelengths, implying less-efficient solar cells.[19] Moreover, as Br increases from 0% to 20% (x =0 to x = 0.2 in $MAPb(I_{1-x}Br_x)_3$), the device efficiency drops from 16.14 % to 15.26 %, almost unchanged to its initial efficiency. It is worth noting that the MAPI device efficiency in this study is higher than the result from **Chapter 4**. This is mainly due to the optimization on fabricating perovskite layer, the spin coating process changed from five steps to one step, resulted in better film quality. However, a further increase in Br content leads to a dramatic decrease in photovoltaic parameters and device performance. When x = 0.5, the device efficiency reduces to 9.32 %, mainly due to a large decrease in J_{sc}. When x = 0.75, the device colour changes from dark brown to red, and device performance further drops to 5.94 %. In the case of complete Br substitution (x = 1.0), the device efficiency drops down to 2.02 %. The result reveals that to achieve satisfactory solar cell performance for mixed halide system; there is an efficiency maximum based on the amount of Br substitution. Devices below x = 0.2 have much higher PCE than those with greater Br composition.

The effect of bromide substitution on the stability of the devices can be measured using the current-voltage curves of the above devices under continuous light illumination for a period of five hours. The normalised device efficiency loss as a function of illumination time is illustrated in Figure 5-14. It is obvious that all devices experience degradation within experiment time, the degree of which depends directly on the Br content. Specifically, at x = 0, which means no Br substitution, the device degraded to ~15 % of its original efficiency in five hours. The degradation becomes less severe when x = 0.1, which indicates that Br substitution could effectively improve solar cell stability. Further increase in Br composition to x = 0.2 leads to significant improvement in device stability; there is still ~64 % of its initial efficiency remaining after five hours. It is worth noting that when x > 0.2, although there is still an enhancement in device stability, the trends become less significant as compared with x < 0.2. In contrast, when x = 0.5, 0.75 and 1.0, the efficiency of the devices is much lower than the performance from x = 0, 0.1 and 0.2. This slight improvement in stability becomes less favourable for solar cell application. Based on the above results, it can be concluded that the best combination of the efficiency and stability for Br-I mixed halide perovskite devices is obtained when x = 0.2. Interestingly, this observation is in agreement with previous work

done by Jong et al., in which they combined computational work and chemical bonding analysis and suggested that the best match between device efficiency and stability can be obtained at $x = 0.2$ in the Br-I mixed halide system.[24]

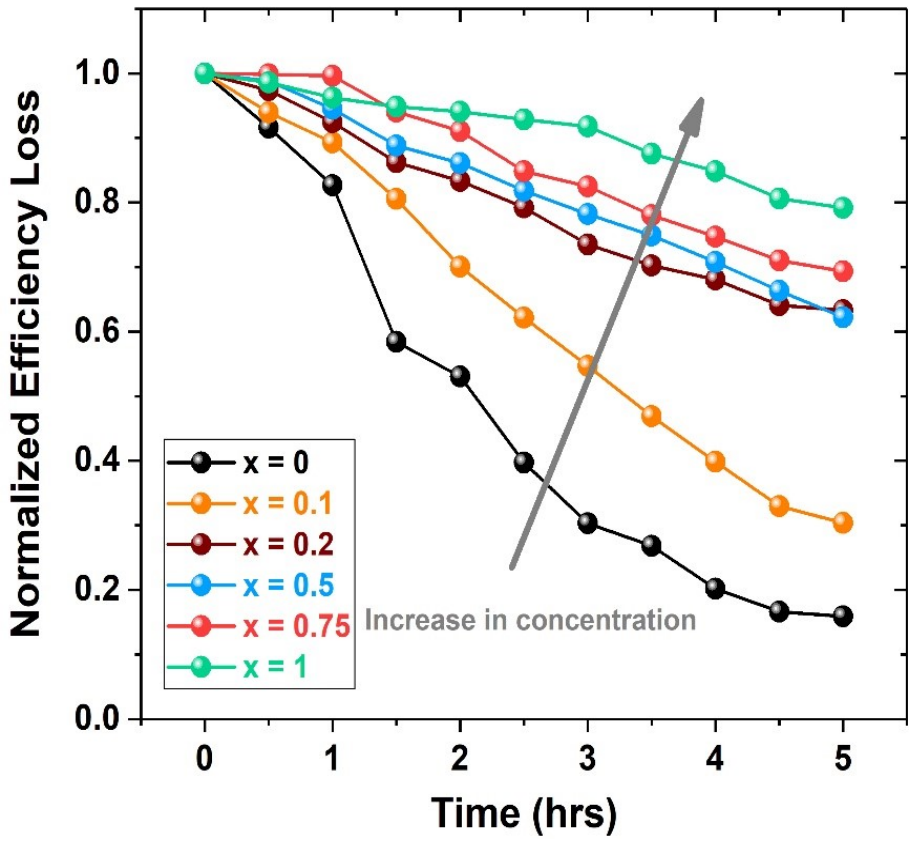


Figure 5-14: Normalised efficiency loss for devices with bromide composition of between $x = 0$ to $x = 1.0$ in $MAPb(I_{1-x}Br_x)_3$ under continuous solar simulator illumination.

Furthermore, the stability result is also in good agreement with the superoxide and UV-Vis measurements (Figure 5-10) that more Br content leads to less superoxide formation and therefore more film and device stability. This further emphasizes the key role of superoxide species on the degradation reaction under the oxygen and light condition. Although partial replacement of I by Br leads to more stable devices and the optimum Br content for best combinations of device and stability is decided, the degradation still occurs and the stability is not great enough. To further improve the device stability a newly developed iodide salt treatment technique was developed.

Iodide Treatment on Mixed Halide Device Efficiency and Stability

The stability of $CH_3NH_3Pb(I_{1-x}Br_x)_3$ perovskite solar cells can be increased by substitution of more iodide by bromide, and $x = 0.2$ gives the best combination of efficiency and operational stability. Nevertheless, there is still space to improve the stability of the devices even at $x = 0.2$, concerning the effect of Methylammonium Iodide (MAI) salt treatment on mixed halide perovskite devices to further improve device stability.

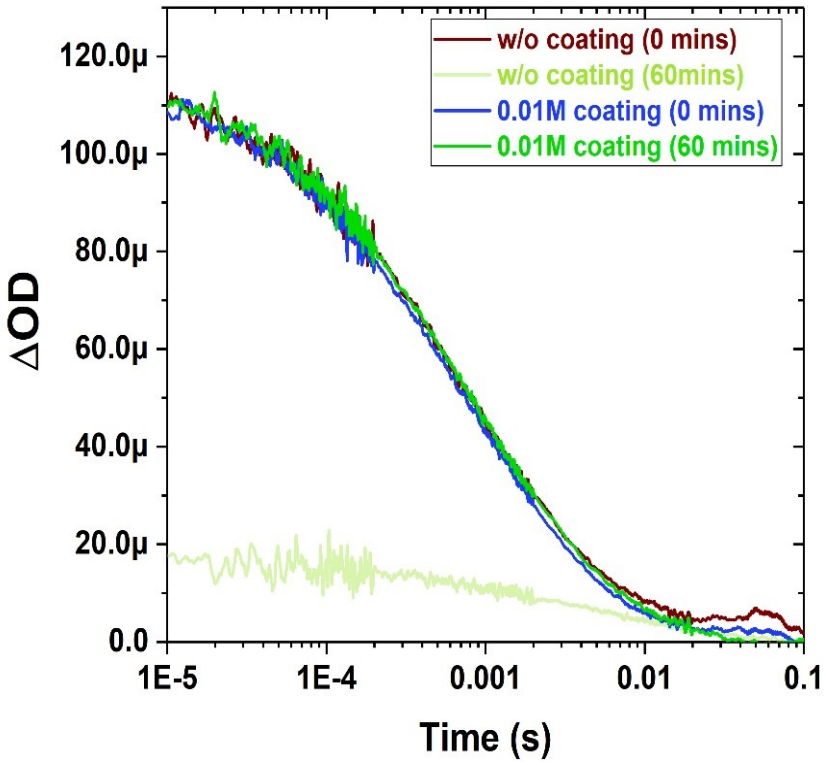


Figure 5-15: Transient absorption spectra traces for $x = 0.2$ in $MAPb(I_{1-x}Br_x)_3$ film composition, with and without a 0.01M salt treatment after 0 and 60 minutes of exposure to oxygen and light illumination.

To gain first insight into the role of bromide substitution and the impact of film passivation with MAI salt treatment, the effect of MAI salt on the yield of charge separation was studied. In this experiment, mixed halide perovskite samples with $x = 0.2$ were produced, and the films were coated with 10 mM MAI salt solutions and characterized using Transient Absorption Spectroscopy (TAS), the result is shown in Figure 5-15. It reveals the variation of the amplitude of ΔOD (optical density) as a function of time for the 20 % bromine composition ($x = 0.2$) , with and without MAI salt coating before and after 60 minutes of exposure to light illumination and dry air flux. It is observed that decay traces follow the recombination between the electrons in the TiO_2 electron transport layer and holes on the

Spiro-OMeTAD hole conductor. Moreover, this result clearly shows that the untreated film undergoes degradation, where the initial amplitude of the ΔOD signal decreases dramatically after 60 minutes of exposure to oxygen and light. As a comparison, almost no drop in the initial amplitude of the ΔOD signal is shown in the film with 10 mM of MAI treatment. It is obvious from this experiment that MAI salt treatment could passivate the Br-I mixed halide films and slow down their degradation upon light and oxygen stress.

To evaluate the iodide passivation effect on the efficiency and stability of mixed halide perovskite solar cells using MAI salts as passivating agents, a mixed halide perovskite solar cell was fabricated consisting 10 % and 20 % of bromide content (corresponding to x = 0.1 and 0.2 in $MAPb(I_{1-x}Br_x)_3$) and treated with MAI salts in a varied concentration of 1 mM, 5 mM and 10 mM. x = 0.1 and 0.2 were chosen for further investigation since these two Br compositions lead to significant stability improvement with very little loss in device efficiency. The Power Conversion Efficiency (PCE) of these devices was measured as a function of exposure to a combination of light and oxygen and the External Quantum Efficiency (EQE) spectra for selected devices were measured simultaneously to cross-check the measurement from current-voltage characterization, all PCE and EQE results along with a summary of device parameters are shown in Figure 5-16. It can be seen from Figure 5-16 (a) and (c) that for both x = 0.1 and x = 0.2 in $MAPb(I_{1-x}Br_x)_3$, the incorporation of MAI salt leads to a decrease in all parameters and a drop in overall solar cell performance. In particular, in contrast with devices with no iodide coating, in 1 mM of MAI coating, the efficiency of the solar cell at x = 0.1 drops slightly from 15.85 % to 15.79 %. Similarly, for x = 0.2, the device efficiency for 1 mM MAI coating is 14.53 % as compared with 15.26 % of the non-coated device. However, for both 10% and 20% Br content, the addition of more concentrated MAI salt treatment resulted in a dramatic decrease in the values of V_{oc}, J_{sc} and FF, leading to much lower cell efficiency. At 10 mM of MAI concentration, the V_{oc}, J_{sc} and FF are 1.00 V, 19.66 $mAcm^{-2}$, 0.60, and 11.73 % for 10 % Br, whilst for 20 % Br those values are 1.00 V, 19.22 $mAcm^{-2}$, 0.61, and 11.64 %. Both are lower than without coating.

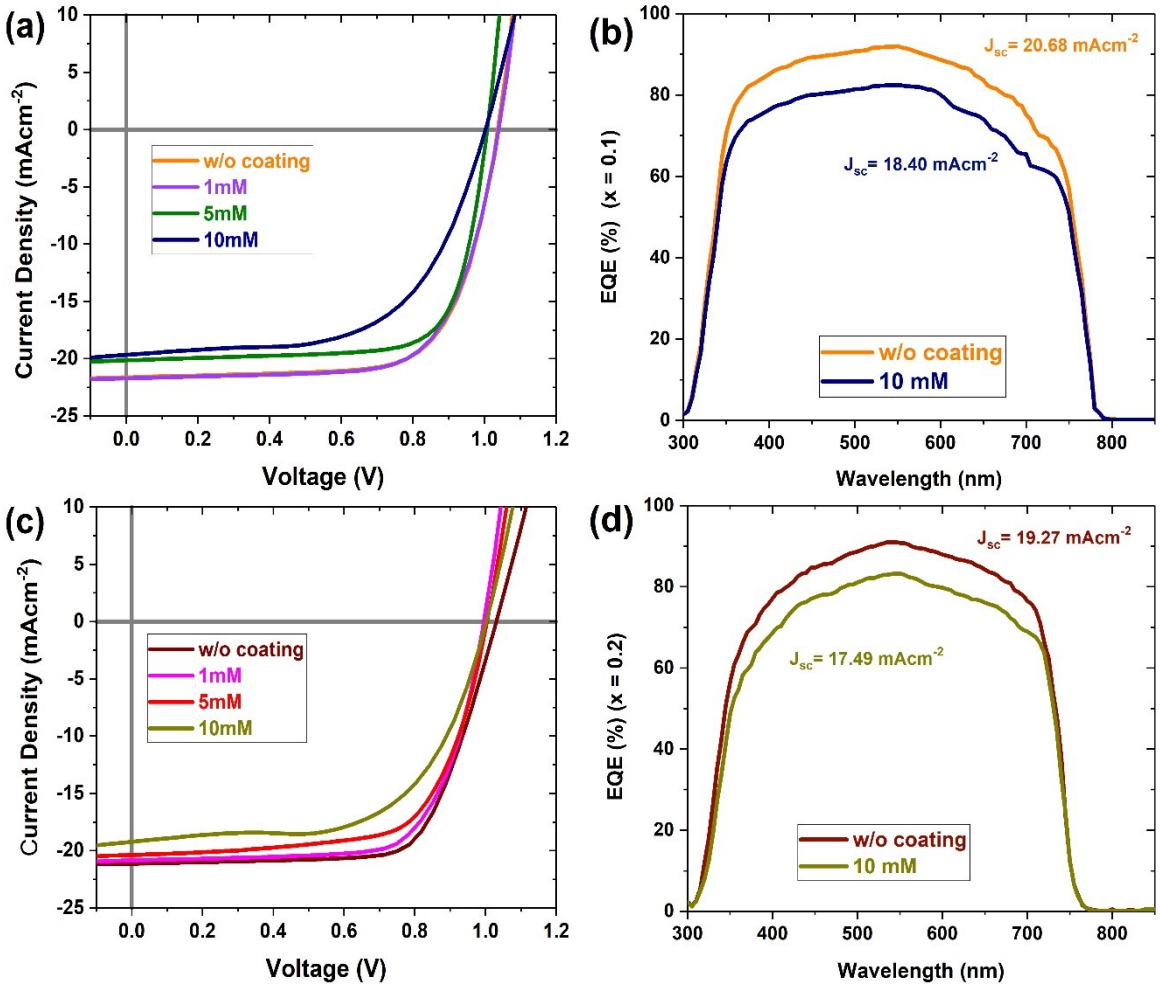


Figure 5-16: **(a)** Current-voltage curves of $MAPb(I_{1-x}Br_x)_3$ (x=0.1) perovskite devices with different concentrations of MAI coating; **(b)** EQE spectra of same devices without MAI and with 10 mM of MAI coating at x = 0.1; **(c)** Current-voltage curves of $MAPb(I_{1-x}Br_x)_3$ (x=0.2) perovskite devices with different concentrations of MAI coating; **(d)** EQE spectra of the same devices without MAI and with 10 mM of MAI coating at x = 0.2. (Open circuit voltage: V_{oc}; short circuit current density: J_{sc}; Fill Factor: FF; External Quantum Efficiency: EQE.)

Table 5-4: Photovoltaic parameters for devices based on $MAPb(I_{1-x}Br_x)_3$ perovskite films in the composition of x = 0.1 and 0.2 without and with different MAI salt concentrations. (Open circuit voltage: V_{oc}; short circuit current density: J_{sc}; Fill Factor: FF; Power Conversion Efficiency: PCE.)

Device Type	MAI concentration	Pixel Area (cm^2)	V_{oc}(V)	J_{sc} ($mAcm^{-2}$)	FF	PCE (%)
x = 0.1	0	0.12	1.04	21.63	0.71	15.85
	1mM	0.12	1.04	21.70	0.70	15.79
	5mM	0.12	1.01	20.13	0.74	15.08
	10mM	0.12	1.00	19.66	0.60	11.73
x = 0.2	0	0.12	1.03	21.14	0.70	15.26
	1mM	0.12	1.00	20.85	0.70	14.53
	5mM	0.12	1.00	20.38	0.67	13.70
	10mM	0.12	1.00	19.22	0.61	11.64

Based on these observations, it is therefore suggested that the presence of MAI as the passivating agent at all tested concentrations suppressed the device performance with respect to non-treated devices. The External Quantum Efficiency (EQE) spectra in Figure 5-16 (b) and (d) further proved results from J-V characterizations, in which addition of MAI salt displays narrower and lower EQEs from 300 to 850 nm, relative to those without MAI treatment for both 10% and 20% Br content. This indicated a lower charge carrier transportation efficiency in MAI coated solar cells as compared with non-coated ones. Moreover, at 20% Br content, the wavelength at which EQE starts to drop is ~ 700 nm, which is lower than the value for 10% Br. This blue-shift of the EQE spectra is consistent with observations from UV-Vis spectroscopy, and is related to the increases of the bromide content reducing the optical properties and is consistent with our J-V results in Figure 5-13. Besides, the integrated Jsc obtained from EQE spectras in (b) and (d) reaches values of 20.68 $mAcm^{-2}$ and 18.40 $mAcm^{-2}$ for uncoated and coated mixed halide perovskite at $x = 0.1$. When $x = 0.2$, these values are 19.27 $mAcm^{-2}$ for uncoated solar cell and 17.49 $mAcm^{-2}$ for coated one. All results are within 10 % of deviation from J-V measurement; this further confirmed that accuracy of the PCE.

Finally, the iodide salt passivation impact on the stability of the Br-I mixed halide perovskite solar cells is considered. As discussed earlier in this chapter, the photo and oxygen-induced degradation of the perovskite films and devices proceeds at a different timescale depending on the rate of oxygen diffusion. The perovskite devices can degrade within a few hours, whereas for films the complete degradation can be extended to a few days or weeks. Based on this mechanism, we examined device stability in two timescales, in which the short run lasts for five hours, and the long run lasts for 500 hours in the same condition.

The short-run stability was first evaluated for Br-I mixed halide perovskite devices under different concentrations of MAI coating. The normalised PCE as a function of illumination time for both $x = 0.1$ and $x = 0.2$, which corresponds to 10% and 20 % bromide content respectively, are demonstrated in Figure 5-17. It can be found that under both bromide contents, the mixed halide solar cells can be stabilized via MAI coating. For instance, at $x = 0.1$ without iodide coating, the mixed halide perovskite solar cells retains ~ 31% of its initial performance after five hours illumination, this is higher than pristine MAPI devices as previously reported but still quite rapid in terms of degradation. In using the MAI coating, devices become more stable. More importantly, mixed halide device stability is directly

correlated with the concentration of the MAI salt. Devices treated with more concentrated MAI salt resulted in greater stability under light and oxygen, which can be seen clearly in tested bromide contents. It can be argued that in the short run, oxygen diffusion occurs predominantly at the surface of the crystal lattice and generates superoxide from the sites of iodide vacancies. The MAI salt could effectively fill in the iodide vacancies to inhibit superoxide formation, thereby slowing down the degradation process and improving device stability. It worth noting that although greater concentration of MAI salt could potentially passivate more iodide vacancies in the crystal lattice and effectively reduce the superoxide yields, the fact that vacancies/defects are not uniformly distributed at the surface means that there might be areas where MAI salt is too much so that material agglomerated into clusters on top of the perovskite, this constrains efficiency of charge transport and could be one reason that reduction in device efficiency is observed upon MAI salt coating. However, the trend achieved from this is in good agreement with the finding that MAI salt treatment could reduce iodide vacancies, lowering the superoxide formation and producing films and devices with greater stability.

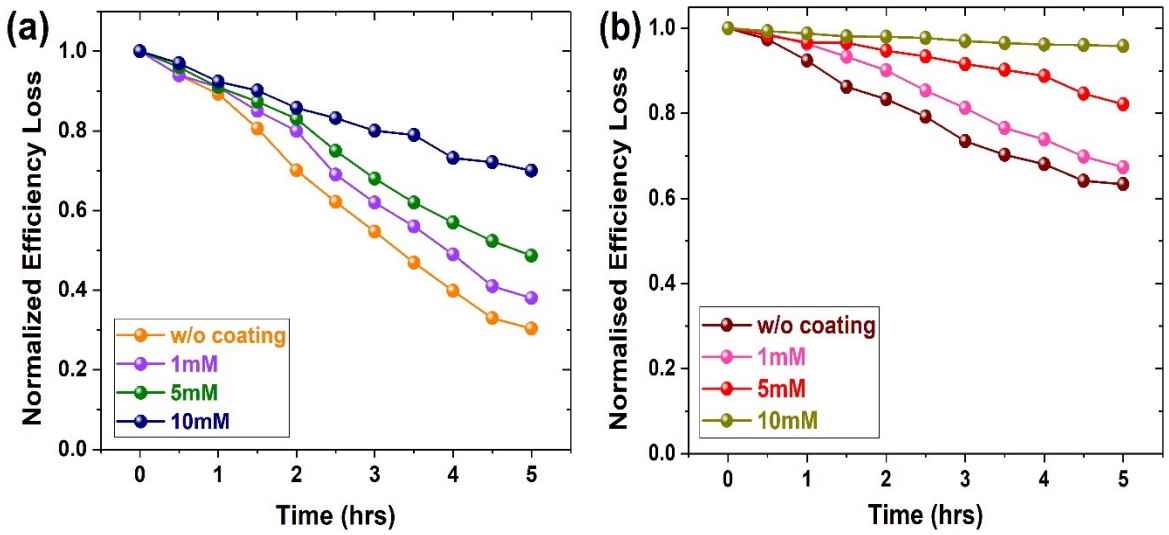


Figure 5-17: **(a)** short-term stability (normalised efficiency loss) for Br-I mixed halide perovskite devices with different concentrations of MAI salt coating at $x = 0.1$. **(b)** Short term stability (normalised efficiency loss) for Br-I mixed halide perovskite devices with different concentrations of MAI salt coating at $x = 0.2$.

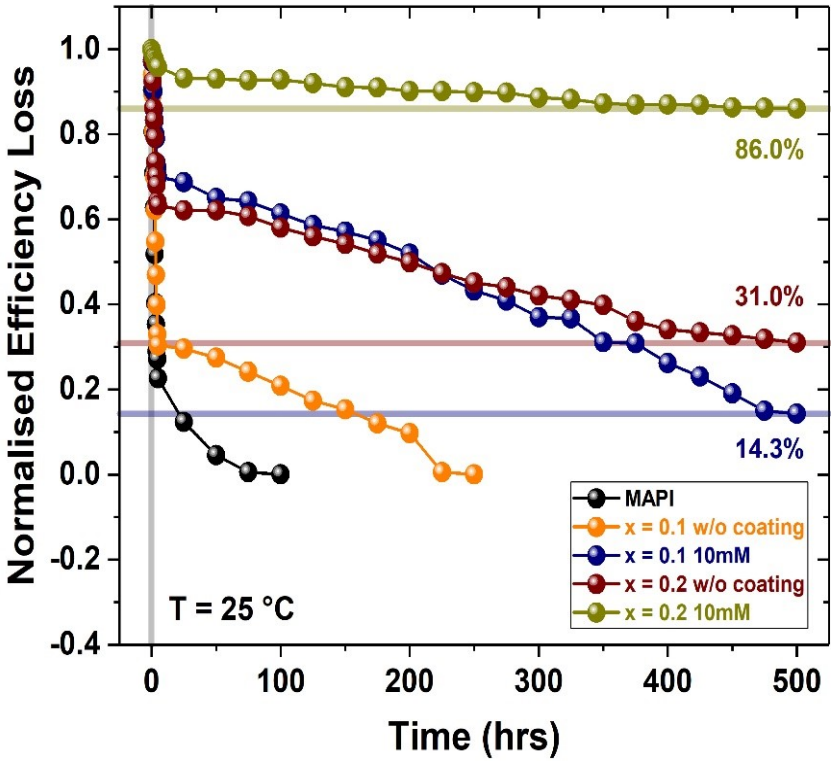


Figure 5-18: Long-term stability test (normalised efficiency loss) for devices employing only MAPI (black); Br-I mixed halide perovskite devices without (orange) and with 10 mM of methylammonium iodide (MAI) (navy) salt coating at x = 0.1; and Br-I mixed halide perovskite devices without (dark red) and with 10 mM MAI salt coating (orange) at x = 0.2. All devices are tested under illumination for 500 hours.

The influence of MAI salt coating for long-term stability of perovskite solar cells with bromide substitution is then considered. To do this, the selected solar cells were measured in a prolonged period under continuous light illumination and obtained results are shown as Figure 5-18. It shows that pristine MAPI devices undergo complete degradation within 100 hours, Br content devices without MAI treatment are relatively more stable, with complete degradation occuring after 250 hours for x = 0.1 and 14.3 % efficiency remaining for x = 0.2. In contrast, mixed halide perovskite devices treated with MAI coating demonstrate a prolonged lifetime in the longer term. Specifically, at x = 0.2, a device with 10 mM MAI salt treatment achieved a remarkable result that after 500 hours of continuous illumination there was still 86% efficiency remaining. Moreover, Figure 5-18 shows that in the long run, the device degradation process is less rapid than in the short run. This is consistent with the hypothesis that at this timescale, oxygen starts to diffuse into the interior of the particles, whereas device performance and photovoltaic parameters are more dependent on iodide vacancies from the surface. Therefore, less rapid device degradation is observed in the long run.

5.5. Conclusion

In this chapter, the strategy of MAI salt coating for the efficiency and stability of the MAPbI and Br-I mixed halide perovskite solar cells were tested. Thin-film passivation with MAI iodide salts leads to reduced superoxide formation and enhanced film and device stability for pristine MAPbI solar cells, albeit at the expense of device efficiency. The amount of MAI salt plays an important role on the film quality and device stability. However, it appears to be unhelpful on relieving the hysteresis effect and should be utilized within an appropriate concentration. For Br-I mixed halide perovskite system, the degradation can be also attributed to the superoxide formation from the oxygen diffusion into the perovskite layers. Substitution of I with Br resulted in a considerable improvement in the film and device stability due to a reduction of iodide vacancies inside crystal structure upon Br replacement that create stronger H-bonding, but lower efficiency due to unfavourable optical properties. The presence of MAI passivating agent improves stability for Br-I mixed halide devices, but suppressed device performance. It is found that $x = 0.2$ in MAPb $(I_{1-x}Br_x)_3$ with 10 mM of MAI treatment shows the best combination of device efficiency and stability. The overall combined results improved our fundamental understanding of the degradation phenomena in perovskite solar cells, and provide an effective strategy for greatly improving the long-term stability. The limitation of MAI salt on device efficiency motivated us to investigate alternative passivating agents, the in-depth study of which is introduced in **Chapter 6**.

5.6. References

[1] C. Eames, J.M. Frost, P.R. Barnes, B.C. O'Regan, A. Walsh, M.S. Islam, *Nature Communications* **2015**, *6,* 7497.

[2] J.M. Azpiroz, E. Mosconi, J. Bisquert, F. De Angelis, *Energy & Environmental Science* **2015**, *8,* 2118.

[3] W. Zhang, V.M. Burlakov, D.J. Graham, T. Leijtens, A. Osherov, V. Bulović, H.J. Snaith, D.S. Ginger, S.D. Stranks, *Nature Communications* **2016**, *7,* 11683.

[4] G. Richardson, S.E. O'Kane, R.G. Niemann, T.A. Peltola, J.M. Foster, P.J. Cameron, A.B. Walker, *Energy & Environmental Science* **2016**, *9,* 1476.

[5] T.Y. Yang, G. Gregori, N. Pellet, M. Grätzel, J. Maier, *Angewandte Chemie* **2015**, *127,* 8016.

[6] A. Walsh, D.O. Scanlon, S. Chen, X. Gong, S.H. Wei, *Angewandte Chemie International Edition* **2015**, *54,* 1791.

[7] H. Yuan, E. Debroye, K. Janssen, H. Naiki, C. Steuwe, G. Lu, M.l. Moris, E. Orgiu, H. Uji-i, F. De Schryver, *The Journal of Physical Chemistry Letters* **2016**, *7,* 561.

[8] N. Aristidou, I. Sanchez-Molina, T. Chotchuangchutchaval, M. Brown, L. Martinez, T. Rath, S.A. Haque, *Angewandte Chemie* **2015**, *127,* 8326.

[9] D. Bryant, N. Aristidou, S. Pont, I. Sanchez-Molina, T. Chotchuangchutchaval, S. Wheeler, J.R. Durrant, S.A. Haque, *Energy & Environmental Science* **2016**, *9,* 1850.

[10] F.T. O'Mahony, Y.H. Lee, C. Jellett, S. Dmitrov, D.T. Bryant, J.R. Durrant, B.C. O'Regan, M. Graetzel, M.K. Nazeeruddin, S.A. Haque, *Journal of Materials Chemistry A* **2015**, *3,* 7219.

[11] N. Aristidou, C. Eames, I. Sanchez-Molina, X. Bu, J. Kosco, M.S. Islam, S.A. Haque, *Nature Communications* **2017**, *8,* 15218.

[12] M. Grätzel, *nature* **2001**, *414,* 338.

[13] A. Calloni, A. Abate, G. Bussetti, G. Berti, R. Yivlialin, F. Ciccacci, L. Duo, *The Journal of Physical Chemistry C* **2015**, *119,* 21329.

[14] H.-S. Kim,N.-G. Park, *The Journal of Physical Chemistry Letters* **2014**, *5,* 2927.

[15] H.J. Snaith, A. Abate, J.M. Ball, G.E. Eperon, T. Leijtens, N.K. Noel, S.D. Stranks, J.T.-W. Wang, K. Wojciechowski, W. Zhang, *The Journal of Physical Chemistry Letters* **2014**, *5,* 1511.

[16] E. Unger, E. Hoke, C. Bailie, W. Nguyen, A. Bowring, T. Heumüller, M. Christoforo, M. McGehee, *Energy & Environmental Science* **2014**, *7,* 3690.

[17] W. Tress, N. Marinova, T. Moehl, S.M. Zakeeruddin, M.K. Nazeeruddin, M. Grätzel, *Energy & Environmental Science* **2015**, *8,* 995.

[18] J. Wei, Y. Zhao, H. Li, G. Li, J. Pan, D. Xu, Q. Zhao, D. Yu, *The Journal of Physical Chemistry Letters* **2014**, *5,* 3937.

[19] S. Pont, D. Bryant, C.-T. Lin, N. Aristidou, S. Wheeler, X. Ma, R. Godin, S.A. Haque, J.R. Durrant, *Journal of Materials Chemistry A* **2017**, *5,* 9553.

[20] P. Fedeli, F. Gazza, D. Calestani, P. Ferro, T. Besagni, A. Zappettini, G. Calestani, E. Marchi, P. Ceroni, R. Mosca, *The Journal of Physical Chemistry C* **2015**, *119,* 21304.

[21] M. Ledinský, P. Löper, B. Niesen, J. Holovský, S.-J. Moon, J.-H. Yum, S. De Wolf, A. Fejfar, C. Ballif, *The Journal of Physical Chemistry Letters* **2015**, *6,* 401.

[22] T. Yin, Y. Fang, X. Fan, B. Zhang, J.-L. Kuo, T.J. White, G.M. Chow, J. Yan, Z.X. Shen, *Chemistry of Materials* **2017**, *29,* 5974.

[23] J.H. Noh, S.H. Im, J.H. Heo, T.N. Mandal, S.I. Seok, *Nano letters* **2013**, *13,* 1764.

[24] U.-G. Jong, C.-J. Yu, J.-S. Ri, N.-H. Kim, G.-C. Ri, *Physical Review B* **2016**, *94,* 125139.

CHAPTER 6

Phenylethylammonium Iodide as a Surface Passivation Agent for Enhanced Efficiency and Stability of $CH_3NH_3PbI_3$ Perovskite Films and Solar Cells

6.1. Abstract

Organic-inorganic halide perovskite materials have emerged as useful alternatives to conventional solar cells, but device stability remains a concern. Recent research has demonstrated that the formation of superoxide species under exposure of the perovskite to light and oxygen leads to the degradation of $CH_3NH_3PbI_3$ (MAPI) perovskites. In particular, it has been revealed that iodide vacancies in the perovskite structure are key sites in facilitating superoxide formation. In Chapter 5, the methylammonium iodide (MAI) salt coating has shown to be effective on reducing the superoxide formation, thus improve photoactive layer and device stability. However, this is achieved on the premise of sacrificing device efficiency. Recent studies have shown that iodide salt with bulkier organic cations could lead to better film quality and stability. Inspired by this, in Chapter 6, the passivation of MAPI films with an alternative iodide salt, namely phenylethylammonium iodide ($PhEtNH_3I$, PEAI) is introduced. The PEAI coating can significantly enhance film and device stability under light and oxygen stress, without compromising power conversion efficiency. These observations are consistent with the iodide salt treatment reducing iodide vacancies and therefore lowering the yield of superoxide formation and improving stability. The present study elucidates a pathway to the future design and optimisation of perovskite solar cells with greater stability.

6.2. Introduction

Over the past few years, methylammonium lead halide perovskite (e.g. $MAPbX_3$, i.e. $CH_3NH_3PbX_3$, where X is I-Br) materials have garnered a significant amount of interest as the archetypal material for perovskite devices due to their distinctive optoelectronic properties, such as a high extinction coefficient, [1] excellent charge carrier mobility and lifetimes,[2] long charge diffusion length,[3] and solution processability at low temperature.[4] Ever since Miyasaka *et al.* developed the first perovskite solar cells (PSCs) in 2009 with a power conversion efficiency (PCE) of 3.8%,[5] the performance of PSCs has increased at an unprecedented rate, with the highest certified PCE currently at 23.7 %.[6] This startling rise in device efficiency, as well as low fabrication costs and aesthetic versatility[7] have projected PSCs to be a promising commercial technology for the solar cell industry.[8] As an emerging technology, research in the perovskite field is currently focused on overcoming several obstacles before commercialization is feasible. Likewise, the identification of large-scale production methods, the improvement of long-term stability, the development of flexible solar cells and non-toxic devices are the key objectives currently under scientific investigation.[9, 10]

Whilst device efficiencies continue to increase rapidly, the stability of perovskite solar cells (PSCs) remains a serious barrier to commercialization. As of today, studies have shown that a group of external conditions such as water/moisture, oxygen ingress, elevated temperature, structural transformations, ultra-violet light exposure and sealing techniques all cause degradation of the perovskite photoactive layer and result in unstable devices.[11-20] This, in turn, has led to the development of various strategies to enhance film and solar cell stability. These strategies include: modification of the crystal with caesium ions[21]; replacing organic groups with larger cations such as formamidinium cations[22]; partially replacing iodide with bromide to obtain mixed-halide perovskites; encapsulating devices with hydrophobic polymer layers;[23-25] introducing chromium oxide-chromium (Cr_2O_3/Cr) interlayers to prevent metal contacts from reacting with the perovskite layer;[26] fabricating solar cells with all-solution-processed metal oxide charge transport layers;[27] and applying surface passivation to $CH_3NH_3PbI_3$ (MAPI) layers with oleic acid.[28] A recent study also reveals that $Zn_{0.8}Cd_{0.2}S$ nanoparticles (ZCS) doped in (6,6)-phenyl-C61-butyric acid methyl ester (PCBM) could improve electron transport within the electron transporting layer (ETL) and

effectively suppress interfacial charge recombination, enhancing material and device stability.[29] Among these, interface passivation is one of the most widely used techniques to improve the efficiency and stability of the perovskite solar cells.[30]

The word "passivation" refers to a process that results in a material that is less affected by external conditions. For perovskite solar cells, it generally includes "chemical passivation", which reduces the surface defects trap states to optimize charge carrier transport through different interfaces;[31, 32] or "physical passivation", which prevents sensitive functional layers from exposure to external environment to avoid solar cell degradation.[33] In general, PSCs contains 6 major interfaces, they are (a) transparent conductive substrate/electron transport layer (ETL) ("/" means interface); (b) interface of ETL/perovskite; (c) interface between the perovskite grain boundaries (GBs); (d) interface of perovskite/hole transporting layer (HTL); (e) interface of HTL/electrode and (f) interface between electrode materials and atmospheric condition.[33] In this project, attention will be paid particularly to the perovskite active layer and its adjacent interfaces. As for the grain boundary (GB) passivation, Supasai et al. first reported that PbI_2 can be used as a GB passivating agent for perovskite solar cells.[34] This was followed by many articles on elucidating possible mechanisms of delivering PbI_2 into the grain boundary of the perovskite layer and it was observed that PbI_2 can be either self-formed or by thermal or vapour treatment.[35-38] Furthermore, researchers also found that organic fullerenes such as PCBM and its derivatives can also be used to passivate both grain boundaries within the perovskite and the perovskite/HTLs interface, resulting in higher device efficiency, lower hysteresis and longer solar cell stability.[39-41] However, despite many studies and achievements, the choices of effective passivation agents are still limited. Moreover, the knowledge on how to introduce them into the perovskite system, as well as the mechanisms and influence of these passivators on grain boundaries and interfaces on enhancing solar cell stability are under dispute and requires further investigation.[41]

Previous research has shown that the combination of light and oxygen is known to cause degradation of perovskite films and solar cells.[42] This degradation is caused by the formation of superoxide (O_2^-) upon exposure of the MAPI photoactive layer to a combination of light and oxygen.[43-45] More importantly, we demonstrated that iodide vacancies (V_I) present within the MAPI crystal lattice are the most energetically favourable defect site to facilitate superoxide formation from atmospheric O_2.[46] These observations suggest that inhibiting superoxide formation at iodide vacancies in MAPI films could enhance material

lifetime and device stability. As such, preliminary studies of thin-film passivation with Methylammonium Iodide (MAI) revealed an improvement in device stability but at the expense of efficiency.[46] As such, it is essential to identify alternative passivating agents that can enhance both stability and efficiency.

In this chapter, the use of phenylethylammonium iodide ($PhEtNH_3I$ or PEAI) as a passivating agent is explored. Interestingly, such iodide salts carrying bulky cations, namely phenyl ethylammonium (PEA^+), have also recently been applied to form 2D/3D hybrid structured perovskites.[47] These lowered dimensional perovskites have shown to exhibit better stability than the purely 3D analogues.[47, 48] However, the origin of this enhanced stability is not fully understood. Moreover, the effect of light and oxygen on perovskites comprising PEA cations has not yet been explored. Nevertheless, these findings indicate that PEAI may be suitable for use as a passivating agent. Herein, we show that an alternative iodide salt, namely PEAI, as a passivating material can lead to improved device stability whilst maintaining a good power conversion efficiency (PCE). Specifically, within a certain concentration, ($\leq$10 mM) PEAI passivation effectively fills the voids and pin-holes, resulting in an improved film morphology. Also observed is a longer photoluminescence lifetime in the perovskite material, which is indicative of effective passivation of surface defect trap-states; this being consistent with a reduction in iodide vacancies. The mitigation of trap-mediated recombination is further evidenced by Transient Absorption Spectroscopy (TAS) measurements, which show that in PEAI-treated films there is a greater yield of hole-transfer to the Spiro-OMeTAD hole-conductor as compared with both the pristine MAPI and methylammonium iodide (MAI) salt coated MAPI layers. Crucially, the passivation of MAPI films with PEAI leads to a significant decrease in production of superoxide - a species that is known to cause the breakdown of perovskite films.[43, 46] The present observations suggest that PEAI salt passivation is an effective procedure to improve the operational stability and efficiency of PSCs.

6.3. Experimental

Materials & Synthesis: All chemicals were used as received, including methylammonium MAI (99.9%, Dyesol), lead (II) iodide (99%, Sigma-Aldrich), titania nanoparticles (18NR-T, Dyesol) and Spiro-OMeTAD (≥ 99.5%, Lumtec). The phenylethylammonium (PEAI) iodide salt was synthesised according to the previously described process.[46] The phenylethylamine 33% wt solution in ethanol (6.2 mL, 0.046 mol) was cooled down in an ice bath. Hydroiodic acid 55% wt solution in water (10 mL, 0.073 mol) was then added dropwise with vigorous stirring. The reaction was stirred at 0 °C until a white-yellowish solid was precipitated from the solution. Ethanol (5 mL) was added to ensure full precipitation of the solid. Recrystallization of the product in diethyl ether several times can afford the pure compound as white crystalline solid.

Film Fabrication: All films were deposited onto clean glass substrates of *c*. 10 mm × 10 mm in size. Substrates were cleaned sequentially in water, acetone and isopropyl alcohol (IPA) under sonication for 10 minutes during each washing cycle. The Laurell Technologies WS-650MZ-23NPP spin coater was used to fabricate the films. A 1.25 M solution of MAPI was formed by adding PbI_2 in a 1:1 molar ratio with methylammonium iodide (MAI) in a solvent mixture of 7:3 γ-butyrolactone (GBL) to dimethyl sulfoxide (DMSO). The solution was then spin-coated onto the substrates using a one-step spin program of 4000 rpm for 30 seconds under a nitrogen atmosphere inside a glove box. In the meantime, the substrate was treated with diethyl ether (~500 μL) drop-casting. The films were then annealed at 100°C for 15 minutes.

Iodide Salt Coatings: A 0.01 M iodide salt solution was prepared by dissolving the salt (phenylethylammonium iodide and MAI) in a 1:4 solvent mixture of isopropyl alcohol (IPA) and chlorobenzene (CB). A 100-μL aliquot of this solution was then dripped onto the perovskite films with a 20-second loading time before spinning at 4000 rpm.

Device Fabrication: Fluorine doped titanium oxide (FTO) coated glass substrates (TEC15, Pilkington) were first etched with Zn powder and aqueous hydrochloric acid (37%) followed by cleaning sequentially in distilled water, acetone and IPA. The compact TiO_2 blocking layer was made by preparing a precursor solution containing 0.5 mL titanium isopropoxide

(Aldrich), 35μL hydrochloric acid (37%) and 5 mL anhydrous ethanol. A 150 μL aliquot of these solutions was deposited on the substrate and spin-coated at 5000 rpm for 30 seconds, and then annealed at 500 °C for 45 minutes. The mesoporous TiO_2 layer was prepared by diluting the titania paste (18NR-T, Dyesol) with ethanol (2:7 mass ratio) and was deposited on the blocking layer. The layer was then dried on a hotplate at 80 °C for 10 minutes and subsequently sintered at 500 °C for 45 minutes. The perovskite layer MAPI was prepared using a one-step spinning program, the same as that mentioned in the film fabrication. In instances where the iodine salt layer was used, 2.5 mM, 5 mM, 10 mM and 20 mM solutions of phenylethylammonium iodide (PEAI) with IPA were prepared respectively. The solution was then spin coated onto the perovskite layer. The Spiro-OMeTAD hole-conductor layer was spin coated on top in a solution of 72.3 mg/mL 2,2',7,7'-tetrakis-(N,N-di-p-methoxyphenylamine) 9,9'-spirobifluorene (Spiro-OMeTAD) powder in 1 mL anhydrous chlorobenzene. The Spiro-OMeTAD solution contained additives including 17.5-μL lithium bis(trifluoromethane) sulfonimide lithium salt (Li-TFSl) and 28.8 μL 4-tert-butylpyridine (tBP). Finally, a 100 nm thick gold contact was evaporated under vacuum (~10^{-6} Torr at a rate of 0.2 nm/s) with an active pixel area of 0.12 cm^2.

Current-Voltage (JV) Measurements: The J-V characteristics were measured using an AM1.5 solar simulator (Oriel Instruments) and a Keithley 2400 source meter. Calibration was performed with a silicon photodiode prior to measurement. The scans were performed at a rate of 0.125 V/s for both the forward scan (from J_{sc}, short circuit current density, to V_{oc}, open circuit voltage) and backward scan (in the opposite direction). During the stability measurements, a slow scan rate (0.005 V/s) was used in an attempt to minimize hysteresis effects encountered during the J-V scan. Cells were placed unmasked under continuous 1 sun illumination during ageing and were masked during each scan to ensure the active area (0.12 cm^2) was the same for all measuring devices.

Superoxide Measurements: A stock 31.7 μM solution of the hydroethidine (HE) probe was prepared by dissolving 10 mg HE in 10 mL of dry toluene; sonication was used to facilitate miscibility. Films were then immersed into 10 mL of 0.317 μM solution created from the stock solution. Photoluminescence spectra were recorded using the excitation wavelength of 520 nm and slit widths of 10 mm on a Horiba Jobin-Yvon Fluorolog-3 spectrofluorometer.

Ageing Conditions: Films were sealed in a controlled environment, where dry air was gassed through for the duration of the degradation and illumination was provided by a tungsten lamp equipped with a UV-blocking filter as previously reported.[42]

Spectroscopy: UV-Vis was performed on a Lambda 25 UV-Vis spectrophotometer from PerkinElmer. X-ray diffraction patterns were measured on a high-resolution diffractometer (PANalytical X'Pert PRO MRD) using Ni-filtered Cu K_α radiation at 40 kV and 40 mA. Scanning Electron Microscope (SEM) measurements were carried out on an LEO 1525 Field Emission Scanning Electron Microscope (FEGSEM) operated at 10 kV using an in-lens detector. Time-Correlated Single-Photon Counting (TCSPC) measurements were performed with a Horiba Deltaflex modular fluorescence lifetime system that incorporates a PPD-900 detector. Sample excitation was achieved with a 635nm LED (Horiba N-635L) at an intensity of 18 pJ/pulse and a rate of 1MHz. The half-life of the prompt pulse was 100 ps. Samples used in microsecond transient absorption spectroscopy experiments were taken from a nitrogen-filled glovebox in a sealed quarts cuvette and excited with a dye laser (Photon Technology International Inc. GL-301) with pump threshold fluence~15 μJcm^{-2} and frequency 4Hz. An N_2 laser (Photon Technology International Inc. GL-3300) was used to pump the dye laser. The transient changes in the absorption of the sample were captured with a 100 W tungsten lamp (Bentham IL1) on an orthogonal optical axis to the excitation beam. The probe wavelength was adjusted by a monochromator. A silicon photodiode (Hamamatsu Photonics, S1722-01) was used to detect the probing beam, and the signal was then filtered and amplified (Costronics Electronics). Finally, the signal was displayed by a digital oscilloscope (Tektronix DPO3012).

6.4. Results and Discussion

The impact of using PEAI salt as a passivating material on perovskite films was analysed first. To determine the optimum amount of PEAI needed, a range of concentrations of this material on top of the MAPI film was used, and a comparative study with the uncoated MAPI film made. In this study, films were fabricated on top of clean glass substrates as described in the experimental methods section and the perovskite surface passivation procedure with iodide salts is shown in Figure 6-1.

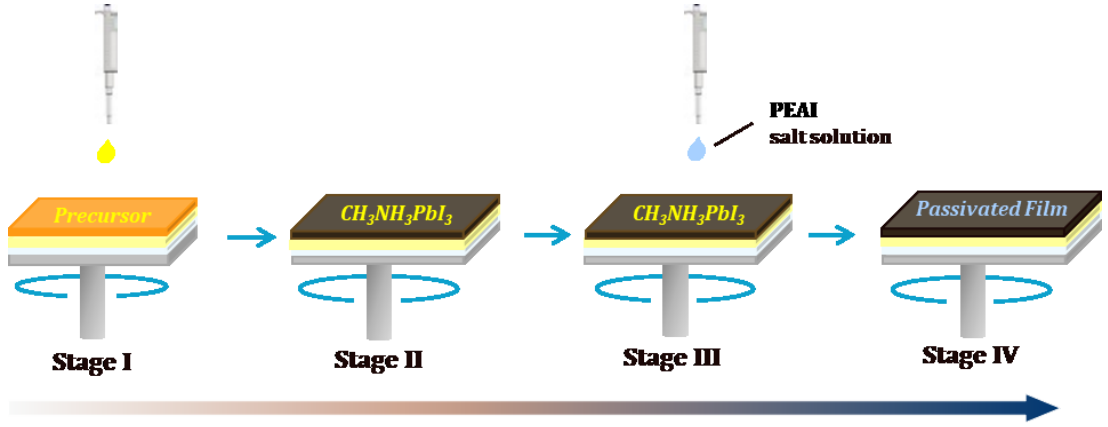


Figure 6-1: Schemes of PEAI iodide salt passivation method for perovskite solar cells with $CH_3NH_3PbI_3$ (MAPI) as an active layer.

This now raises the question of whether, through perovskite engineering, it would be possible to slow the oxygen-induced degradation of the MAPI layer while retaining its favourable optoelectronic properties. Passivating the surface of MAPI by introducing a solution of a salt with a bulkier organic cation could conceivably fulfil these requirements. We hypothesized that the PEAI coating layers might potentially stabilize the MAPI in two distinct ways, as illustrated in Figure 6-2. The solution-processed MAPI layer contains $CH_3NH_3^+$ (MA^+) and I^- vacancies at grain boundaries, which are exposed to the film surface, as shown in Figure 6-2 (a). These defects in the crystal lattice are areas of high surface free energy that are most susceptible to being attacked by superoxide species when exposed to air.[13] Therefore, excess mobile ions (PEA^+ and I^-) from PEAI coating solution could potentially fill in both types of vacancy to passivate the film, shown as (b). Besides, the fact that PEA^+ is a bulkier cation than MA^+ means that it could potentially fill the defects better than the MAI salt coating, which was used previously and mentioned in **Chapter 4**. Alternatively, the MA^+ and I^- ions on the MAPI surface could be displaced by the ions from the coating layer solution. This

would result in the MAPI core being augmented with a thin shell of alternative perovskite. A shell employing a superoxide resistant PEA^+ cation with a bulky alkyl group could potentially afford excellent stability to the MAPI film without affecting its electronic or optical properties by generating an oxygen diffusion barrier (shown as a brown shell in Figure 6-2 (c)) that could reduce the superoxide O_2^- formation. Therefore, it is important to investigate whether or not the PEAI is effective in passivating the perovskite layer to improve the long-term stability of the film and devices.

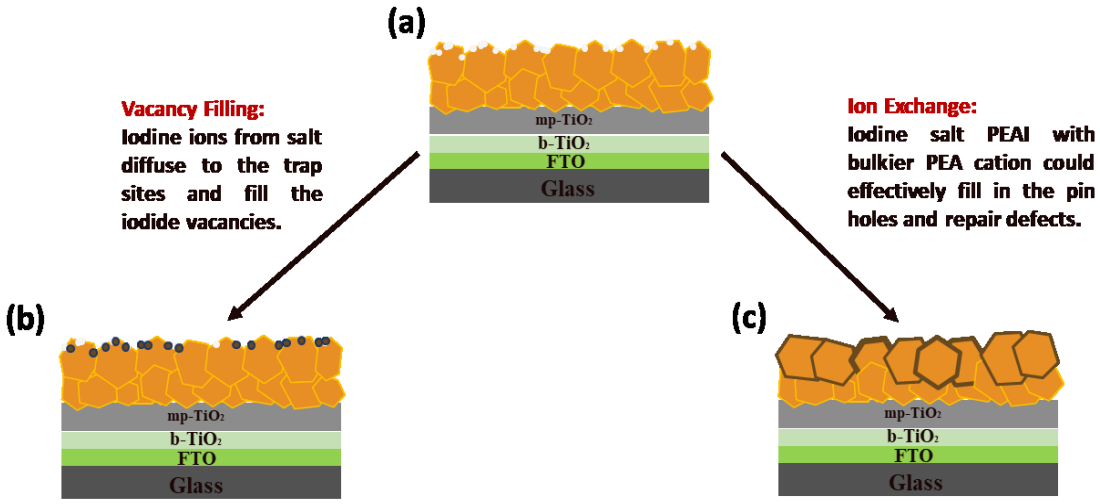


Figure 6-2: Illustration of two possible modes of direct iodine salt coating of PEAI salt solution on top of $CH_3NH_3PbI_3$ (MAPI) layers. **(a)** Cross section of the multicrystalline MAPI layer with $CH_3NH_3^+$ (MA^+) and I^- vacancies (surface defects shown as white semicircles). The excess ions such as PEA^+ and I^- present in the PEAI coating layers could potentially fill the surface lattice vacancies (shown as brown circles) to passivate the film shown as **(b)**. Alternatively, the excess ions could displace surface PEA^+ and/or I^- through ion exchange to generate a composite perovskite with a MAPI core being coated inside a stabilized perovskite outer layer incorporating the alternating PEA^+ cation as shown in **(c)**.

The impact of using PEAI salt as a passivating material on perovskite films was analysed first. To determine the optimum amount of PEAI needed, we used a range of concentrations of this material on top of the $CH_3NH_3PbI_3$ film and made a comparative study with the uncoated $CH_3NH_3PbI_3$ film. Following sample fabrication, X-ray Diffraction (XRD) was used to probe the crystalline nature and structure of the films, as shown in Figure 6-3. The key diffraction peaks at 14.2°, 28.5° and 43.3° correspond to the (110), (220) and (330) lattice orientations of orthorhombic halide perovskite respectively.[49] This result shows that when the concentration of PEAI salt is less than or equal to 10 mM, the passivated films exhibit a pure crystal structure akin to that for the pristine perovskite, which crystallizes in the expected orthorhombic $Pan2_1$ space group.[49] Furthermore, the peak intensity of the perovskite films

passivated with a low concentration of PEAI (≤ 10 mM) did not change in comparison to the unpassivated perovskite film, implying that the PEAI salt passivation does not damage the film or modify its structure. Increasing the PEAI concentration to 20 mM resulted in a decrease in intensity of the major peaks. Moreover, in the 20 mM coated sample, the diffraction peak at 28.5° splits, which is likely due to a reduction of phase symmetry.

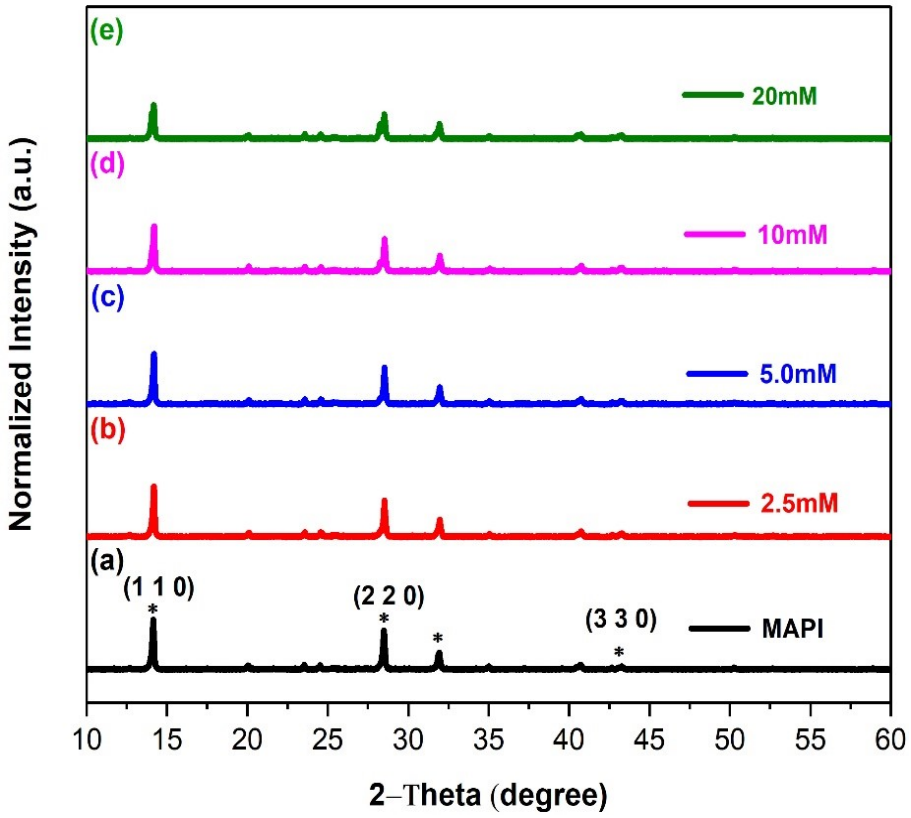


Figure 6-3: X-ray diffraction spectra of the **(a)** non-passivated perovskite film and phenylethylammonium iodide ($PhEtNH_3I$, PEAI) salt passivated perovskite films with various iodide salt concentrations of **(b)** 2.5 mM, **(c)** 5.0 mM, **(d)** 10 mM and **(e)** 20 mM.

Next, a top-view Scanning Electron Microscopy (SEM) analysis was conducted to inspect the morphology of the MAPI films with and without PEAI passivation. Figure 6-4 (a), shows that without PEAI passivation, there are voids and pinholes (marked as yellow circles) within the perovskite film. However, (b) and (c) show that the addition of PEAI salt (≤ 10 mM) can effectively tackle these morphological imperfections. On the other hand, (d) reveals that when the PEAI concentration increases to 20 mM, the salt begins to aggregate into clusters (shown as bright areas) at the perovskite surface, which is consistent with the observation from XRD analysis and is likely to have a negative impact on the optoelectronic properties of the device.

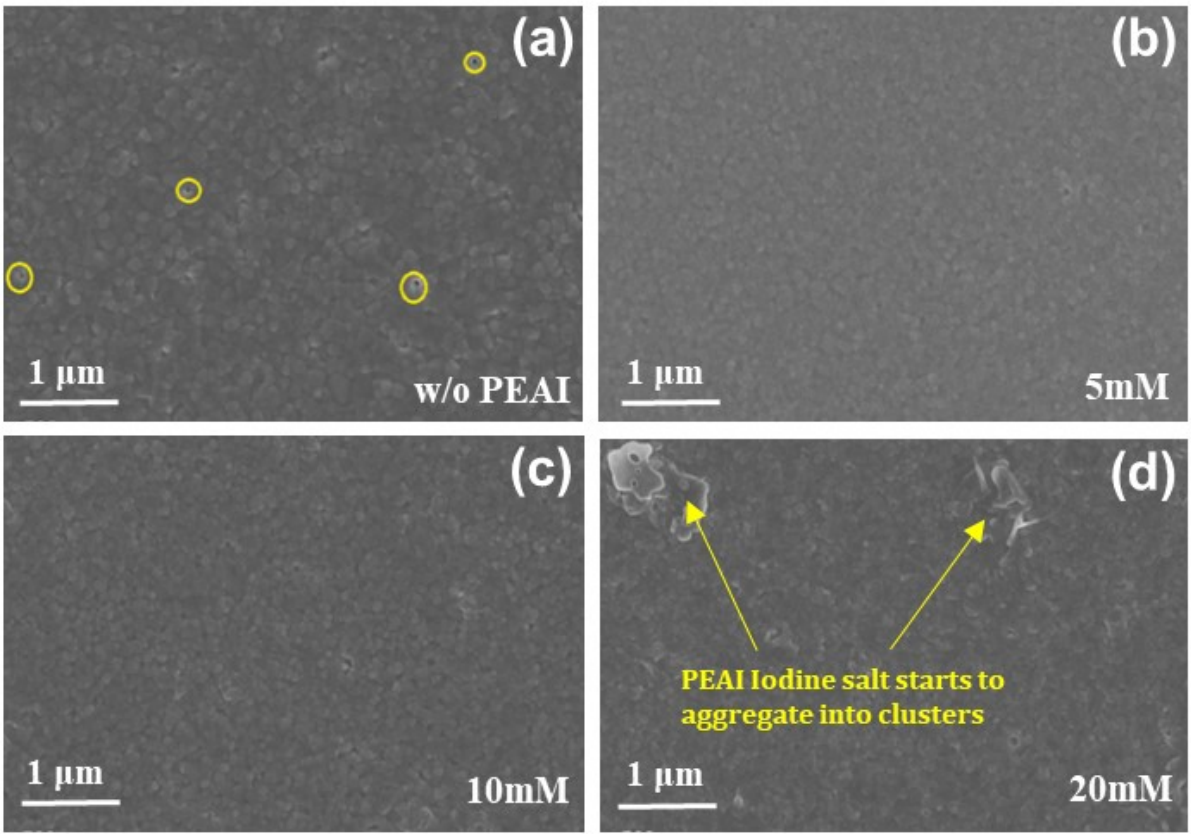


Figure 6-4: Top-view SEM images of the non-passivated MAPI perovskite film **(a)** and phenylethylammonium iodide ($PhEtNH_3I$, PEAI) salt passivated perovskite films with different iodide salt concentrations of **(b)** 5 mM, **(c)** 10 mM and **(d)** 20 mM.

The optical properties of the perovskite films before and after passivation by PEAI were studied by examining the impact of the PEAI salt on the absorption spectrum of the perovskite film using UV-Vis absorption spectroscopy. Figure 6-5 presents the steady-state absorption spectrum of MAPI before and after coating the film with different concentrations of PEAI. It is clear from Figure 6-5 (a) that for concentrations up to 10 mM, the PEAI passivated films show almost identical absorption characteristics relative to the uncoated reference. On the other hand, as the iodide salt concentration increases to 20 mM, the absorption peaks at both ~480 nm and ~750 nm are notably lower in intensity, as shown more explicitly in the inset in Figure 6-5. It is apparently that beyond optimum concentration, the PEAI salt appears to be detrimental to the absorption of the photoactive layer.

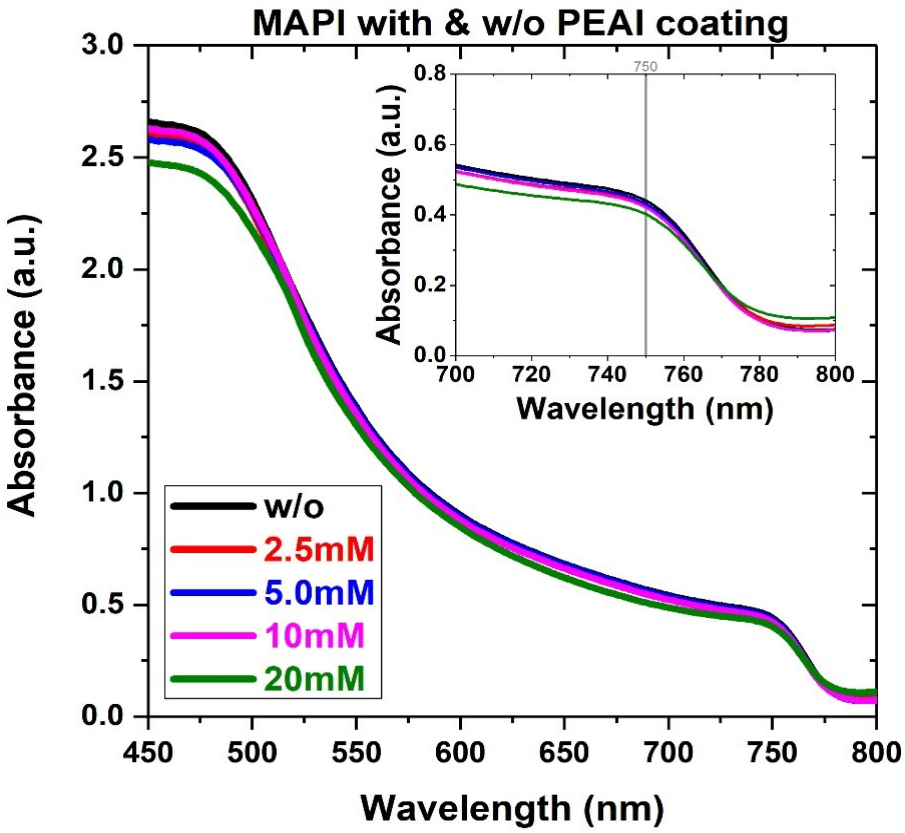


Figure 6-5: UV-Vis absorbance data collected from methylammonium lead iodide (MAPI) films coated with various concentrations of phenylethylammonium iodide ($PhEtNH_3I$, PEAI) of 2.5 mM (red), 5.0 mM (blue), 10 mM (pink) and 20 mM (green). Inset: UV-Vis absorbance data in the range of 700–800 nm.

Next, the stability of the uncoated film and the film treated with 10 mM PEAI was examined on exposure to light and oxygen over a measurement period of three days. It is clear from the data presented in Figure 6-6 (a) and (b) that the stability of MAPI films was enhanced by the application of the PEAI salt treatment, from without coating, to 10 mM. Figure 6-6 (c) shows that the stability enhancement (as a result of passivating the perovskite film with PEAI) is related to the concentration of the iodide salt solution used. As the concentration of the salt solution is progressively increased (in the range from 0 mM to 10 mM) the stability of perovskite film is also increased. When using an optimized PEAI salt concentration (10 mM), there is little to no observable degradation over the time frame examined. This implies that film stability could be improved significantly using PEAI salt treatment, and this concentration (10 mM) may serve to passivate iodide defects within the perovskite films as discussed below.

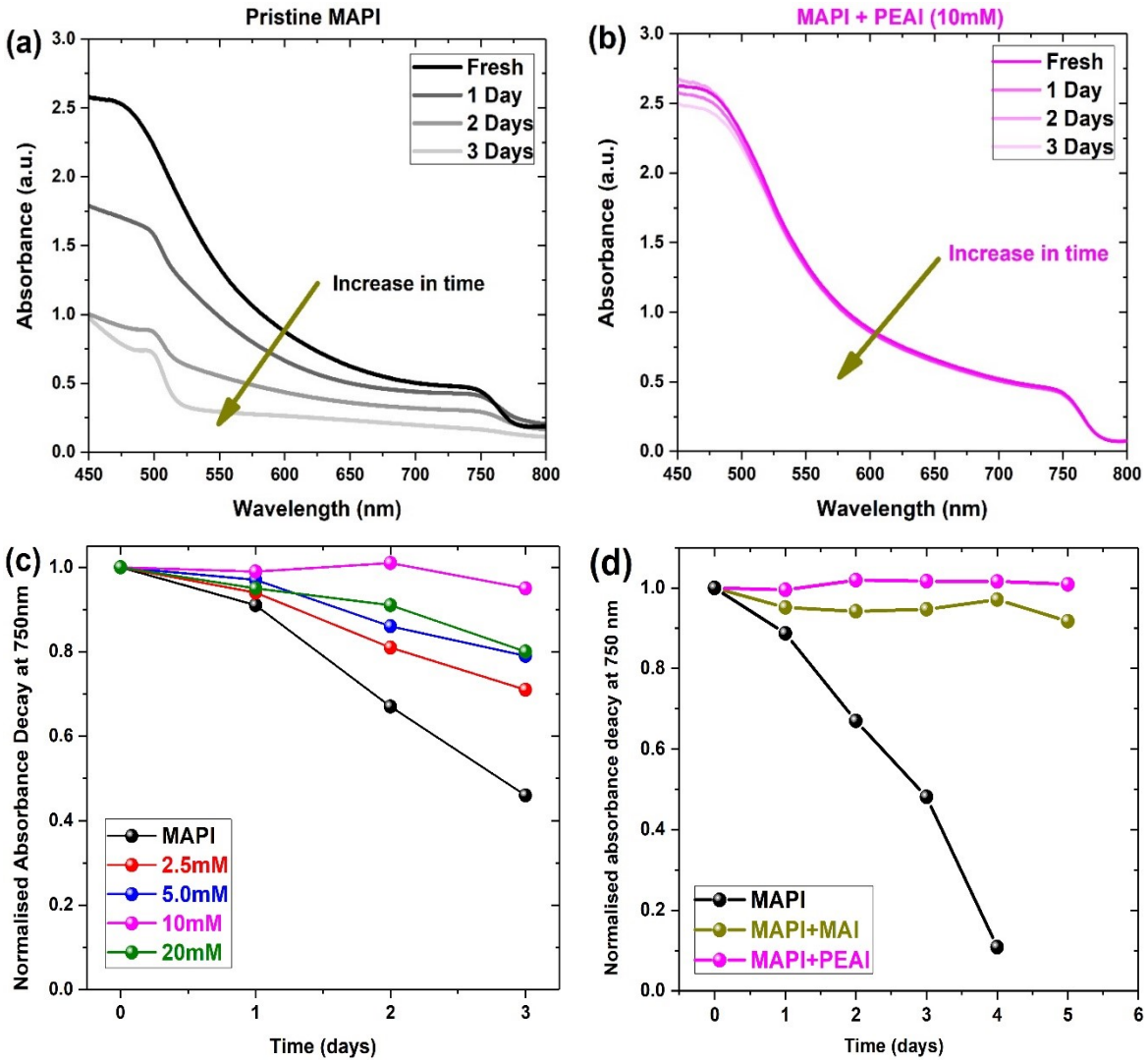


Figure 6-6: (a) UV-Vis absorption spectra of samples of a pristine MAPI film; (b) MAPI coated with 10 mM of phenylethylammonium iodide ($PhEtNH_3I$, PEAI); (c) Normalised absorbance decay at 750 nm for the stability of pristine MAPI and MAPI coated with different concentrations of PEAI. Films were aged under dry air flow and illumination (25 mW/cm^2) for a period of three days; (d) Normalised absorbance decay at 750 nm under illumination (25 mW/cm^2) and dry air flow for pristine MAPI and MAPI coated with PEAI, methylammonium iodide (MAI), films were measured under the same condition as in (a) to (c) for five days.

Figure 6-6 (d) illustrates a further comparison of a film stability test for pristine MAPI and MAPI coated with phenylethylammonium iodide (PEAI; 10 mM) and methylammonium iodide (MAI; 10 mM). Under prolonged five-day continuous illumination, it is clear that pristine MAPI undergoes rapid degradation with film absorbance reduced to 10 % of the original value in four days. In contrast, MAPI treated with both iodide salts experiences more film stability even after five days. Particularly, MAPI coated with PEAI salt decays less severely than that coated with MAI salt. This implies that film with PEAI salt resulted in more-stable perovskite films.

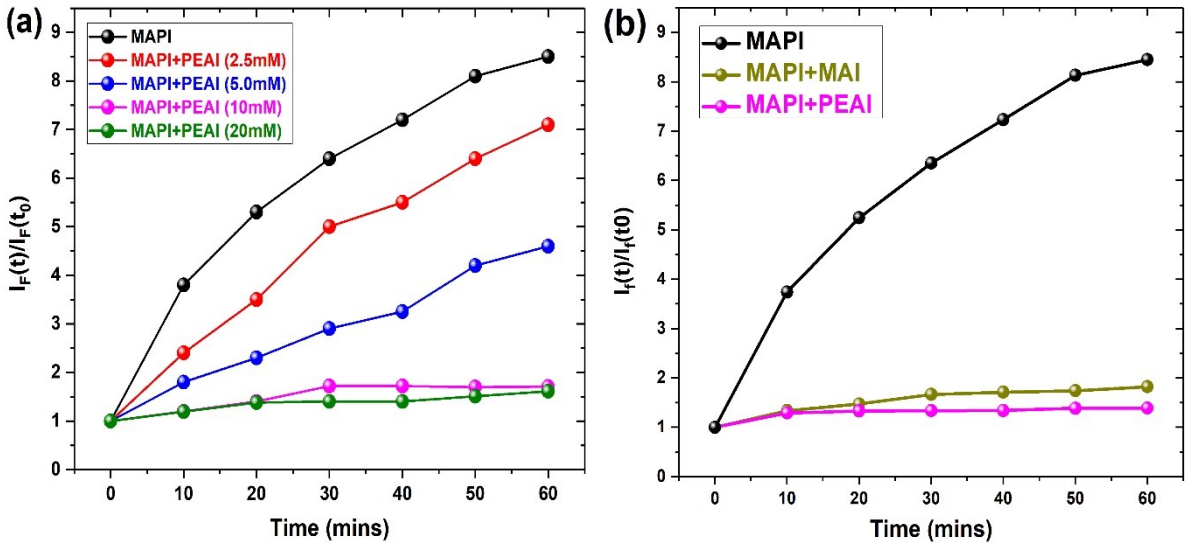


Figure 6-7: (a) Superoxide yield plot comparing the generation of superoxide for MAPI treated with different concentrations and without phenylethylammonium iodide ($PhEtNH_3I$, PEAI) salt passivation. The normalised fluorescence intensity increase of the HE probe at 610 nm (excitation at 520 nm). $I_F(t)$ is the fluorescence maximum at time t, whilst $I_F(t_0)$ is the background fluorescence intensity. $I_F(t)/ I_F(t_0)$ ratio corresponds to yield of superoxide generation for perovskite films. (b) Superoxide yield plot comparing the generation of superoxide for pristine MAPI and MAPI coated with PEAI and methylammonium iodide (MAI).

To confirm whether PEAI salt treatment can effectively inhibit the formation of the superoxide species (O_2^-), and thus enhance the stability of the MAPI film, the yield of superoxide was determined using a technique described previously.[46] The superoxide generation was monitored over the course of 60 mins and the O_2^- yield was determined every 10 minutes. As can be seen in Figure 6-7 (a), all films exposed to light and oxygen lead to the formation of superoxide (O_2^-). However, it is clear that increasing the concentration of PEAI salt leads to much lower yields of superoxide, which ultimately results in better film stability. More specifically, the yield of superoxide is progressively reduced as the salt concentration is increased to 20 mM. Furthermore, in Figure 6-7 (b), when comparing MAPI coated with a different iodide salt, it was observed that although both PEAI and MAI salt show much lower yields of superoxide generation, the generation yield for MAI salt coating is slightly more than one with PEAI coating. The result further confirmed our hypothesis that the larger PEA^+ cation could potentially fill in the surface vacancies more effectively when exposed to oxygen, resulting in less superoxide O_2^- formation and greater film stability.

To gain further insight into the role of PEAI treatment and the impact of salt passivation on iodide defects, Time-Correlated Single Photon Counting (TCSPC) experiments were conducted on MAPI samples treated with a range of concentrations (2.5 mM, 5.0 mM, 10

mM and 20 mM) of PEAI salt. The TCSPC (time-correlated single-photon counting) technique is used to observe the correlation between iodide vacancies and photoluminescence lifetime, where reduced iodide defects mean the number of trap states for non-radiative recombination is also decreased, resulting in longer emission lifetimes. In view of the kinetic decay traces presented in Figure 6-8, iodide vacancies act as non-radiative recombination centres in the perovskite active layer and when present in high numbers they manifest themselves in a short photoluminescence lifetime, as is the case for pristine MAPI (Figure 6-8, shown as the black trace).

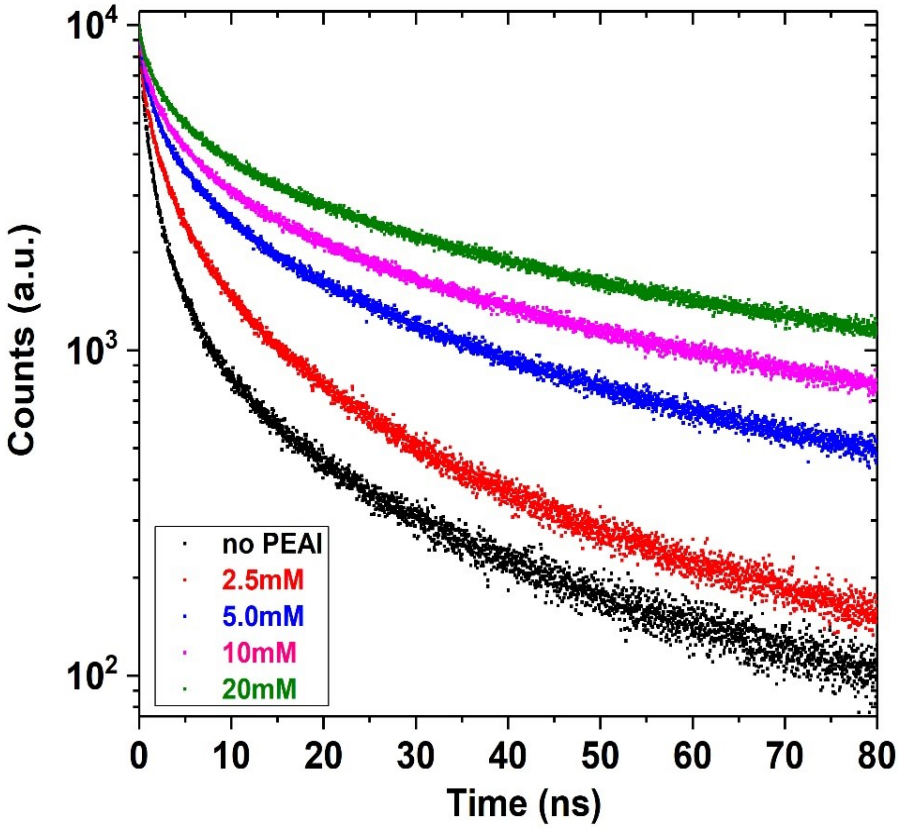


Figure 6-8: Time-Correlated Single-Photon Counting (TCSPC) measurement for non-passivated perovskite film (black) and phenylethylammonium iodide ($PhEtNH_3I$, PEAI) salt passivated with different concentrations of 2.5 mM (red), 5.0 mM (blue), 10 mM (pink) and 20 mM (green).

However, also shown in Figure 6-8 is that the lifetime drastically increases as a function of the concentration of PEAI coating. This implies that improved stability can be attributed to the PEAI salt treatment, as iodide vacancies are central to the production of superoxide in the presence of light and oxygen. Combining this with findings described earlier supports that there is a strong correlation between PEAI treatment and film stability. Increased concentration of PEAI salt could effectively passivate the film by reducing the presence of

the problematic iodide defects that generate superoxide, which is a key component resulting in film degradation.

Thus far, it is shown that passivation of iodide defects using PEAI salts reduces the rate of superoxide production and enhances film stability. The next step was to test the effect of PEAI treatment on operating perovskite solar cells (PSC) devices. Devices were fabricated and characterized as described in the experimental section (Section 6.3). In summary, devices were fabricated with fluorine-doped tin oxide (FTO)/compact TiO_2/mesoporous TiO_2/MAPI/Spiro-OMeTAD/Au 'mesoscopic' architecture and the current density-voltage (J-V) characteristics were analysed both initially, and over time whilst exposing the devices to light and dry air. The current-voltage curves for devices with different concentrations of PEAI salt are depicted in Figure 6-9 and are all recorded in reverse scan (FB-SC).

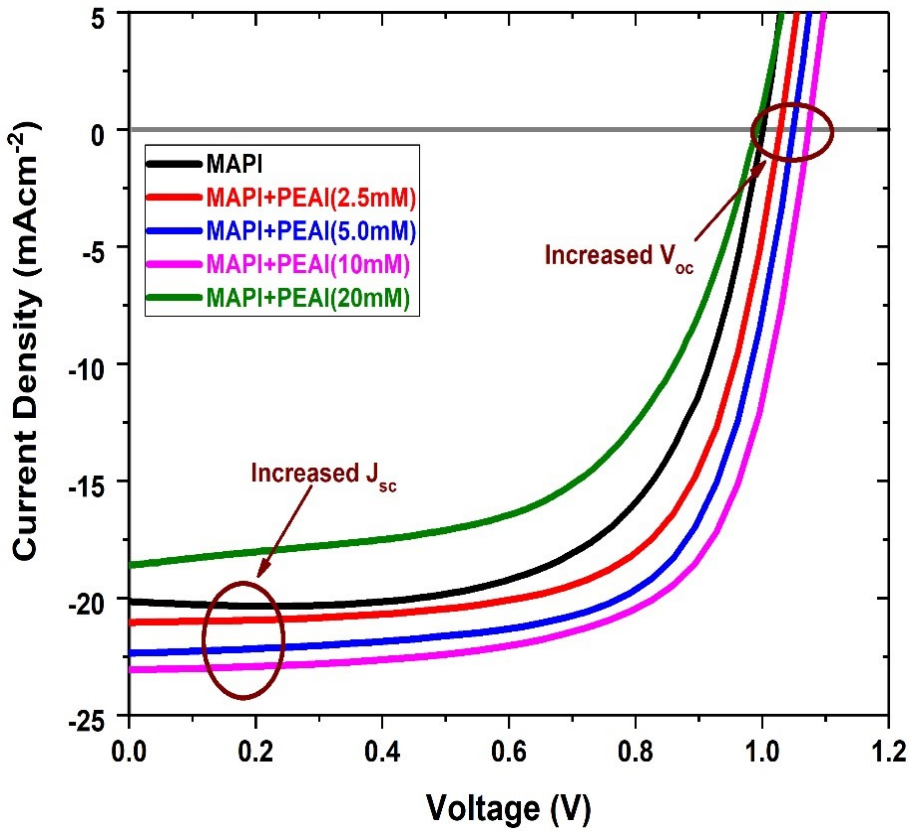


Figure 6-9: The current-voltage measurement of initial performances of devices without and with various concentrations of PEAI coating. All devices are fabricated in FTO/compact-TiO_2/mesoporous-TiO_2/perovskite (salt)/Spiro-OMeTAD/Au architecture and are recorded under reverse scan (FB-SC).

Figure 6-9 illustrates that PEAI passivation with 10 mM concentration (pink trace) resulted in a significant improvement (29.2%) of device efficiency relative to devices employing pristine, uncoated, MAPI layers (black trace). Specifically, the reference cell without PEAI

passivation exhibits open circuit voltage (V_{oc}), short circuit density (J_{sc}) and Fill Factor (FF) of 1.00 V, 20.16 $mAcm^{-2}$ and 0.64 respectively, leading to a Power Conversion Efficiency (PCE) of 12.95 %. However, as can be seen in Figure 6-9 and Table 6-1, the use of perovskite layers coated with a 10 mM solution of PEAI (pink trace) increases the power conversion efficiency of the device. The most effective device employed perovskite layers treated with 10 mM PEAI and exhibited a PCE of 16.73 % with V_{oc} of 1.07 V, J_{sc} of 23.07 $mAcm^{-2}$, and FF of 0.68. A further increase of the PEAI concentration to 20 mM is found to be detrimental to the device performance (green trace). This observation is consistent with the notion that at higher salt concentrations, the greater aggregation of PEAI into clusters occurs. This, in turn, may hinder fundamental processes such as interfacial charge transfer such as hole-transfer from the $CH_3NH_3PbI_3$ photoactive layer to the Spiro-OMeTAD layer. This is detrimental to the PCE.

The current-voltage characteristics along with the photovoltaic performance parameters for coated and uncoated devices measured under reverse scan (FB-SC) and forward scan (SC-FB) conditions are summarised in Table 6-1 and Figure 6-10.

Table 6-1: Device performance parameters of initial performance for devices based on the various concentrations of $PhEtNH_3I$ (PEAI) coated on MAPI perovskite films. (FB-SC = reverse scan and SC-FB = forward scan; V_{oc} = open circuit voltage, J_{sc}, = short circuit density, FF = Fill Factor, PCE = Power Conversion Efficiency.)

Device Type	Pixel Area (cm^2)	Scan Direction	V_{oc} (V)	J_{sc} ($mAcm^{-2}$)	FF	PCE (%)
MAPI (Ref.)	0.12	FB-SC	1.00	20.16	0.64	12.95
		SC-FB	0.99	17.06	0.49	8.35
+PEAI (2.5mM)	0.12	FB-SC	1.03	21.04	0.66	14.55
		SC-FB	1.02	22.91	0.53	12.46
+PEAI (5.0mM)	0.12	FB-SC	1.05	22.36	0.67	15.95
		SC-FB	1.00	21.37	0.66	14.20
+PEAI (10mM)	0.12	FB-SC	1.07	23.07	0.68	16.73
		SC-FB	1.05	22.95	0.67	16.01
+PEAI (20mM)	0.12	FB-SC	0.99	18.61	0.58	10.72
		SC-FB	0.99	18.93	0.43	8.15

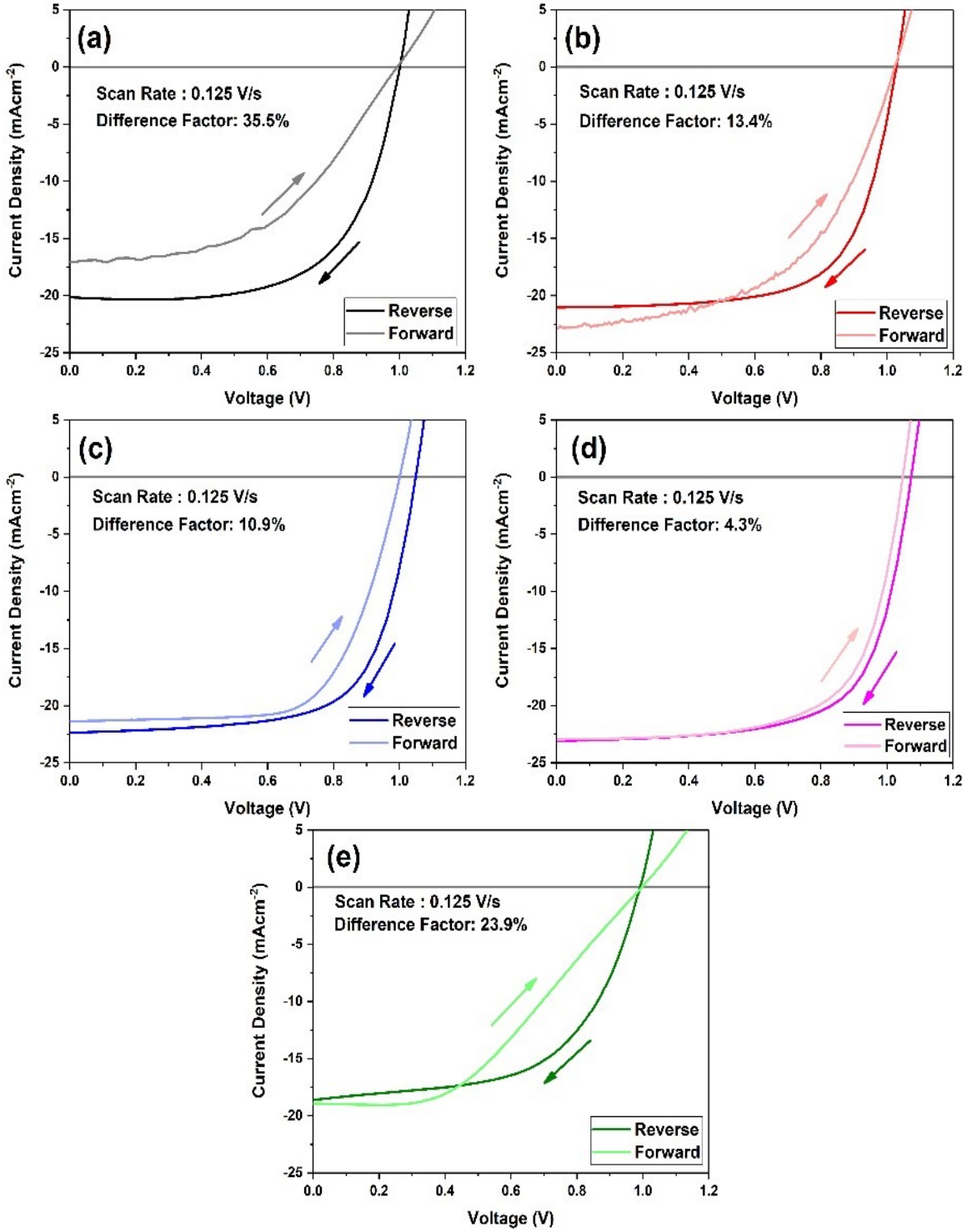


Figure 6-10: Influence of the PEAI concentration on current-voltage hysteresis of the MAPI devices. The devices are measured in reverse scan (FB-SC) and forward scan (SC-FB) under simulated AM1.5 100 mW cm^{-2} sunlight with **(a)** MAPI (black), **(b)** 2.5 mM (red), **(c)** 5 mM (blue), **(d)** 10 mM (pink) and **(e)** 20 mM (green) $PhEtNH_3I$ (PEAI) salt coated on $CH_3NH_3PbI_3$ (MAPI) perovskite solar cells. The scan rate is 0.125 V/s for all devices.

It is worth noting that all devices suffer from a hysteresis effect, which depends primarily on scan rate and scan direction. The forward scan (SC-FB) and reverse scan (FB-SC) of all

devices are recorded and presented in Table 6-1. To describe the difference between the efficiency of forward scan and reverse scan, a difference factor is used, according to the equation (4) from **Chapter 5.**

As shown in Figure 6-10, at a scan rate of 0.125 V/s, there is a significant decrease from 35.5 % to 13.4 % in a difference factor with 2.5 mM PEAI as compared with pristine MAPI devices. This implies that the PEAI treatment could effectively reduce the hysteresis effect; further increasing the concentration of PEAI alleviates the hysteresis effect. Specifically, at 10 mM the difference factor is as little as 4.3%. However, a further increase in the concentration of PEAI to 20 mM means the difference factor rises back to 23.9 %. Based on the above results, PEAI treatment can effectively reduce the hysteresis effect, resulting in more-reproducible perovskite devices.

To investigate the influence of light and oxygen on device stability, the degradation of device efficiency for the same set of samples (with and without PEAI coatings) in dry air under continuous 1 Sun illumination for a period of 5 hours were tested every 30 minutes, with the results shown in Figure 6-11 (a). The results indicate that the stability of the cells improves by increasing the concentration of PEAI salt incorporated into the device. The exposure of devices using an uncoated MAPI perovskite layer to light and dry air for 2.5 hours leads to a ~50% drop in the power conversion efficiency (PCE). In contrast, devices containing PEAI coated perovskite layers (eg.10 mM PEAI) exhibit almost no obvious drop in efficiency (~3.2%) over the same ageing period. These findings clearly demonstrate that the PEAI salt coating can dramatically improve device stability. Taken together, the data presented in Figure 6-11 (a) strongly indicates that this improvement in stability can be attributed to the PEAI salt coating resulting in passivation of iodide defects leading to a lower yield in superoxide generation.

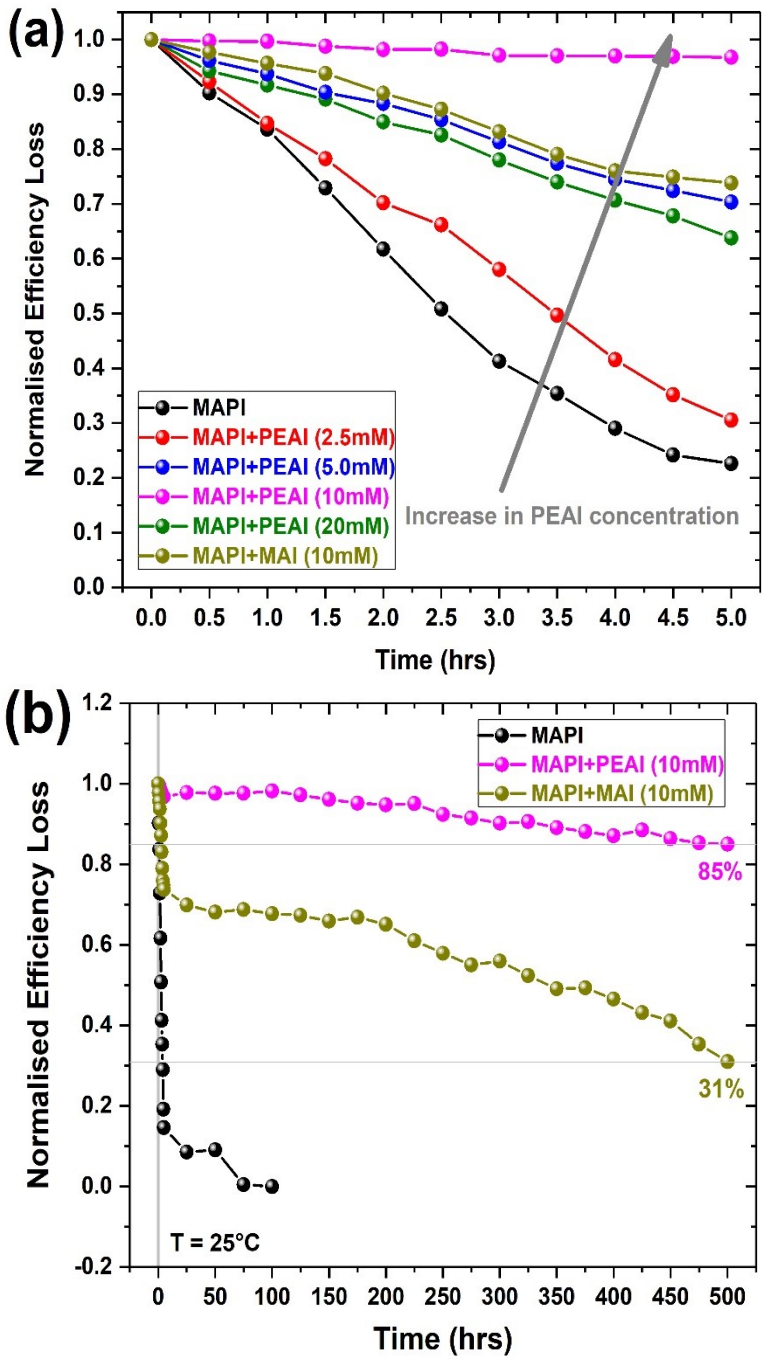


Figure 6-11: (a) Short term stability test (normalized efficiency loss) for devices with and without phenylethylammonium iodide (PEAI) coating in various concentration of 2.5 mM (red), 5.0 mM (blue), 10 mM (magenta), 20 mM (green) and with methylammonium iodide (MAI) coating (dark yellow) for a period of 5 hours; (b) Long term stability test (normalized efficiency loss) for devices employing MAPI (black) without and with phenylethylammonium iodide (PEAI) coating in 10 mM (magenta) and with 10 mM methylammonium iodide (MAI) coating (dark yellow) for a period of 500 hours. The temperature is constantly at 25°C.

Figure 6-11 (b) shows the long term operational stability of solar cells comprising a photoactive layer based on MAPI coated with MAI (dark yellow) and PEAI (magenta). Devices were tested under constant temperature (T = 25 °C) and continuous illumination for a period of 500 hours. These data show that both PEAI and MAI coating agents can enhance

device stability relative to devices based on uncoated MAPI layers, which completely degraded after 100 hours. However, PEAI is found to be much more effective than CH_3NH_3I at enhancing stability in the long run. The device efficiency with PEAI coating dropped to 85 % of its original efficiency after 500 hours, whereas for device with MAI coating this value reduced to 31 %, although the degradation rate was not as rapid as in the first five hours. More importantly, in the case of MAI, the improvement of stability is obtained at the expense of the initial PCE. In contrast, the use of PEAI (magenta trace) is found to improve the initial PCE relative to the control device based on an untreated film.

Having achieved optimum concentrations of PEAI salt for devices, the solar cell performance of two coating agents, namely PEAI and MAI, was compared. In this case, the initial device performance of the two passivating salts relative to uncoated MAPI solar cell, as well as the corresponding external quantum efficiency (EQE) spectra of these devices is shown in Figure 6-12. It can be seen clearly from Figure 6-12 (a) that with PEAI treatment, the device maintains its efficiency and is higher than uncoated MAPI solar cells. As a contrast, with MAI coating, the device efficiency dropped rapidly. The result from Figure 6-12 (b) further show that PEAI-containing solar cell displayed a broader and improved EQE from 350 to 800 nm with respect to device without iodide coating. The EQE of the PEAI coated device reached over ~92 %, whereas that of the pristine device and MAI coated devices reached only ~86 % and ~76 %. This improvement in EQE can be attributed to the better morphology of the perovskite film resulting from more effective defect passivation with PEAI salt. The result also consistent with the observation from SEM (Figure 6-4). Moreover, the J_{sc} obtained from EQE spectra for PEAI coated device, pristine device and MAI coated device are consistent with the parameters shown in Table 6-1, these further verify the accuracy of the J-V measurement.

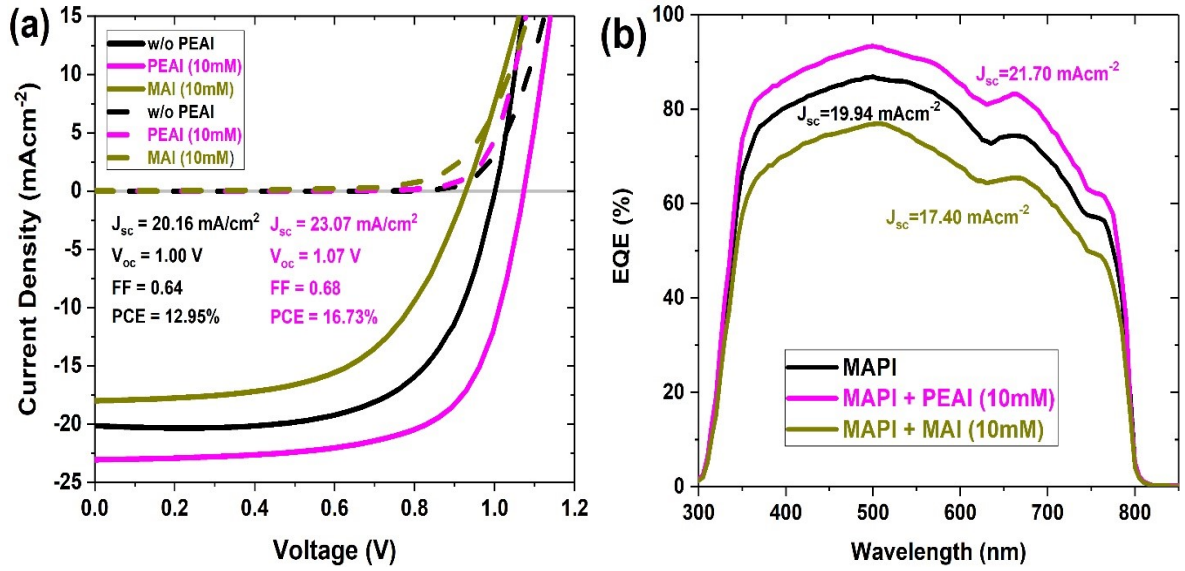


Figure 6-12: (a) Current-voltage measurement of initial performances of devices without iodide salt coating (black), with 10 mM of PEAI (magenta) and 10 mM of MAI (dark yellow) salt coating. Devices were measured using xenon lamp AM1.5 simulated solar spectrum at a scan rate of 0.125 V/s. The initial device is held at open circuit conditions for 60 seconds to stabilise and then scanned from 0 V to 1.2 V, both illuminated current (solid line) and dark current (dash line) are recorded. (b) The EQE spectra of devices without and with various concentrations of PEAI coating. All devices are fabricated in FTO/compact-TiO_2/mesoporous-TiO_2/perovskite (salt)/spiro-OMeTAD/Au architecture.

A key question that now arises relates to the reason(s) why devices coated with PEAI exhibit higher efficiency than those coated with MAI. Further evidence can be gained by probing the yield of charge separation in glass/mesoporous TiO_2/MAPI (salt)/Spiro-OMeTAD (salt = untreated, PEAI, MAI) samples via Transient Absorption Spectroscopy (TAS). Details of our TAS set-up are given in the experimental section, and are published elsewhere.[50] Briefly, samples were probed at a wavelength of 1600 nm, which is characteristic of the absorption of oxidised Spiro-OMeTAD. Therefore, the population of holes in the hole-transport material as a function of time could be measured after exciting the MAPI photoactive layer at 510 nm. This means that the initial amplitude of the TAS trace shows the relative yield of charge transfer from the MAPI valence band into the highest occupied molecular orbital of Spiro-OMeTAD. The result is shown in Figure 6-13.

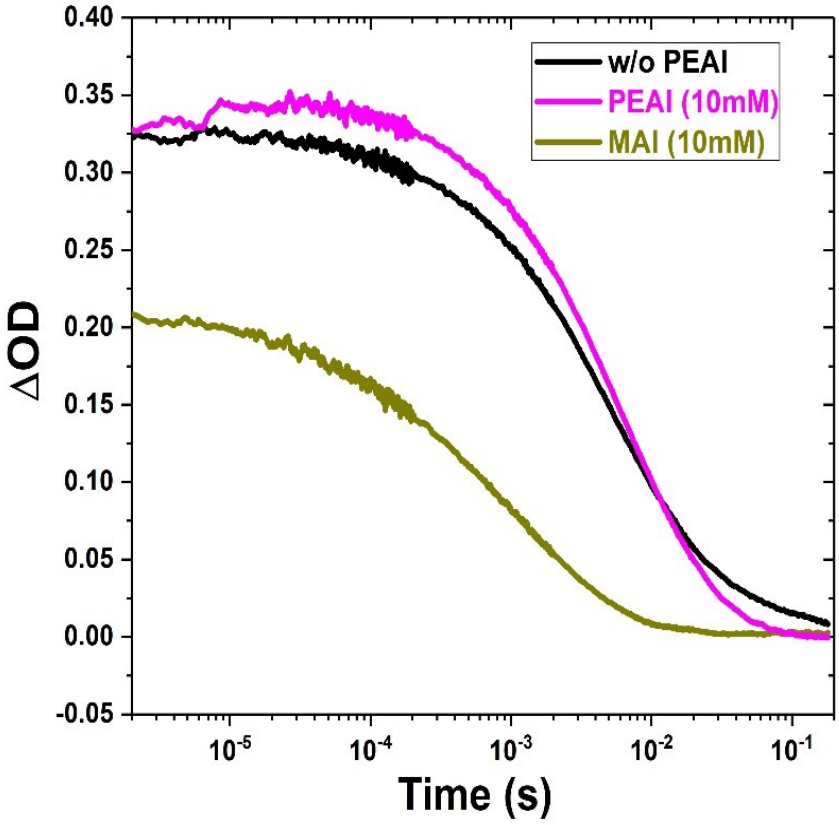


Figure 6-13: Transient absorption spectroscopy kinetic decays of MAPI films without iodide salt coating (black), with 10 mM PEAI (magenta) and 10 mM MAI (dark yellow) salt coating. All samples were excited with a pump wavelength of 567 nm and an average pulse power of 25 μJ cm^{-2}. The probe wavelength of 1600 nm was used to probe the resulting holes in spiro-OMeTAD.

It can be seen from Figure 6-13 that the yield of hole-transfer (measured as the ΔOD value at 1 μs) is slightly higher in the case of PEAI (10 mM) treated MAPI than for untreated MAPI. In the case of MAI (10 mM) treatment, however, a drastic reduction of the hole-transfer yield is observed. This result suggests that the reason for the improved efficiency of Perovskite Solar Cells (PSCs) that incorporate PEAI as opposed to MAI lies in the perovskite/hole-transport material interface, with the latter treatment impeding the charge separation process severely. One reason for this is likely to be the enhanced conjugation in PEAI, which accommodates the hole-transfer process. Nevertheless, the Transient Absorption Spectroscopy (TAS) data provide a compelling argument for the superiority of PEAI (relative to MAI) as a passivating material in PSCs, as the stability can be enhanced without harming charge separation within the device.

Finally, the reproducibility of PEAI salt treatment as compared with standard MAPI procedure is investigated. To do so, the device efficiency from a group of 54 devices with 10 mM of PEAI (optimum concentration) and another group of 54 devices of standard MAPI without any treatment are measured. The statistical distribution of the power conversion efficiency (PCE) for two groups of devices are shown in Figure 6-14.

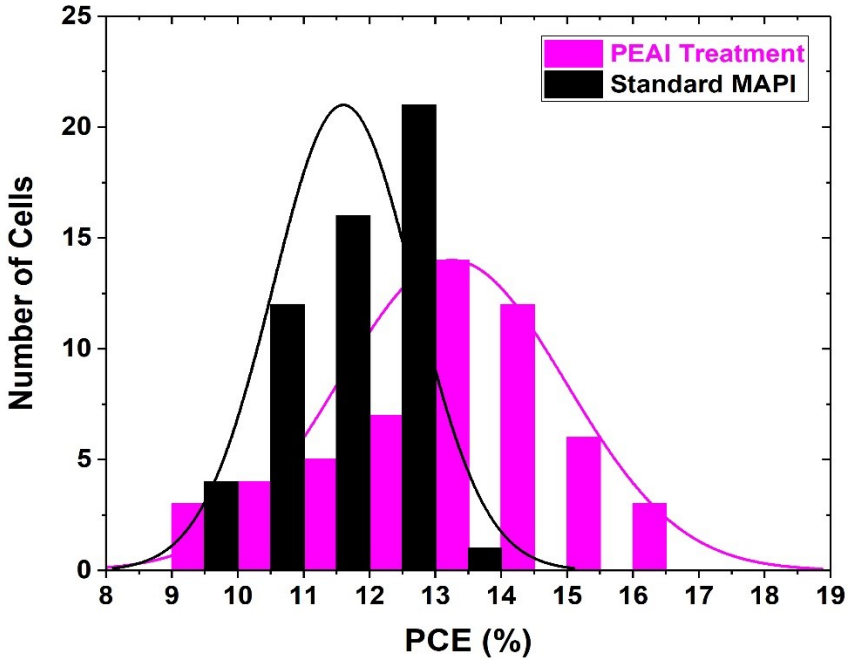


Figure 6-14: Histogram of the power conversion efficiency (PCE) obtained for 54 devices with PEAI salt coating (magenta) and 54 devices pristine MAPI (black). (All devices are measure in reverse scan and are fabricated at different time)

Overall, it can be clearly identified that although PEAI treated solar cells give higher device performance than MAPI without treatment, the latter possess the advantage of being more reproducible than the former method. The origin of this is not clear yet but is likely due to the increased fabrication step from PEAI coating. Crucially, the PEAI iodide salt as a passivating agent has proved to be more efficient than MAI in terms of improving solar cell stability and maintaining device efficiency. In fact, its limitation on reproducibility inspired us to modify this technique and develop a more reproducible fabrication procedure. This result paved the way for our future research.

6.5. Conclusion

In this chapter, a detailed study that combines microscopy, spectroscopy techniques and solar cell optoelectronic characterization has been performed. The focus has been made on evaluating the effect of using PEAI salt as a passivating agent on perovskite films and devices. Firstly, the utilization of PEAI coatings could effectively enhance the stability of MAPI perovskite solar cells (PSCs). This is due to the fact that PEAI salt could effectively passivate the iodide vacancies at the surface of the MAPI photoactive layer, suppressing the formation of the superoxide yield and retarding film and device degradation. Secondly, the concentration of the PEAI salt is considered to be the major factor that determining good solar cell performance. For all of the devices with a variety of PEAI concentration studied herein the highest efficiency has bee achieved for device with 10 mM concentration of PEAI salt coating. More importantly, the solar cell efficiency of PEAI treated MAPbI was much higher than the uncoated MAPI devices. This is an advantage over the MAI salt, which was found to be detrimental to the device performance. Thirdly, unlike MAI passivating agent, which shows obvious hysteresis effect on device measurement, the PEAI salt can help alleviate the hysteresis effect of MAPI perovskite solar cells, thereby also improve device reproducibility. Finally, transient absorption spectroscopy studies show that the use of PEAI as a passivating agent enhances hole-transfer from the perovskite to the hole transporting material (Spiro-OMeTAD). In summury, these observations suggest that thin film passivation using PEAI can effectively improve the performance of perovskite solar cells both in terms of efficiency and stability, the latter of which is crucial for their further development and commercialization. The unsatisfied reproducibility from using PEAI lead to the development of a novel facile additive assisted treatment and will be introduced in detail in **Chapter 7.**

.

6.6. References

[1] Z. Xiao, Y. Yuan, Q. Wang, Y. Shao, Y. Bai, Y. Deng, Q. Dong, M. Hu, C. Bi, J. Huang, *Materials Science and Engineering: R: Reports* **2016**, *101,* 1.

[2] C. Wehrenfennig, G.E. Eperon, M.B. Johnston, H.J. Snaith, L.M. Herz, *Advanced Materials* **2014**, *26,* 1584.

[3] D. Shi, V. Adinolfi, R. Comin, M. Yuan, E. Alarousu, A. Buin, Y. Chen, S. Hoogland, A. Rothenberger, K. Katsiev, *Science* **2015**, *347,* 519.

[4] J.H. Heo, M.H. Lee, H.J. Han, B.R. Patil, J.S. Yu, S.H. Im, *Journal of Materials Chemistry A* **2016**, *4,* 1572.

[5] A. Kojima, K. Teshima, Y. Shirai, T. Miyasaka, *Journal of the American Chemical Society* **2009**, *131,* 6050.

[6] W.S. Yang, B.-W. Park, E.H. Jung, N.J. Jeon, Y.C. Kim, D.U. Lee, S.S. Shin, J. Seo, E.K. Kim, J.H. Noh, *Science* **2017**, *356,* 1376.

[7] W. Zhang, G.E. Eperon, H.J. Snaith, *Nature Energy* **2016**, *1,* 16048.

[8] N.J. Jeon, J.H. Noh, Y.C. Kim, W.S. Yang, S. Ryu, S.I. Seok, *Nature Materials* **2014**, *13,* 897.

[9] A. Abate, J.P. Correa-Baena, M. Saliba, M.S. Su'ait, F. Bella, *Chemistry–A European Journal* **2018**, *24,* 3083.

[10] X. Fu, L. Xu, J. Li, X. Sun, H. Peng, *Carbon* **2018**.

[11] T.A. Berhe, W.-N. Su, C.-H. Chen, C.-J. Pan, J.-H. Cheng, H.-M. Chen, M.-C. Tsai, L.-Y. Chen, A.A. Dubale, B.-J. Hwang, *Energy & Environmental Science* **2016**, *9,* 323.

[12] A.J. Pearson, G.E. Eperon, P.E. Hopkinson, S.N. Habisreutinger, J.T.W. Wang, H.J. Snaith, N.C. Greenham, *Advanced Energy Materials* **2016**, *6,* 1600014.

[13] H. Yuan, E. Debroye, K. Janssen, H. Naiki, C. Steuwe, G. Lu, M.l. Moris, E. Orgiu, H. Uji-i, F. De Schryver, *The Journal of Physical Chemistry Letters* **2016**, *7,* 561.

[14] J.A. Christians, P.A. Miranda Herrera, P.V. Kamat, *Journal of the American Chemical Society* **2015**, *137,* 1530.

[15] J. Yang, B.D. Siempelkamp, D. Liu, T.L. Kelly, *ACS Nano* **2015**, *9,* 1955.

[16] A.l.M. Leguy, Y. Hu, M. Campoy-Quiles, M.I. Alonso, O.J. Weber, P. Azarhoosh, M. Van Schilfgaarde, M.T. Weller, T. Bein, J. Nelson, *Chemistry of Materials* **2015**, *27,* 3397.

[17] R.K. Misra, S. Aharon, B. Li, D. Mogilyansky, I. Visoly-Fisher, L. Etgar, E.A. Katz, *The Journal of Physical Chemistry Letters* **2015**, *6,* 326.

[18] Y. Han, S. Meyer, Y. Dkhissi, K. Weber, J.M. Pringle, U. Bach, L. Spiccia, Y.-B. Cheng, *Journal of Materials Chemistry A* **2015**, *3,* 8139.

[19] W. Nie, J.-C. Blancon, A.J. Neukirch, K. Appavoo, H. Tsai, M. Chhowalla, M.A. Alam, M.Y. Sfeir, C. Katan, J. Even, *Nature Communications* **2016**, *7,* 11574.

[20] M. Asghar, J. Zhang, H. Wang, P. Lund, *Renewable and Sustainable Energy Reviews* **2017**, *77,* 131.

[21] F. Bella, P. Renzi, C. Cavallo, C. Gerbaldi, *Chemistry–A European Journal* **2018**.

[22] W. Li, Z. Wang, F. Deschler, S. Gao, R.H. Friend, A.K. Cheetham, *Nature Reviews Materials* **2017**, *2,* 16099.

[23] F. Bella, G. Griffini, J.-P. Correa-Baena, G. Saracco, M. Grätzel, A. Hagfeldt, S. Turri, C. Gerbaldi, *Science* **2016**, *354,* 203.

[24] H.C. Weerasinghe, Y. Dkhissi, A.D. Scully, R.A. Caruso, Y.-B. Cheng, *Nano Energy* **2015**, *18,* 118.

[25] I. Hwang, I. Jeong, J. Lee, M.J. Ko, K. Yong, *ACS Applied Materials & Interfaces* **2015**, *7,* 17330.

[26] M. Kaltenbrunner, G. Adam, E.D. Głowacki, M. Drack, R. Schwödiauer, L. Leonat, D.H. Apaydin, H. Groiss, M.C. Scharber, M.S. White, *Nature Materials* **2015**, *14,* 1032.

[27] J. You, L. Meng, T.-B. Song, T.-F. Guo, Y.M. Yang, W.-H. Chang, Z. Hong, H. Chen, H. Zhou, Q. Chen, *Nature Nanotechnology* **2016**, *11,* 75.

[28] G. Abdelmageed, H.R. Sully, S. Bonabi Naghadeh, A. El-Hag Ali, S.A. Carter, J.Z. Zhang, *ACS Applied Energy Materials* **2018**, *1,* 387.

[29] Y. Li, C. Feng, H. Cheng, Z.S. Wang, *Solar RRL* 1800222.

[30] P. Zhao, B.J. Kim, H.S. Jung, *Materials Today Energy* **2018**.

[31] Y. Li, Y. Zhao, Q. Chen, Y. Yang, Y. Liu, Z. Hong, Z. Liu, Y.-T. Hsieh, L. Meng, Y. Li, *Journal of the American Chemical Society* **2015**, *137,* 15540.

[32] N. Arora, M.I. Dar, M. Abdi-Jalebi, F. Giordano, N. Pellet, G. Jacopin, R.H. Friend, S.M. Zakeeruddin, M. Grätzel, *Nano Letters* **2016**, *16,* 7155.

[33] A.N. Cho,N.G. Park, *ChemSusChem* **2017**, *10,* 3687.

[34] T. Supasai, N. Rujisamphan, K. Ullrich, A. Chemseddine, T. Dittrich, *Applied Physics Letters* **2013**, *103,* 183906.

[35] Q. Jiang, L. Zhang, H. Wang, X. Yang, J. Meng, H. Liu, Z. Yin, J. Wu, X. Zhang, J. You, *Nature Energy* **2017**, *2,* 16177.

[36] P. Cui, D. Wei, J. Ji, D. Song, Y. Li, X. Liu, J. Huang, T. Wang, J. You, M. Li, *Solar RRL* **2017**, *1,* 1600027.

[37] M.L. Petrus, Y. Hu, D. Moia, P. Calado, A.M. Leguy, P.R. Barnes, P. Docampo, *ChemSusChem* **2016**, *9,* 2699.

[38] W. Peng, B. Anand, L. Liu, S. Sampat, B.E. Bearden, A.V. Malko, Y.J. Chabal, *Nanoscale* **2016**, *8,* 1627.

[39] Y. Shao, Z. Xiao, C. Bi, Y. Yuan, J. Huang, *Nature Communications* **2014**, *5,* 5784.

[40] Y. Fang,J. Huang, *Advanced Materials* **2015**, *27,* 2804.

[41] P.W. Liang, C.C. Chueh, S.T. Williams, A.K.Y. Jen, *Advanced Energy Materials* **2015**, *5,* 1402321.

[42] D. Bryant, N. Aristidou, S. Pont, I. Sanchez-Molina, T. Chotchunangatchaval, S. Wheeler, J.R. Durrant, S.A. Haque, *Energy & Environmental Science* **2016**, *9,* 1655.

[43] N. Aristidou, I. Sanchez-Molina, T. Chotchuangchutchaval, M. Brown, L. Martinez, T. Rath, S.A. Haque, *Angewandte Chemie* **2015**, *127,* 8326.

[44] F.T. O'Mahony, Y.H. Lee, C. Jellett, S. Dmitrov, D.T. Bryant, J.R. Durrant, B.C. O'Regan, M. Graetzel, M.K. Nazeeruddin, S.A. Haque, *Journal of Materials Chemistry A* **2015**, *3,* 7219.

[45] N. Aristidou, C. Eames, M.S. Islam, S.A. Haque, *Journal of Materials Chemistry A* **2017**, *5,* 25469.

[46] N. Aristidou, C. Eames, I. Sanchez-Molina, X. Bu, J. Kosco, M.S. Islam, S.A. Haque, *Nature Communications* **2017**, *8,* 15218.

[47] I.C. Smith, E.T. Hoke, D. Solis-Ibarra, M.D. McGehee, H.I. Karunadasa, *Angewandte Chemie* **2014**, *126,* 11414.

[48] Y. Liao, H. Liu, W. Zhou, D. Yang, Y. Shang, Z. Shi, B. Li, X. Jiang, L. Zhang, L.N. Quan, *Journal of the American Chemical Society* **2017**, *139,* 6693.

[49] A. Poglitsch,D. Weber, *The Journal of Chemical Physics* **1987**, *87,* 6373.

[50] R.J. Westbrook, D.I. Sanchez-Molina, D.J. Manuel Marin-Beloqui, D.H. Bronstein, D.S.A. Haque, *The Journal of Physical Chemistry C* **2018**, *122,* 1326.

CHAPTER 7

A Facile Iodide Salt Additive Assisted Treatment for Enhanced Efficiency, Stability and Reproducibility of $CH_3NH_3PbI_3$ Perovskite Films and Solar Cells

7.1. Abstract

In this chapter, a novel iodide salt assisted anti-solvent treatment in the preparation of the $CH_3NH_3PbI_3$ (MAPI) layer using Phenylethylammonium Iodide (PEAI) as the passivating agent is discussed. We comprehensively studied the effect of this technique using a combination of characterization techniques and find that this Iodide Salt Assisted Anti-solvent Treatment (ISAAT) could effectively lead to the filling of the surface defects of the perovskite layer, thereby enhancing the morphology and crystallinity of the perovskite films. The power conversion efficiency (PCE) of the device incorporating the appropriate amount of PEAI into the anti-solvent achieved an efficiency of 17.93%, which is significantly higher than devices without additive treatment. We further observed that devices produced with this ISAAT method are more stable than the corresponding devices without treatment and comparable with devices employing direct PEAI treatment. More importantly, this ISAAT method shows more reproducibility than the established PEAI treatment. This facile technique elucidates a more effective pathway to the future design and optimisation of perovskite solar cells with greater long-term stability and reproducibility.

.

7.2. Introduction

Exposure of $CH_3NH_3PbI_3$ to a combination of light and dry oxygen resulted in superoxide (O_2^-) formation, which leads to the breakdown of the perovskite crystal structure between the oxygen species from atmosphere and the methylammonium cation was demonstrated in **Chapter 5**.[1, 2] This reaction is believed to cause the degradation of the perovskite layer, thereby lowering the lifetime of both perovskite films and devices.[3] Subsequently, it was shown that this superoxide generation is most likely mediated via iodide vacancies/defects located in the perovskite crystal structure. This, in turn, leads to the development of a technique, in which the Methylammonium Iodide (MAI) salt is directly coated on top of the perovskite layer to passivate these defects.[1] The method could effectively reduce the yield of superoxide generation and enhance film and device stability.

This investigation was extended to the mixed bromine/iodine (Br/I) anion Perovskite Solar Cells (PSCs) and the correlation between the yield of superoxide formation upon oxygen diffusion and light illumination and the stability of the devices as a function of bromide (Br) concentration was observed. Specifically, one of our observations was that as more iodide ions were replaced by bromide ions with smaller particle sizes, the greater the reduction in the hydrogen-bond (H-bond) distances are observed between methylammonium cation and the anion lattice, leading to a shrinkage in the cell volume. The result implies that the number of halide vacancies or defects present in the perovskite is also decreased. Thereby, fewer superoxide species are formed due to the contracted crystal structure, which resulted in enhanced films and devices stability under light and oxygen stress. (manuscript submitted to the journal of Energy & Environmental Science)

Furthermore, we examined that appropriate concentrations of MAI salt are also effective in improving the stability of mixed halide perovskite solar cells. Our studies revealed two important outcomes: first, the majority of the defects within the mixed halide perovskite layers can be passivated by employing iodide salt coating; second, the stability of the Br/I mixed halide devices can be increased by progressively enhancing the concentration of the salt coating up to an optimal amount. The results provide evidence that MAI iodide salt treatment is effective in reducing halide vacancies and creating more-stable perovskite films and devices. However, the improvement in solar cell stability using MAI salt treatment is

achieved by compromising device efficiency, which limited this technique for a wider application.[1] To address this problem, in **Chapter 6**, we introduced an alternative iodide salt, namely Phenylethylammonium Iodide (PEAI) with the bulkier organic component as the passivating agent on Methylammonium Lead Iodide (MAPI) solar cells. We demonstrated that the PEAI salt is more efficient in obtaining stable films and solar cells while improving the device efficiency. We provided an explanation by using Transient Absorption Spectroscopy (TAS) on the origin of the PEAI coated devices being more efficient than MAI coated devices as well as examined the optimal concentration of PEAI that could lead to the best device efficiency and long-term stability.

Direct iodide salt coating with PEAI, although enhancing device efficiency and stability, lowers device reproducibility. The main reason behind this is likely due to the increased fabrication steps, which makes it harder to achieve reproducibility for high device efficiency. Therefore, it is important to upgrade our iodide coating method with fewer fabrication steps while maintaining their benefit on passivating iodide vacancies. Interestingly, recent work from Boopathi et al. has shown that adding alkali metal halide salts into the perovskite precursor solution could enhance the morphology and crystallinity of the perovskite films, resulting in devices with more stability and higher efficiency.[4] Moreover, some studies also show that incorporating hole-transporting material (Spiro-OMeTAD) into the anti-solvent could generate a perovskite/Spiro-OMeTAD heterojunction structure that resulted in improved crystallinity and reduced interfacial losses.[5] The whole process becomes easier and more reproducible since no additional deposition of the hole-transporting layer is needed. Inspired by these studies, it is rational to suppose that iodide salt could potentially be introduced into the perovskite precursor solution simultaneously with the anti-solvent. In this chapter, we present a novel Iodide Salt Assisted Anti-solvent Treatment (‘ISAAT’), where PEAI salt is incorporated into the perovskite precursor films through anti-solvent prior to perovskite formation.

7.3. Experimental

7.3.1. $CH_3NH_3PbI_3$ Film with Iodide Salt Assisted Anti-solvent Treatment (ISAAT)

A 1.25 M solution of $CH_3NH_3PbI_3$ (MAPI) precursor was produced by adding PbI_2 in a 1:1 molar ratio with Methylammonium Iodide (MAI) in a solvent mixture of 1:9 γ-butyrolactone (GBL) to dimethylformamide (DMF). The solution was then spin-coated onto the substrates using a one-step spin program of 4000 rpm for 30 seconds under a nitrogen atmosphere inside a glovebox. In cases where the ISAAT method was introduced, an appropriate amount of PEAI iodide salt was mixed with IPA and the solution dissolved in diethyl ether. The resulting anti-solvent (~500 µL) was drop cast on top of the precursor solution for seven seconds after the one-step spin coating. The iodide salt-penetrated perovskite was then annealed at 100°C for 15 minutes. The details of the three methods to produce MAPI film are depicted in Figure 7-1. For all films and devices, the electron transporting layers (c-TiO_2, mp-TiO_2) and hole-transporting layers (Spiro-OMeTAD) are fabricated using the same method as mentioned in previous chapters.[1]

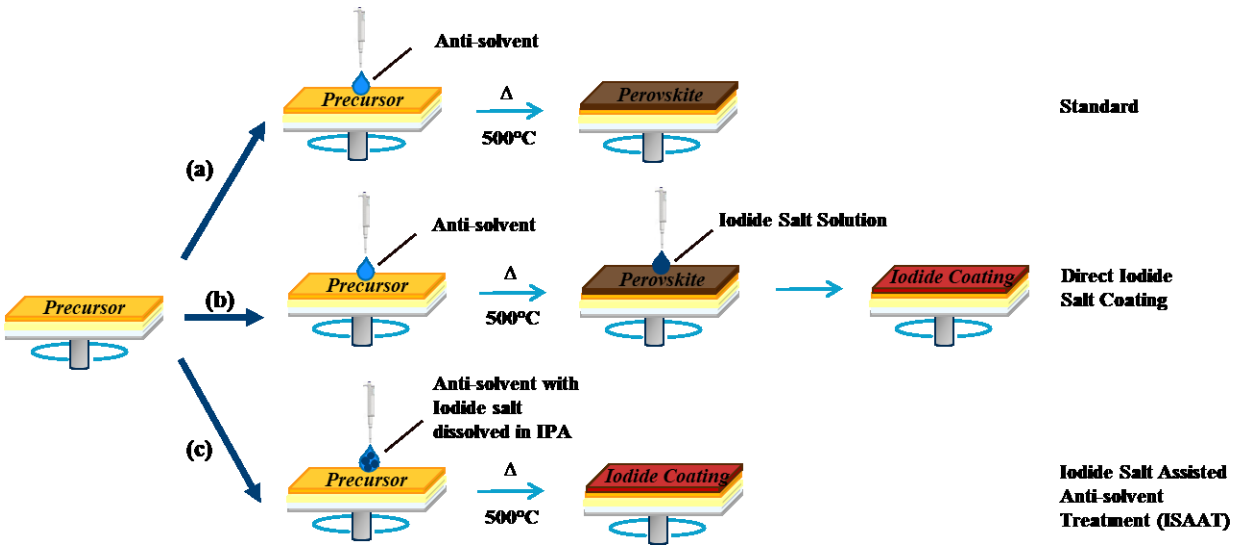


Figure 7-1: Schematic representation of three different methods of fabricating perovskite solar cells with $CH_3NH_3PbI_3$ (MAPI) as an active layer. **(a)** Standard Method; **(b)** direct iodide salt coating; **(c)** Iodide Salt Assisted Anti-solvent Treatment (ISAAT).

7.4. Results and Discussion

The effect of Iodide Salt Assisted Anti-solvent Treatment (ISAAT) on optical properties of the perovskite layers was analysed. To this end, the selected concentration of PEAI salt dissolved in IPA is mixed with diethyl ether (DE) and dripped on the precursor solution for MAPI based perovskite solar cells. The samples were then characterized using ultraviolet-visible (UV-vis) absorption spectra, and the result is shown in Figure 7-2. It can be seen that all films reveal explicit absorption in the visible wavelength ranging from 450 nm to 750 nm. Specifically, increasing the concentration of PEAI in the anti-solvent leads to an improvement of the absorption intensity and the strongest absorption is observed when 15 mM of PEAI is present in the DE anti-solvent. Further increases in the PEAI concentration to 20 mM resulted in a decrease in absorption intensity. In particular, there is a reduction in the absorbance peak at 750 nm for 20 mM PEAI as compared with other samples, indicating that the morphology and crystallinity of the perovskite film are less favourable. The results showed that the ISAAT treatment with PEAI salt up to 10 mM could be used in MAPI perovskite films without damaging the surface. However, further increases in the PEAI concentration to 20 mM resulted in a decrease in absorption intensity. In particular, there is a reduction in the absorbance peak at 750 nm for 20 mM PEAI as compared with other samples, implying that at this concentration the morphology and crystallinity of the perovskite film is less favourable. It further revealed that, similar to methylammonium iodide (MAI) salt, which was applied previously in our study as well as appeared in other literature as self-assembled passivation layer at grain boundary,[6] there is a limitation required in terms of the amount of PEAI being used in anti-solvent.[1] The effect of excess amount of PEAI on perovskite films and solar cells will be investigated later in this chapter. Nevertheless, the UV-Vis result on MAPI samples provides initial evidence that the ISAAT treatment with PEAI salt can be applied in MAPI perovskite films without lowering the surface absorption characteristics.

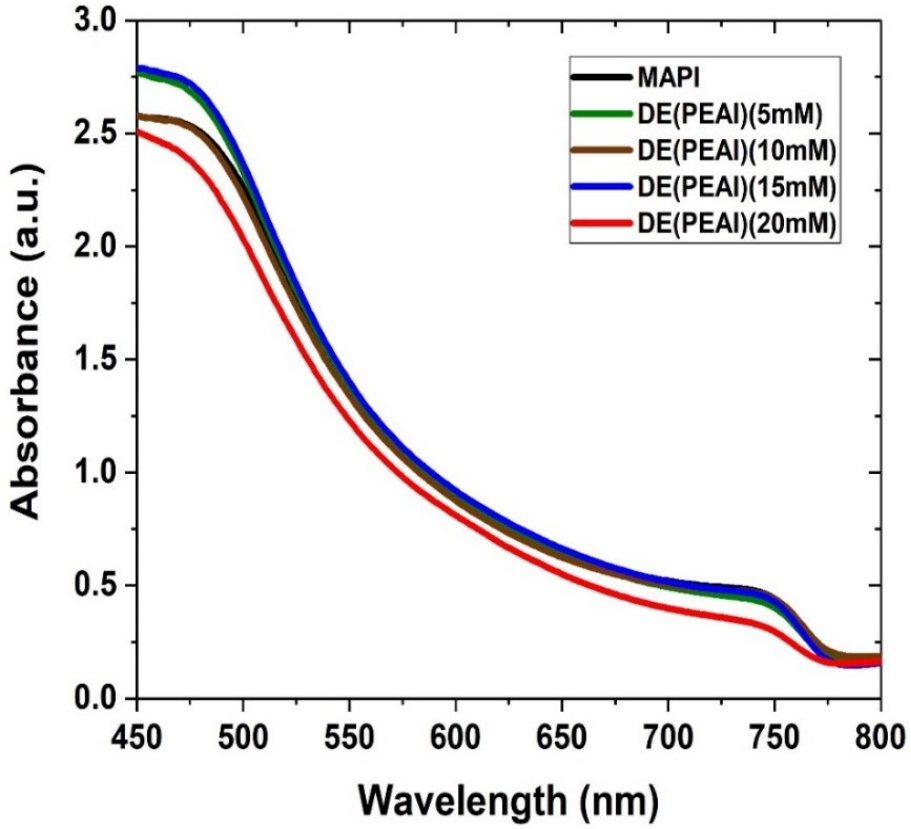


Figure 7-2: UV-Vis absorbance collected from $CH_3NH_3PbI_3$ (MAPI) perovskite films without (black) and with various concentrations of phenylethylammonium iodide ($PhEtNH_3I$, PEAI), Iodide Salt Assisted Anti-Solvent Treatment (ISAAT) at a concentration of 5 mM (green), 10 mM (brown), 15 mM (blue) and 20 mM (red) (DE =diethyl ether).

Next, we consider the impact of ISAAT treatment on the stability of the perovskite films towards oxygen and light. Identical samples from Figure 7-2 were measured under light and oxygen stress for a period of 14 days, the variation of absorption intensity for samples at different days were recorded and normalized. The absorbance intensity of individual samples were demonstrated in Figure 7-3 (a) to (e) as follows. The colors used to represent samples with different concentration of PEAI salt mixed in DE antisolvent are same as in Figure 7-2.
It should be pointed out that all samples during oxygen and light soaking were fixed inside a vial which was sealed with a parafilm. A syringe with Si dry agent and filled with cotton is inserted into the cap of the vial in order to eliminate the influence from humidity/moisture.

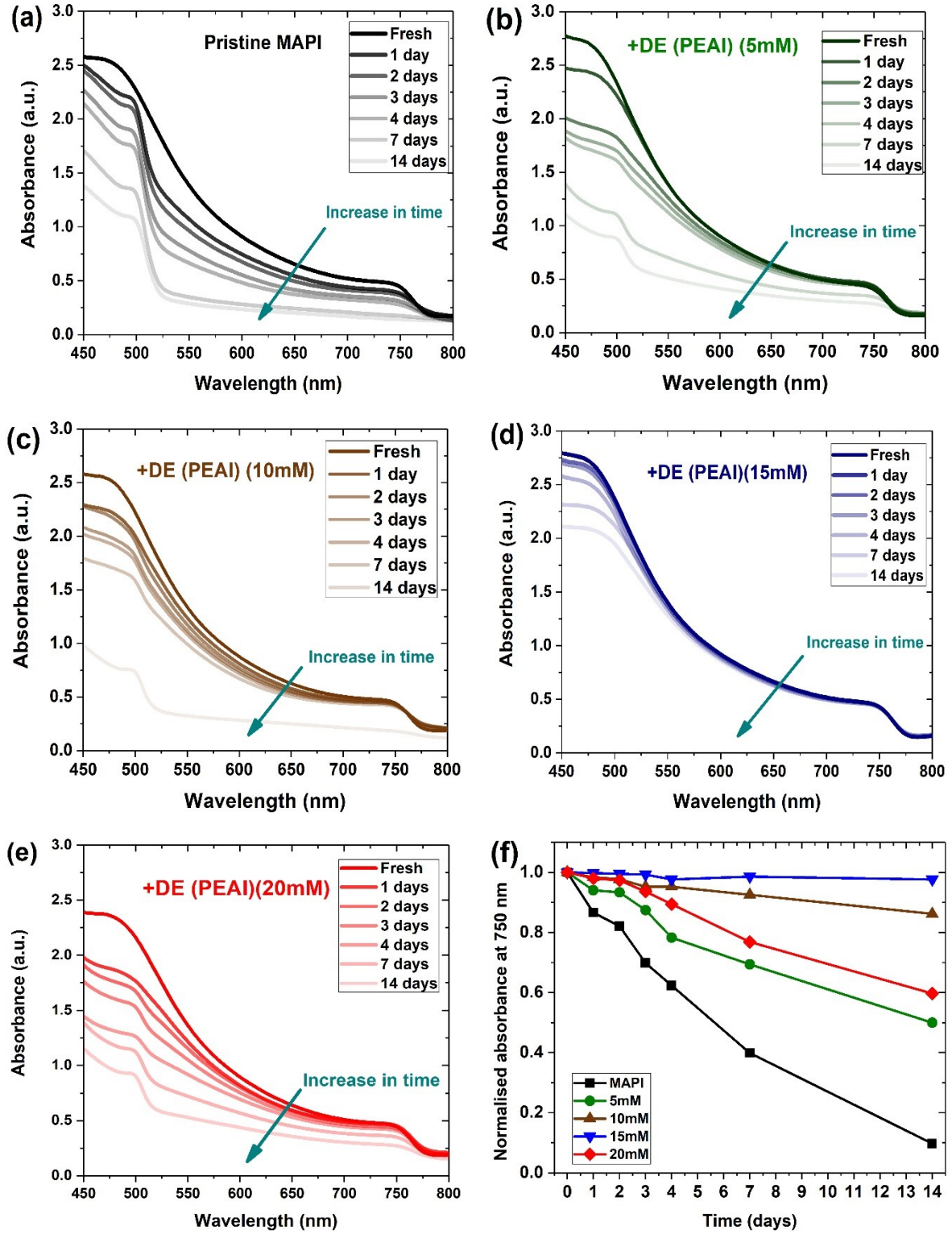


Figure 7-3: UV-Vis absorption spectra of **(a)** pristine MAPI film (black); **(b)-(e)** MAPI films incorporating various concentrations of phenylethylammonium iodide ($PhEtNH_3I$, PEAI) Iodide Salt Assisted Anti-solvent Treatment (ISAAT) under dry air and light illumination for a period of 14 days. (DE represents anti-solvent of diethey ether); **(f)** Normalized absorbance decay at 750 nm for pristine MAPI and MAPI with different concentrations of PEAI using ISAAT treatment. Films were aged under dry air flow and illumination (25 mW/cm^2) for a period of 14 days**.**

According to the absorbance spectra (a) to (e) it can be seen that all samples undergo degradation upon exposure to oxygen and light within the testing period. However, the rate of degradation is different and is related to the concentration of PEAI used in the IAAST treatment. Specifically, the strength of absorbance in MAPbI film without PEAI incorporation significantly decreased with degradation time, which according to the previous study is attributed to the perovskite decomposing under the action of oxygen and light with lead iodide being formed and the colour of films turning from dark shiny brown to yellow.[1, 2] The incorporation of 5 mM PEAI (green) in anti-solvent slightly stabilizes the perovskite film, but not enough to prevent it from decomposing after three days. Further increasing the concentration of PEAI leads to more stable perovskite films under oxygen and illumination and slowing down the rate of degradation as can be seen in (b) and (c). In the case of 15 mM PEAI in diethyl ether (DE) (Figure 7-3 (d)), although some absorption intensity is lost, little to no degradation is observed within 14 days. According to the photographs, the films look identical before and after 14 days of the degradation test. To obtain a more explicit comparison of the stability, we normalized absorbance intensity at 750 nm for each sample, and the result is shown in Figure 7-3 (f). It can be observed that at 15 mM of PEAI treatment, there is almost no degradation within 14 days of the degradation test. In contrast, other samples experience certain degrees of degradation. Therefore, it can be suggested that the stabilization of the MAPI perovskite film can be ascribed to the PEAI salt treatment and the rate of degradation can be tuned from adjusting the iodide concentration in diethyl ether (DE). In addition, a limitation exists in terms of the dosage range of PEAI being used, concentration over 20 mM resulted in a decrease in absorbance strength and less stable perovskite film, as already shown in Figure 7-2 and Figure 7-3 (e). Nevertheless, this study clearly shows that PEAI applied in anti-solvent could enhance the stability of the perovskite films. Inspired by this discovery, the origin of this phenomenon was further investigated (see below).

To gain further insight into the effect of PEAI concentration in ISAAT on the mechanism of charge transport among the perovskite films we carried out steady-state photoluminescence (PL) and time-resolved photoluminescence (TRPL) measurements, as illustrated in Figure 7-4 (a) and (b).

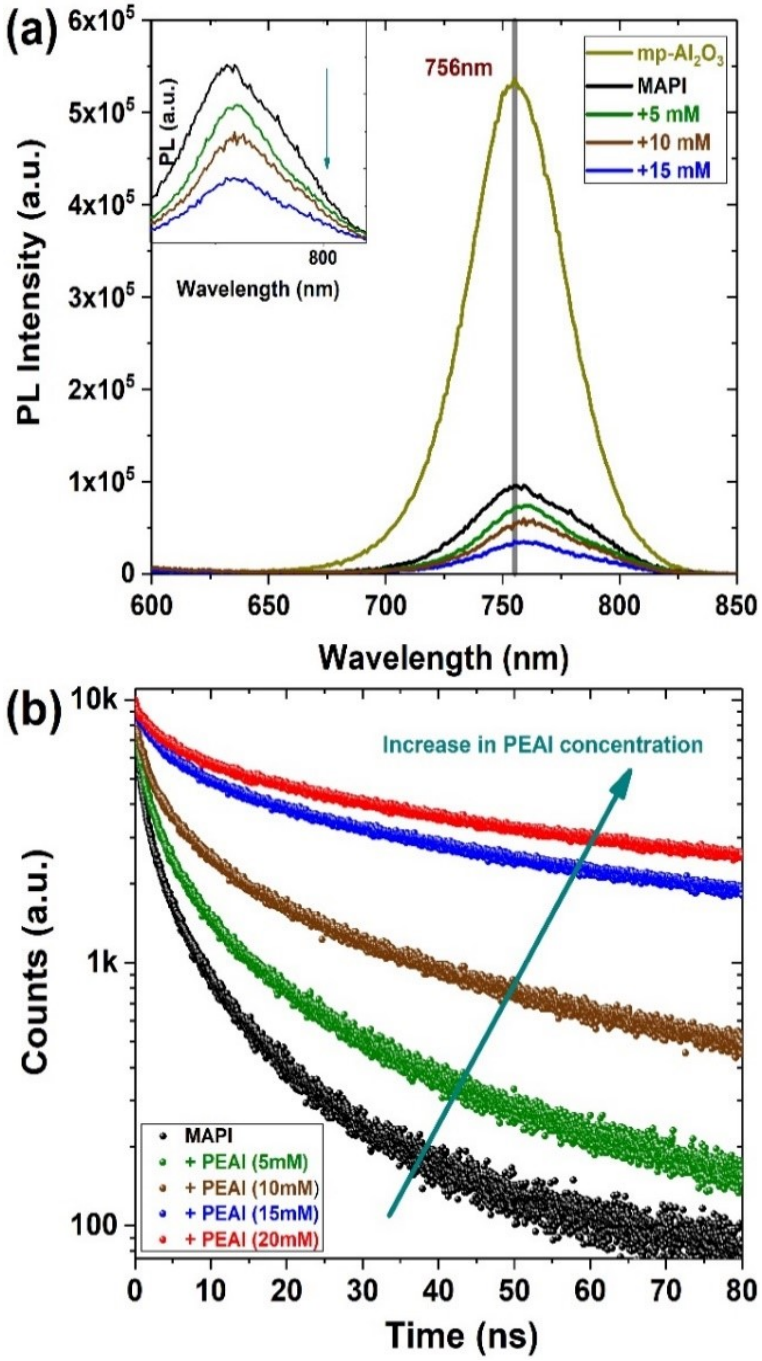


Figure 7-4: (a) Steady-state photoluminescence (PL) spectra of MAPI perovskite films with and without various concentrations of PEAI Iodide Salt Assisted Anti-solvent Treatment (ISAAT) (all samples use diethyl ether as anti-solvent). Inset: PL intensity changes for different concentrations of PEAI assisted anti-solvent treatment. **(b)** Time-correlated single-photon counting (TCSPC) spectra of $CH_3NH_3PbI_3$ (MAPI) perovskite films with and without various concentrations of PEAI iodide salt assisted anti-solvent treatment (ISAAT).

In this experiment, the samples were fabricated in an architecture of glass/TiO_2/MAPI (with/without ISAAT). The standard reference is glass/mp-Al_2O_3. We use glass substrates to avoid quenching at the interfaces and use mp-Al_2O_3 as it does not undergo quenching during

measurement.[7] It is widely known that recombination of electron-hole pairs could release energy and generate photoluminescence (PL) emission and the more recombination of electron-hole pairs leads to greater PL intensity, resulting in lower solar cell efficiency.[8] Figure 7-4 (a) reveals clearly that by applying ISAAT treatment, the PL intensity is reduced as compared to the sample with only mp-Al_2O_3. The inset image further demonstrates that the PL emission can be progressively reduced by increasing the PEAI concentration. Thus, the decreased emission intensity can be attributed to the PEAI salt treatment, which resulted in a lower recombination of charge carriers. This measurement provides strong evidence that applying ISAAT treatment with PEAI salt could help to achieve higher efficiency of the perovskite solar cells.

So far, some important outcomes have been achieved: (1) PEAI (with appropriate concentration) Iodide Salt Assisted Anti-solvent Treatment (ISAAT) can enhance the perovskite film stability under oxygen and light illumination; (2) The ISAAT treatment could effectively lower charge recombination within perovskite films, implying more charge carrier transport and high device efficiency. In previous chapters, it was established that PEAI iodide salt treatment could effectively passivate perovskite films by filling the iodide vacancies that exist at the surface of the crystal. This, in turn, leads to less superoxide generation upon light illumination and oxygen diffusion, thereby directly retarding film and device degradation.[9] We also realize that in case of direct PEAI coating, the perovskite film is already formed and vacancies exist in both the surface and the bulk region of the crystal. In this case, very little PEAI material could penetrate into the bulk side of the perovskite crystals and passivate the iodide vacancies inside owing to the relatively larger PEA^+.[10].[11] In contrast, for the ISAAT treatment, the PEAI is introduced at the time of the anti-solvent dripping. At this moment the perovskite film is not yet formed, and the only precursor layer is the deposit on top of the substrate. Under these conditions, the introduction of the PEAI could potentially change the presence of iodide ions inside the perovskite structure upon annealing so that perovskite with fewer iodide vacancies on both the surface and the bulk side formed.[12] In addition, the annealing process could facilitate diffusion of iodide ions from PEAI salt such that iodide ions could more efficiently fill the vacancy/defect sites as compared with direct PEAI coating, in which no further annealing process is required. Therefore, the ISAAT treatment could complete the same task as direct PEAI coating to passivate the perovskite film, whilst no further fabrication step is required. This facile procedure makes ISAAT treatment better than conventional iodide salt coating and potentially implies more device reproducibility.[13]

To obtain further evidence that PEAI-involved ISAAT treatment is indeed passivating iodide defects rather than due to some other effect, we carried out time-resolved photoluminescence (TRPL) characterization, in which the decay spectra of the MAPI perovskite films without and with different concentrations of PEAI used in ISAAT treatment were measured, and these are shown in Figure 7-4 (b). The data clearly shows that the ISAAT treatment with PEAI iodide salt could improve the stability of the perovskite films. Moreover, increasing the PEAI concentration inside the anti-solvent leads to an increased photoluminescence lifetime. This observation is consistent with our previous investigation in Figure 7-4 (a) that ISAAT treatment could reduce the number of iodide vacancies and defects and therefore the number of trap states for non-radiative recombination, resulting in longer emission lifetimes.

It is worth noting that recent researches on some widely used passivation agents such as PbI_2 and PCBM have shown that they can help to improve the crystallization of the perovskite grains, which is responsible for better surface morphology, higher device efficiency and longer stability.[12, 14-25] Therefore, to understand the effect of ISAAT treatment on these properties, we used X-Ray Diffraction (XRD) and Scanning Electron Microscopy (SEM) to investigate the films prepared with and without ISAAT treatment. The XRD pattern is shown in Figure 7-5 (a), the main characteristic diffraction peaks of all samples are marked with asterisks and at 14.12°, 28.44°, 31.98° and 43.2° correspond with the (110), (220), (310), and (330) planes, respectively.[26] This indicates the formation of the tetragonal perovskite crystal structure and the peak positions are in agreement with the reported results.[4, 27] Moreover, there is no secondary phases appeared due to the formation of other species (e.g., PbI_2 or MAI etc.),[28] which means that all samples are measured fresh without degradation. Importantly, the intensities of the perovskite peaks were enhanced significantly upon using the PEAI involved ISAAT treatment as compared with pristine MAPI. This indicates that the introduction of ISAAT does not affect the crystal structure of the MAPbI. It leads to the formation of the highly crystalline perovskite films. A further increase in PEAI concentration to 20 mM (red) lowers the intensities in all major characterization peaks and a superposition appears at 28.44°. It further confirmed that beyond optimum concentration of PEAI, the surface morphology is getting worse and might have PEAI material agglomerated on top of the crystal to damage the surface morphology as well as reduce the optical and electrical properties. Alternatively, the fact that PEAI was dissolved in IPA solution before introducing

into the anti-solvent means that excess IPA is present when PEAI exceeds their optimum quantity and is likely to corrode the perovskite layer and is harmful to the crystals.

To obtain insight into the impact of ISAAT treatment on the crystallinity variation, we estimate the average size of the perovskite crystals according to the full-width-half-maximum (FWHM) value of the diffraction peak at 14.12°. We estimated the average crystallite sizes using the Scherrer equation, Equation (1) as follows:[29]

$$\boldsymbol{D = \frac{0.89\lambda}{\beta cos\theta}} \qquad \textbf{(1)}$$

Where D represents the average crystallite size, λ is the wavelength of the X-rays, β is the FWHM of the diffraction peak and θ is the diffraction angle; the constant value 0.89 is known as Scherrer shape factor and is a characteristic of a certain particle. The result of the FWHM value and corresponding average crystallite size as a function of the concentration of PEAI is shown in Figure 7-5 (b).

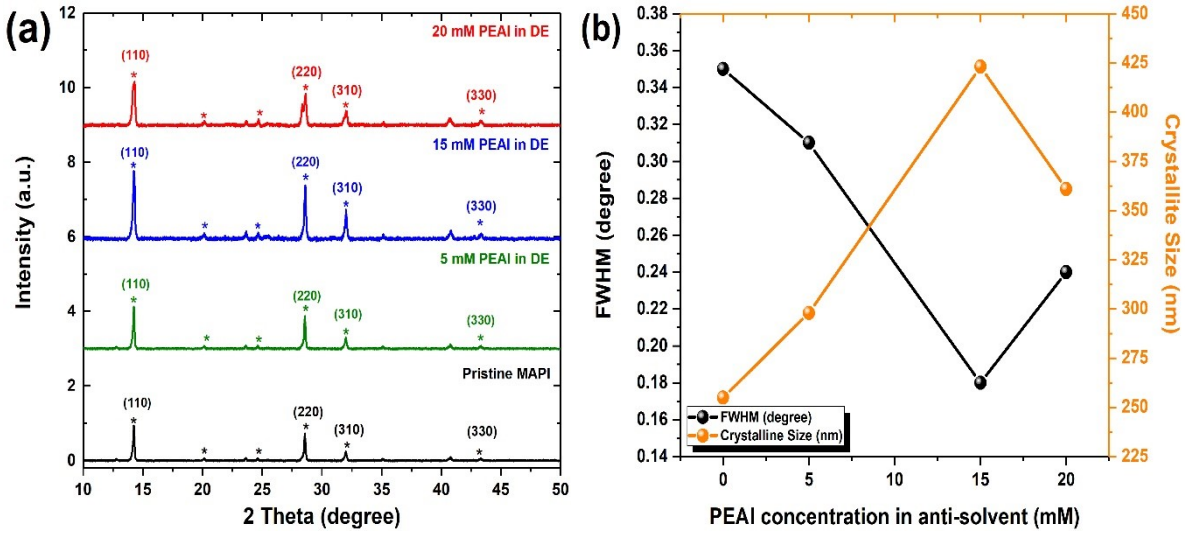


Figure 7-5: (a) XRD patterns of $CH_3NH_3PbI_3$ (MAPI) perovskite layers prepared with PEAI iodide salt assisted anti-solvent treatment (ISAAT) at various concentrations: 0 mM (black), 5 mM (green), 15 mM (blue) and 20 mM (red); and (b) the FWHM value (black) and average crystallite sizes (orange) of perovskite thin films as a function of various PEAI concentrations in anti-solvent.

It can be seen that both FWHM values and crystallite size are closely related to the concentration of PEAI salt present in anti-solvent. Specifically, up to 15 mM (PEAI), the FWHM value decreases as more PEAI is introduced, suggesting the formation of more

crystalline perovskite films. Moreover, the estimated crystal size of the perovskite crystals is enhanced from ~249 nm without ISAAT treatment to ~423 nm with 15 mM of PEAI, which is the greatest among other concentrations. Further increases of the concentration of PEAI to 20 mM leads to a larger FWHM and smaller crystallite size in contrast to values from 15 mM. The result provides direct evidence that ISAAT treatment could improve crystallinity of the perovskite layers.

The effect of ISAAT treatment on the surface morphology of the perovskite films by applying SEM characterization for MAPI without and with different concentrations of PEAI based ISAAT treatment was investigated and the obtained images is depicted in Figure 7-6. From the top-view images, it can be observed that MAPI perovskite film with the conventional method is accompanied by many small pinholes. The inner image reveals a higher magnification scale, and we could see that crystals are not very clear with a particle size of around 200 nm, which is close to the estimation from Figure 7-5 (b). Interestingly, on applying the ISAAT treatment, the pinholes disappeared, and the film quality is improved as crystals can be seen more clearly in the grain boundary. More importantly, the crystal size is progressively increased and becomes larger with more PEAI added as compared with pristine MAPI. The best film quality is observed when 15 mM of PEAI is participated in the ISAAT treatment, as can be seen in Figure 7-6 (d). The crystal size, in this case, is around 400 nm, which is significantly larger than the counterpart with other PEAI concentrations, indicating that ISAAT with PEAI could affect crystal growth and increase the grain size of the perovskite films. This is consistent with previous observations that better crystallinity is achieved by adding 15 mM of PEAI into the anti-solvent. It is worth noting that further increase in the PEAI concentration to 20 mM resulted in a reduction of the film morphology as the crystal and grain boundary become rather vague and indistinct. This is mainly due to the fact that PEAI is introduced to the anti-solvent by being dissolved in the IPA solvent, which is harmful to the perovskite surface. This observation further confirmed the previous results of UV-Vis and X-Ray Diffraction (XRD) measurement that upon adding 20 mM of PEAI into the system, both absorbance strength and diffraction peaks are decreased. Moreover, as can be seen from Figure 7-6 (b) to (d), the grain boundaries (GBs) appear relatively brighter and more explicit than the nearby grains. As a contrast, this phenomenon does not appear in MAPI without PEAI, implying that the PEAI salt under ISAAT treatment is mainly located at the grain boundaries of the perovskite crystals and is responsible for controlling charge carrier trapping. As mentioned earlier, the iodide vacancies, which cause

the degradation of the perovskite layers, are also presented mostly at the grain boundary,[9, 30] this partially explains the reason PEAI based ISAAT could effectively passivate the iodide vacancies and enable improved device performance.

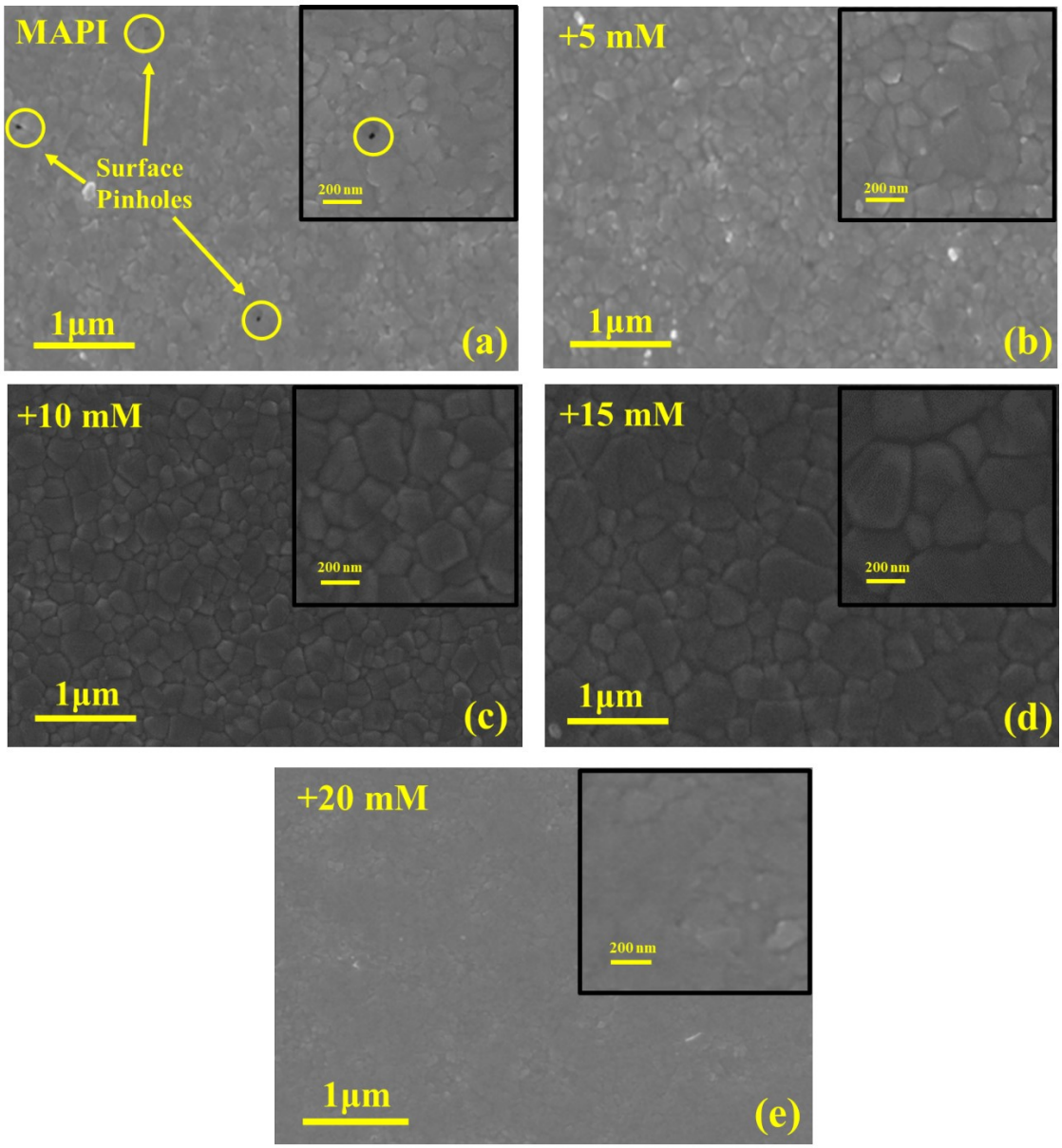


Figure 7-6: Top-view SEM images of the **(a)** non-passivated MAPI perovskite film and films employing phenylethylammonium iodide ($PhEtNH_3I$, PEAI) Iodide Salt Assisted Anti-solvent Treatment (ISAAT) with different iodide salt concentrations of **(b)** 5 mM, **(c)** 10 mM, **(d)** 15 mM and **(e)** 20 mM. Inset: Corresponding SEM images of each film with higher magnification.

According to the above observations, the ISAAT treatment could enhance the film stability. Whether this increase in stability is due to the passivation of vacancy defects, thus reducing superoxide generation was then investigated. The superoxide yield is determined for the samples with and without PEAI involved ISAAT treatment. The result of this study is presented in Figure 7-7 as follows.

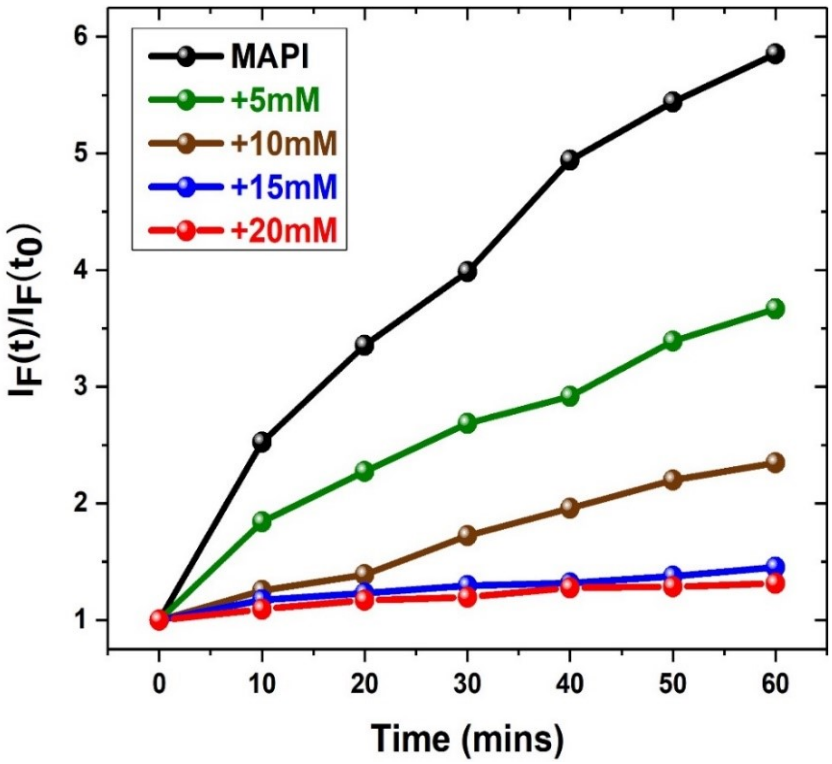


Figure 7-7: Superoxide yield plot comparing the generation of superoxide for $CH_3NH_3PbI_3$ (MAPI) treated with and without phenylethylammonium iodide ($PhEtNH_3I$, PEAI) Iodide Salt Assisted Anti-solvent Treatment (ISAAT) (the iodide salt is first dissolved in IPA and then mixed with diethyl ether as an anti-solvent). The normalised fluorescence intensity increase of the hydroethidine (HE) probe at 610 nm (excitation at 520 nm). $I_F(t)$ is the fluorescence maximum at time t, whilst $I_F(t_0)$ is the background fluorescence intensity. $I_F(t)/ I_F(t_0)$ ratio corresponds to the yield of superoxide generation for perovskite films.

It can be seen obviously that the ISAAT treatment is very helpful in reducing the superoxide formation. The result is in agreement with our previous observation that iodide vacancies play a key role in the superoxide formation. The number of iodide defects that are critical in the superoxide generation is reduced as more PEAI treatment is applied to the MAPbI perovskite layer. More specifically, at 15 mM in concentration, there is almost no superoxide formed within 60 minutes. This implies that major iodide vacancies could be effectively filled with PEAI treatment and little to no oxygen molecules are reduced to form superoxide species. Taken together, the result shows that perovskite films can be stabilized via ISAAT treatment.

The effect of PEAI involved ISAAT treatment on the yield of photo-induced charge separation at MAPI/hole transport material interfaces under light and oxygen was then considered. The rate of charge separation losses has been shown to be directly related to the decay of device efficiency in operating perovskite solar cells.[31] The yield of charge hole-transfer from the perovskite and hole-transport layer, Spiro-OMeTAD, was measured with transient absorption spectroscopy as described in the experimental section in **Chapter 3.** In this study, films without and with different concentrations of PEAI salt in diethyl ether anti-solvent are examined in a structure of glass/mp-Al_2O_3/MAPI (ISAAT)/Spiro-OMeTAD. All samples are probed at 1600 nm followed by excitation at 458 nm. The change in optical density ΔOD as a function of time with 10 minute intervals for all samples are recorded, as shown in Figure 7-8 (a) to (e) and the ΔOD result at 1 μs was detected and normalised against the starting value, at which the samples are fresh and have not been exposed to the degradation conditions. The result is shown in Figure 7-8 (f). It can be clearly observed from Figure 7-8 (a) to (e) that the relation between ΔOD and ageing time (length of time that samples are exposed to oxygen and light condition) is such that the rate of decay is getting progressively slower while increasing the concentration of PEAI in ISAAT treatment as compared with pristine MAPbI. At 15 mM, the rate of decay is minimal, whilst at a lower PEAI concentration, perovskite charge losses are significant within the time frame explored. The normalized charge optical density losses value in Figure 7-8 (f) further confirms this trend. Moreover, the time taken for the charge decay to drop to 50 % of its original value is observed to be 10 minutes for MAPbI and 40 + minutes for ISAAT treatment with 5mM PEAI iodide salt, whilst the values for ISAAT treatment at a higher concentration are beyond 60 minutes. This result further confirmed that the ISAAT treatment enhances film stability to light and oxygen and allows films to retain their optoelectronic properties for longer periods of time.

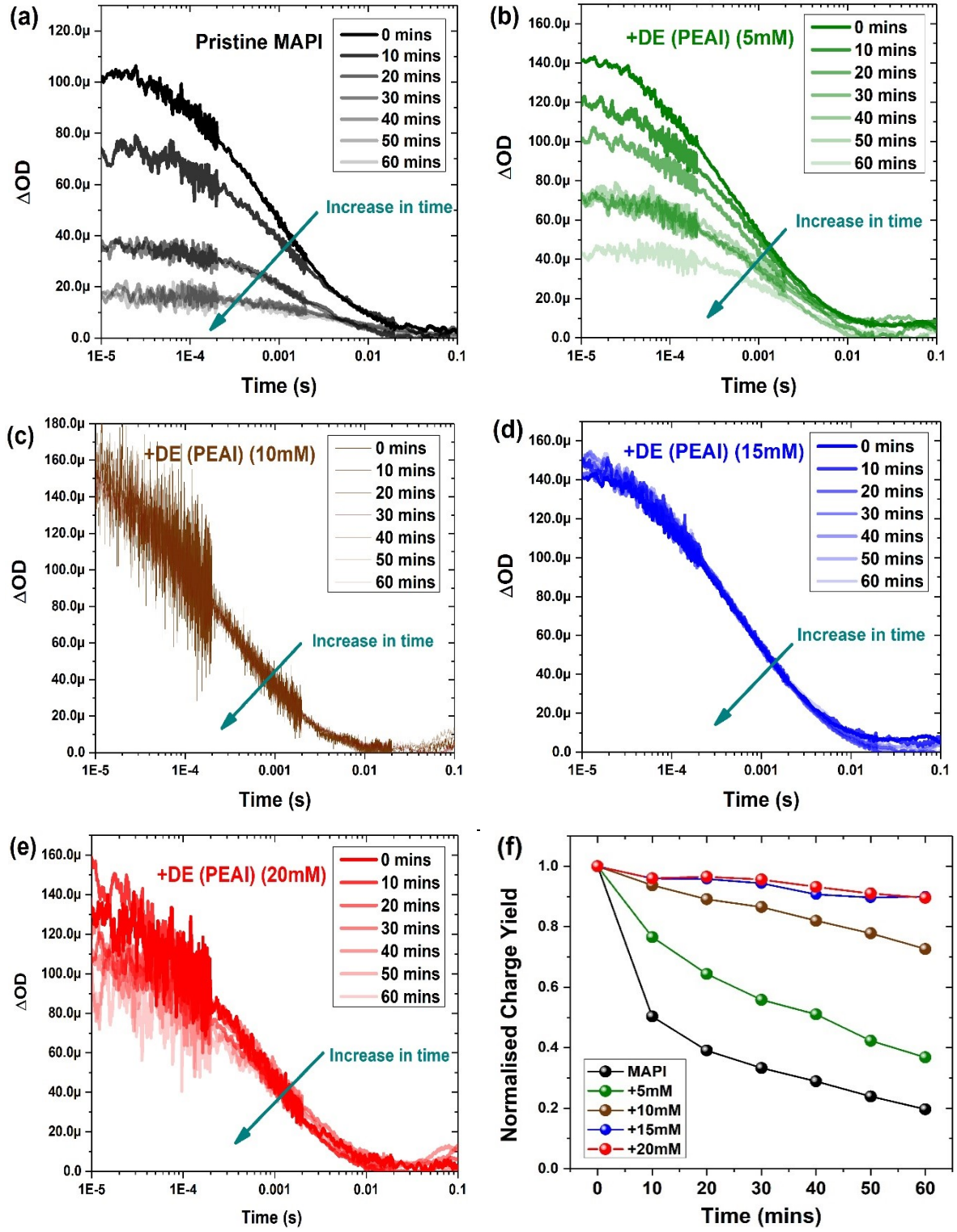


Figure 7-8: Raw transient absorption spectroscopy data, showing the obtained kinetic decay traces for $CH_3NH_3PbI_3$ (MAPI) films **(a)** without PEAI salt and **(b)-(e)** with various concentrations of PEAI Iodide Salt Assisted Anti-solvent Treatment (ISAAT). **(f)** Normalized decay of charge separation losses for the above films over a period of 60 minutes. All films were probed at 1600 nm (tracking concentration of Spiro-OMeTAD hole-polarons) following excitation at 458 nm. (Optical density = ΔOD.)

We next investigated the effect of ISAAT treatment with PEAI on the optical density (ΔOD) prior to degradation. To this end, MAPI perovskite films without ISAAT treatment and with ISAAT treatment containing 15 mM of PEAI are characterized with Transient Absorption Spectroscopy (TAS). The initial amplitude optical density ΔOD as a function of time up to 0.1 seconds for both samples is illustrated in Figure 7-9.

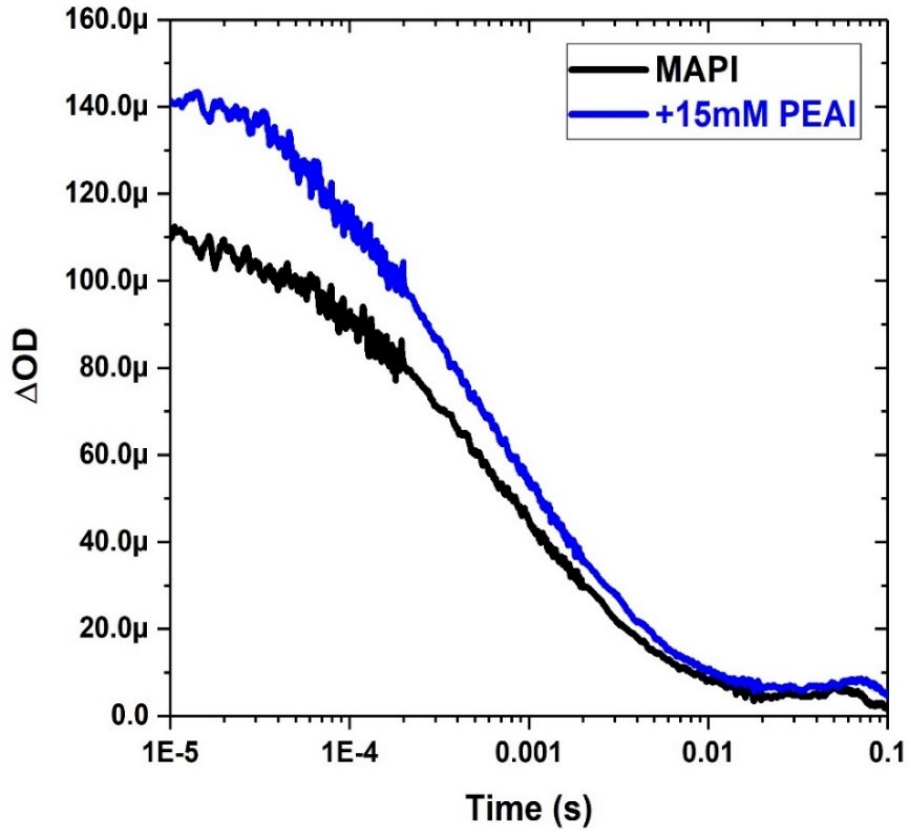


Figure 7-9: Transient absorption spectroscopy kinetic decays of $CH_3NH_3PbI_3$ (MAPI) films without iodide salt coating (black) and with 15 mM PEAI (blue) Iodide Salt Assisted Anti-solvent Treatment (ISAAT). The samples were excited with a pump wavelength of 567 nm and an average pulse power of 25 μJ cm^{-2}. The probe wavelength of 1600 nm was used to probe the resulting holes in Spiro-OMeTAD.

It is worth noting that the decay traces for both two samples presented in Figure 7-9 follow the recombination between the electrons in the TiO_2 layer and holes on the Spiro-OMeTAD layer. It can be seen that the amplitude of hole-transfer (measured as the ΔOD value at 1 μs) is slightly higher in the case of 15 mM PEAI involved ISAAT treatment (blue) than for MAPI without ISAAT treatment. This result suggests that incorporating ISAAT treatment could initiate a more effective charge separation process as opposed to no such treatment. Moreover, the result implies that the ISAAT treatment with an optimum concentration of PEAI iodide salt (15 mM) could potentially achieve devices with higher power conversion

efficiency. Taken together, the ISAAT treatment with PEAI could improve film stability by passivating the iodide vacancies/defects, enlarging the crystal size and retarding the superoxide formation.

The effect of film passivation via ISAAT treatment on the efficiency, stability and reproducibility of the MAPbI perovskite solar cells was then investigated, first by examining device performance using a different concentration of PEAI salt existing in the anti-solvent. In this case, devices without ISAAT treatment and with 5 mM, 10 mM, 15 mM and 20 mM in PEAI concentration in ISAAT treatment were fabricated and current-voltage measurement recorded. The dark and light current-voltage curves and their corresponding External Quantum Efficiency (EQE) spectra are shown in Figure 7-10. The photovoltaic parameters under different scan direction are summarized in Table 7-1. It can be seen that ISAAT treatment with PEAI salt increases device efficiency to a remarkable value. The improvement in device efficiency is correlated with the concentration of PEAI being used in the anti-solvent. A device fabricated with conventional anti-solvent treatment ended up with 13.94 % of device efficiency (FB-SC), with photovoltaic parameters of 1.02 V, 21.27 $mAcm^{-2}$ and 0.64 in V_{OC} (open circuit voltage, J_{sc} (short circuit density) and, FF (Fill Factor) respectively. With the ISAAT treatment, all device parameters are enhanced. At 15 mM, the device reached its highest PCE of 17.93 % (FB-SC), which is ~ 28.6 % improvement of its original device performance. Further increasing in PEAI concentration leads to a drop of PCE back to 14.55 % (FB-SC), which is lower than the value from 15 mM, but still higher than MAPI devices without ISAAT treatment. The corresponding External Quantum Efficiency (EQE) spectrum exhibited in Figure 7-10 (b) further confirmed the result of the current-voltage characterization. All devices can achieve a broad plateau of EQE values over 85 % in the visible range from 450 to 750 nm, demonstrating excellent charge carrier transportation efficiency, which is in good agreement with the results obtained from steady-state photoluminescence (PL) and time-resolved PL. Further to this, increased PEAI concentration leads to a gradual enhancement of EQE values, which provides evidence of improved efficiency from J-V curves. Moreover, the integrated J_{sc} calculated from EQE spectrum are within 2% deviation as compared with the J_{sc} values from current-voltage measurement, which further confirmed the accuracy of the J-V measurement.

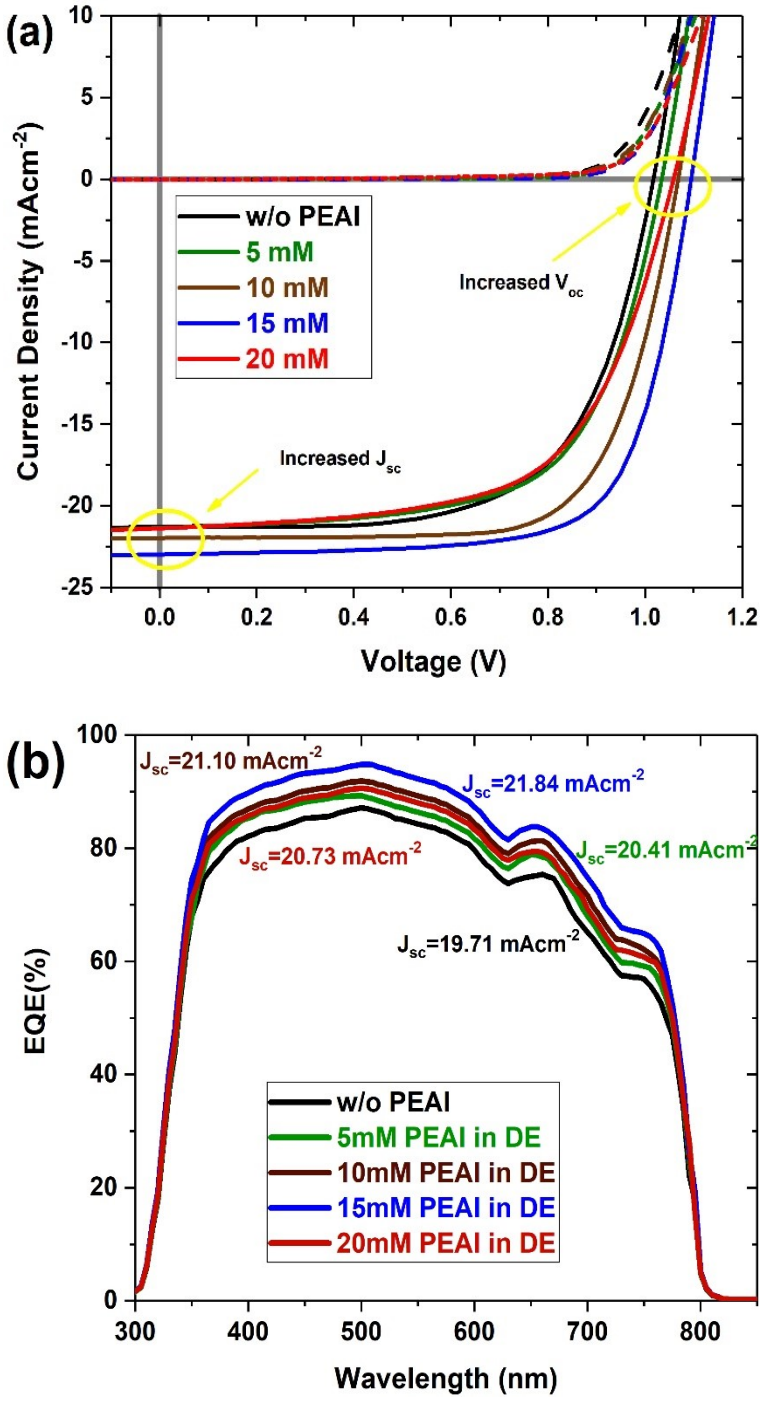


Figure 7-10: (a) Current-voltage measurement of initial performances of devices without and with various concentrations of PEAI Iodide Salt Assisted Anti-solvent Treatment (ISAAT). All devices are fabricated in [FTO/compact-TiO_2/mesoporous-TiO_2/MAPI(ISAAT)/Spiro-OMeTAD/Au] architecture and are recorded under reverse scan (FB-SC). (b) External Quantum Efficiency (EQE) spectra of the corresponding devices.

Table 7-1: Device performance parameters of the initial performance for devices based on the various concentrations of PEAI Iodide Salt Assisted Anti-solvent Treatment (ISAAT) coated on $CH_3NH_3PbI_3$ (MAPI) perovskite films. (FB-SC = reverse scan; SC-FB forward scan; V_{oc} = open circuit voltage; J_{sc}, = short circuit density; FF = Fill Factor; PCE = Power Conversion Efficiency.)

Device Type	Pixel Area (cm^2)	Scan Direction	V_{oc} (V)	J_{sc} ($mAcm^{-2}$)	FF	PCE (%)
MAPI (Ref.)	0.12	FB-SC	1.02	21.27	0.64	13.94
		SC-FB	0.96	18.63	0.60	10.63
+PEAI (5mM)	0.12	FB-SC	1.03	21.36	0.64	14.12
		SC-FB	1.03	21.31	0.55	12.18
+PEAI (10mM)	0.12	FB-SC	1.07	21.97	0.70	16.54
		SC-FB	1.06	20.91	0.69	15.31
+PEAI (15mM)	0.12	FB-SC	1.09	22.97	0.71	17.93
		SC-FB	1.08	22.70	0.70	17.05
+PEAI (20mM)	0.12	FB-SC	1.06	21.93	0.63	14.55
		SC-FB	1.06	21.38	0.61	13.82

Next, we investigated the hysteresis behaviour on MAPbI solar cells fabricated without and with varied concentrations of PEAI in the ISAAT treatment, as shown in Figure 7-11. The hysteresis effect is observed in all devices, but the severity is different with respect to the variation of PEAI composition in anti-solvent. To better describe the hysteresis effect on device performance, we use the equation described from **Chapter 5** to work out the difference factor for each solar cell.

As shown in Figure 7-11, at a standard scan rate of 0.125 V/s, all devices exhibit a certain degree of hysteresis. Specifically, a value of 23.7 % for the difference factor is measured for pristine MAPbI cell, whereas for the device under ISAAT treatment with 5 mM PEAI the value drops dramatically to 13.7%. This indicates that using ISAAT treatment, even with a small amount of PEAI could effectively alleviate the hysteresis effect. Further increasing the PEAI reduces even more hysteresis. The difference factor for 10 mM PEAI existing in the anti-solvent is 7.43 %, and for 15 mM of PEAI the difference factor reaches a minimum of 4.91 %. Further increase PEAI to 20 mM again is harmful to hysteresis, with the difference factor rising up to 5.01 %.

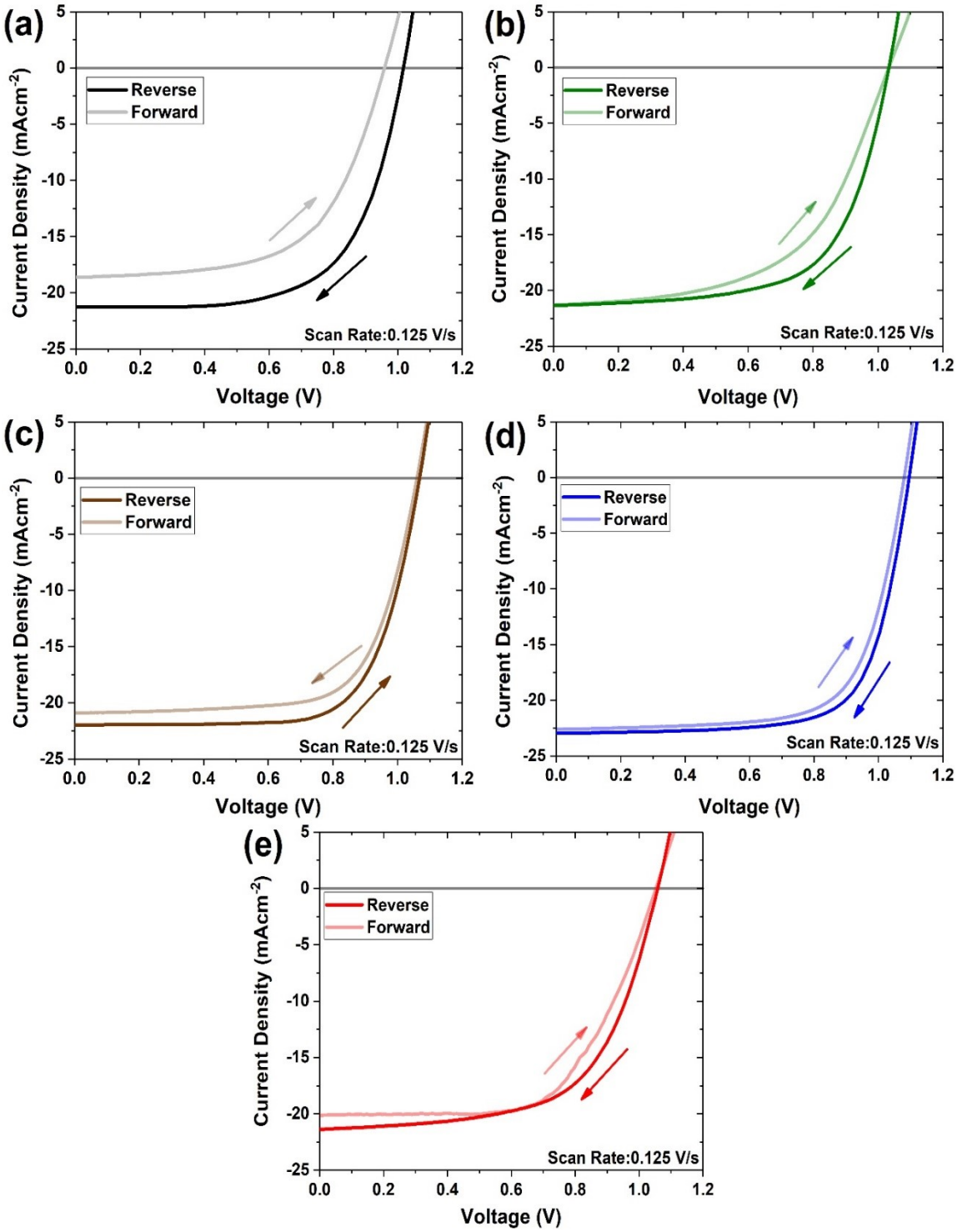


Figure 7-11: Influence of the PEAI concentration on current-voltage hysteresis of the MAPI devices. The devices are measured in reverse scan (FB-SC) and forward scan (SC-FB) under simulated AM1.5 100 mW cm^{-2} sunlight with (a) MAPbI (black), (b) 5 mM (green), (c) 10 mM (brown), (d) 15 mM (blue) and (e) 20 mM (red) PEAI salt contained in anti-solvent on MAPI perovskite solar cells. The scan rate is 0.125 V/s for all devices.

In addition to the pursuit of satisfactory device performance, ensuring the long term stability of the perovskite solar cells is a major concern of our project. Previous observations have shown that the ISAAT is helpful for improving perovskite film stability, whether it is effective on solar cells stability becomes the next objective. Accordingly, the ISAAT treatment effect on MAPI perovskite device stability was next considered. Similarly to studies in **Chapters 5** and **6**, we examined device stability both in the short run (within five hours) and in the long run (within 500 hours) due to different oxygen diffusion mechanisms.[1] As compared with no ISAAT treatment in MAPI perovskite solar cell, devices with ISAAT treatment directly lead to improvement in the solar cell stability. More importantly, from Figure 7-12 (a) it is clear that the enhanced in device stability is correlated with the concentration of iodide salt in the anti-solvent. In particular, a device with 15 mM of PEAI shows best short-term device stability where the efficiency remains 96 % of its original value before degradation test, indicating little to no degradation within five hours. The long-term stability test in Figure 7-12 (b) further compares the stability of two different PEAI coatings. It can be seen that although both PEAI treatment leads to dramatic improvements in device stability in the long run relative to MAPbI device without PEAI coating, the ISAAT treatment exhibits even higher stability than using direct PEAI coating, with still 90 % efficiency remaining after 500 hours. The origin of this improvement is possibly due to the more effective iodide defects passivation obtained from ISAAT treatment, causing more inhibition on superoxide formation. It is worth pointing out that the optimum PEAI concentration for the conventional method is 10 mM, whereas for novel ISAAT the optimum concentration for PEAI is 15 mM. This difference in concentration implies that the novel treatment could potentially deliver more PEAI species into the perovskite layer and help to passivate more iodide vacancies or trap sites. The results on stability, as well as those obtained from J-V characterization and hysteresis measurement provide solid evidence that the ISAAT treatment is more effective than direct PEAI coating.

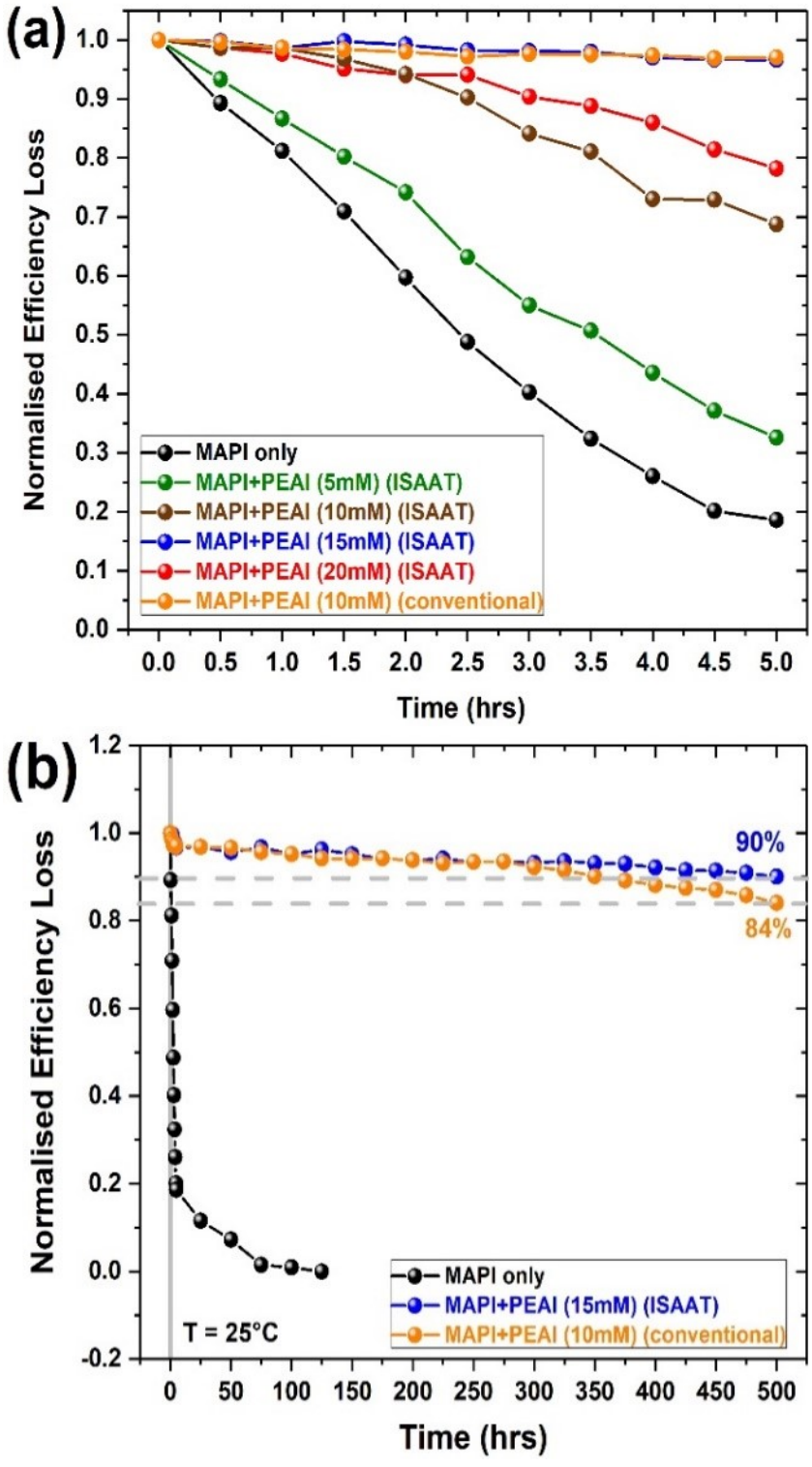


Figure 7-12: (a) Short term stability test (normalised efficiency loss) for devices with and without phenylethylammonium iodide ($PhEtNH_3I$, PEAI) Iodide Salt Assisted Anti-solvent Treatment (ISAAT) in various concentrations of 5 mM (green), 10 mM (brown), 15 mM (blue) and 20 mM (red) for a period of 5 hours. (b) Long term stability test for devices employing MAPI (black) without iodide salt coating, with 15 mM PEAI Iodide Salt Assisted Anti-solvent Treatment (ISAAT) (blue) and with 10 mM of PEAI employing conventional salt coating (orange) for a period of 500 hours. The temperature was kept at a constant 25°C.

In **Chapter 6**, we have pointed out that the disadvantage of using direct PEAI coating is that it introduced more fabrication steps as compared with standard method, and resulted in less device reproducibility as it increases uncertainty in the iodide salt loading step. In contrast, the novel ISAAT treatment eliminates the extra iodide salt loading step so that the fabrication is as easy as making pure MAPI layer. Therefore, the final key question is will this facile technique more reproducible than the conventional PEAI coating method? To verify this, we evaluated the device performance from a group of 54 devices with 15 mM of PEAI (optimum concentration) in ISAAT treatment and compared them with another group of 54 reference devices in which direct PEAI coating is used. The statistical distribution of the photovoltiac parameters of V_{oc}, J_{sc}, FF and PCE from two groups of solar cells are shown in Figure 7-13. It can be concluded that devices fabricated with ISAAT treatment have higher efficiency and are more reproducible than those made using conventional PEAI treatment. This result is in good agreement with our observations from J-V measurement.

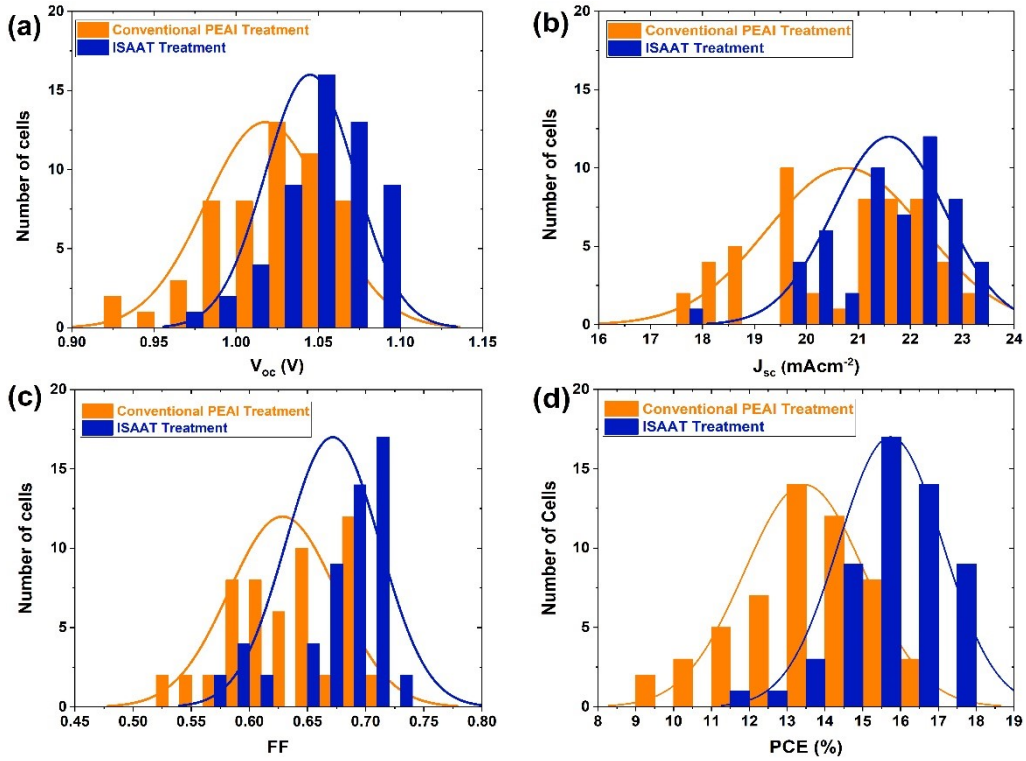


Figure 7-13: Histogram of the J-V measurement in reverse scan (FB-SC) obtained for 54 devices with conventional PEAI treatment (orange) and 54 devices with novel ISAAT treatment, including comparison of all photovoltaic parameters (a) V_{oc}, (b) J_{sc}, (c) FF and (d) PCE.

7.5. Conclusion

In this chapter, a pioneered new approach of passivation strategy named Iodide Salt Assisted Anti-solvent Treatment (ISAAT) has been demonstrated. For this study, the PEAI salt is still utilized as a passivating agent, but is mixed into diethyl ether (DE) anti-solvent piror to MAPI layer formation rather than conventional direct coating. To summarize, the results demonstrate that under appropriate concentration, the ISAAT treatment could effectively improve the absorption intensity and lower charge carrier recombination of perovskite photoactive layer. It also reduces superoxide generation and slow down photo- and oxygen-induced degradation on the MAPI active layer, hence retard film and device degradation. Moreover, the amount of PEAI applied is still a key factor on solar cell performance and can be tailored to achieve best device efficiency. It is observed that the optimum solar cells are obtained when 15 mM concentration of PEAI is involved in ISAAT treatment, which leads to a power conversion efficiency (PCE) of 17.93 % and only a 4.91 % difference factor of hysteresis. This greater in efficiency relative to pristine MAPI device is likely due to the ISAAT treatment enlarges crystallite sizes and filled vacancies at grain boundaries of the MAPI crystals, which lower charge carrier recombination traps and enable improved device performance. The alleviation in hysteresis effect of using ISAAT as compared with conventional PEAI coating remains obscure, but is likely due to the reduction in ion migration upon more vacancies/defects being filled using novel treatment. The lifetime studies on devices show that under operation in atmospheric conditions, the ISAAT treatment could offer greater efficiency and stability for MAPI perovskite solar cells both in terms of short run test (5 hours) and long run test (500 hours). The ISAAT treatment could yield devices with long-term stability even better than using direct PEAI coating. This can be attuibuted to the fact that under ISAAT treatment, the PEAI passivating agent could fill iodide vacancies both in the surface and in the bulk side of the MAPI crystals. Therefore, it takes even longer time for oxygen diffusion into the MAPI crystals and further lowers the yields of superoxide. Finally, this ISAAT treatment exhibited more reproducibility than direct PEAI coating due to easier fabrication steps. This facile and effective treatment technique with excellent device performance, in the long run, renders a significant impact for future solar cell design with greater efficiency, reproducibility and stability.

7.6. References

[1] N. Aristidou, C. Eames, I. Sanchez-Molina, X. Bu, J. Kosco, M.S. Islam, S.A. Haque, *Nature Communications* **2017**, *8,* 15218.

[2] N. Aristidou, I. Sanchez-Molina, T. Chotchuangchutchaval, M. Brown, L. Martinez, T. Rath, S.A. Haque, *Angewandte Chemie* **2015**, *127,* 8326.

[3] D. Bryant, N. Aristidou, S. Pont, I. Sanchez-Molina, T. Chotchunangatchaval, S. Wheeler, J.R. Durrant, S.A. Haque, *Energy & Environmental Science* **2016**, *9,* 1655.

[4] K.M. Boopathi, R. Mohan, T.-Y. Huang, W. Budiawan, M.-Y. Lin, C.-H. Lee, K.-C. Ho, C.-W. Chu, *Journal of Materials Chemistry A* **2016**, *4,* 1591.

[5] P. Chen, E. Wang, X. Yin, H. Xie, M. Que, B. Gao, W. Que, *Journal of Colloid and Interface Science* **2018**, *532,* 182.

[6] D.-Y. Son, J.-W. Lee, Y.J. Choi, I.-H. Jang, S. Lee, P.J. Yoo, H. Shin, N. Ahn, M. Choi, D. Kim, *Nature Energy* **2016**, *1,* 16081.

[7] F.T. O'Mahony, Y.H. Lee, C. Jellett, S. Dmitrov, D.T. Bryant, J.R. Durrant, B.C. O'Regan, M. Graetzel, M.K. Nazeeruddin, S.A. Haque, *Journal of Materials Chemistry A* **2015**, *3,* 7219.

[8] K. Vanheusden, W. Warren, C. Seager, D. Tallant, J. Voigt, B. Gnade, *Journal of Applied Physics* **1996**, *79,* 7983.

[9] L. Wang, D. Moghe, S. Hafezian, P. Chen, M. Young, M. Elinski, L. Martinu, S.p. Kéna-Cohen, R.R. Lunt, *ACS Applied Materials & Interfaces* **2016**, *8,* 23086.

[10] M.I. Saidaminov, A.L. Abdelhady, B. Murali, E. Alarousu, V.M. Burlakov, W. Peng, I. Dursun, L. Wang, Y. He, G. Maculan, *Nature Communications* **2015**, *6,* 7586.

[11] Z. Wang, Z. Shi, T. Li, Y. Chen, W. Huang, *Angewandte Chemie International Edition* **2017**, *56,* 1190.

[12] Q. Chen, H. Zhou, T.-B. Song, S. Luo, Z. Hong, H.-S. Duan, L. Dou, Y. Liu, Y. Yang, *Nano Letters* **2014**, *14,* 4158.

[13] I. Hwang, I. Jeong, J. Lee, M.J. Ko, K. Yong, *ACS Applied Materials & Interfaces* **2015**, *7,* 17330.

[14] X. Fang, J. Ding, N. Yuan, P. Sun, M. Lv, G. Ding, C. Zhu, *Physical Chemistry Chemical Physics* **2017**, *19,* 6057.

[15] Z. Wu, S.R. Raga, E.J. Juarez-Perez, X. Yao, Y. Jiang, L.K. Ono, Z. Ning, H. Tian, Y. Qi, *Advanced Materials* **2018**, *30,* 1703670.

[16] P. Zhao, B.J. Kim, H.S. Jung, *Materials Today Energy* **2018**.

[17] C. Ran, Y. Chen, W. Gao, M. Wang, L. Dai, *Journal of Materials Chemistry A* **2016**, *4,* 8566.

[18] Y. Wang, S. Dong, Y. Miao, D. Li, W. Qin, H. Cao, L. Yang, L. Li, S. Yin, *IEEE Journal of Photovoltaics* **2017**, *7,* 550.

[19] G. Kakavelakis, T. Maksudov, D. Konios, I. Paradisanos, G. Kioseoglou, E. Stratakis, E. Kymakis, *Advanced Energy Materials* **2017**, *7,* 1602120.

[20] Z. Zhu, Q. Xue, H. He, K. Jiang, Z. Hu, Y. Bai, T. Zhang, S. Xiao, K. Gundogdu, B.R. Gautam, *Advanced Science* **2016**, *3,* 1500353.

[21] L. Wang, C. McCleese, A. Kovalsky, Y. Zhao, C. Burda, *Journal of the American Chemical Society* **2014**, *136,* 12205.

[22] C. Wang, D. Zhao, Y. Yu, N. Shrestha, C.R. Grice, W. Liao, A.J. Cimaroli, J. Chen, R.J. Ellingson, X. Zhao, *Nano Energy* **2017**, *35,* 223.

[23] T. Supasai, N. Rujisamphan, K. Ullrich, A. Chemseddine, T. Dittrich, *Applied Physics Letters* **2013**, *103,* 183906.

[24] T.J. Jacobsson, J.-P. Correa-Baena, E. Halvani Anaraki, B. Philippe, S.D. Stranks, M.E. Bouduban, W. Tress, K. Schenk, J.l. Teuscher, J.-E. Moser, *Journal of the American Chemical Society* **2016**, *138,* 10331.

[25] F. Jiang, Y. Rong, H. Liu, T. Liu, L. Mao, W. Meng, F. Qin, Y. Jiang, B. Luo, S. Xiong, *Advanced Functional Materials* **2016**, *26,* 8119.

[26] K. Tanaka, T. Takahashi, T. Ban, T. Kondo, K. Uchida, N. Miura, *Solid state Communications* **2003**, *127,* 619.

[27] M.M. Lee, J. Teuscher, T. Miyasaka, T.N. Murakami, H.J. Snaith, *Science* **2012**, 1228604.

[28] M.L. Agiorgousis, Y.-Y. Sun, H. Zeng, S. Zhang, *Journal of the American Chemical Society* **2014**, *136,* 14570.

[29] J.I. Langford,A. Wilson, *Journal of Applied Crystallography* **1978**, *11,* 102.

[30] R.L. Milot, R.J. Sutton, G.E. Eperon, A.A. Haghighirad, J. Martinez Hardigree, L. Miranda, H.J. Snaith, M.B. Johnston, L.M. Herz, *Nano Letters* **2016**, *16,* 7001.

[31] D. Bryant, N. Aristidou, S. Pont, I. Sanchez-Molina, T. Chotchuangchutchaval, S. Wheeler, J.R. Durrant, S.A. Haque, *Energy & Environmental Science* **2016**, *9,* 1850.

CHAPTER 8

CONCLUSIONS AND FUTURE OUTLOOK

Over the past few years, organic-inorganic halide perovskite materials have emerged as attractive alternatives to conventional photovoltaic devices. Nevertheless, the operational stability of this type of device remains a big challenge for both scientific and industrial communities. The principle objective of this thesis has been to build up fundamental understanding on primary mechanism behind the degradation of the perovskite solar cells under a combination of external environmental conditions.

With this goal in mind, the state of the history and development of solar cells was reviewed. In particular, a review was made on the recent progress on perovskite solar cells and on the stability of the perovskite solar cells from various external conditions. From these reviews, the research area was identified where gaps in our knowledge are hindering the development of more stable solar cells, that is, to have in-depth understanding on the mechanistic insight of perovskite photoactive layers and their possible impacts on the efficiency and stability of the corresponding solar cells under a combination of light illumination and oxygen stress.

Chapter 4 began by establishing a standard fabrication procedure to obtain reproducible and satisfied perovskite solar cells as this builds up the foundation for future research. Meanwhile, the influence of a variety of factors were studied, which helped to gain more knowledge on the interaction of interfaces different interfaces and inspired my further research. Subsequently, we observed that under light and oxygen, the active superoxide (O_2^-) species could directly affect the stability of perovskite solar cells and the rate of this degradation process is determined by perovskite crystal size: devices with smaller size in photoactive layer resulted in higher yield of superoxide, which cause more rapid device degradation. Therefore, minimizing the superoxide formation becomes a clear research objective.

Chapter 5 is based on the knowledge obtained from earlier results. In this chapter, attention is paid on further identifying the most energetically favourable site for superoxide generation, and realized that it was the iodide vacancies, particularly present on the surface of the perovskite crystals, is a key elecment that leads to superoxide formation. This suggests that for obtaining more stable perovskite solar cells, effort should be made to eliminate or to reduce the suface iodide defects in order to inhibit the generation of superoxide on exposure to light and oxygen. This particular objective in turn led to a development of a suface passivation technique, in which a methylammonium iodide (MAI) is coated on top of the MAPI perovskite films. Further investigation shows that this method could effectively reduce the surface iodide defects and suppress the superoxide formation. The theory also applicable to MAPI based solar cells with Spiro-OMeTAD as hole transfer materials (HTMs). The strength of this thin film surface passivation technique was then verified on the Br-I mixed halide perovskite solar cells, and proved that it can also help to improve the stability by effectively decreasing the iodide defects present in the surface of active layer. However, MAI salt coating method is tested to lower the device overall performance for both standard and Br-I mixed halide perovskite solar cells and a compromise have to be made for devices with greater stability. This motivated the search for alternative passivating agents.

Chapters 6 and 7 bring more focus on application and modification of the established surface passivation techniques. Through a combination of microscopy, spectroscopy techniques and solar cell device optoelectronic characterizations it was shown that the PEAI coatings could enhance the stability of MAPI perovskite solar cells (PSCs). Thin-film passivation with a 10 mM concentration of phenylethylammonium iodide (PEAI) salt could effectively passivate the iodide vacancies at the surface of the MAPI photoactive layer. This leads to a reduction of the superoxide yield and directly resulted in the improvement of device stability.PEAI salt can effectively reduce the surface defects, inhibiting superoxide formation and alleviate the hysteresis effect of MAPI perovskite solar cells, hence improve device stability while maintaining high efficiency. This suggests that PEAI is more suitable as a surface passivation agent the previously used MAI salt. However, both PEAI and MAI treatment involved with additional deposition step in the fabricaton process. The analysis on reproducibility of PEAI coating for devices has revealed that this additional step causes an obvious bias in the optoelectronic parameters, leading to relatively larger deviation as compared with MAPI solar cells without treatment. This led to the development of a novel iodide salt assisted anti-solvent treatment (ISAAT). The PEAI salt was selected as the

passivation agent and mixed it into diethyl ether (DE) anti-solvent. The result shows that ISAAT treatment could effectively fill in the iodide vacancies, improve film crystallinity and enlarge the crystal size, thus reduce formation of superoxide species upon exposing MAPI photoactive layer to light and oxygen. The device study shows that ISAAT treatment could also obtain higher efficiency and long term stability than MAPI perovskite solar cells. The optimum solar cells are obtained when 15 mM concentration of PEAI is involved in ISAAT treatment, which leads to a champion device performance of 17.93 % and only a 4.91 % difference factor for hysteresis. More importantly, this ISAAT treatment is simple and more reproducible than direct PEAI coating.

In performing this research, some of the research bottlenecks identified in **Chapter 2** have been addressed. Whilst introducing some achievements obtained from this research, it is necessary to make some suggestions on additional work that need to carry on after this project. First, the main focus of this project was to identify superoxide formation under a combination of light and oxygen, whether or not this active species are more activated from other combinations of factors such as moisture/light, temperature/light etc. remains unclear and require further investigation. Second, the iodide vacancies exist both in surface and in the bulk side of the perovskite crystal. Although the surface defects play a decisive role on the stablity of the devices, the fact that more defects exist in the bulk side than at the surface means that there is a large potential to develop a technique that could allow agent to passivate the bulk side defects, which will resulted in more defects trap sites being filled and potentially obtain more stable devices. Third, the PEAI salt used in our project resulted in formation of 3D perovskite and exhibited great stability, whereas previous research had shown that PEAI incorporated directly into the perovskite precursor solution forms 2D or 2D-3D lower dimensional perovskites. It is likely that the ways of introducing the PEAI materials could potentially alter the dimension of the perovskite crystal structure, this need further study to identify.

To sum up, the mechanistic insight that was built as well as the simplicity of the treatment technique developed for this project, in the long run, renders a great opportunity for future solar cell development with greater efficiency, reproducibility and stability.